



HAL
open science

Development of a 88Sr atom interferometer

Chen-Hao Feng

► **To cite this version:**

Chen-Hao Feng. Development of a 88Sr atom interferometer. Physics [physics]. Université de Bordeaux, 2021. English. NNT : 2021BORD0241 . tel-03464296

HAL Id: tel-03464296

<https://theses.hal.science/tel-03464296v1>

Submitted on 3 Dec 2021

HAL is a multi-disciplinary open access archive for the deposit and dissemination of scientific research documents, whether they are published or not. The documents may come from teaching and research institutions in France or abroad, or from public or private research centers.

L'archive ouverte pluridisciplinaire **HAL**, est destinée au dépôt et à la diffusion de documents scientifiques de niveau recherche, publiés ou non, émanant des établissements d'enseignement et de recherche français ou étrangers, des laboratoires publics ou privés.

THÈSE PRÉSENTÉE
POUR OBTENIR LE GRADE DE
DOCTEUR
DE L'UNIVERSITÉ DE BORDEAUX
ECOLE DOCTORALE SCIENCES PHYSIQUES ET DE
L'INGÉNIEUR
LASERS, MATIÈRE ET NANOSCIENCES

Par **Chen-Hao FENG**

Développement d'un interféromètre atomique avec atomes de
 ^{88}Sr

Sous la direction de : **Andrea BERTOLDI**
Co-directeur : **Philippe BOUYER**

October 25th 2021

Membres du jury :

M. Kai BONGS	University of Birmingham	Rapporteur
M. Florian SCHRECK	University of Amsterdam	Rapporteur
M. Philippe TAMARAT	Université de Bordeaux	Président
M. Timothy KOVACHY	Northwestern University	Examineur
M. Sebastian BLATT	Max-Planck-Institute for Quantum Optics	Examineur
M. Andrea BERTOLDI	Université de Bordeaux	Directeur
M. Philippe BOUYER	Université de Bordeaux	Co-directeur

Titre : Développement d'un interféromètre atomique avec atomes de ^{88}Sr

Résumé : L'interférométrie atomique est une technologie quantique en pleine maturité qui fournit l'une des approches les plus précises pour explorer la physique fondamentale, par exemple pour rechercher la matière noire, et un jour pour observer les ondes gravitationnelles dans la gamme de fréquences de 10 mHz à 10 Hz. Les interféromètres atomiques standard utilisent des transitions à deux photons de Bragg ou de Raman pour la manipulation cohérente des ondes de matière. Dans une configuration de Michelson pour la détection des ondes gravitationnelles à l'aide d'atomes, deux bras orthogonaux sont utilisés. Deux bras orthogonaux sont construits pour rejeter le bruit du laser, de la même manière que les interféromètres optiques. Les interféromètres atomiques qui utilisent une transition d'horloge optique pour la manipulation cohérente sont moins affectés par le bruit technique du laser et, par conséquent, les détecteurs à ligne de base unique deviennent plus efficaces. Les détecteurs à ligne de base unique deviennent réalisables.

Au LP2N, nous construisons un gradiomètre verticale du champ de gravité sur l'interférométrie atomique en utilisant des atomes de strontium sondés sur une transition d'horloge. Le dispositif expérimental final mettra en œuvre une fontaine atomique de 6 mètres de haut pour réaliser la gradiométrie avec deux ou plusieurs nuages atomiques séparés.

Dans ma thèse, je présente la réalisation du dispositif expérimental dans tous ses sous-systèmes, et les premières expériences avec des atomes à une température autour du millikelvin, obtenues avec le premier étage de refroidissement qui utilise de la lumière bleue. Le système laser pour la deuxième phase de refroidissement rouge et pour la manipulation cohérente est prêt ; entre-temps, nous avons réalisé un ralentisseur Zeeman à double fréquence qui améliore le flux atomique d'un facteur six. Nous présentons également l'étude d'un schéma original permettant d'obtenir une interaction lumière-atome pulsée et rapide dans une cavité à largeur de raie étroite en exploitant le décalage de Stark comme un commutateur à large bande passante ; cette technique pourrait ouvrir la voie à l'utilisation de cavités à largeur de raie étroite - et notamment à leur montée en puissance élevée - dans plusieurs contextes, comme l'interférométrie atomique et l'information quantique.

Mots clés :

interférométrie atomique
métaux alcalino-terreux
interactions atome-cavité

UMR 5298 – Institut d'Optique d'Aquitaine. Université de Bordeaux. Rue François Mitterrand -
33400 TALENCE.

&

Laboratoire Photonique, Numérique et Nanosciences (LP2N)

Title : Development of a ^{88}Sr -atom interferometer

Abstract : Atom interferometry is a maturing quantum technology which provides one of the most precise approaches to explore fundamental physics, e.g. to search for dark matter, and one day to observe gravitational waves in the frequency range from 10 mHz - 10 Hz. Standard atom interferometers use Bragg or Raman two-photon transitions for the coherent manipulation of matter waves. In a Michelson configuration for atom-aided gravitational waves detection, two orthogonal arms are built to reject laser noise, in the same way as optical interferometers. Atom interferometers utilizing an optical clock transition for coherent manipulation are less affected by the technical noise of the laser, and as a result that single baseline detectors become feasible.

At LP2N, we are building a vertical gravity-gradiometer based on atom interferometry using strontium atoms probed on such a clock transition. The final experimental setup will implement a 6-meter tall atomic fountain to realize gradiometry with two or more separated atomic clouds.

In my dissertation, I present the realization of the experimental setup in all its sub-systems, and the first experiments with atoms at millikelvin temperature obtained with the first cooling stage with blue light. The laser system for the second red cooling phase and for the coherent manipulation is ready; meanwhile, we realized a dual-frequency Zeeman slower that improves the atomic flux by a factor of six. We also present a study of an original scheme to achieve pulsed and fast light-atom interaction in a narrow-linewidth cavity by exploiting the Stark shift as a high bandwidth switch; this technique could open to the use of narrow-linewidth cavities – and notably their high power buildup - in several contexts, like atom interferometry and quantum information.

Keywords :

atom interferometry

alkaline-earth metals

atom-cavity interactions

**UMR 5298 – Institut d’Optique d’Aquitaine. Université de Bordeaux. Rue François Mitterrand -
33400 TALENCE.**

&

Laboratoire Photonique, Numérique et Nanosciences (LP2N)

Acknowledgements

This thesis work is based on the ALCALINF project developed in the Laboratoire Photonique Numérique et Nanosciences (LP2N), and supported by the French National Research Agency (ANR).

I genially thank my thesis director Andrea BERTOLDI. The day-to-day scientific guidance he offered from the beginning ensures the possibility of completing my PhD project with fruitful results. I want to thank Marco PREVEDELLI, from whom I learned a lot about science plus the rigorous and modest attitude to research. I also would like to thank my thesis co-director and the group leader Philippe BOUYER; the scientific exchanges are valuable. Many thanks to the jury members, my reporters Kai BONGS and Florian SCHRECK, my examiners Timothy KOVACHY and Sebastian BLATT, and the jury president Philippe TAMARAT. They took their precious time to evaluate my work.

I appreciate the delightful communications and teamwork with Paul ROBERT, who joined us as a PhD student to continue the ALCALINF project in the last year of my thesis. I want to send gratefulness as well to Dylan SABULSKY. He offered kindness to read my manuscript with his sharp mind and critical view, introducing different aspects of thesis writing.

I thank all my colleagues from the BIARO team with Hodei, Devang, Max, Grigor, Jeanvan, and Louisa; colleagues from the MIGA team with Benjamin, Xinhao, Joseph, and Grégoire; the AUFRONS team with Simon, Vincent, Romain, Jean-Baptiste, Guillaume, Adèle, and Maxime; the iXAtom team with Brynle, Simon, Pierrick, and Quentin; also the colleagues from ICE team with Baptiste, Gabriel, Romain, Vincent, and Célia. All of you people make the Cold Atom in Bordeaux (CAB) a great platform to explore different branches of cold atom science.

Also, I acknowledge the mechanic support from Philippe, our electronics technicians Arnaud and Jean-Hugues, and the administrative support from Stéphanie and Fabien.

Last but not least, I would like to thank my family, who is my backbone when I pursue my professional career, and my friend Bruno, who shows up in my life at important moments and lightens up my way in the darkness. Special thanks are sent to Lingling, who accompanied me to go through the Master and PhD time and encouraged me to encounter difficulties. I also feel grateful to Luara, Shu Li, Yingjing, Liangying, Wenjing, Yunuo, Michel, Jean-Michel, Hanyu, Xiangtai, Jian Zhang, Shuai Liu, Lei Hou, and Ming Fu. Thank you for all your warmth to make me feel settled down, especially in the first winter after leaving home and arriving in France.

Contents

Introduction	5
1 Atom interferometry with clock transitions	8
1.1 Atom interferometry	9
1.1.1 Quantum probes: cold atoms	9
1.1.2 Two-photon transition	11
1.1.3 Single-photon transition	12
1.2 ALCALINF	14
1.2.1 Experimental platform	15
1.2.2 Atom optics	16
1.3 Prospects for clock transition inteferometry: AEDGE	17
1.3.1 Dark matter	19
1.3.2 Gravitational waves	20
1.3.2.1 Cosmological sources	20
1.3.2.2 Detectors	21
2 The sub-microkelvin ⁸⁸Sr-atom interferometer	28
2.1 Strontium	29
2.1.1 Natural abundance	29
2.1.2 The atomic structure of strontium	30
2.1.2.1 The first-stage cooling transition	31
2.1.2.2 Repumping transitions	31
2.1.2.3 The second-stage cooling transition	32
2.1.2.4 The clock transition	32
2.1.2.5 The dark state	33
2.1.2.6 Isotopic shifts	33
2.1.3 The sensitivity to magnetic field	36
2.2 The magneto-optical trap	36

2.2.1	The blue MOT	37
2.2.2	The red MOT	37
2.3	The coherent manipulation on the clock line	39
3	Experimental apparatus	40
3.1	Vacuum system	43
3.1.1	Atomic source	43
3.1.1.1	The oven	43
3.1.1.2	The 2D MOT	44
3.1.1.3	The Zeeman slower	44
3.1.1.4	The pumping stages	45
3.1.2	Science cell	46
3.2	Magnetic field coils	46
3.3	High-power and frequency-stabilized laser at 461 nm	49
3.3.1	1 W laser at 461 nm by frequency doubling	49
3.3.1.1	Frequency-doubling system	50
3.3.1.2	Design for the cavity	53
3.3.1.3	Conversion efficiency	55
3.3.1.4	Stability	56
3.3.1.5	Relative intensity noise	57
3.3.1.6	Geometrical beam shape	59
3.3.1.7	Beat-note locking	59
3.3.2	Optical power enhancement by injection locking	61
3.3.2.1	Injection locking realization	62
3.3.2.2	Spatial corrections of laser beam	66
3.3.2.3	The laser diode temperature controller	66
3.3.2.4	The laser diode current controller	69
3.3.2.5	Long-term stability improvement under consideration	70
3.3.3	Doppler-free blue spectroscopy at $^1S_0 - ^1P_1$ transition	71
3.3.3.1	Locking of the blue laser system to the $^1S_0 - ^1P_1$ transition	72
3.4	Narrow-linewidth and frequency-stabilized laser at 689 nm and 698 nm	77
3.4.1	Linewidth narrowing of the red-cooling laser and the clock laser	79
3.4.2	Doppler-free red spectroscopy at at $^1S_0 - ^3P_1$ transition	82
3.4.3	Optical cavity drift cancellation through red spectroscopy	84
3.5	Repumpers at 707 nm and 679 nm	87

3.5.1	Wavemeter-based multi-frequencies stabilization	87
3.5.1.1	Hardware	88
3.5.1.2	Software	91
3.6	FPGA-based experimental control system	93
4	Preliminary results with cold atoms	97
4.1	Atomic source	98
4.1.1	The two-dimensional MOT	98
4.1.2	Single-frequency Zeeman slower	99
4.1.3	The atomic transfer	102
4.2	Cold atoms with the blue MOT	103
4.2.1	The capture velocity	103
4.2.2	Number of atoms and loading rate in the 3D-MOT	103
4.2.3	The repumpers	104
4.3	The analysis of upgraded Zeeman slower	105
4.3.1	The numerical model	106
4.3.2	The single-frequency Zeeman slower	109
4.3.2.1	The atomic trajectories	109
4.3.2.2	The modified velocity distribution	112
4.3.2.3	The atomic flux	112
4.3.3	The dual-frequency Zeeman slower	112
4.3.3.1	The atomic trajectories	112
4.3.3.2	The modified velocity distribution	114
4.3.3.3	The atomic flux	114
4.3.4	The enhancement of atomic flux	118
5	Fast control of atom-light interaction via light shift in a narrow-linewidth cavity	120
5.1	Limitation in narrow-linewidth-cavity-assisted atom interferometry	121
5.2	The fast control of the atom-light interaction via a light shift	123
5.2.1	The AC Stark shift	131
5.2.2	The scattering rate	135
5.2.3	Trade-off between energy shift and scattering rate	139
5.2.4	The time interaction between atoms and the light	142
5.2.5	The phase error	144

6 On the horizon	145
6.1 Fast control of atom-light interaction via magnetic-field induced transition . .	146
6.1.1 The magnetic-field-induced transition	146
6.1.2 Fast control of atom-light interaction with magnetic field	147
6.1.2.1 Choice of atomic species	147
6.1.2.2 The scheme	149
6.1.2.3 Some critical parameters to consider	149
Appendix	157
A FPGA-based experimental control system	158
B Fast magnetic-field switch	169
C Atomic source design	171
D Science cell design	173
E Scientific production	177
Bibliography	180

Introduction

Motivation

Dark matter, the driving "force" of the expansion of our universe, is one of the most "spooky" substances to observe since it rarely interacts with itself or with conventional matter via absorbing or emitting photons. Therefore, both its existence and composition are mysterious and complex to understand. The in-depth exploration of dark matter is of great significance since dark matter is five times more abundant than observable matter in the universe, producing sufficient gravitational force to hold the entire galaxies. Without dark matter, individual galaxies would rotate too quickly, leading bound clusters to fall apart, Sun-like stars and Earth-like planets would be impossible to arise, and "we," the human-kind, may not exist.

Throughout history, natural philosophers edge closer and closer to the truth about dark matter. Friedrich Wilhelm Bessel, in 1844 firstly drew attention to a "dark companion" only based on its gravitational effects on observed stars [1]. A few years later, Urbain Le Verrier proposed the existence of a "dark planet" to explain the abnormal recession of the perihelion of Mercury [2]. Besides the discussion of dark matter in the form of "dark companion" and "dark planet," in 1877, Angelo Secchi encouraged the explorations on "dark nebulae" [3]. At the end of the 19th century, astronomical scientists began to question if the dark region scattered in the sky was either due to scarcity of stars or to the presence of absorption along the line of sight. To settle these disputes, William Henry Wesley, who served as an assistant secretary of the Royal Astronomical Society for 47 years, proposed that:

"It is better to solve the question experimentally. For this purpose [the author] repeated many times the experiment of sprinkling small splashes of Indian ink upon paper with a brush, revolving the paper

between each sprinkling, so to avoid the chance of showing any artificial grouping in lines due to the direction in which the spots of ink were thrown from the hairs of the brush." [4]

Nowadays, with the tremendous technological advances in precision measurements, the first direct detection of gravitational waves emitted from the mergers of black holes and neutron stars is revealed by light interferometry from LIGO/Virgo [5]. The gravitational wave detection opens a new window for exploring dynamics of cosmological structure formation and evolution of galaxies [6], which are potentially transparent to electromagnetic radiation. Ground-based cold atom experiments with much less systematic errors will complement the search for astrophysical and cosmological sources in the mid-frequency range between 10 mHz and 1 Hz, where terrestrial light interferometry cannot. An interdisciplinary experiment based on atom interferometry platform, atomic experiment for dark matter and gravity exploration (AEDGE) [7], is proposed to explore these two most appealing topics in the frontiers of fundamental physics: dark matter and gravitational waves.

The AEDGE mission will benefit from both the fruitful results and the technology used in experiences operating laser interferometry over a considerable distance and is under construction. The mission also relies on proposed cold-atom interferometry projects. As one of the key "pathfinders," matter-wave laser interferometric gravitation antenna (MIGA) experiment [8] employs an array of atomic interferometers optically linked with each other at a 150-m-long optical cavity to mitigate Newtonian noise at low frequencies. Since each single atom interferometer using atoms ^{87}Rb is operated at a two-photon process, two orthogonal baselines are required to reduce technical noise from laser systems. Considering an upgraded-version of MIGA with a single baseline, in the LP2N laboratory (Laboratoire Photonique, Numérique et Nanosciences, Talence, France), a prototype with ^{88}Sr atoms under single-photon transition has been set up from the very beginning and studied.

Thesis organization

This thesis consists of two main parts: first, the technical details and preliminary results from a ^{88}Sr atom interferometer are presented in Chapter 3 and Chapter 4; then, the theoretical analysis for one practical method to overcome the limitations imposed by the finite lifetime

of photons in narrow-linewidth-cavity-enhanced atom interferometry is reported in Chapter 5.

Chapter 1 introduces the theoretical atomic physics on which is based on atom interferometry and expounds upon the motivations and prospects for an atom interferometer utilizing clock transitions.

Chapter 2 focuses on the discussion of a strontium atom interferometer prototype that we realize in the laboratory, including atomic properties of selected species, cold atom cloud preparation, and the configuration of an atom interferometer.

This thesis marks the beginning of the experiment, and **Chapter 3** describes our laser, electronics, and vacuum systems, which are of particular use to future students of this project.

Chapter 4 gives the preliminary results about the 3D-blue MOT, and we present a novel atomic source based on a double-frequency Zeeman slower for enhancing atom flux.

Narrow-linewidth-cavity-assisted atom interferometry is in vogue due to the high-power and high-quality optical modes to drive diffraction pulses. To overcome its finite response time, we present, in the **Chapter 5**, the analysis about fast enabling/disabling atom-light interaction in a narrow-linewidth cavity via an auxiliary electromagnetic radiation field.

We conclude with **Chapter 6**, an outlook on the strontium atom interferometer experiment. In the future, we consider a scattering-free approach with magnetic field-induced transitions to bypass the effect of finite response time in a narrow-linewidth cavity.

Chapter 1

Atom interferometry with clock transitions

Cold atoms are often a core quantum technology for precision measurements in fundamental physics. The evidence of radiation pressure from light on atoms (Lebedev, Nichols, and Hull, 1901) [9, 10] and the measurement of the deflection of individual sodium particles by a sodium lamp (Frisch, 1933) demonstrated the ability to manipulate the atoms. The invention of laser fundamentally required development for the production of cold atomic samples with light, e.g., Doppler cooling (Wineland as well as Dehmelt, 1975) [11], optical molasses (Lett, 1988) [12], Zeeman slowing (Phillips, 1982) [13], magneto-optical trapping (Raab, 1987), and the cooling and trapping of atoms (Chu, 1985) [14]. Following these breakthroughs and with the advent of evaporative cooling, Bose-Einstein condensation was demonstrated [15, 16]. Modern cold atom experiments are test beds that demonstrate state-of-the-art measurements in quantum metrology [17], inertial navigation [18], timekeeping [19], and quantum communication [20].

Sec.1.1 studies the benefits introduced by single-photon-transition atom interferometry in search of GW with cold atoms. Next, Sec.1.2 reports the experimental realization of a cold strontium gravity gradiometer at the LP2N; it is based on atom interferometry using strontium atoms interrogated on the clock transition. Sec.1.3 summarizes the capabilities of AEDGE in fundamental physics, astrophysics, and cosmology, and DM and GW detections have higher priorities. The advantages of atom interferometry compared with light interferometry for the

interest of GW detection are resumed.

Contents

1.1	Atom interferometry	9
1.1.1	Quantum probes: cold atoms	9
1.1.2	Two-photon transition	11
1.1.3	Single-photon transition	12
1.2	ALCALINF	14
1.2.1	Experimental platform	15
1.2.2	Atom optics	16
1.3	Prospects for clock transition inteferometry: AEDGE	17
1.3.1	Dark matter	19
1.3.2	Gravitational waves	20

1.1 Atom interferometry

Atom interferometry has rapidly developed within the last three decades, with the technique being the core of new quantum high-precision inertial sensors employed to measure earth's rotation rate with Sagnac-effect gyroscopes [21, 22], estimate gravity acceleration (g) with gravimeter [23, 24, 25], determine Newtonian constant of gravity (G) [26, 27], sense earth's gravity gradient [28], test the equivalence principle of general relativity [29], probe the interplay between gravitational and quantum physics [30, 31].

1.1.1 Quantum probes: cold atoms

Compared with macroscopic masses (like bulky mirrors in light interferometer), cold atoms are microscopic and reproducible masses with well-defined classical and quantum properties.

The adoption of cold atoms as probes for precision measurements can drastically minimize the systematic errors, thanks to their small size and the precise control of their dynamics.

Fundamentally, cold-atom interferometry is a probe of local spacetime and could, in the correct configuration, be a valid technique to observe GWs: atomic wave packets are set in a coherent superposition of internal and/or external state [32], and any physical effect causing the change of spacetime during the free evolution of wave packets can be encoded into the phase of quantum interference, where atoms travel along different trajectories connecting the initial and the final state of a system.

Considering external degrees of freedom, atom interferometers take advantage of the matter-wave duality of particles postulated by de Broglie in 1923 [33],

$$\begin{aligned}\lambda_{dB} &= \frac{h}{p} \\ &= \frac{h}{mv}\end{aligned}\tag{1.1}$$

where the proportionality factor h is Planck's constant, m and v are the particle mass and velocity, respectively. Unlike photons that always move at the speed of light c , the particle wavelength varies with its velocity. The de Broglie wavelength of cold and ultracold atoms, with velocities at a level of mm/s or cm/s, is comparable to $1\ \mu\text{m}$ or higher. Consequently, atom interferometry can potentially reach higher inertial sensitivity than optical counterparts. State-of-the-art precision of atom interferometry in inertial sensing is $10^{-9}\ \text{g}$ in the case of acceleration, and $10^{-8}\ \text{rad/s}/\sqrt{\text{Hz}}$ for the rotation rates.

For the internal degrees of freedom, two long-lived states (like long-lived hyperfine ground states $|g_0\rangle$ and $|g_1\rangle$) are selected. Initially, a cold atomic cloud is prepared at state $|g_0\rangle$. The first optical beam splitter ($\pi/2$ light pulses) implemented at $t = T_0$ gives rise to a quantum superposition state for each atom with equal probability at state $|g_0\rangle$ and $|g_1\rangle$. Meanwhile, the light pulses impart extra momenta $\hbar\vec{k}_{\text{eff}}$, equal to the photon recoil, to the atomic wavepacket at state $|g_1\rangle$, which imposes a velocity difference between state $|g_1\rangle$ and $|g_0\rangle$ of $\hbar k_{\text{eff}}/m$. Then two wavepackets in different states travel along separated interferometer paths. During the free evolution period (T), two atomic wavepackets experience a different inertial field (F) and accumulate a different phase. Then, the wavepackets interact with an atom optic mirror (π pulses) at $t = T_0 + T$. This mirror light pulse simultaneously imparts

a momenta exchange and switches the internal state for each atom at state $|g_0\rangle$ and $|g_1\rangle$. After another free-evolution T , second $\pi/2$ light pulse at $t = T_0 + 2T$ combines two atomic wavepackets and encodes the differential phase accumulated on the two atomic trajectories into measurable atomic state populations. The final phase difference ($\Delta\phi$) gives information on the inertial forces felt by the atoms during the free evolution. If an atom interferometer is mean to sense gravity, $\Delta\phi = -k_{\text{eff}}g(2T)^2$; if instead it senses rotations, $\Delta\phi = 2\Omega k_{\text{eff}}vT^2$.

1.1.2 Two-photon transition

An atom interferometer typically realized with alkali atoms implements the atom optics elements with two-photon transition, notably applying two counter-propagating beams ($\vec{k}_{\text{eff}} = \vec{k}_1 + \vec{k}_2$), red detuned from an optical transition and in a lambda (Λ) configuration. The two-photon transition leads to a negligibly small occupancy of the excited state $|e\rangle$ to avoid spontaneous emission from the short-lived excited state, e.g., about 300 ns for the optical state in rubidium, thus the loss of coherence. The two lasers frequency difference is adjusted to be equal to the atom recoil kinetic energy (external freedom of atom) in addition to internal energy shift between two well-defined hyperfine ground states ($|g_0\rangle$ and $|g_1\rangle$) (internal freedom of atom).

The first GW detector relying on an atomic gravity-gradiometer has been proposed in [34]. In this scheme, a GW propagating along z -direction with "+" polarization in the Transverse - Traceless (TT) Gauge causes the most significant normal flat space expansion/contraction at the xy plane. The amplitude of GW signal scales with the distance between two test masses (atom interferometers). The detector, oriented radially, gives maximal spacetime strain sensitivity. In contrast, the one orientated along the z -axis provides a minimum. Notably, in this nearly one-dimensional atom interferometry, atoms and light travel mainly along one direction (x or y) and remain approximately constant at the orthogonal yz or xz -plane.

The propagation phase dominates the differential readout in atom interferometry. Lagrangian is integrated along atom's geodesic; the wavepackets separation phase, in which the average classical four-momenta is integrated over the null geodesic connecting two endpoints of atomic interferometer arms; and the laser interaction phase. From [34], the differential

phase shift is estimated as,

$$\phi_{\text{diff}} \propto \hbar k_2 L . \quad (1.2)$$

In the spacetime diagram (see Fig. 1.1), two atom-interferometers forming a long-baseline gradiometer are separated by a distance of $x_2 - x_1$ and are commonly probed with two counter-propagating lasers. At each interaction node, where the atomic wavepackets experience splitting, reflection, and recombination, the presence of both laser light is required to implement the two-photon process. One of the two lasers (\vec{k}_1) defines the time at which each atom-light interaction occurs. The other laser (passive one) (\vec{k}_2) is always on. At times 0 , T , and $2T$, these so-called control laser pulses are common to both interferometers. Hence, the related technical noise, e.g., laser vibrations, laser phase, and frequency noise, is common-mode rejected in the differential measurement.

With the long separation between two atom-interferometers, to enhance the strain sensitivity of the GW detector, both vibration and laser phase noise from the passive laser arise significantly. Due to the finite time, $\tau = (x_2 - x_1)/c$ required by the control laser pulses to travel from x_1 to x_2 , the noise from the passive laser is not in common mode and is encoded in the gradiometric phase. One solution to overcome this finite time τ imposed limitation in a two-photon transition atom interferometry is to build the second baseline, which doubles the project budgets. Alternatively, the passive laser can be removed by implementing single-photon transition atom interferometry.

1.1.3 Single-photon transition

As proposed in [35], the existence of a long-lived excited clock state in alkali earth element, e.g., about 118 s for ^{87}Sr [36], allows using only one single laser beam to manipulate the atomic wavefunction. In a gravity-gradiometer configuration (see Fig. 1.2), the primary laser is taken to be at $x = x_1$, the left-hand side of the figure. The atom is initially prepared in the ground state. The first pulse at time $t = 0\text{s}$ is a $\pi/2$ pulse which splits the atom wavefunction into two parts. After time T , a π pulse is fired to deflect the two atomic trajectories to converge, even changing the internal atomic state. The final $\pi/2$ pulse recombines the two wavefunctions. The interferometric configuration uses one laser's light to manipulate the

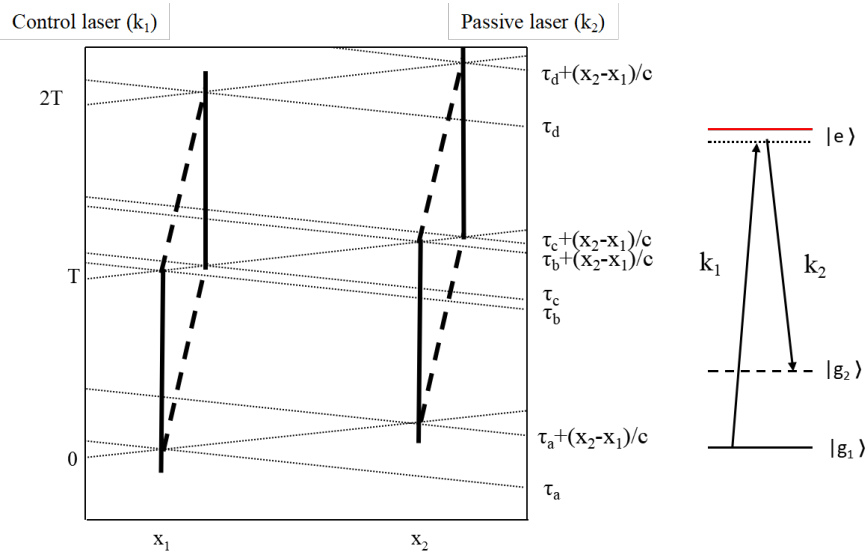


Figure 1.1: Two-photon atomic GW interferometry sensor.

coherent superposition instead of two counter-propagating beams.

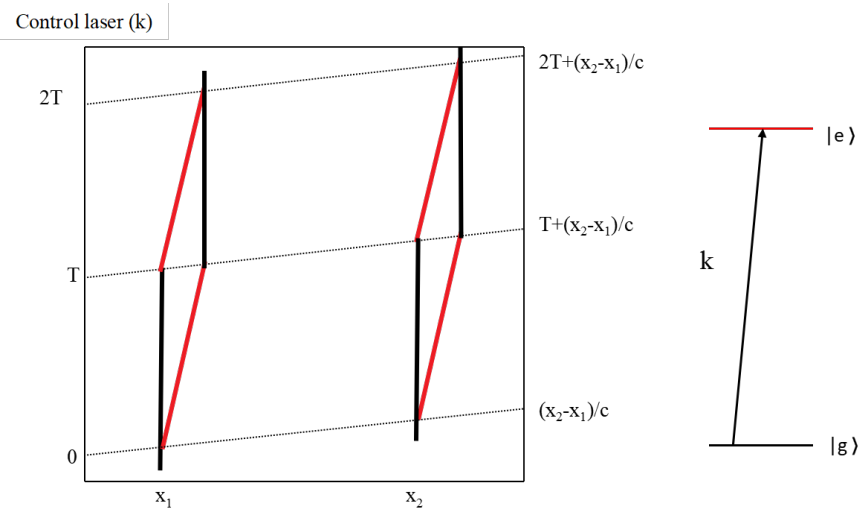


Figure 1.2: In the single-photon atomic GW interferometry sensor with gravity-gradiometer configuration, two ensembles at distance of $x_2 - x_1$ interrogate with the very same laser field for coherently splitting, reflection and combination. On the right side, it is the sketch of single-photon transition.

Qualified candidates for this interferometric scheme are thus alkali earth or rare-earth atoms, commonly adopted to implement optical clocks, such as strontium (Sr), ytterbium (Yb), calcium (Ca), and magnesium (Mg). The choice of strontium presents significant advantages, given by the recent demonstration of the state-of-the-art defining optical lattice

clock [37], the rapid production of large atom number BECs [38] as well as the possibility to produce ultra-cold and degenerate samples of fermions [39].

1.2 ALCALINF

In LP2N, a prototype of a large-scale alkali-earth matter-wave interferometer (ALCALINF) is under development. The long-term scientific goal of ALCALINF is to construct a novel large-scale matter-wave interferometer using single-photon manipulation of strontium matter waves. The project will demonstrate gradiometric measurements with at least two correlated Sr-atom interferometers equally distributed vertically (along with earth gravity g). The differential readout of phase in the single-source dual-atom interferometer separated by macroscopic distances refers to the change of gravitational curvature [30]. The evolution of largely delocalized wavepackets coherent superposition raises questions about the relativistic correction arising from the light-travel time between the wavepackets during the atom-light interaction. This 6-meter tall prototype is proposed to address this open problem. It will also be used to study other topics such as the investigation of coherence and decoherence of largely delocalized macroscopic waves [40], the demonstration of correlation metrology for very-long-baseline-atom interferometry, and, more ambitiously, the exploration of a new type of matter-wave interferometer where the delocalized wavepackets coherent superposition is kept for seconds in a lattice configuration [41]. This prototype can improve and inform GW antenna proposals utilizing AI by demonstrating modern AI experimental techniques in the lab.

The equivalence principle causes a technical problem with characterizing gravitational forces: gravitational potentials induce accelerations, which can not be distinguished from accelerations due to a non-inertial reference frame of measurement. This imposes a fundamental challenge to extract gravitational acceleration signals from platform vibrations. A differential configuration like gradiometric measurement can be immune to platform vibration noise. Two spatially separated gravity measurements run simultaneously utilizing a common laser link or reference frame. Vibration-introduced accelerations are in a common mode; however, the gravitationally induced gravity gradient along the axis of the atom interferome-

ter is in a differential mode. Gravity gradiometry can measure the curvature of gravitational potential locally in a vibrationally noisy environment, circumventing the equivalence principle. Therefore, the prototype under construction in the laboratory is also of technological interest.

1.2.1 Experimental platform

A high-flux sub- μK Sr atoms ensemble is prepared with at least of two-stages of cooling and trapping, with a broad transition and a narrow transition in strontium. Further, atoms in the red MOT can be loaded into a dipole trap for additional sub-Doppler cooling techniques.

The atomic ensembles in a vertical free fall will be interrogated using a sequence of interferometric pulses with radiation resonant to the clock transition to drive coherent manipulation pulses. The linewidth of the interrogation laser cannot be more than 20 Hz to maintain a contrast above 10% for a 1-kHz Rabi frequency. To address the clock transition, the laser linewidth must be narrowed down to a level comparable with the natural linewidth of this transition: while we broaden the single-photon excitation of the clock transition by mixing a certain quantity of the dipole-allowed states into the upper clock state through a cone-shaped coil with a magnetic field perpendicular to the probe laser [42, 43] or to the external laser field [44] we narrow the linewidth of the laser by locking it to an ultra-stable Fabry–Pérot (FP) cavity with a Pound–Drever–Hall (PDH) locking technique, with relaxed constraints concerning the constraints fixed in lattice-clocks experiments [45].

Alternatively, the interferometric laser can be operated close to the clock transition to realize a large momentum transfer. A specific coherent manipulation protocol is similar to the one realized in [46].

This high-flux and the low-velocity atomic ensemble is required for the first tests of the coherent laser, first by doing spectroscopy experiments [47] and then by doing a two-pulse (Ramsey interrogation) or a three-pulse (atom-interferometer configuration) interrogation sequence.

After implementing an atom interferometer in the atomic source vacuum cell, the interferometer will be connected to a 6-meter-tall vertical tube to realize gradiometry with two or

more separated atomic clouds.

1.2.2 Atom optics

For the three-pulse atom interferometer, the first pulse serves as an atom-beam splitter, coherently driving the atoms into a superposition of states $|\text{ground clock state}; p\rangle$ and $|\text{excited clock state}; p + \hbar k\rangle$ with $\hbar k$ the driving photon momentum. Over a subsequent T , interrogation interval, the two parts of the atom wavefunction separate vertically by about $\hbar k T / m$, at the time a mirror pulse reverses the relative momenta and internal states. After an identical drift time, a final beam splitter pulse interferes the atom wave packets. The atom fluorescence is recorded using charge-coupled device (CCD) cameras located below the interferometer. Alternatively, a four-pulse atom interferometer can be considered. In this second method, the atoms will spend most of the time in the ground state, preventing the risk of unwanted decays.

Numerous techniques have been implemented to separate atomic waves coherently. The most typical methods are Bragg diffraction [48, 49, 50, 51], stimulated Raman transition [52, 52], and Bloch oscillations [53, 54, 55, 56, 57]. Atoms with Bragg diffraction always stay in the same internal state. The atom interferometric phase is insensitive to several systematic effects thanks to the propagation of the two parts of the wave function in the same internal state along the interferometer. The approaches of coherently manipulating the wavefunction have more stringent requirements for highly collimated atomic sources for better resolving the external degree of freedom or careful analysis for a multiple path fringe pattern [58]. Stimulated Raman transitions split atomic wavefunctions into two distinguished internal states, which allows the detection of the state selective technique due to its internal state labeling [59]. Using Bloch oscillations in optical lattices to scale up the momentum transfer is to impart the atoms with large recoil momenta [53, 56]. The atomic velocity increases by $2v_r$ per oscillation. While optical lattices can generate large momentum separation, the confining potential can cause unwanted systematic effects, which have to be considered.

The sensitivity of an atom interferometer typically scales with the differential momentum transferred to the two wavefunctions along two trajectories. The atom-optics of large momen-

tum transfer (LMT) beam splitters in combination with stimulated Raman transition[52], Bragg transition[60] and Bloch oscillation[53] is preferred to coherently separate matter waves on macroscopic scales or separating and guiding atoms in extended lattices. Applying consecutively additional pulses sequences is one of the practical approaches to increase the spacetime area of the interferometer; hence these sequences enhance the sensitivity of the interferometer sensitivity [61, 62, 46]. For the N -th order diffraction, the atom coherently scatters N photons for the single-photon transition from the laser beam, thereby increasing the recoil momentum to a multiple of $n\hbar k$. This N -th order diffraction linearly increases the phase difference[63] but is limited by the available laser power, where cavity-aided atom interferometry is one solution [64]-combining different schemes like applying multiple sequences of Bloch-Bragg-Bloch beam splitters[65] or N -th order diffractions[51]. The purpose is to enhance the scale factor while featuring a better suppression of noise and systematic uncertainties. The scaling behavior of these techniques and the related systematic errors arising from the LMT manipulation can also be investigated in this prototype.

1.3 Prospects for clock transition inteferometry: AEDGE

There are several proposals for cold atoms in space: ACES [66], MAIUS [67], CAL [68], FOKUS [69], KALEXUS [70], JOKARUS [71]; this work has continuously informed and refined the proposals for atom interferometry in space. Atomic experiment for dark matter and gravity exploration (AEDGE) [7] is a space project based on atom interferometry (see Fig. 1.3), which are sensitive to the fluctuations in the relative phase between two cold-atomic ensembles separated by a distance of L ,

$$\Delta\phi = \omega_A \times (2L) , \quad (1.3)$$

where ω_A is the frequency of the atomic transition used to implement the atom optics, the interaction between DM and cold atom induces variations of the atomic transition ($\delta\omega_A$).

Proposed interactions between dark matter (DM) and the test masses (cold atoms) induce a variation of the atomic transition ($\delta\omega_A$). The passage of GW causes the periodic contraction and expansion of spacetime, specifically the variations of the distance (δL) between two cold

atomic clouds. Both $\delta\omega_A$ and δL lead to the changes in the differential readout of the atom interferometer.

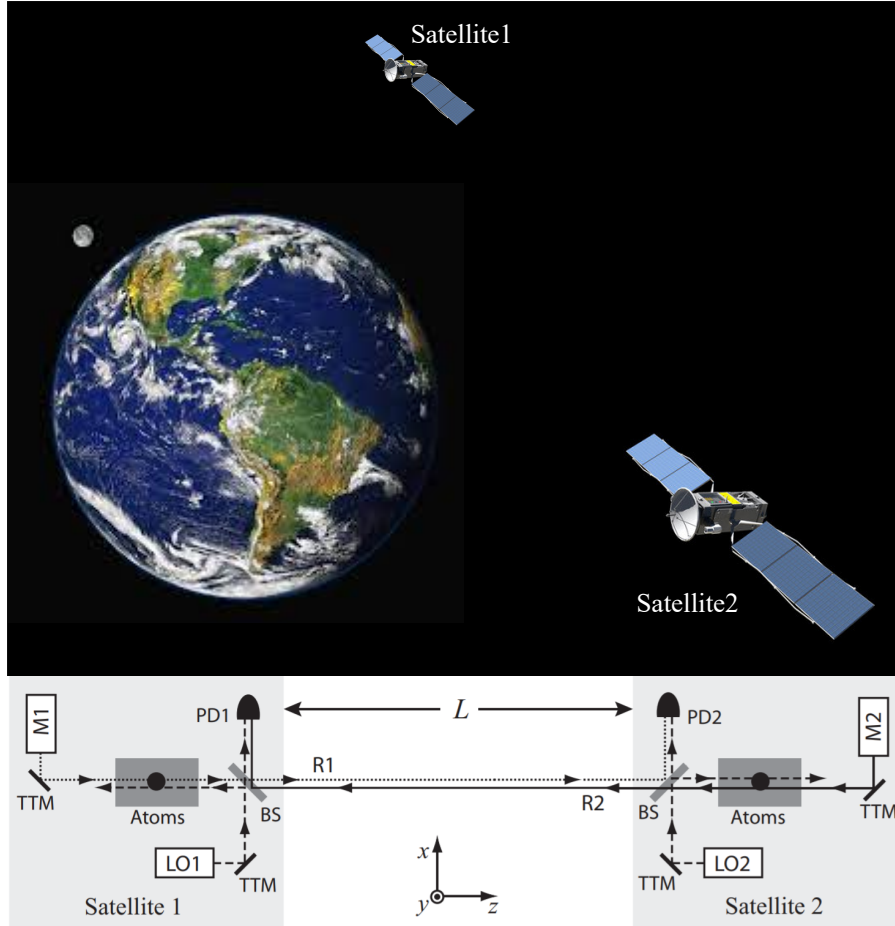


Figure 1.3: Possible experimental scheme. The beams of the two master lasers $M1$ and $M2$, are shown as dotted and solid lines, respectively, with the corresponding reference beams between the two satellites, $R1$ and $R2$. Two local oscillator lasers, $LO1$ and $LO2$ (dashed lines), are phase-locked to $R2$ and $R1$. Photodetectors $PD1$ and $PD2$ measure the heterodyne beat note between the reference beams $R2$ and $R1$ and the corresponding local lasers $LO1$ and $LO2$, respectively, providing feedback for the laser link. Non-polarizing beam splitters are denoted by BS , and tip-tilt mirrors used to control the laser beams' directions are denoted by TTM . For clarity, small offsets between overlapping laser beams have been introduced. The below figure is extracted from [7] under CC-BY 4.0 license, originally from [72].

1.3.1 Dark matter

Measuring the effect from the dynamics of galaxies and clusters on the spectrum of cosmological microwave background (CMB) indicates the existence of DM. It accounts for more than four times the matter-energy density than normal matter in the Universe [73]. So far, all the investigations of the DM rely on the gravitational interaction with normal matter. However, this interaction portal can not probe the composition of DM [74]. Existing theories predict that DM interacts with normal matter, and its physical composition falls into two categories: ultra-light bosonic fields and weakly-interacting massive particles (WIMPs). From particle accelerators to other laboratory experiments, there is no proof of the existence of WIMPs [75]. Ultra-light bosonic fields are the target theory for the DM search considered in AEDGE.

Theoretical extensions of the Standard Model (SM) [76] of particle physics provide elementary particle candidates for DM over a wide mass window: from ultra-light mass at the sub-eV level to Planck scale $\sim 10^{18}$ eV. Ultra-light DM includes several potential candidates, like axion [77] and axion-like dark vector bosons [78]; and light-scalar particles [79] such as moduli, dilatons, or the relaxion.

Ultra-light scalar DM can get coupled linearly to the SM fields. The sensitivity of AEDGE operating in different modes and interacting parameters are shown in Fig. 1 of [7]. Broadband-mode [80] AEDGE (purple lines) is sensitive to the signals from 10^{-4} to 10^2 Hz, in which region gravity gradients determine a root mean square (RMS) signal more significant than that of atomic shot noise. Resonant-mode AEDGE (orange lines) has extended sensitivity between 10^{-16} eV and 10^{-14} eV. Assuming the gravity gradient noise can be mitigated, AEDGE shall be more sensitive than the km-scale ground-based interferometer experiment (green lines). The grey regions show parameter spaces that have been excluded by the MICROSCOPE experiment (blue lines) [81], search for violations of the equivalence principle with torsion balances (red lines), or by atomic clocks (brown lines).

Dark matter can also couple quadratically to the SM fields: AEDGE will also probe extensive new regions of the parameter space for the electron and photon quadratic couplings. The quadratic couplings give rise to a richer phenomenology than that offered by linear couplings. For example, a screening mechanism occurs for positive couplings, which reduces the

sensitivity of terrestrial experiments. This is illustrated in Fig. 2 in [7] by the steep rises in the atomic clock constraints and the sensitivity of a km-scale ground-based interferometer. By comparison, space-based experiments are less affected by the screening mechanism, and AEDGE, therefore, maintains sensitivity at larger masses.

To distinguish a DM signal from other sources, like GW, a relatively constant value set by the mass of the scalar DM needs to be identified instead of a time-varying signal due to the evolution of a binary system, for example. The DM speed distribution may introduce a characteristic modulation over a much longer time [82].

1.3.2 Gravitational waves

General relativity inextricably links a four-dimensional spacetime to gravity [83]. Einstein's field equation forming the core concept of general relativity is,

$$R_{\mu\nu} - \frac{1}{2}Rg_{\mu\nu} + \Lambda g_{\mu\nu} = \frac{8\pi G}{c^4}T_{\mu\nu} . \quad (1.4)$$

Every term on the left-hand side of Eq. 1.4 refers to the curvature of spacetime, and every term on the right-hand side of Eq. 1.4 is related to mass and energy, which is vulgarised by John Wheeler [84] as "mass grips space by telling it how to curve, space grips mass by telling it how to move." Adding any object possessing energy and momentum into a space "warps" the flat spacetime into a curved one. GW are "ripples" in the "fabric" of spacetime propagating at the speed of light. When a GW passes by, it changes the relative distances between test particles moving along geodesics. GW detection thus consists of measuring the relative motion between test masses. Interferometry, both in the context of optics or atomic physics, provides the most sensitive and available tracking tools, respectively, for bulk mirrors and matter waves set in free fall in the measurement bandwidth.

1.3.2.1 Cosmological sources

When designing a GW detector, it is critical to consider several factors, like the GW strength of interest and the distance between the source and the detector. Therefore, we review the properties of many possible sources before introducing different kinds of sensors and comparing them with the AEDGE project.

According to the hot Big Bang model for the earliest universe evolution, massless cosmic strings are formed during a symmetry-breaking phase transition predicted by a spontaneously broken gauge theory [85]. As the universe expands and cools down, a cosmic string intersecting another string or crossing itself generates an isolated cosmic loop. Cosmic loops are dynamic and tend to decay by radiating energy in the form of GW ranging from pHz to kHz [86]. The possible detection of such weak GW bursts would demonstrate the existence of cosmic strings and help understand the evolution of galaxies.

The temperature of the universe is approximately 10^{15} K shortly after the Big Bang [87]. As the universe cooled down to the present-day average temperature of 1.73 K, the universe underwent cosmological scale phase transitions. When two local minima of the free energy (metastable phase) co-exists, the relevant scalar field changes into a new phase via the nucleation of bubbles. The bubbles expand and collide with each other, generating a significant stochastic background of GWs [88]. The production of GW due to first-order phase transition at the electroweak scale [89] is well placed for detection with current technology, like LISA [90]. GW signals can be revealed from their statistical signatures, and they are categorized into stochastic backgrounds (see Fig. 1.4).

Barring the relic GW from the early universe, inspiralling binaries are another primary sources of GWs; in detail, one can mention the merging of binary black holes, binary neutron stars, white dwarfs, and the generation of type 1A ("type one-A") supernovae. Their characteristic strain signature consists of a frequency sweep from low to high frequencies, with an associated increase in speed and intensity. The parameters of each specific signal are strictly determined by the properties of the binary components, like mass and spin. In addition, core-collapse supernovae as burst sources produce large-magnitude GWs within a short duration in the order of a few wave periods. The ability to detect such GWs will pave the way to explore the dynamics of merger systems and pinpoint the progenitors of type 1A supernovae [91].

1.3.2.2 Detectors

GW detection is either conducted in a direct or an indirect approach. Direct detection measures extraordinary small effects on a detector, produced by the tiny distortions of spacetime

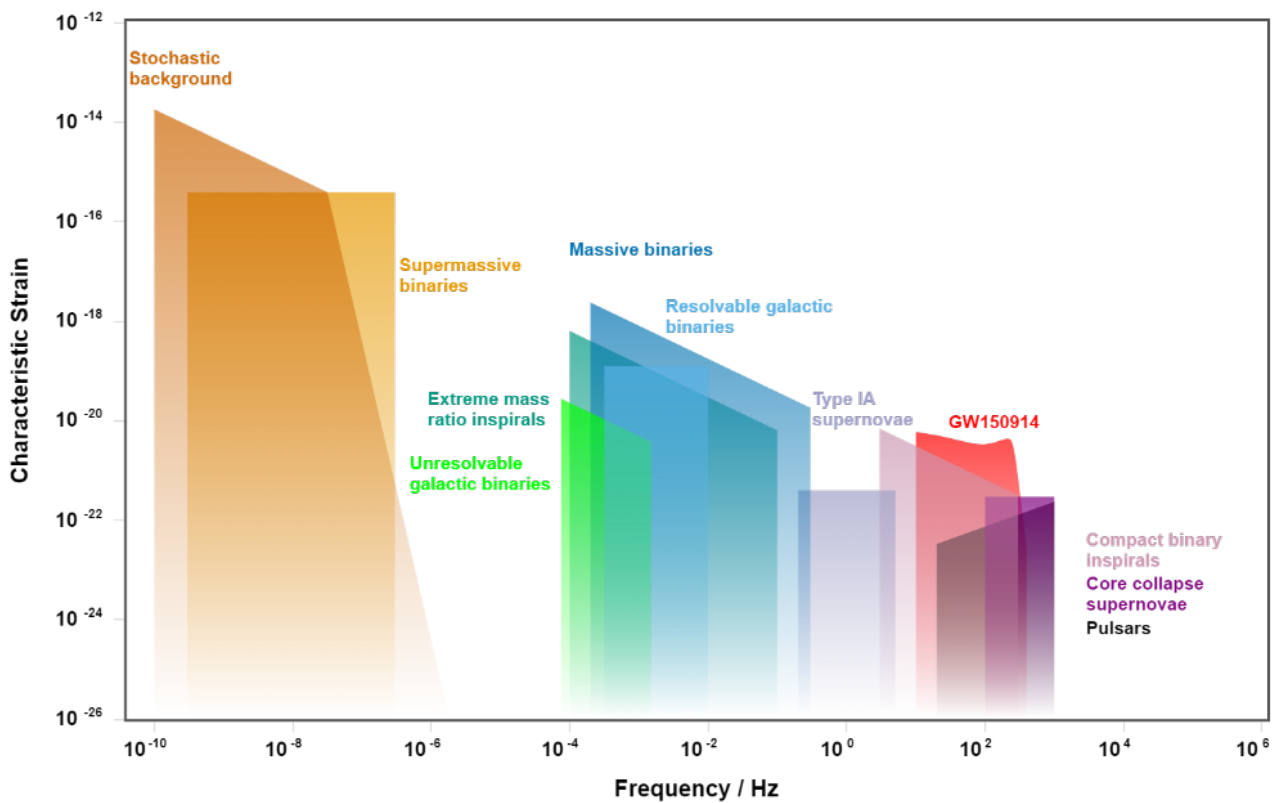


Figure 1.4: Characteristic strain in the frequency domain for various GW sources; notably, the signal relative to the first LIGO detection, e.g., GW150914, is shown in red. The figure has been obtained using the GWplotter tool [92, 93].

due to passing-by GW. For indirect detection, projects are proposed to observe the impact of GW on other detecting signals, like the CMB.

The first realized GW detector is the resonant mass antenna. A passing GW excites the normal modes of an elastic bar or cylinder, located either at room or cryogenic temperature. Force-to-voltage transducers render GWs detectable, in principle. The first operation of such apparatus was reported by Weber in 1966 [94]. A 1.5-ton aluminum antenna was shaped into a cylinder 150 cm long and 60 cm in diameter. It had a fundamental longitudinal vibration mode at a frequency 1660 Hz. Quartz crystals served as strain-gauge transducers and bridged the vibrational mode to an electrical signal. While the sensitivity of such detectors has improved dramatically since the original experiment, no indisputable GW signal has been observed with this style of detector [95].

Measurements of second- and third- order relativistic effects on the observed orbital decay of binary pulsar provides indirect evidence for the existence of gravitational radiation damping, which was first observed in PSR1913+16 by Taylor and Hulse in 1979 [96]. A 305 m radio telescope was employed to measure the pulse arrival-time of the pulsar in the binary system. After tracking the number of elapsed pulse periods for 4.1 years, the orbital period was shown to decay with time. One straightforward interpretation of this phenomenon is that GWs carry away energy from the orbital system and gradually reduce the orbital radius as predicted by general relativity (GR).

A different approach adopting the "pulsar timing" [97] technique exploits the arrival time of pulses from different pulsars as a network of galactic clocks. Large radio telescopes monitor the pulsar tickings and their temporal variations and compare them with the predicted ones. Spacetime disturbances caused by GW affect times-of-arrival and induce "timing residuals" on the expected pulses' arrival time, from which GW information can be inferred. Pulsar timing arrays (PTA) allow the extraction of correlated residual signals among different pulsars dependent on their angular separation and can be exploited to characterize GW signals. The measurement timing interval limits the sensitivity of PTAs. Collaborative projects like the European Pulsar Timing Array (EPTA) [98], the International Pulsar Timing Array (IPTA) [99], and the Square Kilometre Array (SKA) have high strain sensitivities in the $\sim 10^{-9}$ - 10^{-8} Hz frequency band, which is expected to host several signals like those given by the Stochastic

background and supermassive binaries ($\sim 10^9 M_\odot$) thanks to galactic-scale arm lengths (see Fig. 1.5). Very recently, they have announced a possible first GW signal from cosmological strings [100].

Instead of measuring the effects due to GWs on times-of-arrival from pulsars, an interferometer can precisely detect the relative motion induced by GW on probe masses in free fall. Ground-based laser interferometers use suspended bulk mirrors as probe masses and are sensitive to GW in the frequency range of 10-10³ Hz. At low frequency, the limitation is set by thermal, seismic, and Newtonian noise; at the high-frequency region, the setup is limited by shot noise from the light. The LIGO detectors were the first to detect GWs in 2015 [101, 102]. Later, in 2017, Virgo [103] joined in the second detection run. Other instruments contribute to the development of specific technologies, as in the case of GEO600 [104] for the sensitivity enhancement based on the use of squeezed light. Adv-LIGO [105] is operational since 2015, soon followed by Adv-Virgo [106]. TAMA300 [107] is currently under development/construction in Japan with a successor of Kamioka GW Detector (KAGRA) [108] under construction. Einstein Telescope (ET) is a proposed underground instrument, which would be sensitive to GW signals from a few Hz at lower frequencies primarily thanks to the improved seismic conditions. These ground-based detectors are designed to detect relatively weak, transient sources of GW like the last inspiralling phase and merge of compact binary systems. Significantly longer-lived and stronger sources such as resolvable or unresolvable galactic binaries, massive binaries ($\sim 10^6 M_\odot$), and extreme mass ratio inspirals radiate GW at frequencies between 100 μ Hz, and 100 mHz. These signals are obscured on Earth by seismic and Newtonian noise, which represent a fundamental limitation even for future ground-based optical interferometers, even if mitigation schemes based on classical [109] or quantum sensors [110] are being studied. This limitation motivates the long-term effort to realize a space-based interferometer for GW detection: that is the case of the Laser Interferometer Space Antenna (LISA) [111], and several other proposals like the down-scaled version eLISA [112], the Advanced Laser Interferometer Antenna (ALIA) [113], the DECi-hertz Interferometer Gravitational Wave Observatory (DECIGO) [114], the successor of LISA, Big Bang Observer (BBO) [115] and TianQin [116].

There are several terrestrial cold atom experiments under construction like MIGA [8],

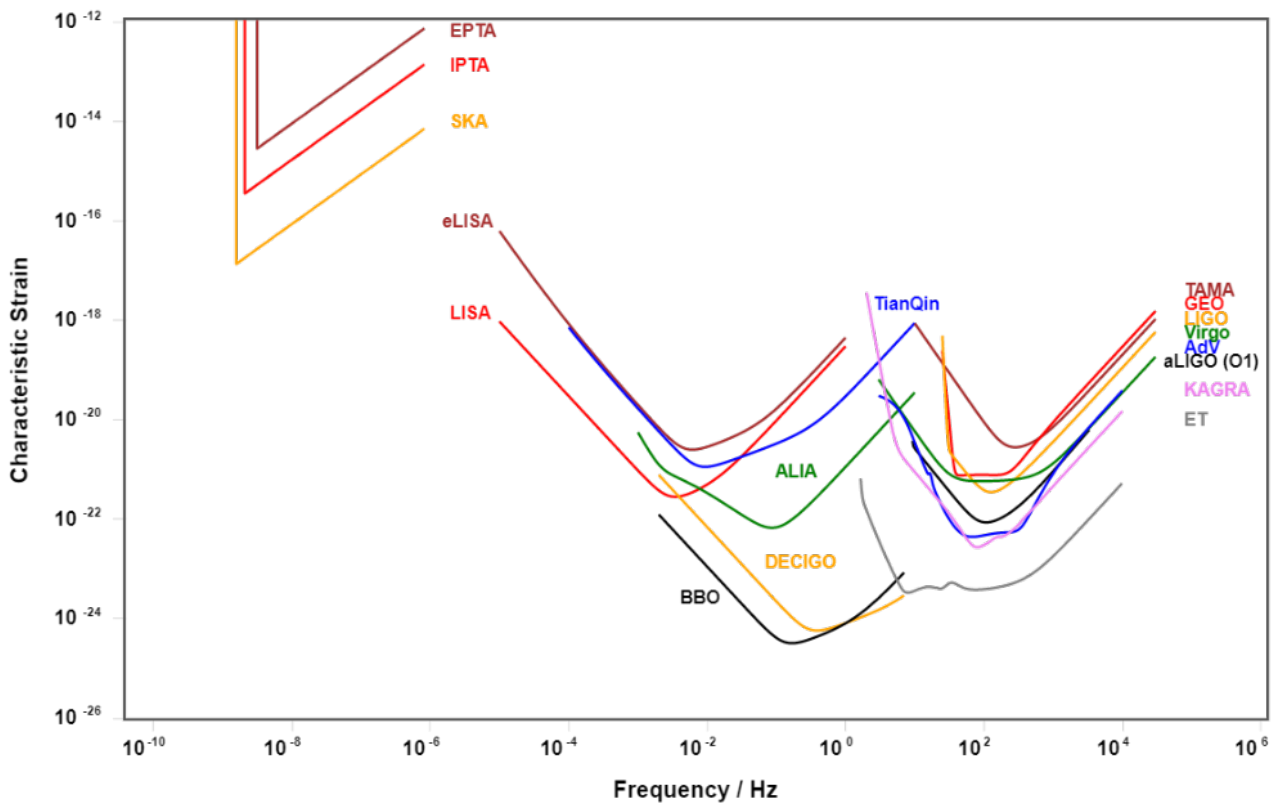


Figure 1.5: Strain sensitivities versus frequency for different kinds of GW detectors. The graph has been obtained using the GWplotter tool [92, 93].

ZAIGA [117] and MAGIS [118], some others are being proposed, such as ELGAR [119] and AION [120]. These experiments will complement the sensitivities of LISA and LIGO/Virgo at the frequency range of 10 mHz to 10 Hz. AEDGE provides an extended search capability for astrophysical and cosmological sources of GW in the same frequency range. It is ideal for observations of mergers involving IMBHs, as seen in Fig. 1.6. This figure shows that AEDGE (assumed here to be operated in resonant mode) would be able to observe the mergers of $6 \times 10^3 M_\odot$ black holes out to very large redshifts, as well as early inspiral stages of mergers of lower-mass binary holes (BH) of $60 M_\odot$, extending the capabilities of terrestrial detectors significantly to earlier inspiral stages. The dashed lines illustrate the observability of binaries with very different masses, namely $3000 M_\odot$ and $30 M_\odot$, which could be measured during inspiral, merger, and ringdown phases out to large redshifts.

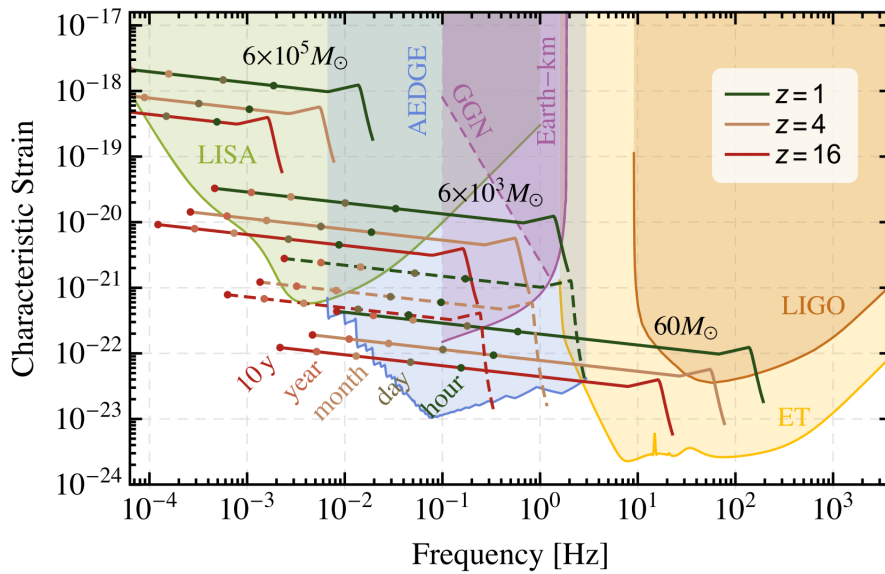


Figure 1.6: Comparison of the strain measurements possible with AEDGE and other experiments shows their sensitivities to BH mergers of differing total masses at various redshifts z , indicating the time remaining before the merger. The solid lines correspond to equal mass binaries and the dashed ones with very different masses, namely $3000 M_\odot$ and $30 M_\odot$. This figure illustrates the potential for synergies between AEDGE and detectors observing other stages of BH infall and merger histories. Also shown is the possible gravitational gradient noise (GGN) level for a km-scale terrestrial detector, which would need to be mitigated for its potential to be realized. The figure is extracted from [7] under CC-BY 4.0 license.

My PhD project is involved in designing a high-flux sub- μ K Sr-atom source and devising

a scheme to implement an effectively pulsed atom-light interaction in a narrow linewidth cavity, useful for cavity-aided atom interferometry that could be useful for AI techniques needed to detect GWs and DM in the AEDGE project.

Chapter 2

The sub-microkelvin ^{88}Sr -atom interferometer

Atom interferometry based on Sr-atoms, using a direct-optical transition for coherently manipulating the atomic wavefunction, allows long- and single-baseline atomic instrument targeting the gravitational wave detection [35]. This Sr-atom interferometry is also insensitive to the technical laser noise. Among the atoms typically adopted in ultracold atomic experiments, the ^{88}Sr -atom has good physical properties: null nuclear spin, thus, simpler electronic structure compared with other isotopes; with the extremely short scattering length, it has much less decoherence among the external degrees of freedom. Hence, the ^{88}Sr -atom can serve as a probe in precision gravity measurements, even at small distances. Sec. 2.1 lists the crucial parameters of Sr-atom isotopes and supports the choice of ^{88}Sr for atom interferometry applications. To avoid too much extension of the cold atoms during the free evolution time, it is necessary to reach lower temperatures. Sec. 2.2 introduces the required and optional cooling stages to prepare the sub-microK atomic ensemble of ^{88}Sr . Sec. 2.3 briefly discusses some future work to complete this atom interferometer.

Contents

2.1	Strontium	29
2.1.1	Natural abundance	29
2.1.2	The atomic structure of strontium	30
2.1.3	The sensitivity to magnetic field	36
2.2	The magneto-optical trap	36
2.2.1	The blue MOT	37
2.2.2	The red MOT	37
2.3	The coherent manipulation on the clock line	39

2.1 Strontium

Sr-atoms (atomic number = 38) with two valence band electrons feature singlet and triplet states. This electronic property gives rise to metastable (clock) states and narrow-linewidth intercombination transitions. The natural strontium is a mixture of four stable isotopes with a strongly varying abundance, and three of them are bosons with zero nuclear spin. One is fermion with non-zero nuclear spin. Choosing a specific isotope among the four alternatives depends on crucial atomic properties like abundance, electronic structure, sensitivity to the external field, and their impact on the final application, such as the presently proposed gravitational wave detector.

2.1.1 Natural abundance

Sr is a soft silver-white and light-yellow metal, forming a dark oxide layer after exposure to the air. Its melting point is at 777 °C. Strontium ovens, used as the atomic source in ultracold atomic experiments, are normally heated to a few hundred degrees to reach sufficient vapor pressure. The natural abundance of stable Sr-atom isotopes increases with increasing mass

number (see Tab. 2.1): ^{84}Sr , ^{86}Sr , ^{87}Sr and ^{88}Sr have abundances in nature of 0.56%, 9.86%, 7.00% and 82.58% respectively. ^{88}Sr -isotope is by far the most abundant and is suitable for our experiment as aforementioned; thus, it provides a high-atomic flux and high-detection sensitivity in atomic interferometry.


	Isotope	Abundance [%]	Atomic mass [u]
^{84}Sr	0.56(1)	83.913425(3)	
^{86}Sr	9.86(1)	85.9092602(12)	
^{87}Sr	7.00(1)	86.908871(12)	
^{88}Sr	82.58(1)	87.9056121(12)	

Table 2.1: Natural abundance and mass of four stable Sr isotopes [121]. The inset picture is from [122].

Other strontium isotopes (> 20 types) are radioactive, like ^{89}Sr with a half-life of ~ 51 days used as a palliative of painful bone metastases, and ^{90}Sr (half-life about 29 years) produced by nuclear fission and which represents a radiation hazard.

2.1.2 The atomic structure of strontium

The ground-state electronic configuration of strontium is shortly written as $[\text{Kr}]5s^2$, which means that two electrons in the $5s$ shell are added to the electron configuration of Krypton. The spectroscopic properties of strontium mainly depend on the two-valence electrons at the outer s -shell, which give rise to triplet and singlet states, with two-electron spins in parallel ($S = 1$) and anti-parallel ($S = 0$) by designating the spin multiplicity as $2S + 1$. If one considers quantum statistics, strontium has both fermionic and bosonic isotopes (see Tab. 2.2): the nuclear spin of all bosonic Sr (^{84}Sr , ^{86}Sr , and ^{88}Sr) is absent ($I = 0$), and nuclear spin equals to $9/2$ for ^{87}Sr . To become a boson, an atom must compose an even total number of electrons, protons, and neutrons; the isotopes (^{84}Sr , ^{86}Sr , and ^{88}Sr) satisfy this requirement, and their nucleons arrange in pair of anti-parallel spin, which produces a vanishing nuclear spin. Then in such even-even nuclei, the nucleons arrange in pairs of anti-parallel spin, and the nuclear spin vanishes. In contrast, the fermionic isotope (^{87}Sr) has non-paired proton-neutron spins ($I = 9/2$).

Isotopes	Neutron number	Statistics	Nuclear spin
^{84}Sr	46	boson	0
^{86}Sr	48	boson	0
^{87}Sr	49	fermion	9/2
^{88}Sr	50	boson	0

Table 2.2: Nuclear properties of Sr isotopes.

2.1.2.1 The first-stage cooling transition

The ground state of the ^{88}Sr atom is $5s^2\ ^1S_0$ ($J = 0$), and it has a strong electric dipole allowed transition ($E1$) with the state $5s5p\ ^1P_1$ ($J = 1$) (see Fig. 2.1). This transition wavelength is ~ 461 nm, and the excited state $5s5p\ ^1P_1$ has a short lifetime ($\tau_{\text{blue}} = 5.22$ ns), translated into a broad transition linewidth $\Gamma_{\text{blue}} = 2\pi \times 30.5$ MHz. According to the selection rules, $5s^2\ ^1S_0 - 5s5p\ ^1P_1$ ($\Delta J = 1$) transition is valid for atomic cooling and trapping; its large scattering rate thanks to the broad transition is good for the first-stage cooling, e.g., Zeeman slower and blue magneto-optical trap (MOT), to effectively slow down hot Sr-atoms effused from an oven.

2.1.2.2 Repumping transitions

Since the broad transition $5s^2\ ^1S_0 - 5s5p\ ^1P_1$ is not 100% closed, the atoms at excited state $5s5p\ ^1P_1$ can decay to $5s4d\ ^1D_2$ state with a branch ratio of 1:50000, and the transition $5s5p\ ^1P_1 - 5s4d\ ^1D_2$ has a decay rate of 620 Hz, corresponding to a lifetime of $\tau = 256\ \mu\text{s}$ [123]. The leaked atoms decay further into the $5s5p\ ^3P_{1,2}$ metastable triplet states with a branching ratio of 2:1, and atoms at state $5s5p\ ^3P_2$ are lost in the blue MOT. To close the $5s^2\ ^1S_0 - 5s5p\ ^1P_1$ transition, one approach is to optically pump the atoms back to ground state $5s^2\ ^1S_0$ by addressing $5s5p\ ^3P_2 - 5s6s\ ^3S_1$ and $5s5p\ ^3P_0 - 5s6s\ ^3S_1$ transitions with two lasers of 707 nm and 679 nm. The 707 nm laser pumps the atoms from $5s5p\ ^3P_2$ to $5s6s\ ^3S_1$, then they decay into $5s5p\ ^3P_{0,1}$ ($\Delta J = \pm 1$). For atoms at state $5s5p\ ^3P_0$, $J = 0 - J = 0$ transition is forbidden, so they can not decay towards $5s^2\ ^1S_0$ state unless other effects like hyperfine-structure mixing in Fermions isotope (^{87}Sr) is considered. The other laser at 679 nm can pump atoms from $5s5p\ ^3P_0$ to $5s6s\ ^3S_1$, then above process is repeated. Other possibilities are indicated in Fig. 2.1.

2.1.2.3 The second-stage cooling transition

The atoms to decay from state $5s5p\ ^3P_1$ to state $5s^2\ ^1S_0$, require one electron spin-flip, as the emission of a single photon is not sufficient. However, due to the spin-orbit interaction between the $5s5p\ ^1P_1$ state and the $5s5p\ ^3P_1$ state, a weak electric dipole ($E1$) transition is allowed, leading to a lifetime of $21.4\ \mu\text{s}$ and a corresponding linewidth of $\Gamma_{\text{red}} = 2\pi \times 7.4$ kHz. With the same detuning frequency and saturation parameter, the photons referring to the $5s^2\ ^1S_0 - 5s5p\ ^1P_1$ transition has much less deceleration force on the atoms compared to the $5s^2\ ^1S_0 - 5s5p\ ^3P_1$ transition. However, the lower linewidth of the red transition results in a lower Doppler temperature. This means that the red MOT can not be used to capture atoms from a thermal atomic beam directly. Still, it can be a second-stage cooling just after the blue MOT to cool atoms down to the millikelvin temperature level and even further into the microkelvin region.

2.1.2.4 The clock transition

The clock transition requires a narrow linewidth and a low sensitivity to the ambient environment. In strontium, the $5s5p\ ^3P_0$ state is typically adopted as an upper state for the clock transition, thanks to its long lifetime. Due to the absence of nuclear spin in bosonic isotopes ($I = 0$), the spin-orbit interaction is null. The dominant decay channel from the $5s5p\ ^3P_0$ level is the $E1M1$ two-photon decay, which is so tiny that the lifetime is estimated at about thousands of years or equivalent to a linewidth at the level of picohertz [124]. The optical transition is weakly allowed for the fermionic counterparts due to spin-orbit-induced and hyperfine interaction mixing. The non-zero magnetic dipole moment couples the $5s5p\ ^3P_0$ state to other states of the same parity, among them the $5s5p\ ^1P_1$ and $5s5p\ ^3P_1$ states. Then, atoms at excited optical state can decay into the $5s^2\ ^1S_0$ state by a simple electric dipole ($E1$) process. The lifetime of the $5s5p\ ^3P_0$ state, in this case, is $118\ \text{s}$ [36] and corresponding to a linewidth of about $1.4\ \text{mHz}$.

Transition	Wavelength λ [nm]	Linewidth Γ [MHz]	Saturation intensity $I_0 = \pi \hbar c / 3 \lambda^3 \tau$ [mW/cm ²]	Maximum acceleration $a_{max} = \Gamma \hbar k / 2m$ [m/s ²]	Doppler temperature $T_D = \hbar \Gamma / (2k_B)$ [μ K]	Recoil temperature $T_r = \hbar^2 k^2 / (k_B M)$ [μ K]
$^1S_0 - ^1P_1$	460.7331	$2\pi \times 30.5$	41	9.3×10^5	720	0.690
$^1S_0 - ^3P_1$	689.2585	$2\pi \times 0.00747$	0.003	155	0.182	0.454
$^3P_2 - ^3S_1$	707.0071	$2\pi \times 6.69$	17	–	–	–
$^3P_0 - ^3S_1$	679.1022	$2\pi \times 1.42$	3.7	–	–	–

Table 2.3: These are the parameters for the blue cooling, red cooling, and two repumpers in ^{88}Sr -atoms.

2.1.2.5 The dark state

Atoms in the $5s5p\ ^3P_2$ state can decay back to the ground state via different pathways: the dominant process is through a magnetic octupole (M2) transition directly connected to the ground state, with a calculated lifetime of 1000 s [125]. The measured value of 520 s [126] explained by radiative decay. Two of these are parity-conserving one-photon decays of magnetic-dipole (M1) and electric quadrupole (E2) type into the $5s5p\ ^3P_1$ state and further back to the ground state; also black-body radiation can excite atoms into the $5s4d\ 3D$ states, from where they decay into the $5s5p\ ^3P_1$ state. The lifetime of atoms in the $5s5p\ ^3P_2$ is thus dependent on the temperature of the environment.

2.1.2.6 Isotopic shifts

The different strontium isotopes have a frequency shift of the spectroscopic lines due to the number of neutrons. The isotope shift is about a few tens of MHz per mass unit concerning ^{88}Sr -atoms, which is larger than its transition linewidth. For the fermionic ^{87}Sr -atom, which has a hyperfine structure, the shift refers to the center of gravity of the spectra. Tab. 2.4 reports the isotopic shifts of the two transitions used for the blue and red laser cooling and the clock transition. The isotopic shifts are of the order of 100 MHz and are then easily obtained with AOMs; this makes it simple to switch isotope in an experimental setup, at least concerning the lasers required to manipulate the atoms.

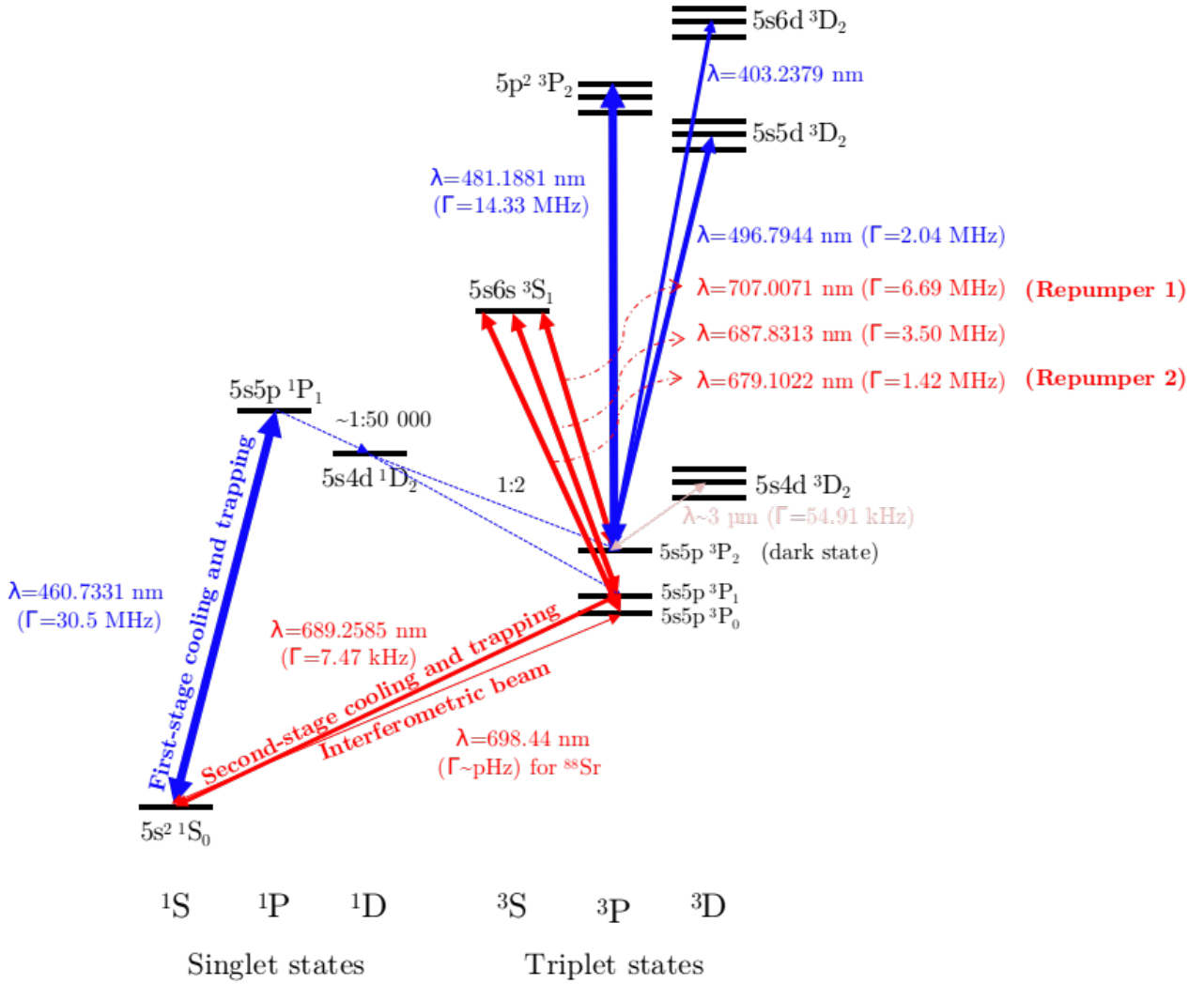


Figure 2.1: Fine structure of ^{88}Sr [121, 36] (not to scale) with their transition frequencies and linewidths. The thickness of the solid line indicates the strength of the transition rate.

Isotopes	$5s^2\ ^1S_0 - 5s5p\ ^1P_1$ [MHz]	$5s^2\ ^1S_0 - 5s5p\ ^3P_1$ [MHz]	$5s^2\ ^1S_0 - 5s5p\ ^3P_0$ [MHz]
^{84}Sr	-270.8	351.49	~ 200
^{86}Sr	-124.8	163.81	~ 100
^{87}Sr	~ -46.5	~ 62.15	~ 54
^{88}Sr	0	0	0

Table 2.4: Frequency shift of stable strontium isotopes with respect to the ^{88}Sr -atom [128].

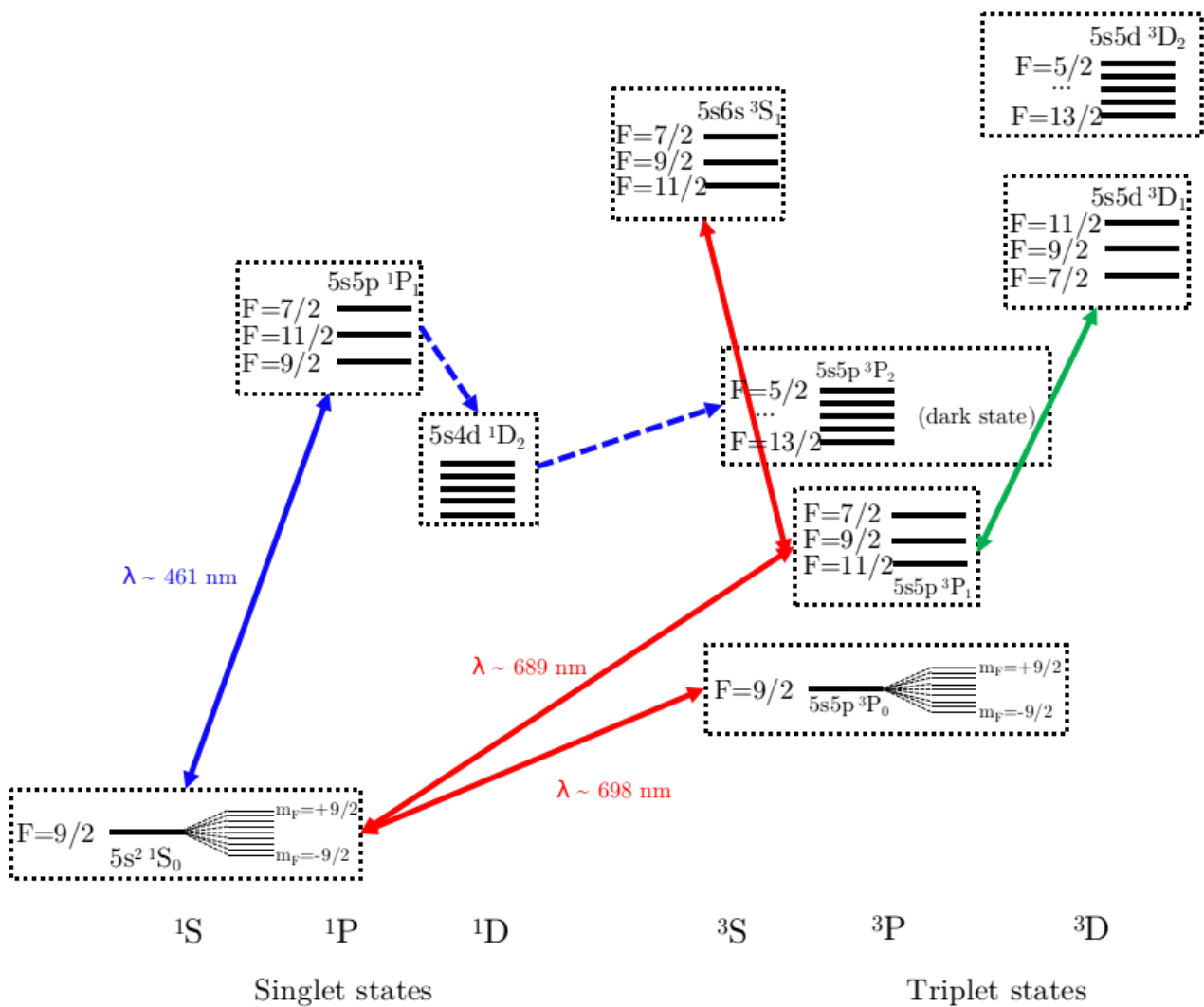


Figure 2.2: Schematic illustration of hyperfine structure (not to scale) for relevant states in ^{87}Sr -atoms. More details about resonance frequency and linewidth of certain transitions can be found for instance in [127]

2.1.3 The sensitivity to magnetic field

Cold atom experiments require precise magnetic field control, e.g., the Zeeman effect applied in the magneto-optical trapping technique. It is used to spatially confine and trap neutral atoms and shift away magnetic-field-sensitive atomic levels in precision spectroscopy. The magnetic sensitivities of the relevant states are often calculated, summarized in Tab. 2.5.

The Zeeman splitting to the first order is written as:

$$\Delta\nu_Z = \frac{g_F m_F \mu_B B}{h}, \quad (2.1)$$

where g_F is the total angular momentum g-factor, μ_B is the Bohr magneton ($\mu_B = 1.4$ MHz/G). The bosonic counterparts of strontium have no nuclear spin ($I = 0$), so $F = J$.

States	^{88}Sr	^{87}Sr				
		F=5/2	F=7/2	F=9/2	F=11/2	F=13/2
$5s^2 \ ^1S_0$	0 ($g_J = 0$)	N/A	N/A	0 ($g_F = 0$)	N/A	N/A
$5s5p \ ^1P_1$	$1.4m_J$ ($g_J = 1$)	N/A	$-0.31m_F$ ($g_F = -2/9$)	$0.056m_F$ ($g_F = 4/99$)	$0.25m_F$ ($g_F = 2/11$)	N/A
$5s5p \ ^3P_0$	0 ($g_J = 0$)	N/A	N/A	0 ($g_F = 0$)	N/A	N/A
$5s5p \ ^3P_1$	$2.1m_J$ ($g_J = 1.5$)	N/A	$-0.47m_F$ ($g_F = -1/3$)	$0.085m_F$ ($g_F = 2/33$)	$0.38m_F$ ($g_F = 3/11$)	N/A
$5s5p \ ^3P_2$	$2.1m_J$ ($g_J = 1.5$)	$-1.2m_F$ ($g_F = -6/7$)	$-0.2m_F$ ($g_F = -1/7$)	$0.25m_F$ ($g_F = 2/11$)	$0.50m_F$ ($g_F = 51/143$)	$0.65m_F$ ($g_F = 6/13$)

Table 2.5: The sensitivity of the states of interest in ^{87}Sr and ^{88}Sr -atoms to the magnetic field in the unit of [MHz/Gauss].

2.2 The magneto-optical trap

The first stage of an ultra-cold atomic experiment concerns the production of the low-temperature atomic ensemble. In the following, we will describe the primary mechanism to achieve ultra-low temperatures for Sr-atoms.

2.2.1 The blue MOT

The 3D-MOT uses red-detuned photons to the $5s^2 \ ^1S_0 - 5s5p \ ^1P_1$ of 30.5 MHz broad transition about $1.5\Gamma_{\text{blue}}$; this transition corresponds to the Doppler temperature of $720 \ \mu\text{K}$ ($v_{\text{rms}} \sim 1 \ \text{m/s}$). Since the broad transition is not fully closed, atoms decay from the state $5s5p \ ^1P_1$ to $5s4d \ ^1D_2$ state about 1 atom in every 10^5 excitations, then with a 1/3 probability fall into the $5s5p \ ^3P_2$ metastable state. To depopulate them, a few alternatives for repumpers are available (see Fig. 2.1). We use two repumpers at 679 nm and 707 nm, easily-accessed with cheap semiconductor lasers, to recycle atoms from atoms at metastable state $5s5p \ ^3P_2$.

2.2.2 The red MOT

The atoms are further cooled by exchanging momentum with photons resonating with a red $5s^2 \ ^1S_0 - 5s5p \ ^3P_1$ intercombination transition. Its linewidth is $\Gamma_{\text{red}} = 2\pi \times 7.4 \ \text{kHz}$, corresponding to a Doppler temperature of $T_D = 179 \ \text{nK}$, i.e., a factor of 4300 times smaller than for the blue transition. Also, for the narrow linewidth cooling, Doppler temperature is less than the recoil temperature $T_r = 460 \ \text{nK}$ for the red transition, where the minimal attainable temperature is $T_r/2$. The second stage is a red MOT operated on a narrower transition, capable of cooling the atoms to thousand-times lower temperatures with million-times higher densities [128]. The atomic sample with low temperature and high density can be efficiently loaded into an optical dipole trap; The third stage is typically evaporative cooling, leading to quantum degeneration, an optional stage dependent on isotopes and experimental requirements.

When enough atoms ($> 10^8$) are present in the metastable state reservoir, the ensemble phase space density is rapidly increased by switching to a red MOT operated on the $5s^2 \ ^1S_0 - 5s5p \ ^3P_1$ intercombination line, which has a wavelength of 689 nm, a linewidth of $\Gamma_{\text{red}} = 2\pi \times 7.4 \ \text{kHz}$ and a corresponding recoil temperature of 460 nK.

The 3D-MOT atomic ensemble cooled on the blue line has a temperature of $\sim 1 \ \text{mK}$, which means a Doppler distribution so broad that only a tiny fraction of atoms could interact with a laser at 689 nm with a linewidth of 1 kHz or less. For this reason, the effective linewidth of the red cooling laser must be initially increased to capture all the atoms from the blue MOT;

to this end, several approaches have been developed, as the chirping of the red laser or in the generation of a comb of lines spanning the required spectrum. After a phase in which both the blue cooling laser and the broadened red one are present, the blue light is turned off, and then the effective linewidth of the red laser is reduced to its minimum, so the cooling of the atomic ensembles down to the sub-microkelvin regime. Here, the expansion velocity of the atomic sample is about 1 cm/s or less, which is already suitable for its required use in an atom interferometer.

The dipole trap (optional)

If an even-lower temperature is required, the cold atomic sample obtained in the red MOT can optionally be transferred into an optical dipole trap a crossed optical dipole trap [129] or add delta-kick collimation [130].

The scattering properties of an atomic species determine the efficiency of evaporative cooling, then the stability of a degenerate gas. The ⁸⁴Sr atom offers an excellent scattering length of $a = 123a_0$, which is large enough for elastic collisions to implement an efficient evaporative cooling, the not sufficient to dominate detrimental three-body recombination losses (upper limit of three-body collision rate $\propto a^4n^2$). The low natural abundance (0.56%) can be overcome by an efficient loading into optical dipole trap [38]. ⁸⁶Sr has an intermediate abundance (9.86%) and large scattering length ($a = 800a_0$), which imposes fast three-body losses. Evaporative cooling is performed at low densities in a large optical dipole trap [131]. Fermionic ⁸⁷Sr with scattering length $a = 90a_0$ and large nuclear spin $I = 9/2$ is a favorable isotope to reach quantum degeneracy. ⁸⁷Sr degenerate Fermi gas also has been obtained via sympathetic cooling mediated by a BEC of ⁸⁴Sr [132]. ⁸⁸Sr is the most abundant isotope (82.58%); however, up to now, only condensates with a limited number of atoms have been reported. This limitation is set due to the ⁸⁸Sr-atom small and negative scattering length ($a = -2a_0$), and the inefficient evaporative cooling being replaced by the sympathetic cooling with another coolant like the ⁸⁷Sr-atom [133]. Recently, a new technique using laser cooling as the only cooling mechanism to produce quantum degeneracy gas has been reported in [134].

2.3 The coherent manipulation on the clock line

To estimate the total fraction of atoms left at the detected state at the end of the interferometric sequence, it is necessary to evaluate the integral of excitation probability for each pulse. The excitation probability is related to the phase-space properties of the atomic cloud and can be calculated as such [135]

$$P_{\text{exe}} = 2\pi \int \int r f(v) n(r, t) \left(\frac{\Omega_0(r)}{\Omega_{\text{eff}}(r, v)} \right)^2 \sin^2 \left(\frac{\Omega_{\text{eff}}(r, v)}{2} t \right) dr dv, \quad (2.2)$$

where $f(v)$ is the velocity distribution, $\Omega_0(r)$ is the spatially-dependent Rabi frequency and $n(r, t)$ is the transverse atomic density distribution. Unlike for the fermionic strontium isotope, where the Rabi frequency can easily reach the kilohertz regime, for bosonic isotopes, the single-photon clock transition is very small, and an effective linewidth for the $5s^2 \ ^1S_0 - 5s5p \ ^3P_0$ transition can be obtained, for example, by magnetic field induced spectroscopy, a small, controllable fraction of the nearby $5s5p \ ^3P_1$ state into the $5s5p \ ^3P_0$ state. In this way, we obtain a Rabi frequency [42],

$$\Omega_0 = \alpha \sqrt{IB}, \quad (2.3)$$

where I is the interrogated light intensity, and B is an externally applied magnetic field. In Chp. 5, we use this technique as a "switch" to coherently manipulate atom and interferometric beam coupling. And the effective Rabi frequency associated with a beam splitting light of wavenumber k is

$$\Omega_{\text{eff}}(r, v) = \sqrt{\Omega_0^2(r) + (kv)^2}. \quad (2.4)$$

Chapter 3

Experimental apparatus

One of the significant tasks within the framework of this thesis is constructing the sub-microKelvin ^{88}Sr atom interferometer platform. This chapter is dedicated to the technical details about the vacuum and the laser systems.

In Sec. 3.1 and Sec. 3.2, we present the mechanical design of the needed vacuum systems, for both atomic source and science cell, as well as the anti-Helmholtz magnetic field coils. They are essential elements to produce a good MOT in the science cell. A high power and frequency-stabilized laser system is required for a high-atom-flux atomic source. Two solutions are typically adopted to this aim: frequency doubling a tapered amplified infrared ECDL laser source (see Sec. 3.3.1), or power-enhancing by optical injection locking of slave diode laser (see Sec. 3.3.2). The absolute frequency of these lasers is obtained via saturated spectroscopy on the $5s^2\ ^1S_0 - 5s5p\ ^1P_1$ transition. The atoms escaping the cooling transition and eventually falling in the state $5s5p\ ^3P_2$ dark to the blue light are put back in the cooling cycle thanks to two repumpers at 679 nm and 707 nm, frequency stabilized using a wavelength meter (see Sec. 3.5). The atoms produced in the blue MOT are then transferred to the second cooling stage, again a MOT but operated on a much narrower transition. The cooling laser red-detuned to $5s^2\ ^1S_0 - 5s5p\ ^3P_1$ transition cools mK-temperature atoms further to sub- μK with million-times higher densities. The requirements for the red cooling laser are a linewidth of 1 kHz or less, i.e., much less than the transition linewidth, and its frequency stabilization close to the $5s^2\ ^1S_0 - 5s5p\ ^3P_1$ transition; only a few mW of power are required, due to the very low saturation intensity of the cooling transition. To satisfy these require-

ments, the laser adopted for the red cooling is firstly locked to a high-finesse cavity to narrow its linewidth, and then it is adopted to probe the $5s^2\ ^1S_0 - 5s5p\ ^3P_1$ transition at 689 nm (see Sec. 3.4.2). The error signal obtained with the saturated spectroscopy is used to stabilize the long-term drift of the high-finesse cavity where both the red cooling laser and the clock laser are stabilized (see Sec. 3.4.3). We use the same high-finesse cavity for the clock laser and the red-cooling laser; the high-reflectivity coatings on the cavity mirrors are optimized for 698 nm, but it is still effective at 689 nm (see Sec. 3.4.1). Fig. 3.1 illustrates the arrangements of the above laser systems in the Sr atom interferometer. To control the experimental sequence, synchronizing the instruments, triggering the events constituting an experimental controller, and dynamically adjusting its parameters, we realized an FPGA-based control system, detailed in Sec. 3.6.

Contents

3.1	Vacuum system	43
3.1.1	Atomic source	43
3.1.2	Science cell	46
3.2	Magnetic field coils	46
3.3	High-power and frequency-stabilized laser at 461 nm	49
3.3.1	1 W laser at 461 nm by frequency doubling	49
3.3.2	Optical power enhancement by injection locking	61
3.3.3	Doppler-free blue spectroscopy at $^1S_0 - ^1P_1$ transition	71
3.4	Narrow-linewidth and frequency-stabilized laser at 689 nm and 698 nm	77
3.4.1	Linewidth narrowing of the red-cooling laser and the clock laser	79
3.4.2	Doppler-free red spectroscopy at $^1S_0 - ^3P_1$ transition	82
3.4.3	Optical cavity drift cancellation through red spectroscopy	84
3.5	Repumpers at 707 nm and 679 nm	87
3.5.1	Wavemeter-based multi-frequencies stabilization	87
3.6	FPGA-based experimental control system	93

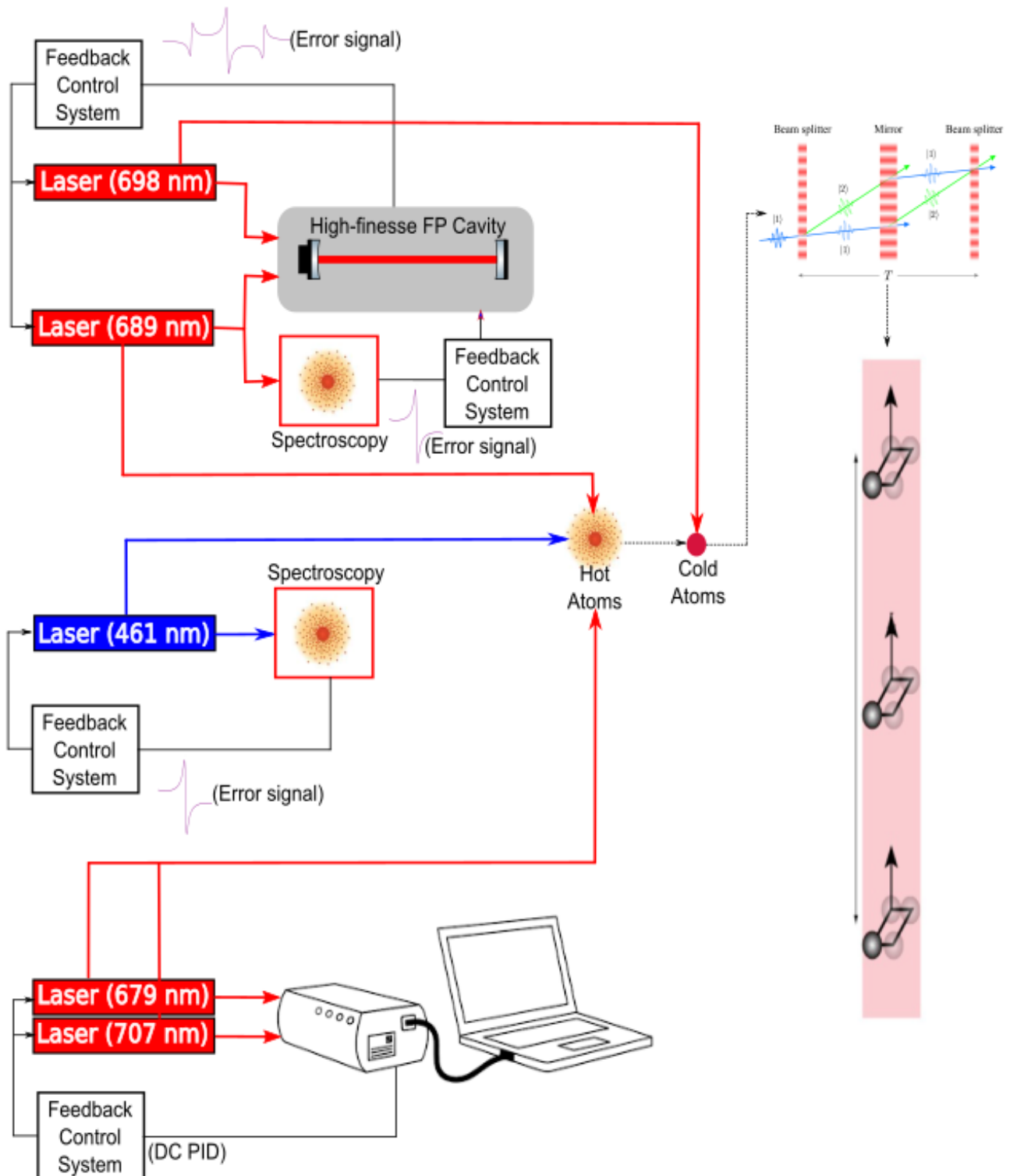


Figure 3.1: Layout design of laser systems in Sr atom interferometer.

3.1 Vacuum system

The vacuum system is mainly divided into the atomic source and science cell regions, and they have different requirements for vacuum level: the experiments take place in the science cell, which is under ultra-high-vacuum pressure to reduce collision rate with background atoms, thus enhancing the lifetime of the cold atomic sample, and minimizing the decoherence for the clock spectroscopy; however, the vacuum level in the atomic source is not demanding.

3.1.1 Atomic source

The high-flux atomic source is based on a recent compact-design [136, 137] (see Fig. 3.2). The development of the Sr atomic source has been done in collaboration with the group of D. Wilkowski in Singapore (MAJULAB), and the design of the main vacuum chamber is attached in Appx. C. The source combines a 2D MOT exploiting permanent magnets and a space-demanding Zeeman slower using the magnetic field produced by the same magnets; the result is a compact and efficient setup. As indicated by [136], the compact setup can avoid undesired effects like vacuum contamination in Zeeman slowers and black-body radiation due to hot Sr oven.

The material of the atomic source uses stainless steel for its low out-gassing rate, tolerance to high temperature, low eddy currents, low magnetization, and inexpensive cost. Since stainless steel has no supreme performance in out-gassing, we conduct a standard bake-out procedure of heating the atomic source to ~ 300 °C, with a temperature rising rate of 10 °C/h, for one to two days before utilization to reduce its out-gassing.

3.1.1.1 The oven

The shortest way of the main chamber is the oven's plug, which is designed to be as close as possible to the center of 2D MOT. The oven is a cylindrical container with an aperture of 25 mm diameter, where 5 g of Sr granules with natural abundance (99% purity, Alfa Aesar) are filled in the oven. Due to the high melting temperature of Sr, the oven is typically heated up to 550 °C for sufficient vapor pressure, which leads to the oven lifetime being a few years. To minimize atomic beam divergence, an array of 400 micro-sized Nozzle tubes is frequently

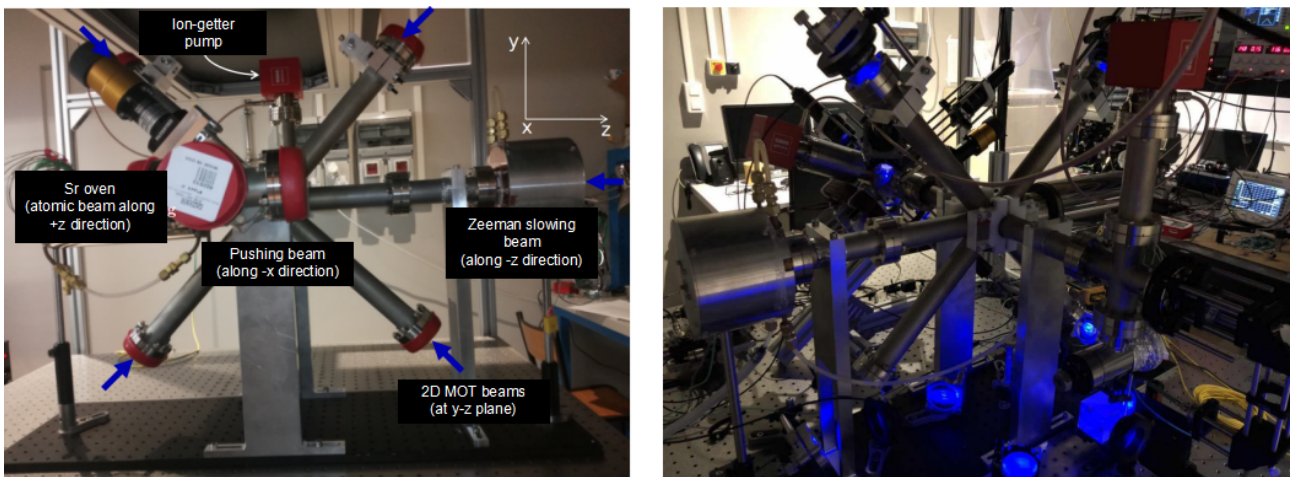


Figure 3.2: Compact atomic source setup, in which the main chamber is a CF40 8 ways cross made of stainless steel 304SS. The left picture has been taken at the beginning when we tested the vacuum, right picture is the setup under operation.

mounted at the oven aperture, separately heated to an even higher temperature than the oven to avoid deposit of Sr on the Nozzle. The THERMOCOAX cold ends heating wire has a length of 200 cm with a resistance of 11 Ohms.

3.1.1.2 The 2D MOT

To avoid the deposit of Sr on the viewports (AR coating: 390 nm - 570 nm, reflected loss at 461 nm: $< 0.5\%$) for optical access, the four ways of the 2D MOT are as long as possible, ~ 30 cm. A transversely loaded 2D MOT is employed to capture atomic beam ejecting from a high-temperature oven. This transverse cooling is realized compactly, where the 2D MOT center sits 15 cm away from the Sr oven. Four packets of permanent magnets (Neodymium Block Magnets N750-RB, Eclipse Magnetics Ltd) produce a quadruple magnetic field (about 50 G/cm) for 2D MOT. The remaining perpendicular two ways (14 cm long) is for transferring atoms trapped in 2D MOT into the science chamber (see Fig. 3.3) via a weak pushing beam nearly resonant light.

3.1.1.3 The Zeeman slower

The tails of the magnetic field (field vector pointing along an axis perpendicular to atomic propagation along) can be used for Zeeman slower, which is space-demanding. The Zeeman

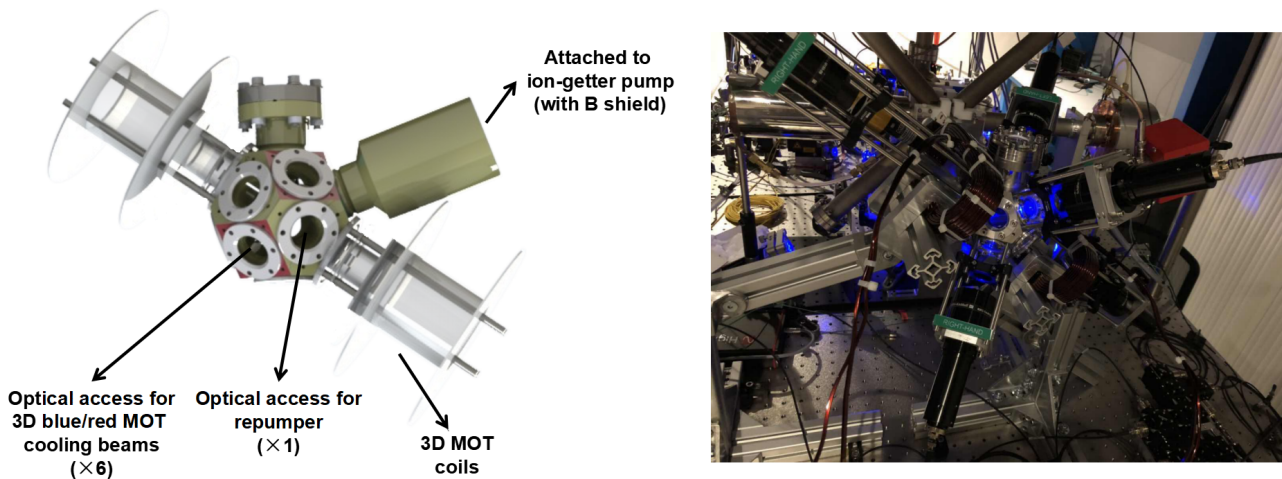


Figure 3.3: Science cell (left) design in Solidworks (right) experimental setup.

slowing beam is shone from a sapphire window opposite the oven (>15 cm away from the 2D MOT center). The viewport is made of sapphire instead of standard glass since its surface is more scratch-resistant and less sensitive to etching from aggressive materials. Permanently heating the viewport at ~ 380 °C can prevent the deposit from hot Sr atoms. For safekeeping, this viewport is enclosed by an extra stainless-steel box with another clear window, whose temperature can be maintained to room temperature through water cooling.

Pushing beam The remaining perpendicular way is for pushing beam to guide atoms from 2D MOT to science cell.

3.1.1.4 The pumping stages

An all-metal angle valve from MDC Vacuum (1.5" port, 2-3/4" CF flanges) allows for initial pumping, and one hybrid pump (SAES Getters, NEX Torr D200-5) with the ion pump and getter is attached to the setup. A gate valve is vital for allowing individual ventilation for only one region without disturbing the other, e.g., refilling the oven while not breaking the high vacuum pressure of the science cell. The gate valve is followed by a differential pumping state (22.8 mm length, 2 mm inner diameter), establishing a factor of 1,000 in terms of pressure difference, which satisfies the different vacuum levels requirements in atomic source and science cell. The whole setup is mounted to the optical table via three fixed-height posts.

3.1.2 Science cell

The science cell is a commercial product from a SAES-RIAL company (see Appx. D). We take even more care on the material choice and viewport sealing due to the requirement of its ultra-high vacuum level: the vacuum material is replaced with titanium, instead of stainless steel, thanks to its even lower hydrogen out-gassing and local magnetizations; the high vacuum quality is ensured by first using indium to seal the viewport, then the viewport is connected to the chamber through CF flanges. During the bake-out procedure, it becomes melt and sticky.

Two small but efficient ion-getter pumps with the same model (SAES Getters, NEX Torr D200-5) are attached to the science chamber and atomic source. The science cell maintains ultra-high vacuum level ($<10^{-10}$ mbar) even the atomic source is under operation with a background vacuum pressure of $\sim 10^{-8}$ mbar. Both values are measured with the pump drivers, and $<10^{-10}$ mbar reaches their minimum detectable pressure level, and they are shielded with μ -metal to reduce the effect of stray magnetic fields, especially on the science cell.

The viewports have dimensions compatible with the CF connectors. They are employed for both blue and red optical access, convenient for producing the blue/red MOT and applying repumpers in the science cell.

3.2 Magnetic field coils

The quadruple field gradient along the direction of interest to operate MOT is formed with a pair of coaxial coils in the anti-Helmholtz configuration that currents with the same magnitude flow in opposite directions. The typical design of round-shape coils refers to [138]. However, limited by the geometrical space of our setup, we consider two equal rectangular loops in anti-Helmholtz configuration to produce the required gradient magnetic field (>50 G/cm), corresponding to 80 A current, for the blue MOT. An analytic approach to obtain the required gradient is detailed in the [139]. Since the magnetic field gradient is linearly proportional to the flowing current, the same coil can be used for the red MOT (~ 10 G/cm)

by reducing the operating current by five times. A fast magnetic field switch is developed for this purpose.

We have designed the pair of identical rectangular coils with a number of turns 6×7 and the dimension of $19 \text{ cm} \times 9.5 \text{ cm}$ as shown in Fig. 3.4. The insulated copper wire is purchased from APX company, with a cross-section area of $4.5 \text{ mm} \times 3.15 \text{ mm}$. One constant current power supply is used to send the currents into the two coils. The scalar magnetic field is measured with the help of the Gauss Meter along the axial direction of two coils at different positions. The magnetic field gradients in the vicinity of the zero line of magnetic field and away from the zero line are estimated from both the plots and re-plotted in the same figure.

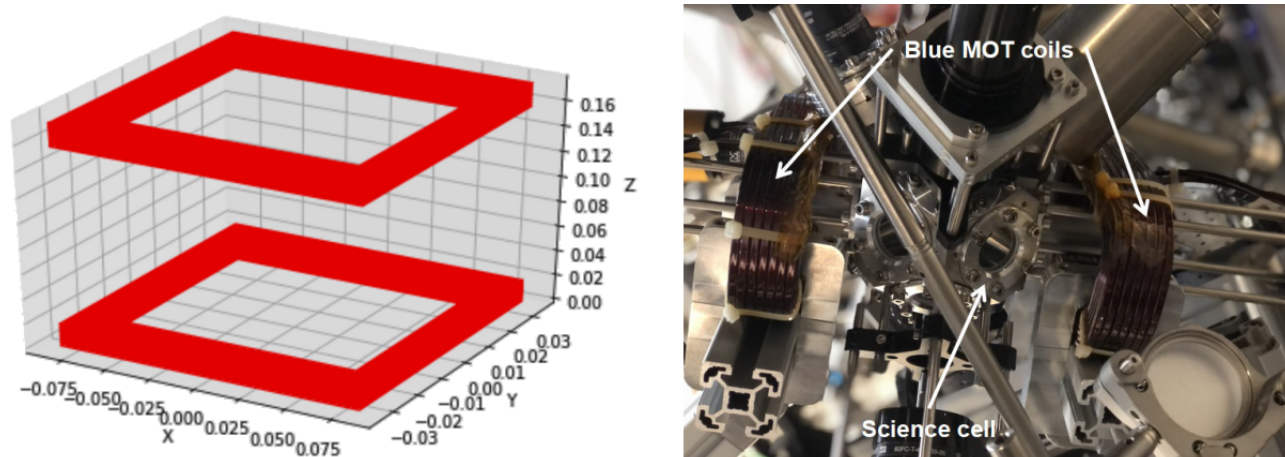
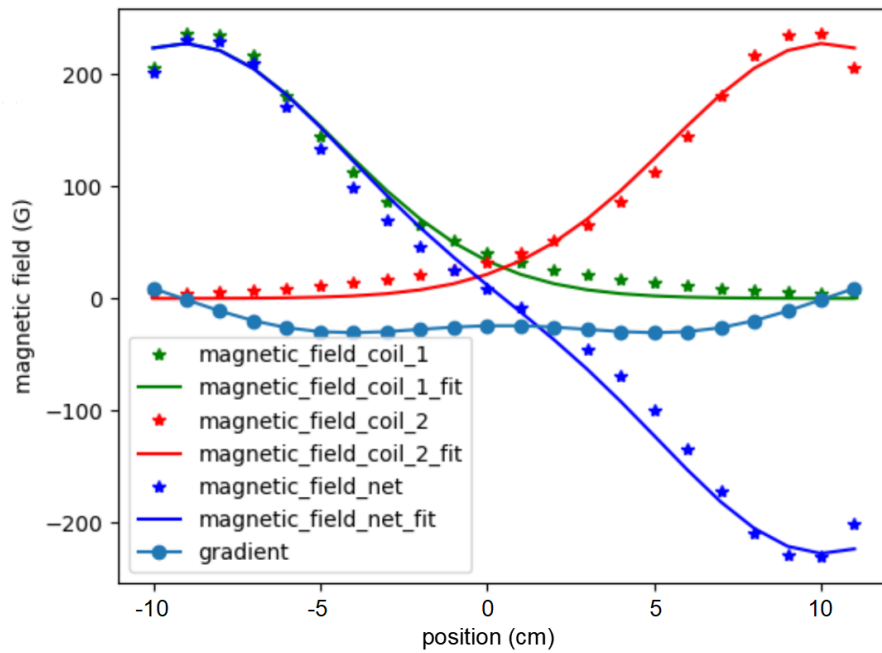
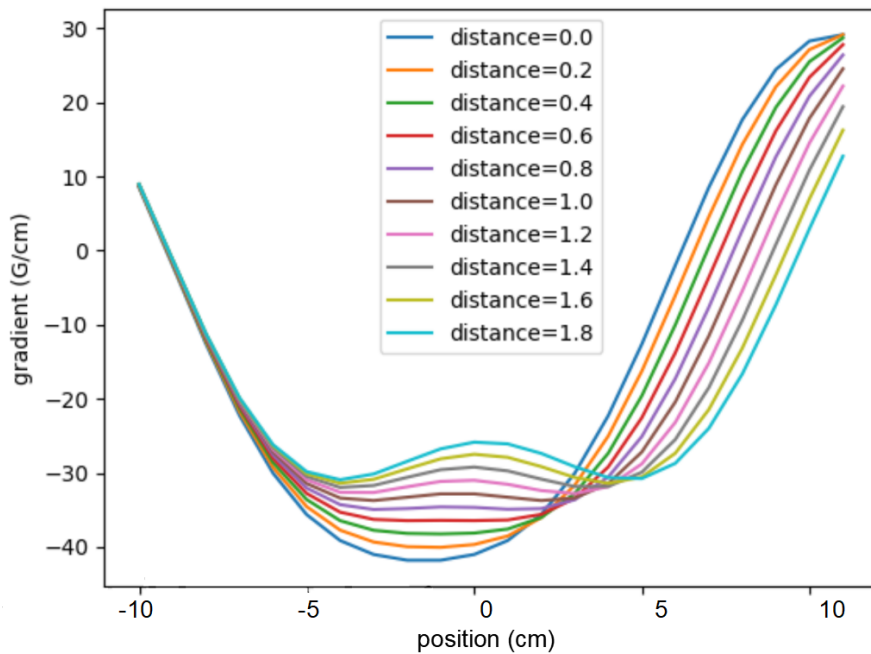


Figure 3.4: Magnetic field coils.

To investigate the homogeneity of the magnetic gradient for the MOT (position = 0 cm), we have measured the magnetic field of coils along the axial direction. Due to the lack of a water-cooling system for the coils, without loss of generality, the current is set at a slightly lower value, e.g., 50 A, to avoid overheating. The measured magnetic field data is fitted with the Gauss function (see Fig. 3.5 (a)), then a maximum homogeneity for B-field gradient is obtained by scanning the distance between the coil and the science cell. From Fig. 3.5 (b), we know that the optimal magnetic field gradient is achieved at a distance of $\sim 0.6 \text{ cm}$ between the coil and the science cell.



a



b

Figure 3.5: (a) Magnetic field produced for 3D MOT; the solid line is a fitting of the discretized points taken from the measurement. (b) Optimal magnetic field gradient is achieved by scanning the distance between the coil and the science cube.

3.3 High-power and frequency-stabilized laser at 461 nm

To magneto-optically trap ^{88}Sr atoms with light on the $5s^2\ ^1\text{S}_0 - 5s5p\ ^1\text{P}_1$ transition, with the saturation intensity of $\sim 42\ \text{mW}/\text{cm}^2$, a high-power blue laser beam at 461 nm with a linewidth at MHz level or less is required. Different approaches are reported in the literature to obtain a few hundreds of mW typically required for this cooling stage: exploiting laser diodes, a technologically simple solution can combine moderate power and narrow linewidth but requires optical injection of one or more slave modules [140]; single-pass second-harmonic (SH) generation with a bulk crystal [141], can achieve high power while doubling the source linewidth but only with large input power.

In our laboratory, we generate 500 mW blue light by injection locking (see Sec. 3.3.2), whereas we obtain 1 W by frequency-doubling an amplified diode laser at 922 nm (see Sec. 3.3.1).

3.3.1 1 W laser at 461 nm by frequency doubling

We obtain a Watt-level continuous and single frequency blue laser at 461 nm by frequency-doubling an amplified diode laser operating at 922 nm via a LBO crystal in a resonant Fabry-Pérot cavity. We achieve a best optical conversion efficiency equal to 87% with more than 1 W output power in the blue and limited by the available input power. The frequency-converted beam is characterized by long-term power stability, residual intensity noise, and geometrical shape. The blue beam has a linewidth at the order of 1 MHz, and we use it to magneto-optically trap ^{88}Sr atoms on the $5s^2\ ^1\text{S}_0 - 5s5p\ ^1\text{P}_1$ transition. The low-finesse, linear-cavity doubling system is very robust, maintains the lock for several days, and is compatible with a tenfold increase of the output power level, which could be obtained with fully-fibered amplifiers [142] and large mode area fibers.

Second-harmonic-generation Frequency doubling involves a nonlinear optical process where the fundamental excitation light interacts with a nonlinear medium (crystal), and this nonlinear process is formulated simply as,

$$P = \epsilon_0(\chi^{(1)}E_\omega + \chi^{(2)}E_\omega^2 + \chi^{(3)}E_\omega^3), \quad (3.1)$$

where P is the induced dipole moment per unit volume, ϵ_0 is the electric constant, E_ω is the electric field amplitude of fundamental laser, and χ is the electrical susceptibility of the dielectric material. Second-harmonic generation (SHG) exploits the second-order effect $\chi^{(2)}$, and the SHG intensity $|A_{2\omega}(L)|^2$ is expressed as [143]

$$|A_{2\omega}(L)|^2 = \frac{4\omega^2}{n_{2\omega}^2 c^2} (\chi^{(2)})^2 |A_\omega|^4 L^2 \text{sinc}^2(\Delta k L / 2), \quad (3.2)$$

where ω is the fundamental laser frequency, $n_{2\omega}$ is the refractive index of the nonlinear crystal at SHG frequency, L is the crystal length, and $\Delta k = 2k_\omega - k_{2\omega} = 2n_\omega \omega c - n_{2\omega} 2\omega c$ is the phase mismatch factor, determining the nonlinear conversion efficiency.

The intensity of the SHG component scales as the square of the fundamental laser intensity $|A_\omega(L)|^2$ and also the crystal length L . An external optical build-up cavity is often used around a long crystal to enhance the pump power at the fundamental frequency. The phase matching is also optimized by tuning the temperature of the nonlinear crystal and adjusting the alignment of the incident fundamental laser to satisfy the requirement of $\Delta k L < \pi$ for sufficient SHG.

3.3.1.1 Frequency-doubling system

SH generation exploiting a traveling-wave cavity [144, 145], commonly folded in a bow-tie configuration for compactness, is widely adopted commercially [146, 147] and offers high power and narrow linewidth at the price of a complex optical system and alignment procedure, high sensitivity to vibration noise and, typically, astigmatism of the output beam.

We demonstrate high power CW operation at 461 nm. Our system exploits frequency doubling of an amplified infrared laser in a linear cavity [148] via a lithium triborate (LBO) crystal. Our solution combines low linear losses, ease of alignment, and high mechanical stability thanks to fewer optical elements. Notably, we obtain an output power of 1 W, competitive with the state-of-the-art, and yet limited only by the available level of input power; the figure could be widely increased as soon as a higher power is available for the fundamental wavelength [149].

Fig. 3.6 depicts the scheme of our frequency doubler. The seed laser light at $\lambda = 922$ nm and with a linewidth < 200 kHz is generated by an extended-cavity diode laser (DL pro, Top-

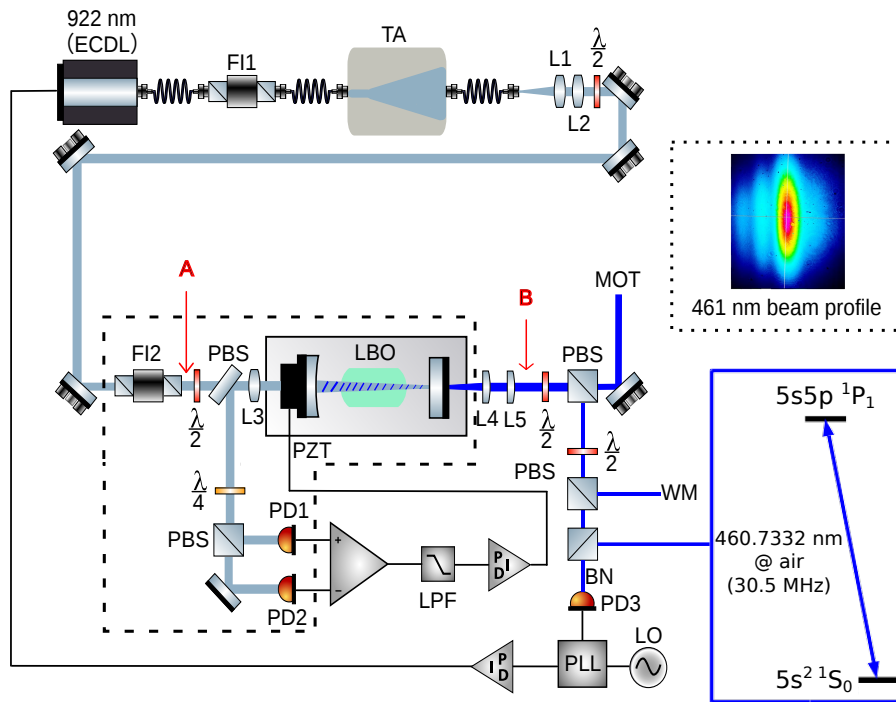
tica) fiber coupled to a tapered amplifier (TA pro, Toptica). The system delivers a maximum output power of 2.2 W in free space, reduced to 1.36 W after coupling it to a single-mode fiber (P1-780PM-FC-1, Thorlabs) to clean the geometrical mode and ease its alignment on the doubling cavity (position A in Fig. 3.6).

Two ~ 60 dB double-stage Faraday isolators (FI1 and FI2) decouple the TA from the seed laser and from the doubling cavity, respectively, thus protecting the system and avoiding frequency and intensity noise due to optical feedback.

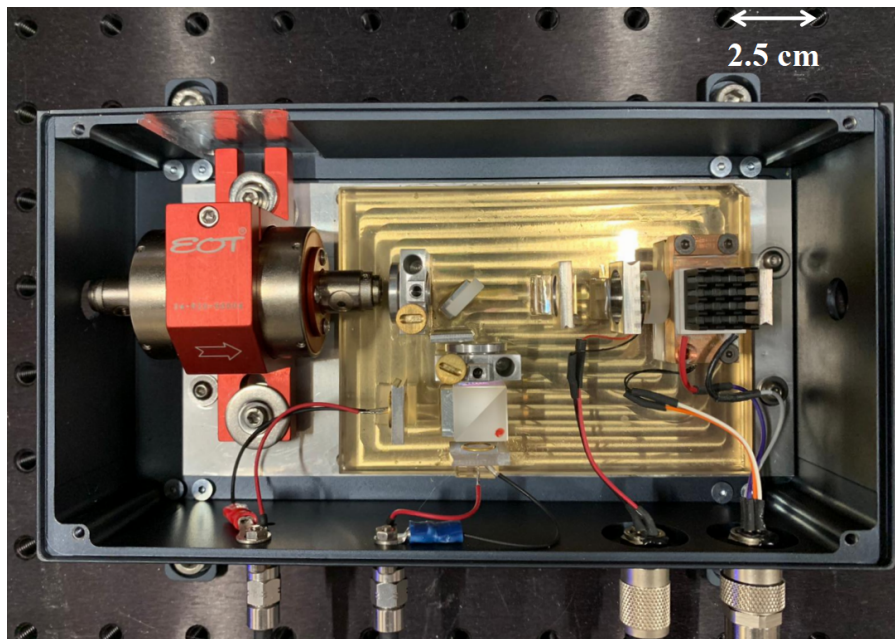
We considered different kinds of nonlinear crystals for the SH generation, as resumed in Tab. 3.1. Periodically-poled crystals operating at quasi-phase-matching condition have been dismissed, despite a promising high conversion efficiency (d_{eff}), because of their major limitations at high power induced by the photo-refractive beam distortion, the blue-induced infrared absorption [150], and thermal effects [151]. β -barium borate (BBO) [152] and bismuth triborate (BiBO) [153] crystals were discarded because of their large walk-off angle (see Tab. 3.1). We opted for a LBO crystal from Crystal Laser characterized by a small walk-off angle, high thermal conductivity, and an overall good long-term stability; its much smaller second-order non-linearity compared to periodically-poled crystals is compensated by a much higher damage threshold, and crystal quality, greater transparency at the operating wavelengths, and lower thermal lensing [154, 155].

Parameters	ppsLT [151]	ppKTP [156]	BiBO [153]	BBO [152]	LBO [144, 145, 155]
Transparency range (nm)	300-5000	350-4500	286-2500	185-2600	160-2600
Phase matching	quasi-phase matching type I	quasi-phase matching type I	critical	critical	critical
d_{eff} (pm/V)	5	10.8	3.42	2	0.75
Walk-off angle (mrad)	0	0	44.5	61.34	9.38
Thermal effects	yes	yes	no	no	no
Angular acceptance (mrad \times cm)	na	55 ($\Delta\theta$) 10 ($\Delta\phi$)	1.05	1.2	6.5

Table 3.1: Key parameters for different kinds of crystals suitable to generate blue light by SH generation.



a



b

Figure 3.6: (a) Frequency doubling setup. The laser power at 922 nm injected to the cavity is measured at position A, the output power at 461 nm at position B. TA: tapered amplifier; FI1, FI2: Faraday isolators; BS: beam splitter; PBS: polarizing beam splitter; PD: photodetector; LPF: low-pass filter; L1, L2, L3: aspherical lenses; L4, L5: cylindrical lenses; WM: wavelength meter. Inset: intensity profile of the output beam at 461 nm. (b) Top view of the elements within the dashed polygon in (a) and enclosed in an aluminum box to improve the thermal stability of the frequency doubling cavity.

3.3.1.2 Design for the cavity

The intracavity LBO crystal imposes several constraints on the design of the doubling cavity [157]. Angle-tuned phase matching is preferable for LBO because of the high-temperature values required for temperature tuning at 922 nm. We perform type I critical phase-matching, taking into account the walk-off angle ρ between the fundamental and frequency-doubled waves. The second harmonic power is fixed by

$$P_{out} = E_{nl}P_{in}^2, \quad (3.3)$$

where P_{in} is the fundamental power inside the crystal, the nonlinear coefficient E_{nl} can be calculated for Gaussian beams by the Boyd and Kleinman formula [158], which in the international system units is given by [159]:

$$E_{nl} = \frac{16\pi^2 d_{eff}^2 L}{\epsilon_0 c \lambda^3 n_{2\omega} n_{1\omega}} e^{-\alpha L} h(\rho, \xi), \quad (3.4)$$

where d_{eff} is the effective nonlinear coefficient of the LBO equal to 0.8 pm/V, $L = 15$ mm is the length of the crystal, $n_{1\omega}$ and $n_{2\omega}$ are the index of refraction for the fundamental and second harmonic frequencies, respectively, equal to 1.6 at the phase-matching angle, and $\alpha = a + b/2$ accounts for absorption of the fundamental waves ($a = 0.03 \text{ m}^{-1}$) and of the second harmonic wave ($b = 0.3 \text{ m}^{-1}$). c is the velocity of light in a vacuum, and ϵ_0 is the permittivity of the vacuum. The function $h(\rho, \xi)$ accounts for the walk-off angle $\rho = 9$ mrad and the focusing parameter of the Gaussian beam $\xi = 1/2z_R$, where z_R is the Rayleigh range of the Gaussian mode of the fundamental beam [158]. With an optimized beam waist of $\sim 40 \mu\text{m}$ for a crystal length equal to 15 mm, Eq. 3.4 predicts that $E_{nl} = 5 \times 10^{-5} \text{ W}^{-1}$. The power P_c circulating in the cavity depends on the power injected in the cavity as [160]:

$$P_c = \frac{T_1 P_{in}}{[1 - \sqrt{(1 - T_1)(1 - l)(1 - E_{nl}P_c)}]^2}, \quad (3.5)$$

where T_1 is the transmission of the input coupler and l is the linear loss in the cavity mainly due to the mirrors and crystal coatings. From Eq. 3.5, P_c is optimized when the transmission of the input coupler is equal to T_{opt} defined as:

$$T_{opt} = \frac{l}{2} + \sqrt{\frac{l^2}{4} + E_{nl}P_{in}}. \quad (3.6)$$

Assuming $P_{in} = 1.19$ W, we choose the input coupler with a transmission equal to 1.2%.

The LBO crystal is tightly fixed on the cavity axis; it has a length of 15 mm and a cross-

section of $3 \times 3 \text{ mm}^2$. The crystal is cut for normal incidence $\theta = 90^\circ$, $\phi = 21^\circ$ at the phase matching at 48°C and has a two-layer antireflection coating working at 922 nm (reflectivity $R < 0.1\%$) and 461 nm ($R < 0.3\%$). The temperature of the LBO crystal is stabilized to the optimal phase-matching temperature of 48°C with long-term stability at the mK level by controlling the temperature of the copper holder where it is fixed with thermally conductive glue. The temperature acceptance curve has a sinc^2 profile with a FWHM of $\sim 3^\circ\text{C}$ for the given length of the crystal [161]. The input mirror of the cavity is concave, has a nominal reflectivity at 922 nm equal to 98.8% and a very high reflection coating at 461 nm ; the output coupler is a flat mirror coated for high reflection at 922 nm and antireflection at 461 nm . The cavity is 18 mm long, and we use the Boyd-Kleinman equations [162] to optimize the conversion efficiency: this results in a radius of curvature of 15 mm for the input mirror, and a fundamental cavity mode with a waist of $\sim 100 \mu\text{m}$ on the input mirror and $\sim 40 \mu\text{m}$ on the output one; the single-pass nonlinear conversion efficiency is evaluated to $\sim 1.0 \times 10^{-4} \text{ W}^{-1}$ [163].

The amplified seed laser beam before the doubling cavity is mode-matched to the fundamental transverse mode of the cavity with a pair of lenses (L1 and L2), whose positions are precisely adjusted utilizing micrometric translational stages. The polarization axis of the input beam is controlled with a $\lambda/2$ waveplate. To further protect the TA from optical feedback – particularly strong when the cavity unlocks – we placed an additional 30 dB optical isolator resulting in an extra 12% insertion loss at the input of the resonator.

The optical cavity is locked to the input seed laser exploiting the modulation-free Hänsch-Couillaud stabilization technique [164]; the cavity length is controlled by a piezo-electric device which translates one of the two mirrors defining the resonator with a 1 kHz bandwidth. By scanning the length of the cavity with PZT, the error signal used for the feedback control is generated (see Fig. 3.7). The doubling efficiency is critically dependent on the mechanical and thermal stability of the system; hence great care was devoted to the design of the doubling cavity. Notably, mechanical robustness has been obtained by gluing the components of the doubling system to a Zerodur plate and enclosing it in an aluminum box to improve its temperature stability passively.

Polarization spectroscopy Polarization spectroscopy is based on the polarization changes of light waves when passing through a crystal [164]. By converting polarization changes in a nonlinear crystal [165] into voltage, an error signal for the servo locking system is obtained. This frequency stabilization technique is free from modulation. Moreover, the error signal is finite over an extensive frequency range, which allows the automatic re-lock of the laser after an accidental jump of frequency.

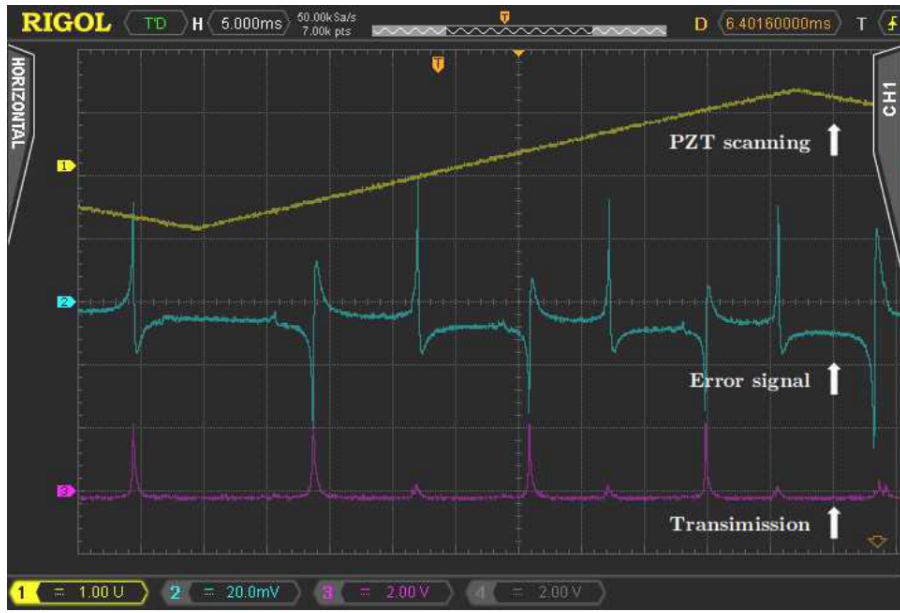


Figure 3.7: Error signal used to lock cavity to incident fundamental laser and transmission of SHG cavity at 461 nm when scanning the PZT applied voltage.

3.3.1.3 Conversion efficiency

We evaluate the doubling cavity conversion efficiency $\epsilon \equiv P_{\text{out}}/P_{\text{in}}$, i.e., the power ratio between the SH output component at 461 nm and the fundamental input one at 922 nm, respectively measured at position B and A in Fig. 3.6. The power of the SH component at 461 nm increases almost linearly with the fundamental laser power (blue circles in Fig. 3.8), indicating that the system works in the strong depletion regime dominated by nonlinear losses. The frequency conversion efficiency also increases, reaching a maximum value equal to 87% with 1.05 W of blue light at 461 nm generated with 1.19 W at 922 nm (red squares in Fig. 3.8). In this configuration, the intra-cavity power calculated using the single-pass conversion

efficiency is ~ 100 W; this value is in good agreement with what is obtained considering the build-up factor for an impedance-matched cavity. By fitting the experimental points with the expected theoretical behavior [163, 166] we: i.) confirm that thermal effects are negligible in our setup; ii.) obtain an input mirror reflectivity at 922 nm of 98.84(1)%, which is very close to the nominal one, and estimate the linear losses in the cavity equal to 0.170(3)%. From these values, we infer a cavity finesse of ~ 490 . Remarkably, the system performances in terms of both output power and conversion efficiency are presently limited by the available input laser power, which could be up-scaled, for example, exploiting fully-fibered solutions [167].

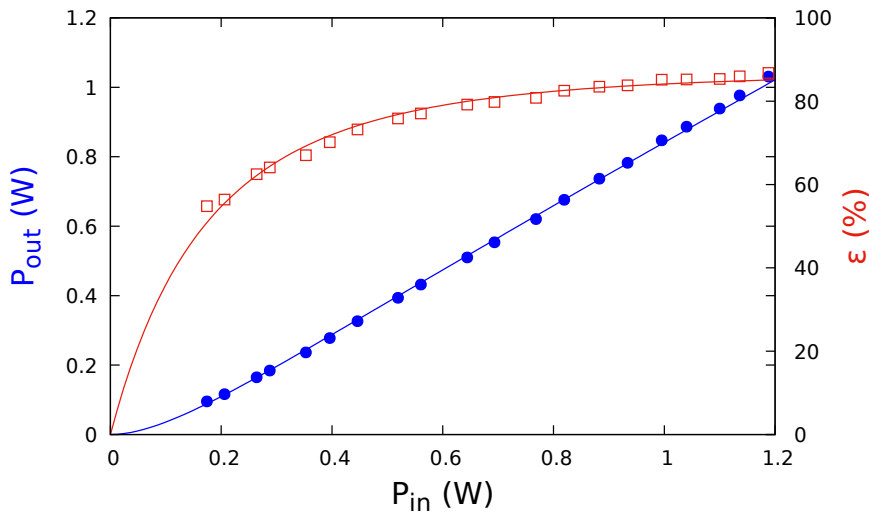


Figure 3.8: Measured output power at 461 nm from the SH module (blue filled circles) and optical conversion efficiency versus incident fundamental laser power (red open squares). The solid lines result by fitting the experimental points with the theoretical curves.

3.3.1.4 Stability

The laser system can operate for a few days without any maintenance. The power stability of the frequency conversion system has been characterized by monitoring the SH power over several hours via an optical power sensor (S142C, Thorlabs) with a resolution of 1 nW and sampling rate of 0.1 Hz: the peak-to-peak fluctuations over four hours are $\sim 1.2\%$ (see Fig. 3.9). However, most fluctuations are strongly correlated with the varying input power (see

the inset of Fig. 3.9), and the uncorrelated relative fluctuations obtained after removing the linear dependence between P_{in} and P_{out} over the same time interval show an Allan deviation of 5×10^{-4} at 10 s decreasing to 7×10^{-5} at 2500 s, with a standard deviation equal to $\sim 5.5 \times 10^{-4}$ (see Fig. 3.10). This residual noise could be explained in terms of the crystal temperature's residual instabilities and the cavity injection pointing.

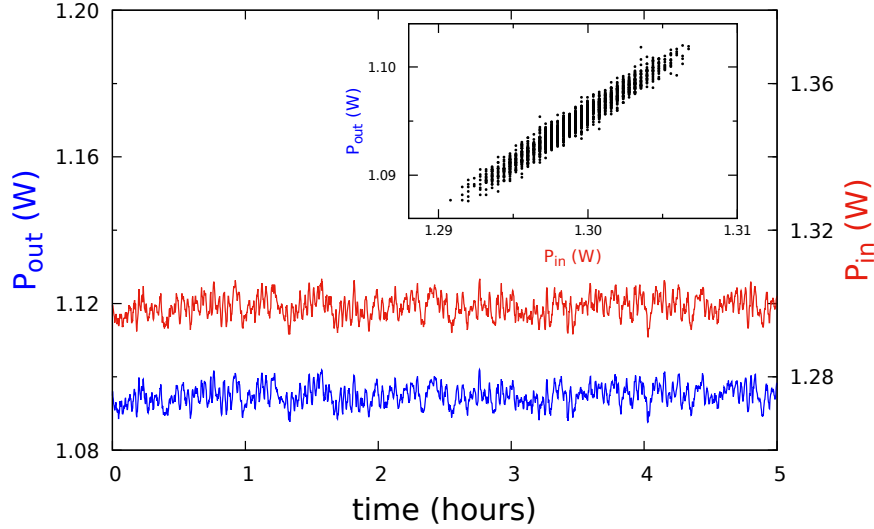


Figure 3.9: Long-term intensity measurement of the SH output at 461 nm (blue curve, left y-axis) and incident fundamental laser at 922 nm (red curve, right y-axis). Inset: output intensity trace versus input intensity trace, demonstrating their strong correlation.

3.3.1.5 Relative intensity noise

We measure the relative intensity noise (RIN) of both the fundamental and frequency-converted components (see Fig. 3.11). The spectrum of the fundamental light component starts at -120 dBc/Hz at 100 Hz, rolls off as f^{-1} till 20 kHz where the slope decreases to $f^{-1/3}$. The SH component shows an excess of noise in the acoustic band on a plateau at -105 dBc/Hz extending till 10 kHz; then, it rolls off with a general f^{-1} trend. The doubling process adds excess intensity noise in the whole Fourier frequency range, as already observed in previously published works based on resonant doubling cavities [168, 169] but not in single pass systems [170].

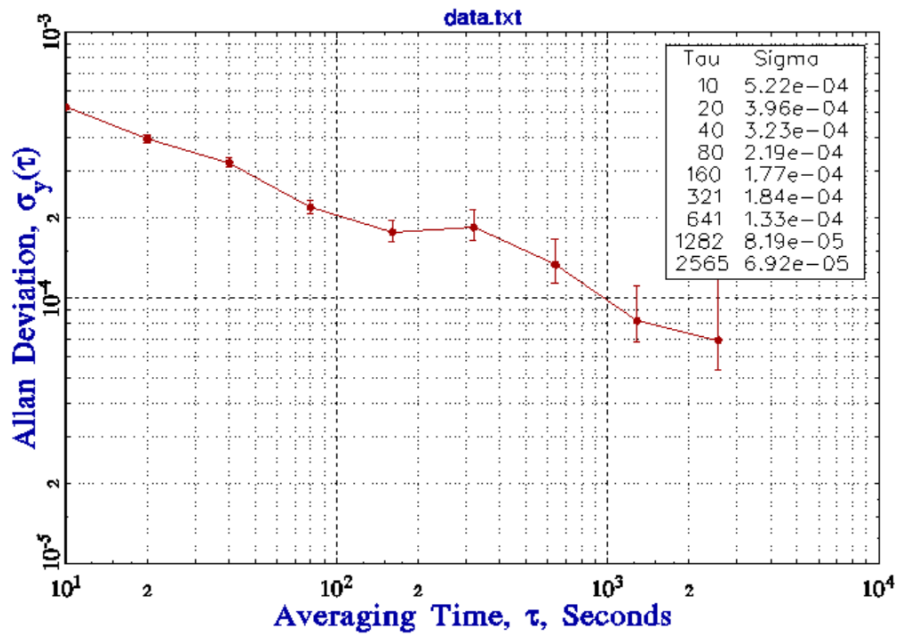


Figure 3.10: The power stability of SHG output after removing the correlation with fundamental laser.

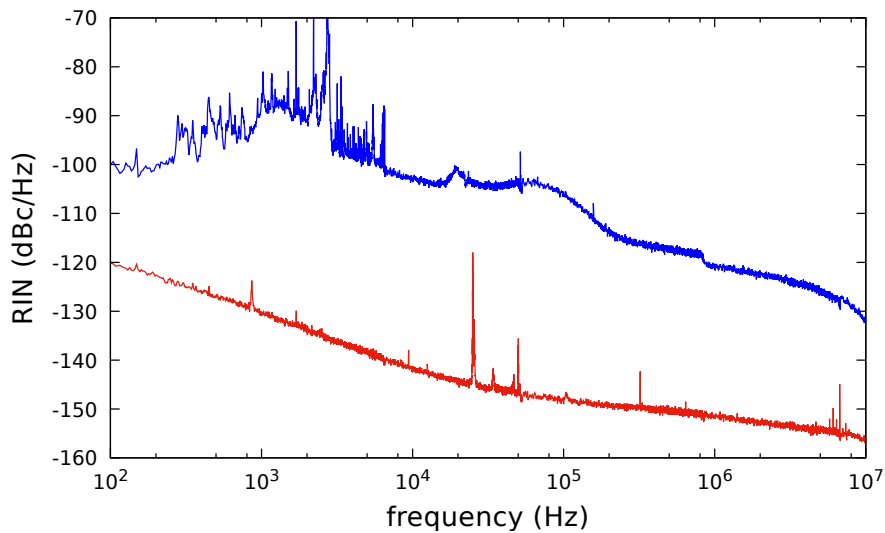


Figure 3.11: Relative intensity noise of the fundamental light component (red curve) and of the SH component transmitted by the doubling cavity (blue curve).

3.3.1.6 Geometrical beam shape

The intense focusing of the fundamental mode on the crystal, imposed to obtain a high conversion efficiency, produces, as a side-effect, the multi-lobe cross-section of the frequency-doubled beam, as shown in the inset of Fig. 3.6 (a). On the left side, the intensity profile of the beam is well described by a sinc^2 function, which results from the windowing imposed by the crystal's angular acceptance (see Tab. 3.1, last row). Such structure is only partially found on the beam's right side because the fundamental cavity mode is offset from the crystal axis, thus producing an asymmetric clipping of the frequency doubling process. To prevent similar problems, the cavity should be glued while monitoring its effective alignment [171]. The central lobe of the output beam contains more than 90% of the power, and we correct its aspect ratio using two cylindrical lenses to improve the single-mode fiber injection efficiency, which is $>50\%$ using a pure silica core PM fiber (PM-S405-XP, Thorlabs).

3.3.1.7 Beat-note locking

To demonstrate the system potential in cold atom physics, we use it to implement a 3-dimensional magneto-optical trap (MOT) for ^{88}Sr atoms, capturing the pre-cooled atomic flux produced by a compact 2D MOT similar to that reported in [137, 172]. The frequency of the SH component is referenced to the Sr spectroscopy via a frequency-shift optical lock with a red detuning $\Delta = 1.5 \Gamma$ with respect to the blue cooling transition $5s^2\ ^1S_0 - 5s5p\ ^1P_1$ transition of ^{88}Sr ($\Gamma \approx 2\pi \times 30.5$ MHz is the transition linewidth) [173].

The SH optical frequency (E_1, ω_1) is frequency-offset-locked to another well-stabilized laser (E_2, ω_2) with a digital phase frequency discriminator (PFD). A beat note is derived from the above two considered optical fields with the same polarization. The error signal in terms of frequency difference is retrieved with a photodetector (bandwidth at 461 nm \sim 200 MHz). The error signal (V_{RF}) is fed into the radio frequency (RF) port of the PFD,

$$V_{RF} \propto E_1 E_2 \cos((\omega_1 - \omega_2)t). \quad (3.7)$$

The PFD (ADF4002, Analog Devices) is configured digitally (see Fig. 3.12) through the programming port in Fig. 3.13, the parameter values are determined by the closed-loop bandwidth. In the SH system, the doubling-cavity is locked to the incident laser with a

bandwidth of ~ 1 kHz, limiting the PFD loop filter (R1, C1, C2) bandwidth to be a few 100 Hz. With the listed parameters in Tab. 3.2, we can obtain a robust frequency locking at a bandwidth of 100 Hz.

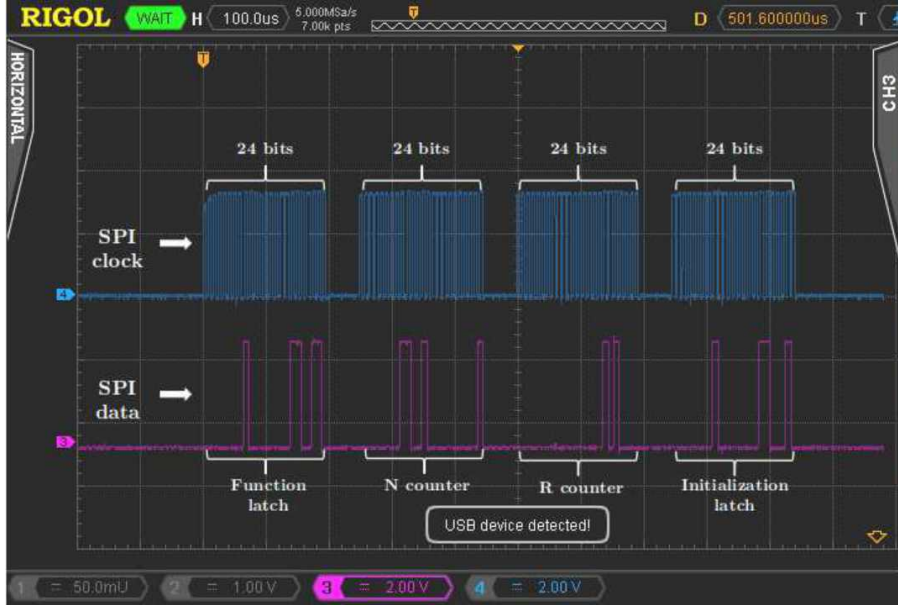


Figure 3.12: SPI timing sequences to configure the PFD.

	Value	Unit	Device	Hardware/Software setting
CLK	40	MHz	ADF4002	Hardware
N/R divider	5000		ADF4002	Software
Charge pump	600	μA	ADF4002	Software
R1	4.7	Ω	Loop filter	Hardware
C1	1000	μF	Loop filter	Hardware
C2	220	μF	Loop filter	Hardware

Table 3.2: Parameters of the frequency locking system.

The resulting linewidth of the servo-controlled blue laser is of the order of one MHz, hence significantly below that of the cooling transition. We use the frequency-converted light to produce the six cooling beams for the 3D MOT with integrated fiber splitters and obtain a stable operation of the trap. More details are presented in the Ch. 4.

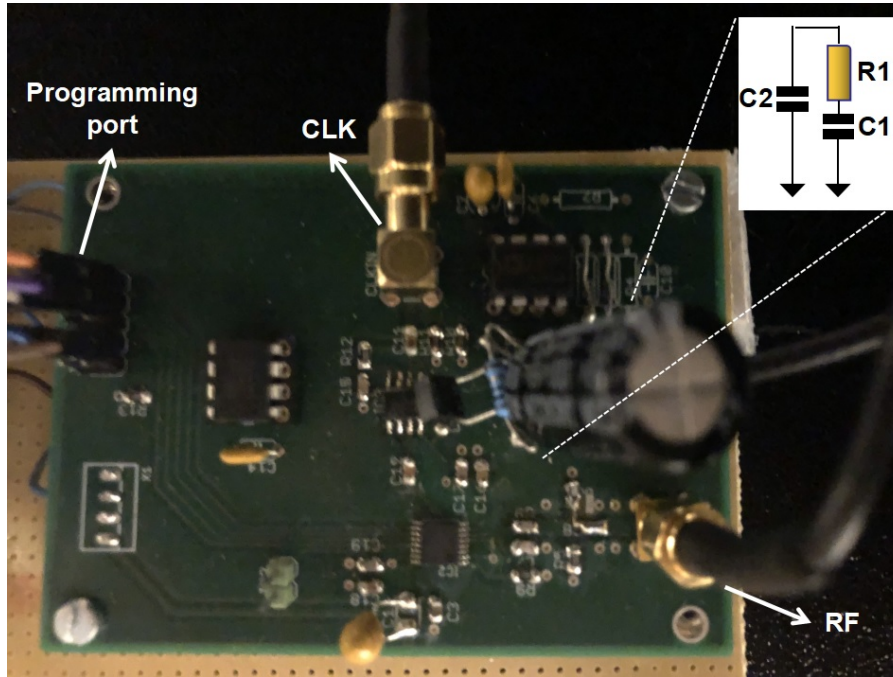


Figure 3.13: PFD electronic circuit. The CLK signal can be provided by the arbitrary waveform generator or the realized DDS, and its frequency is determined by the required red detuning frequency of the blue cooling stage. CLK: clock signal; RF: radio frequency signal.

3.3.2 Optical power enhancement by injection locking

We optically inject the mono-mode laser radiation, called "master" laser, into two multi-mode high-power "slave" laser diodes to produce the desired blue light for the atomic source, 2D MOT plus the Zeeman slower, respectively. Optical injection locking synchronizes the optical frequency and phase of the laser diode cavity with injected light via photon-photon interaction. In other words, the noise level of the high-power laser diode is dramatically reduced by the low-noise, low-power injected light incident into the slave laser's active zone. By implementing this technique, the precision measurement sensors can achieve quantum noise limitation in frequency, and intensity [174].

Injection locking The condition of injecting locking [175] is the "master" laser wavelength λ_1 and the free-running "slave" laser wavelength λ_0 are sufficiently close. The injection forces the "slave" laser to inherit the characteristics, e.g., the coherency, the stability, the noise, and the linewidth, from the "master" laser. The single-pass gain in terms of amplitude can be

approximated according to [176]

$$g(\lambda_1) = \frac{1-r}{i4\pi L} \frac{\lambda_1 \lambda_0}{\lambda_1 - \lambda_0}, \quad (3.8)$$

where r is the effective reflectivity of the two mirrors, separated by a distance L , bounding the intracavity of the slave laser. Therefore, after injecting a signal of intensity I_1 , the amplified power at λ_1 is [176]

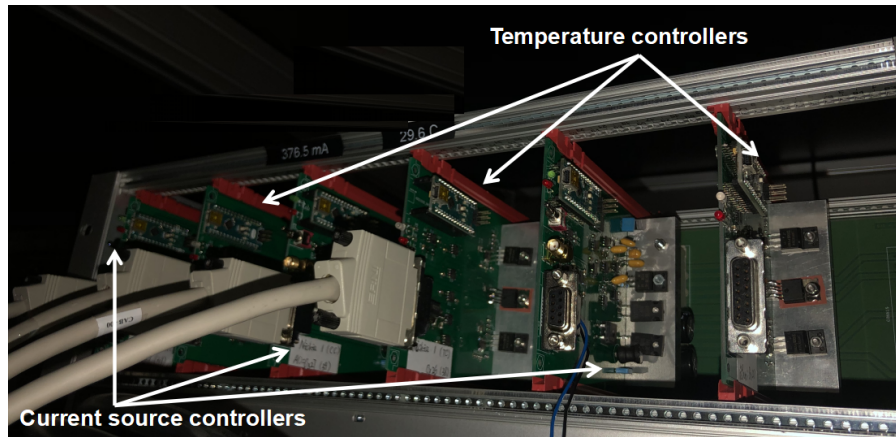
$$I(\lambda_1) = |g(\lambda_1)|^2 I_1 = \left(\frac{1-r}{4\pi L}\right)^2 \left(\frac{\lambda_1 \lambda_0}{\lambda_1 - \lambda_0}\right)^2 I_1. \quad (3.9)$$

After adjusting the injected signal to be precisely at peak oscillation frequency ($\lambda_1 \rightarrow \lambda_0$), the output light intensity is dominated by the overall regenerative gain (second term); instead, the first term related to intracavity losses can be ignored, within a narrow wavelength range, $> 50\%$ the intensity at the multi-mode spectrum of the slave laser can contribute to λ_1 from the master laser [177].

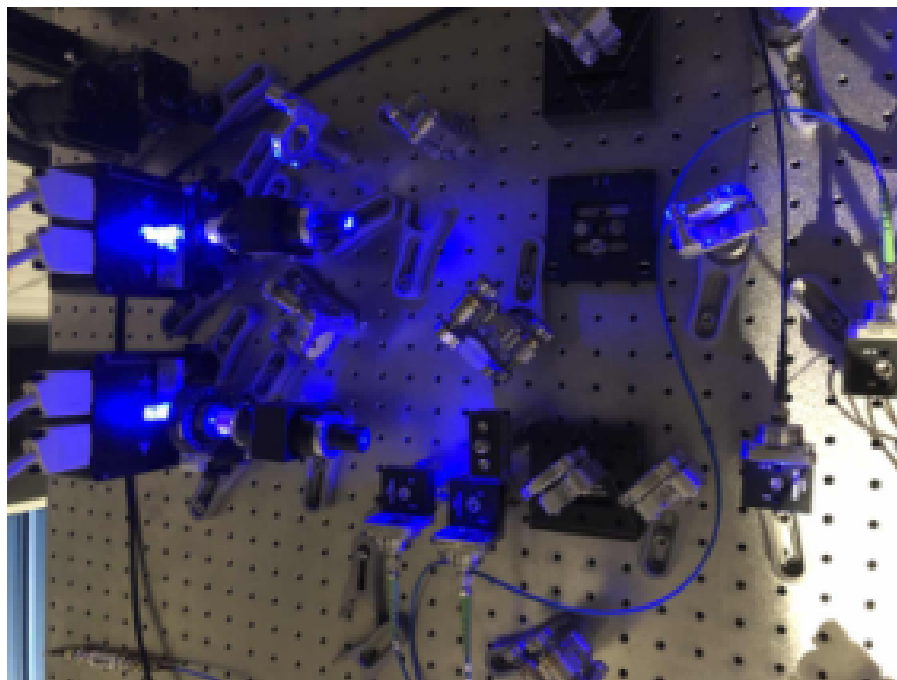
3.3.2.1 Injection locking realization

The schematic of the experimental injection locking setup (see Fig. 3.14) is presented in Fig. 3.15. A fraction of the "master" laser power is amplified by two slave high-power laser diodes through the injection locking technique. For clarity, only one slave laser diode is discussed. We adopt a similar setup for the second one: the optical circuit consists of the locking signal path and the detection system based on the scanning FP interferometer.

We use commercial GaN blue laser diodes (NDB4916, Nichia), delivering a nominal continuous output power of >500 mW around the center wavelength 460.5 nm at the typical operating current of ~ 380 mA. The "slave" beam passes through an optical Faraday rotator (I-40T-5H, Isowave) with polarizing beam splitters on both exit ports. The Faraday rotator also ensures different optical paths for the incoming injection locking beam and the main outgoing "slave" light beam. A $\lambda/2$ wave plate in front of the isolator rotates the polarization of the "slave" laser beam and maximizes the rotator transmission to $>85\%$. A fraction of "master" light (~ 2.5 mW) is injected into the laser diode through a single-mode polarization-maintaining optical fiber (PM-S405-XP, Thorlabs) then the injection port of the rotator. The fiber cleans the transverse mode of the injection beam and makes the alignment and mode matching rather uncritical. The APC fiber with 8° polish facet to avoid the back reflection



a



b

Figure 3.14: Experimental setup of the blue laser diodes injection locking (a) high-power laser diodes controller rack (see Sec. 3.3.2.3 and Sec. 3.3.2.4 for more details on the temperature and current controller respectively) (b) optical circuit.

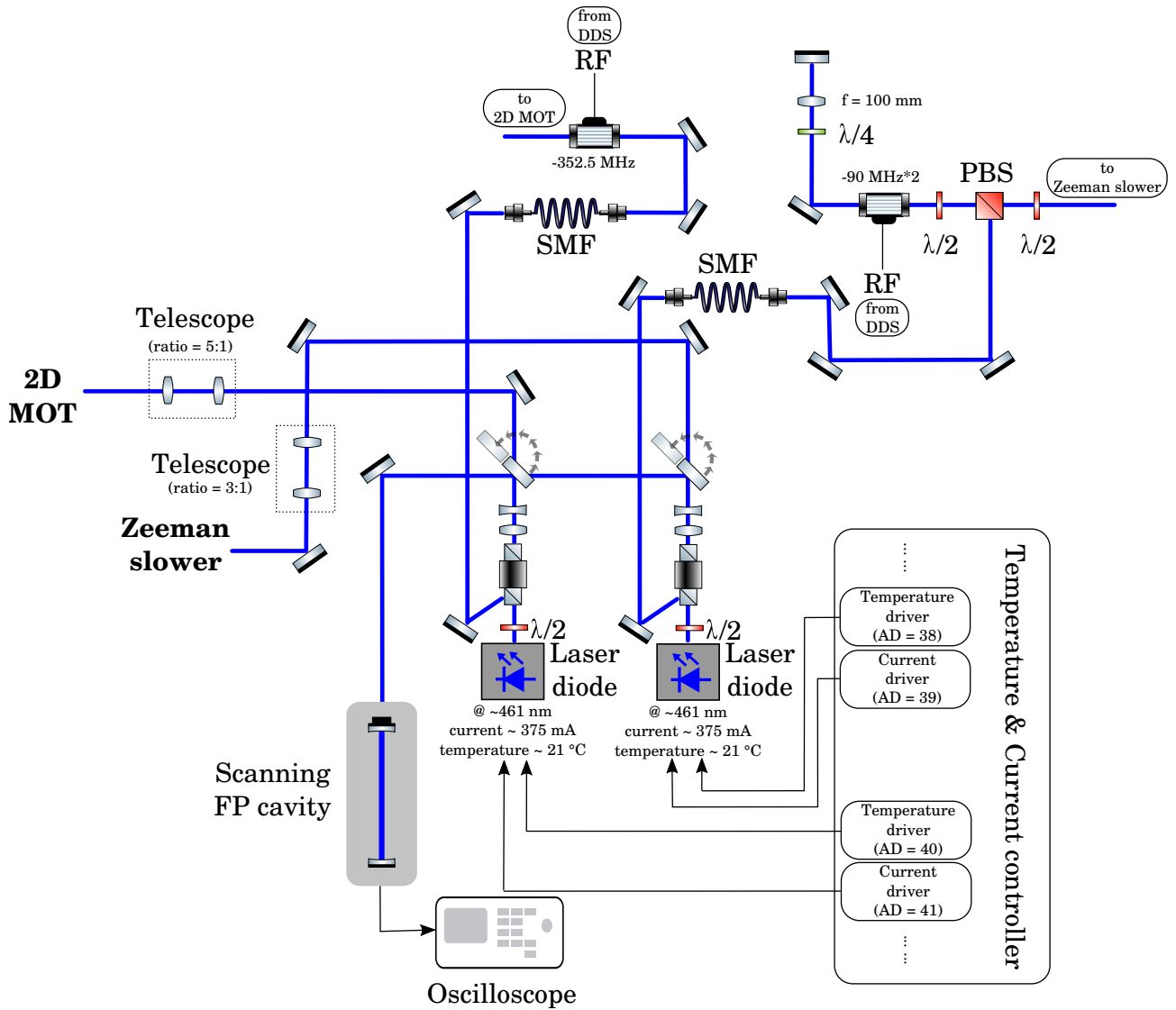


Figure 3.15: Schematic of the blue laser diodes injection locking to generate the high-power blue light at 461 nm.

into the "master" laser is preferred. The determination of the effective focal length of the fiber coupler depends on the parameters of a single-mode fiber: the mode field diameter (MFD) and numerical aperture (NA) at the desired wavelength,

$$f = \frac{\pi D(\text{MFD})}{4\lambda}, \quad (3.10)$$

where D is the $1/e^2$ diameter of the collimated beam incident on the lens. Concerning the transmission losses, common sources are $\sim 1\%$ of the loss rises from the transmission of fiber coupler; $\sim 8\%$ is due to imaging aberration, stray loss, and beam distortion; another 8% comes from Fresnel reflection at fiber end faces.

To maximize the injected light into the "slave" diode, we optimize the spatial mode overlap between the "master" and "slave" light with a pair of mirrors. Concerning the long-term stability of the injection locking, mirror mounts are low-drift versions from Newport.

The output beam from the laser diodes is either sent to the experiment or a scanning FP interferometer (SA210-3B, Thorlabs) for monitoring the locking status, and the optical path is switched by mounting a mirror on the 90° flip mount (TRF90, Thorlabs). The piezoelectrically tunable confocal FP interferometer with a free spectral range (FSR) of 10 GHz and resolution of 67 MHz is insensitive to the input laser beam alignment and temperature fluctuations. A linear saw-tooth voltage in time is applied to the cavity transducer, and the FP transmission can examine the quality of injection locking (see Fig. 3.16). Sharp transmission peaks from the FP cavity indicate a good single-mode operation of the "slave" diode, evidence of its good injection locking. Vanishing peaks are observed in the case of the free-running "slave" laser due to its broad spectrum. The optimal injection is achieved by maximizing the transmission peak, realized with the "slave" diode coarse temperature and finer current tuning.

The transmission spectra from the FP cavity are limited because it only shows the peaks resonant with the cavity longitudinal mode, but not necessarily the whole spectrum of the "slave." To better diagnose whether injection locking suppresses the unwanted frequencies and to assess the optimal power of the "master" laser to seed the "slave" laser, one can consider an optical spectrum analyzer, e.g., from Toptica, or a narrow band interference filter [178]. Now, the seed laser is operated at ~ 2.5 mW for efficient injection locking.

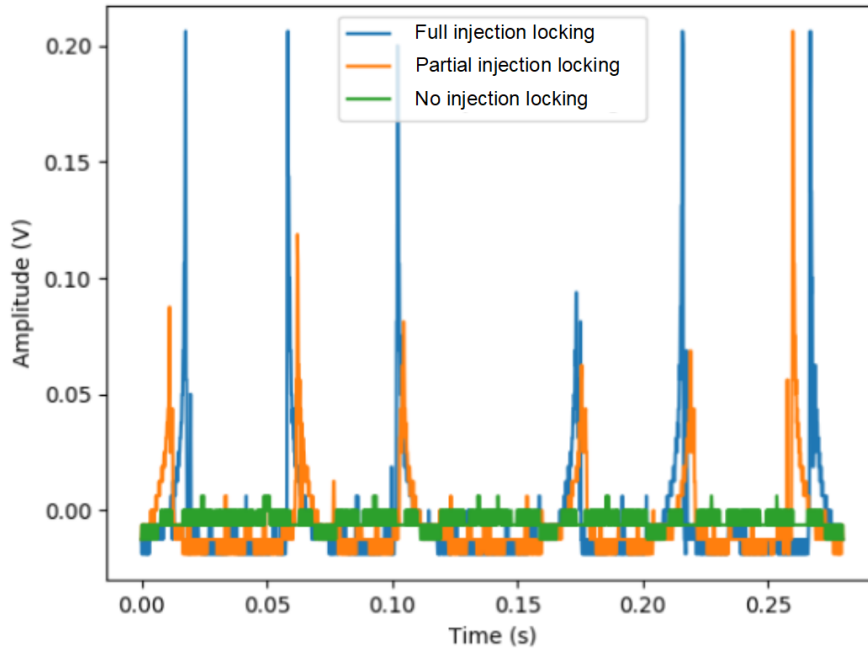


Figure 3.16: FP transmission spectra with full, partial, or null injection locking. The x-axis of time [s] is related to the FP cavity length change.

3.3.2.2 Spatial corrections of laser beam

The "slave" laser mode has a divergence ($\theta_{\perp} = 8.5^{\circ}$ and $\theta_{\parallel} = 23^{\circ}$) with a 1:3 aspect ratio elliptical shape. The "slave" diode is housed in a collimation tube with an aspherical lens (C330TMD-A, Thorlabs), and it has a NA of 0.7 and a focusing length of 3.1 mm. The diameter along the semi-major axis of the elliptical beam is ~ 3.5 mm, less than the clear aperture (=5 mm) of the optical isolator. The "slave" beam profile is circularized by a pair of cylindrical lenses, LK1753L1-A and LJ1402L1-A (Thorlabs), with a focusing lens of -15 mm and 40 mm, respectively. Notably, the cylindrical lenses, with a reflectance of 0.25% at 461 nm, may have more than 1.25 mW reflected power when the laser diode delivers the nominal 500 mW. To avoid the instabilities due to optical feedback, better put these two reshaping lenses after the optical isolator.

3.3.2.3 The laser diode temperature controller

The temperature controller of the "slave" diode, with the temperature sensitivity of 1 nm/20 K, is controlled within 1 mK precision by using a temperature feedback loop, consisting of

the Peltier element, the thermistor, and the electronic feedback circuit. The thermistor's resistor, temperature-dependent, is placed next to the "slave" laser diode and gives the reading of its temperature. The thermistor and Peltier element are included in the laser controller (LDM56/M, Thorlabs). The digital feedback circuit (see Tab. 3.3) is designed to set the desired temperature and change the current passing two dissimilar conductors, thus generating or removing the heat from the system via the Peltier effect. The desired bandwidth and the maximum current to drive the Peltier are of the order of 1 s and 1.25 A, respectively. The speed of the diode settles on the setting temperature is determined by a standard digital Proportional-Integral-Derivative (PID) feedback circuit,

$$\beta(s) = G_p \left(1 + \frac{1}{sT_i} + sT_d \right). \quad (3.11)$$

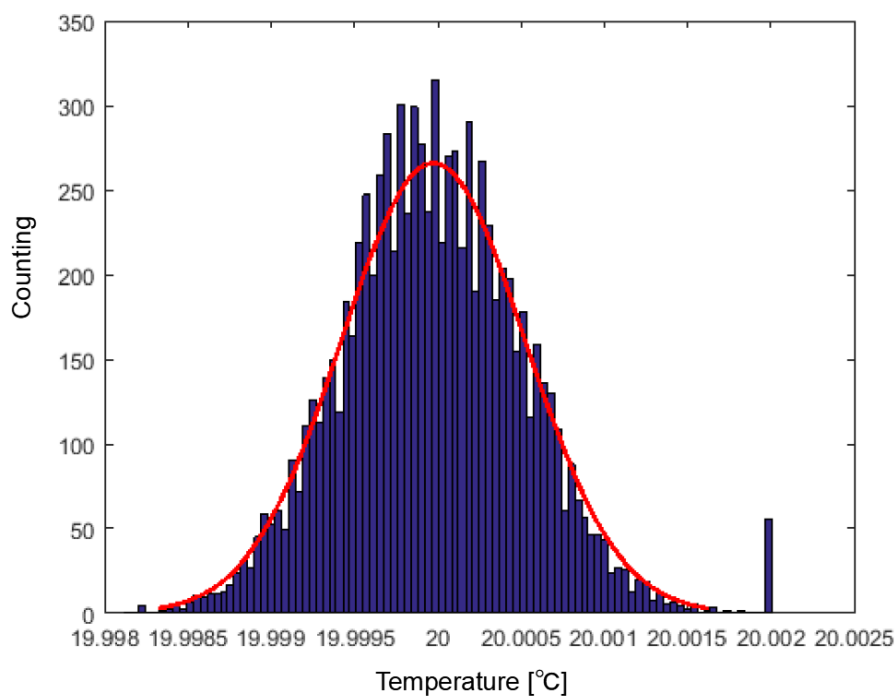
The G_p , T_i , and T_d can be optimized with the PID tuner embedded in Matlab to obtain a fast and robust temperature control system.

	Range	Resolution	Unit
Setting temperature	0-60	10^{-3}	$^{\circ}\text{C}$
Measure temperature	0-60	10^{-6}	$^{\circ}\text{C}$
G_p	$\pm 10^4$	10^{-3}	$\text{mA}/^{\circ}\text{C}$
T_i	0- 10^4	10^{-3}	s
T_d	0- 10^3	10^{-3}	s

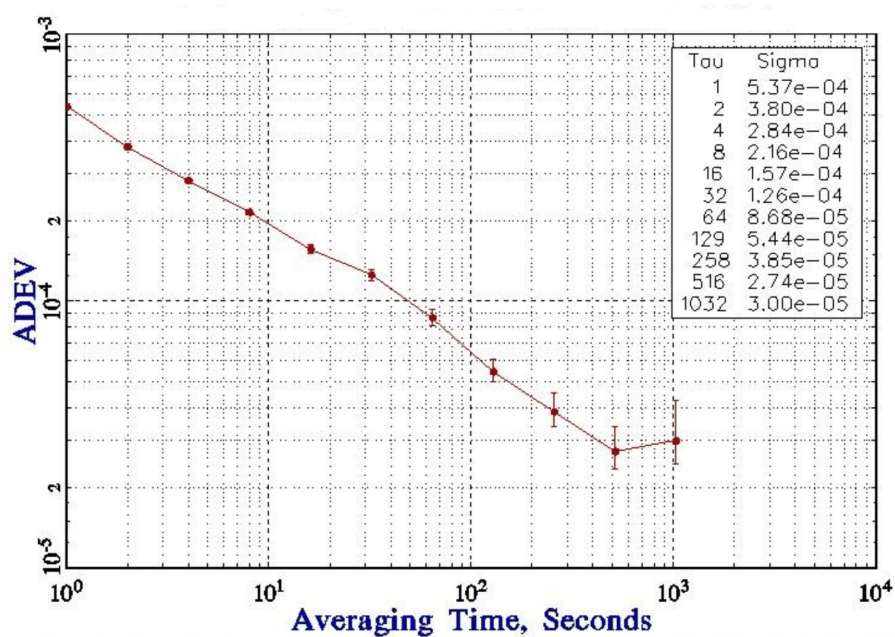
Table 3.3: Performance of the realized temperature controller.

In Fig. 3.17, we characterize the temperature stability achieved with our homemade controller. The temperature of the stabilized system is measured with an independent sensor with a 1 Hz sampling rate. The histogram plot of the temperature samples shows a Gaussian shape with an RMS width of 0.55 mK. The Allan deviation for the measured temperature is $\sim 500 \mu\text{K}$ at 1 s and decreases with a $1/\sqrt{T}$ behavior till $30 \mu\text{K}$.

The response of the thermistor is measured with a 24-bit $\Sigma - \Delta$ analog-to-digital converter (ADC) and the voltage divider formed by the reference resistor, with the low-temperature coefficient of $\pm 10 \text{ ppm}/^{\circ}\text{C}$, and the thermistor. The ADC noise level is at the order of $180 \mu\text{K}$ for one single reading, and it drops to $26 \mu\text{K}$ at the loop bandwidth of 1 Hz. For experiments under the ambient temperature without precise control, the thermal fluctuations can be coupled into the temperature-dependent elements, e.g., the reference resistor and the



a



b

Figure 3.17: Characterization of the temperature stability (a) the histogram plot of the temperature samples (b) the Allan deviation.

connection cables, which mess up the thermistor readings. To overcome this disturbance, an extra resistor (compensation resistor) with a resolution better than the $0.01\text{ }^{\circ}\text{C}$ is added on the electronics board and located reasonably close to the reference resistor. In the future, the readings of the compensation resistor, monitoring the temperature fluctuations, will be considered to compensate for the thermal noise via data processing.

3.3.2.4 The laser diode current controller

A free-running diode laser may cause a frequency change with a pump current of typically $3\text{ MHz}/\mu\text{A}$ [179], but reduce to $0.3\text{ MHz}/\mu\text{A}$ with optical feedback with external gratings. To realize a bare laser diode linewidth of less than 1 MHz requires a current noise below 300 nA RMS . Our designed current controller is 300 times better than this requirement (see Fig. 3.18)). The current noise spectral density of the regulator simulated at 100 mA is from the SPICE software simulation. The measured current noise spectral density is higher than expected, which is suspected due to the bad soldering of one voltage regulator on the PCB board.

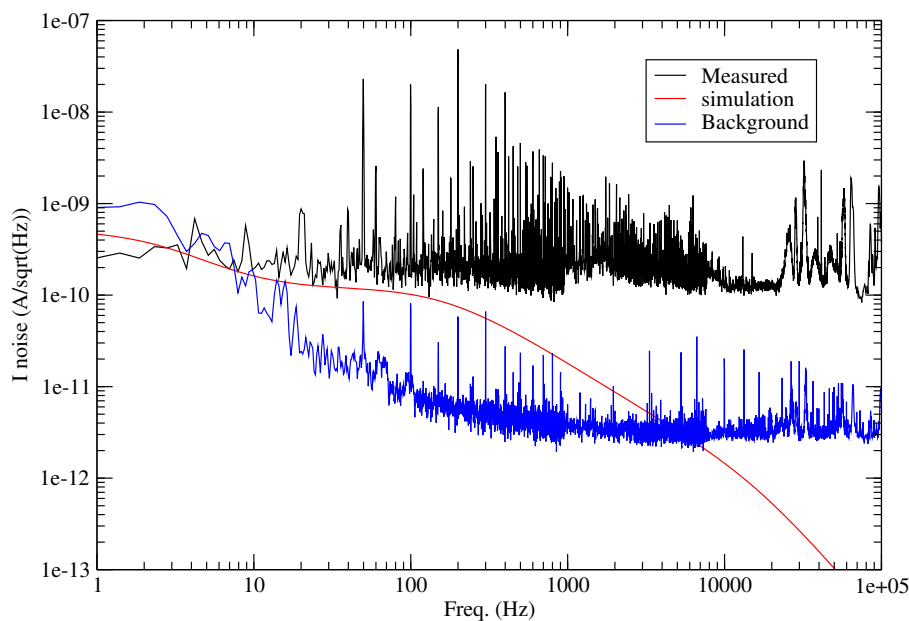


Figure 3.18: Current noise spectral density simulated with SPICE software and measured with the fast Fourier transform (FFT) device.

The ultra-low noise current controller is measured with a setup [180] depicted in Fig.

3.19. Since there is no universal polarity for the current source, we make a different circuit for the current sink. The current source and sink are set to be +100 mA and -100 mA, respectively. Almost all the current flows from the current source to the sink through two directional laser diodes. The 1 M Ω load resistor amplifies uncorrelated current noise and drift. The large-value sensing resistor is a big advantage of amplifying small noise signals; however, it also limits the measurement bandwidth to be a few hundred of kHz.

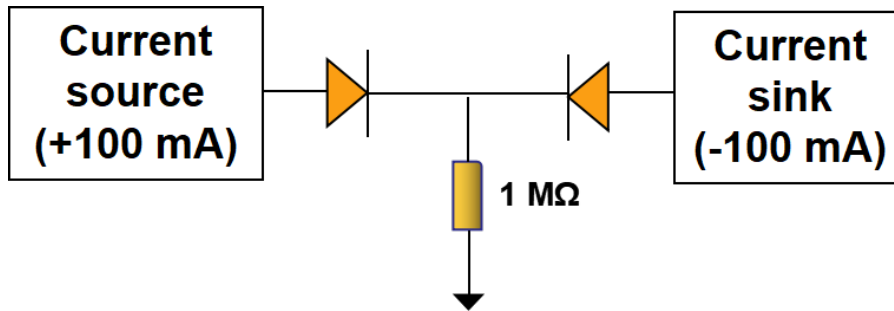


Figure 3.19: Measurement layout for ultra-low noise current controller.

Compared with the Libbrecht-Hall laser driver [181], our current controller (source) uses improved operational amplifiers and voltage references in combination with digital control. Plus that the current modulation input has the sensitivity of 100 $\mu\text{A}/\text{V}$ or less with a bandwidth of about 5 MHz. The features of the circuit are summarized in Tab. 3.4.

	Range	Resolution	Unit
Setting current	0-200 (easily scale to 500)	10^{-3}	mA
Measured current	0-200	10^{-1}	mA

Table 3.4: Performance of the realized current controller.

3.3.2.5 Long-term stability improvement under consideration

Injection locking of diode lasers is extremely sensitive to perturbations. So far, the apparatus has to be regulated every day to optimize the injection performance. To improve the long-term stability, adding an active stabilization of the pump current is under consideration [182].

3.3.3 Doppler-free blue spectroscopy at $^1S_0 - ^1P_1$ transition

Saturation spectroscopy In the experiments of laser cooling and trapping cold atoms, saturated absorption spectroscopy is a frequently-applied technique to lock the lasers to particular atomic transitions (ν_0), resolving the spectral features beyond the Doppler limit and restricted only by the natural transition linewidth (Γ) of interest [183, 184]. Our experiment considers a "pump"-"probe" scheme, where the two lasers with the same laser frequency ν counter propagate through the two-level atoms in the vapor cell operated at the temperature T ; one, the "pump" beam is assumed with very high intensity to saturate the atomic sample that half of the atoms are at the excited state at any given time; the other, the "probe" beam is weak with at least of ten times less intense than the "pump" beam. The overall transmission of the "probe" laser beam through the cell is given by

$$I_{out} = I_{in}e^{-\tau(\nu)}, \quad (3.12)$$

and vapor optical depth $\tau(\nu)$ is

$$\tau(\nu) = \int \tau_0 \frac{\nu_0}{c} (P_1 - P_2) \frac{\Gamma/2\pi}{(\nu - \nu_0 + \nu_0 v/c)^2 + \Gamma^2/4} e^{-mv^2/2kT} dv. \quad (3.13)$$

The overall normalization τ_0 is the optical depth at the center of the resonance line with no "pump" laser. In the case of without "pump" beam ($P_1 = 1, P_2 = 0$), the probe spectrum I_{out} is a Doppler broadened absorption profile in Gaussian shape. With the "pump" beam on ($P_1 = 1/2, P_2 = 1/2$), only the atoms in resonance with both beams contribute to the "probe" absorption profile: if $\nu = \nu_0$, the atoms with velocity $v = 0$ along the beam direction add photons to the "probe" beam through the stimulated emission; however, if $\nu \neq \nu_0$, the atoms do not contribute to the "probe" beam and the "probe" absorption follows the same profile as without the "pump" beam. As a result, an additional spike is at the atomic resonance frequency within a Gaussian profile, an atomic reference line for defining frequency in metrology.

Frequency-modulation spectroscopy The "probe" laser beam power fluctuations often bring sufficient noise to unacceptably degrade such high-resolution spectra. The difficulty is overcome using optical phase modulation, driven with radio frequencies (RF) comparable to the width of the spectral line of interest. The spectral feature is probed by one of

the frequency-modulated sidebands, and the spectral line's absorption (real part) and dispersion (imaginary part) features are measured by the resulting beat signal in-phase and in quadrature, respectively, at the RF modulation frequency [185]. In the experiment, an amplitude-modulation-noise-insensitive sub-Doppler resonance of pure odd symmetry with an excellent signal-to-noise ratio can be observed by adjusting the relative phase of two RFs to generate the beat signal.

3.3.3.1 Locking of the blue laser system to the $^1S_0 - ^1P_1$ transition

Fig. 3.20 (b) depicts schematically our experimental arrangement (see Fig. 3.20 (a)) for locking the blue laser to the $5s^2 ^1S_0 - 5s5p ^1P_1$ transition via the FM saturation spectroscopy. The blue laser at 461 nm from a mono-mode diode laser system (DL pro HP, Toptica) is split into a "pump" and "probe" beam. Its phase is modulated by passing through a resonant electro-optic phase modulator (EO-F30M3-VIS, Qubig) driven at an RF frequency of 29.1 MHz. The trade-off of determining modulation frequency is high sufficient to approach shot noise level and small enough compared with hyperfine splittings and Doppler width. The linearly polarized and elliptical "pump" beam, with a diameter of $\phi = \sqrt{\phi_h \phi_v} \approx 1.41$ mm ($1/e^2$), with $\phi_h = 2$ mm and $\phi_v = 1$ mm, and optical power of $P = 300$ μ W is sent to a focusing lens ($F = 300$ mm) then the vapor cell. The beam waist is $2w_0 = 4\lambda/\pi \cdot F/\phi \approx 125$ μ m, 5 cm away from the center of the vapor cell, where the "pump" beam intensity becomes $I \approx 1/4.53 \cdot P/(2w_0^2) = 424$ mW/cm². The "probe" beam transits a Sr vapor cell and hits a high-bandwidth photodiode. The atomic fluorescence signal is measured as a function of the "probe" frequency (see Fig. 3.21 (a)). This spectrum can be fitted with the Voigt functions for each of the four stable isotopes. We know that ⁸⁸Sr is the most abundant isotope and that the isotope shifts of ⁸⁶Sr is 120 MHz, the full-width-half-maximum of the spectral linewidth for the ⁸⁸Sr peak is ~ 100 MHz. This value ($\delta\omega = \sqrt{\delta\omega_s^2 + \delta\omega_{tr}^2 + \delta\omega_p^2}$) mainly depends on the transverse velocity distribution of atoms ($\delta\omega_{tr}$), and it can be broadened by increasing the laser power ($\delta\omega_s$) and via collisions with the background gas ($\delta\omega_p$) [186].

A steep signal with disperse-like lineshape is resolved with a double-balanced mixer (ZLM-1, Mini-Circuits) driven by a local oscillator from the same RF source as the modulation frequency but with the desired phase shift (see Fig. 3.21 (b)). This error signal sits on a flat,

zero background. Consequently, the zero-crossing of the demodulated signal is accurately centered on the corresponding atomic transition. The signal is dominated by the contribution from closed atomic transitions, which is especially useful when the spectrum in question contains several closely spaced transitions. Such collimated atomic beam is a good tool to frequency stabilize a laser at the MHz level on the strontium transition $5s^2 \ ^1S_0 - 5s5p \ ^1P_1$ (error signal in Fig. 3.21 (b)). We realize a homemade PID servo system designed to maintain the locking for a few days, with a locking bandwidth of 550 kHz (see Fig. 3.22).

The vapor cell is based on a heat pipe, operated at 350 °C with a vapor pressure of 10^{-8} mbar [187], that consists of a vacuum-tight stainless steel pipe with a length of 600 mm and a clear aperture of 18 mm. The thickness is a compromise between large enough to avoid bending at high temperatures and small enough to minimize heat conduction. One 1/8 inch diameter Swagelok valve is attached to the heat pipe for sealing the inner volume and maintaining $\sim 10^{-1}$ mbar buffering gases (noble gases such as Argon) to prevent the viewports from being coated by sublimated Sr. Two CF40 flanges are welded at each end of the pipe both for accessing the heat pipe for the filling and eventually refilling operation and for holding the viewports. The metallic Sr can be put at the center of the heat pipe with a long spoon. The central region is heated to a stabilized temperature using a heating wire wound on the heat pipe. The setup is then thermally insulated with ceramic wool and aluminum foil. Optical-quality Brewster angled fused silica windows are installed to minimize undesired standing waves and optical feedback, and the optics are antireflection (AR) coated at 461 nm.

Power broadening Power broadening is the experimentally measured signal of the spectral linewidth of the atomic transition scales with the radiation intensity I . [188] indicates that the spectral line of an ensemble of identical two-state atoms (S) has a Lorentzian dependence on frequency detuning Δ between laser frequency and atomic resonance,

$$S \propto \frac{1}{2} \frac{I/I_{\text{sat}}}{1 + (\Delta/\beta)^2 + (I/I_{\text{sat}})}. \quad (3.14)$$

The increase of the radiation intensity I can broaden the width of the above Lorentzian profile. As the excitation field becomes more intense, the atoms spend a greater fraction of time at the excited state, reaching a maximum of 1/2 when saturation occurs. The linewidth

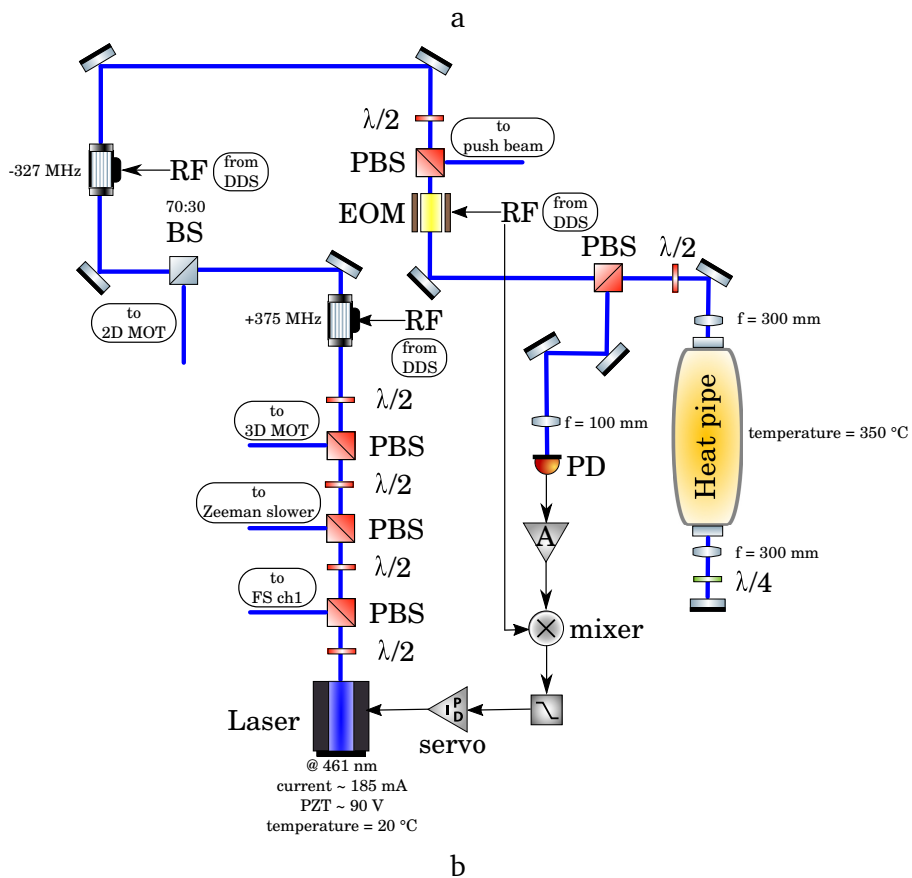
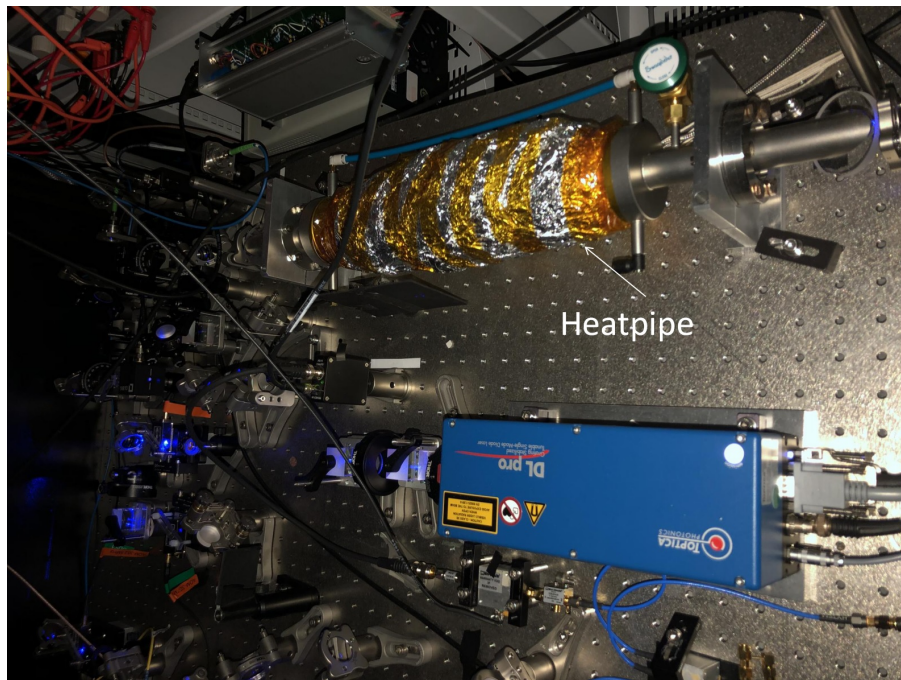
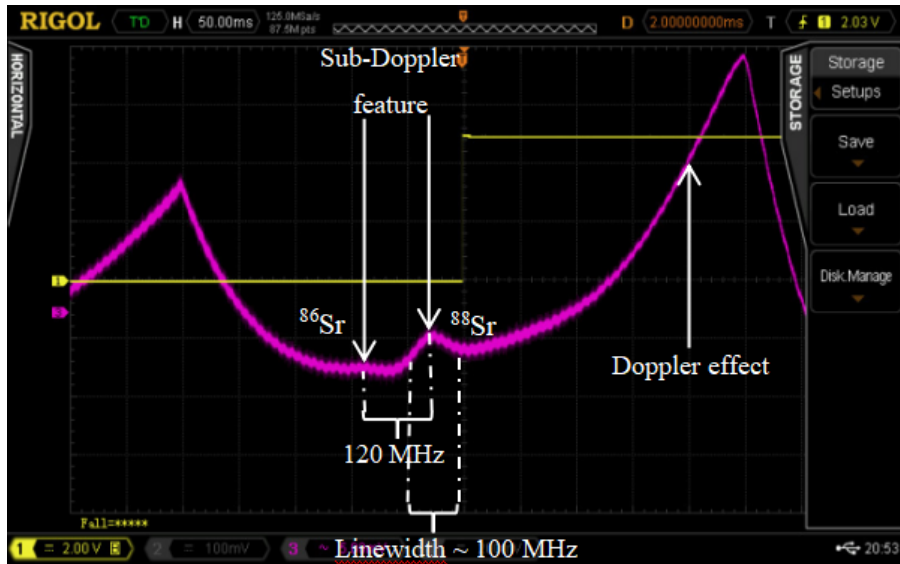
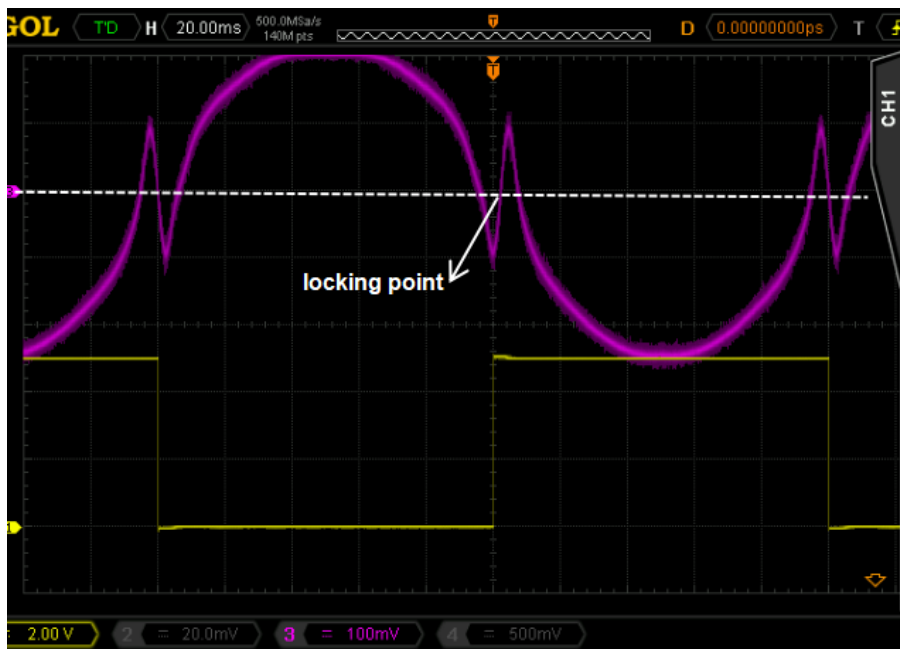


Figure 3.20: (a) Experimental setup relative to blue spectroscopy. (b) Blue spectroscopy schematic. The solid blue line represents the optical path, the solid black one the electrical path. EOM: electro-optic modulator; PD: photon detector; LO: local oscillator; LPF: low-pass filter.



a



b

Figure 3.21: (a) Saturation spectroscopy spike for the $5s^2 \ ^1S_0 - 5s5p \ ^1P_1$ transition. (b) Its demodulated error signal.

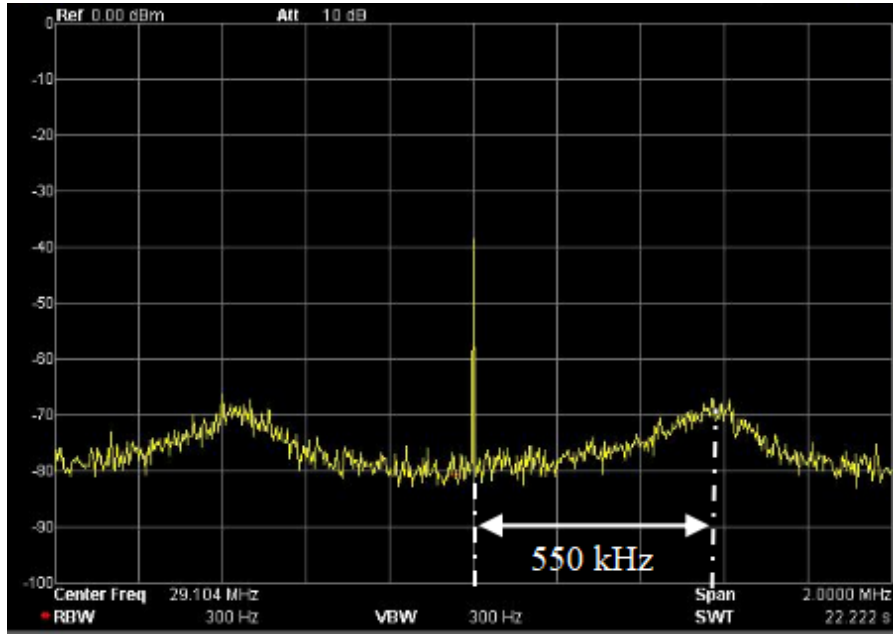


Figure 3.22: Locking bandwidth of PID servo system, acting on the laser current activator, measured with a spectrum analyzer centered at 29.1 MHz, with a span of 2 MHz.

is proportional to the detuning range with saturated excitation power [189]. In our case, the power broadening effect is estimated by $\delta\omega_s = \Gamma_{\text{blue}}\sqrt{1 + I/I_{\text{sat}}} = 30.5\text{MHz} \times 3.32 = 101\text{MHz}$.

There is one $\lambda/2$ waveplate and one PBS in front of the heat pipe to avoid power broadening. The incident power is adjusted by rotating the $\lambda/2$ waveplate.

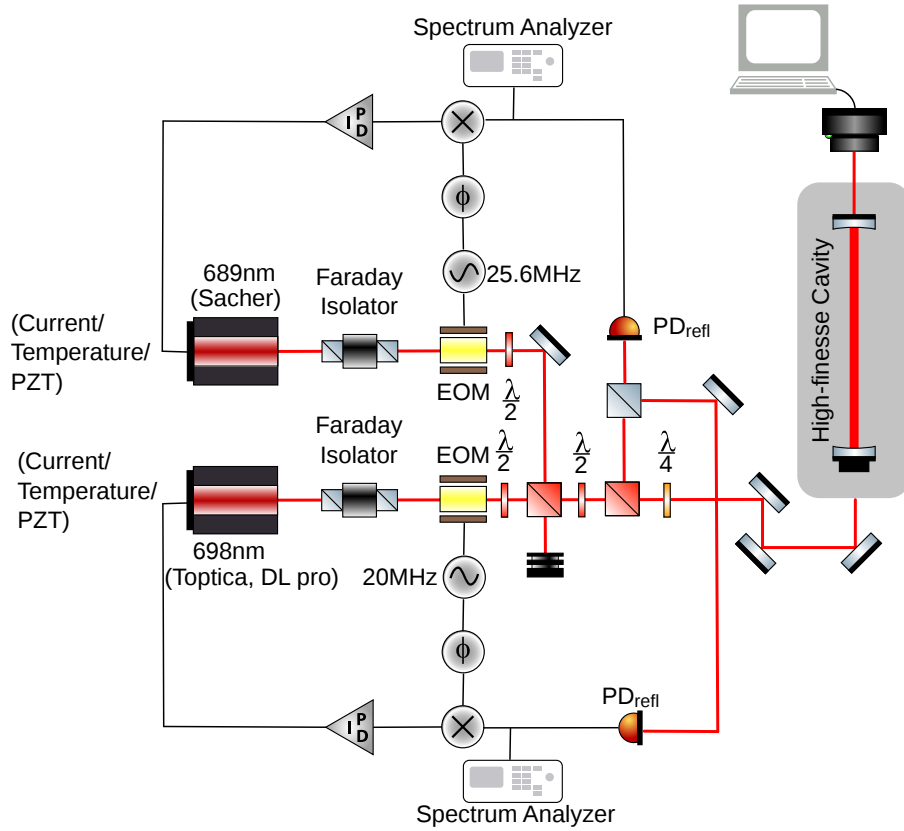
Pressure broadening Sr oven operated at high temperature means high atomic RMS velocities, and hence a short time between consecutive collisions. If this interval is shorter than the lifetime of the excited state, the linewidth can not be resolved and can be broadened. The heat pipe is filled with a buffer gas, typically Argon, to avoid the hot strontium atoms reaching and coating the cold viewports. Therefore the collision broadening occurs either due to Sr-Sr or Sr-Argon. By comparing the lifetime of excited states with the time scale of collisional particles, Sr-Sr collision can not play a big role and can be neglected. However, Argon buffer gas may cause linewidth broadening due to Sr-Argon collision [190].

The pressure broadening on the spectral line is removed by observing the sharpness of the error signal at the same time as charging the Argon buffer gas.

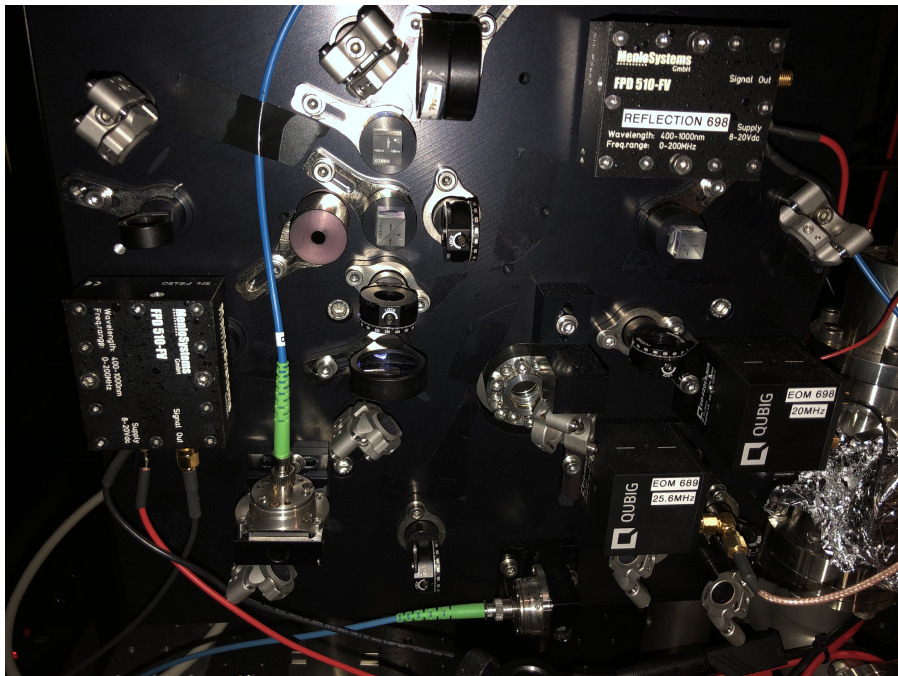
Transit time broadening The transit time broadening is estimated by $\delta\omega_{tr} = 2v/w \cdot \sqrt{2\ln 2} \approx 2.4v/w$ [186], with the atomic velocity of v and the beam waist of w . The interrogated velocity class is $v \approx 0$ m/s, then the $\delta\omega_{tr}$ is ~ 0 MHz.

3.4 Narrow-linewidth and frequency-stabilized laser at 689 nm and 698 nm

Producing the laser light to effectively address narrow and ultra-narrow transitions, as is the case for Sr of the $5s^2 \ ^1S_0 - 5s5p \ ^3P_1$ and $5s^2 \ ^1S_0 - 5s5p \ ^3P_0$ transitions, requires reducing the free-running laser linewidth, typically of the order of a few hundred kHz, by several orders of magnitude. The expected red-cooling laser linewidth is at a few 100 Hz level, much less than the natural linewidth of the narrow transition; for the clock laser, the required linewidth is highly dependent on the applications, e.g., to resolve 1 Hz GW signals, the interferometric laser linewidth has to be better than 1 Hz. This objective is typically achieved with the locking of the laser to one ultra-stable cavity; to fulfill the most extreme laser linewidths, the narrowing can also be obtained down to the kHz level and then to a second ultra-stable cavity. In our experiment, we use the same optical reference cavity (ORC-Cylindric, Menlo) to stabilize the red cooling laser and the clock one. The cavity is mainly coated for ultra-high reflectivity for clock transition and still maintains sufficient finesse for red cooling transition. The spacer and mirrors of the reference cavity are made of ultra-low expansion (ULE) glass and optically bonded together. The cavity is put in a temperature-controlled vacuum chamber ($\sim 8 \times 10^{-9}$ mbar) to reduce the impact of environmental temperature and pressure fluctuating on the cavity length and the refractive index. Each laser is locked to the resonator using the Pound-Drever-Hall (PDH) technique, and to avoid interferences between the two lasers, a different modulation frequency is adopted. More precisely, the two modulation frequencies are separated by a few times the target bandwidth for the two frequency control loops of the MHz order. The two chosen modulation frequencies are 20 MHz for the clock laser and 25.6 MHz for the red-cooling laser. For simplicity, we detail the PDH locking system for the clock laser, and a similar principle is applied for the red laser locking system.



a



b

Figure 3.23: (a) Schematic of the PDH locking setup. (b) Experimental setup (Menlo).

3.4.1 Linewidth narrowing of the red-cooling laser and the clock laser

Pound–Drever–Hall locking There are different ways to lock a laser to an optical resonator; one widely adopted is the so-called PDH method from the name of its inventors [191, 192]. Fig. 3.24 depicts the schematic for the PDH locking. A laser beam $E_0 e^{i\omega t}$ is incident on the FP cavity after being phase-modulated by an EOM, driven by a RF signal with a frequency of Ω . The instantaneous phase of the laser beam is modulated by $\beta \sin(\Omega t)$, where β is modulation depth in radian dependent on RF amplitude or power. Thus, the incident beam into the FP cavity, mainly including three frequencies $(\omega/(2\pi), (\omega + \Omega)/(2\pi), (\omega - \Omega)/(2\pi))$ is,

$$E_{inc} \approx E_0(J_0(\beta)e^{i\omega t} + J_1(\beta)e^{i(\omega+\Omega)t} - J_1(\beta)e^{i(\omega-\Omega)t}), \quad (3.15)$$

where $J_n(\beta)$ is Bessel function. A fraction of the incident beam is reflected with reflection coefficient F (Airy function), $E_{ref} = F E_{inc}$, is written as

$$E_{ref} = E_0(F(\omega)J_0(\beta)e^{i\omega t} + F(\omega + \Omega)J_1(\beta)e^{i(\omega+\Omega)t} - F(\omega - \Omega)J_1(\beta)e^{i(\omega-\Omega)t}). \quad (3.16)$$

A PD is placed just before FP cavity and converts the power of reflected beam ($P_{ref} = |E_{ref}|^2$) into voltage $V_{PD} \propto P_{ref}$. The mixer demodulates the output from PD and produces the error signal, i.e., the frequency difference between the laser and the reference cavity. By adjusting the phase difference between RF and LO, the output of the mixer is only proportional to the imaginary part of P_{ref} , and is named as an error signal,

$$\epsilon = 2\sqrt{P_c P_s} \text{Im}(F(\omega)F^*(\omega + \Omega)) \sin(\Omega t), \quad (3.17)$$

where P_c and P_s are the power at carrier signal and side-band signal respectively. The error signal can be feedback into an actuator of the laser, thus locking the laser to the cavity and narrowing down the laser's linewidth.

Standard diode lasers have a typical linewidth of a few tens of MHz because of the low-finesse (or low-Q) characteristic of diode structure due to the short cavity length (\sim a few 100 μm) and the low reflectivity (\sim 30%) on two facets leads to a wide linewidth of output laser (\sim a few 10 MHz), which impose a huge challenge on the bandwidth of servo systems. Moreover, laser diodes are driven by electrical current, and the doped p-n-junction allows for recombination of an electron with a hole, then produces a photon. The injection current causes heating of the device, and the index of refraction is temperature-dependent, resulting

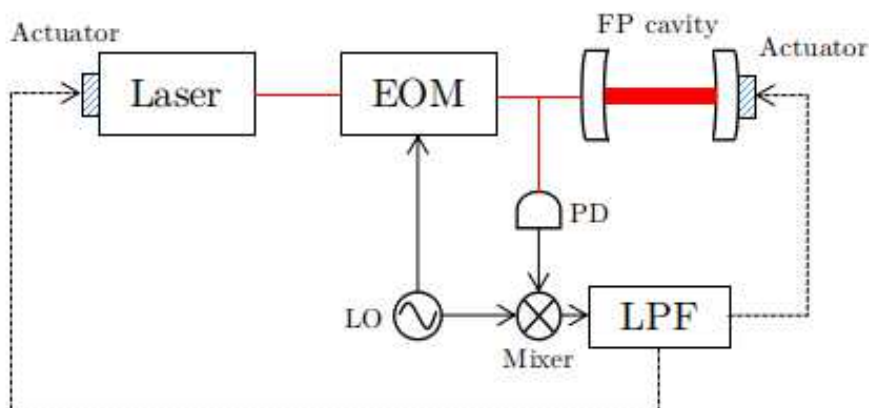


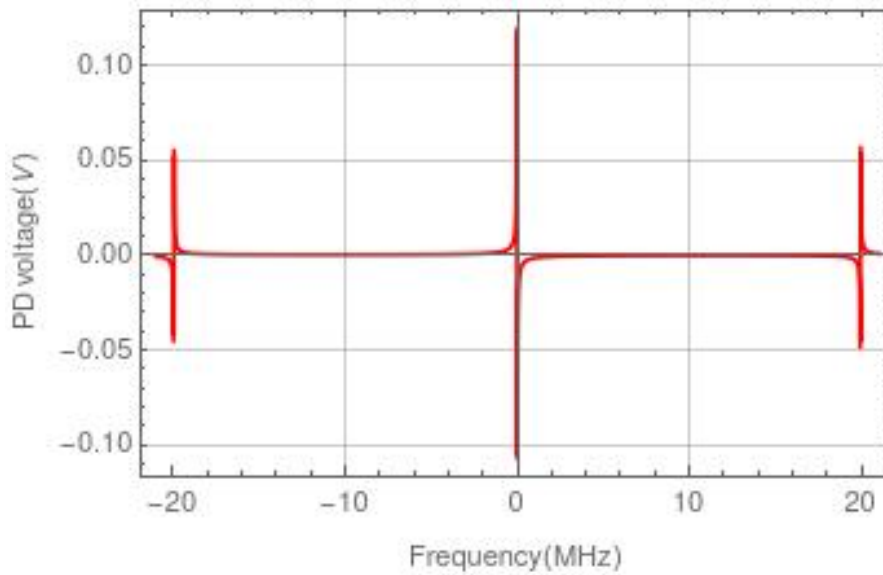
Figure 3.24: Schematic of PDH locking technique. Red solid line represents the optical path, black solid one the electrical path, and the black dashed one the feedback signal. EOM: electro-optic modulator; PD: photodiode; LO: local oscillator; LPF: low-pass filter.

in negative df/dI dependence. Another effect related to electron carriers gives positive df/dI dependence. These two different phenomena dominate at different time scales and must be carefully taken into account to shape the servo system's transfer function correctly. It is not possible to use bare laser diodes directly in a cold atom experiment for all these considerations. Adding an external cavity to the laser diode can narrow the emitted light, thanks to the longer cavity length and the related higher Q-factor. The linewidth of external cavity diode laser (ECDL) benefits from frequency pulling and less mode competition thanks to frequency-dependent reflection from diffraction gratings; the result is a laser linewidth typically below the MHz level. More technical details can refer to [193].

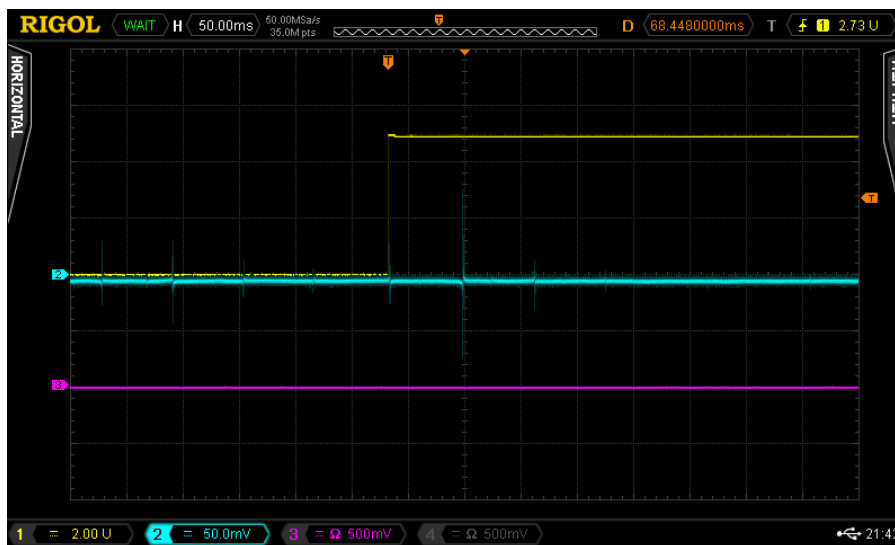
The cavity parameters allow a final sub-Hz linewidth for the 698 nm laser, for which the coating is optimized, and a sub-kHz linewidth for the 689 nm laser. For the red-cooling, at 689 nm, we use an external cavity diode laser from Sacher Lasertechnik, with > 20 mW output power and a linewidth of the order of 200 kHz. We locked the two lasers on the cavity but did not characterize yet the achieved laser stability. To this aim, we plan to use a frequency comb recently installed at LP2N.

In the experiment, we employ the ultra-high finesse cavity characterized by Menlo System (see Tab. 3.5). In combination with the parameters about PDH frequency discriminator listed in Tab. 3.6, we obtain the expected error signal (see Fig. 3.25).

With a high-bandwidth electronics feedback control (see Fig. 3.26) broader than the



a



b

Figure 3.25: (a) Expected PDH error signal for the experimental parameters of our setup, as concerning the 698 nm laser. (b) The error signal of 698 nm laser to the high-finesse cavity.

	Value	Unit
Cavity length	12.1	cm
Free spectral range	1.24	GHz
Finesse	250,000 @ 698 nm	
Linear drift rate	≈ 150	mHz/s
Ambient temperature sensitivity	≈ 4	mK/ $^{\circ}$ C
Ion-Getter pump	10	l/s

Table 3.5: Parameters of ORC-Cylindric reference cavity [194]

	Value	Unit
Modulation depth	0.3	
Photodetector gain	5,000	
Carrier power	90	μ W
Side-band power	10	μ W

Table 3.6: Parameters for PDH frequency discriminator.

dominant noise spectrum from the laser, laser's phase/frequency deviation can be reduced to 10^{-4} of cavity's linewidth (FWHM) [193]. To add stability to the loop, a second servo acting on the PZT can be installed. The required bandwidth is only 100 Hz to 1 kHz. In this way, on a relatively short time scale, the PZT accommodates its output to keep the frequency at its initial value, preventing mode hops.

3.4.2 Doppler-free red spectroscopy at $^1S_0 - ^3P_1$ transition

The narrow transitions $5s^2 ^1S_0 - 5s5p ^3P_1$ with a linewidth of $\Gamma = 7.4$ kHz can be exploited for the efficient laser cooling down to ultra-low temperatures and yields minimum temperatures in the range of μ K but requires the adoption of specific expedients to effectively work on the atomic ensembles have already been cooled down to the mK temperature during the first-stage cooling. The red-cooling laser system at 689 nm is frequency stabilized to another saturated spectroscopy setup, again based on probing hot Sr atoms in an extended heat pipe.

The heat pipe employed for the red spectroscopy on the $5s^2 ^1S_0 - 5s5p ^3P_1$ line is similar to the one for blue spectroscopy; the main differences are due to the much weaker being addressed intercombination transition in the red spectroscopy. Higher atomic pressure is required to obtain the spectroscopic signal, which is obtained by heating the atomic sample

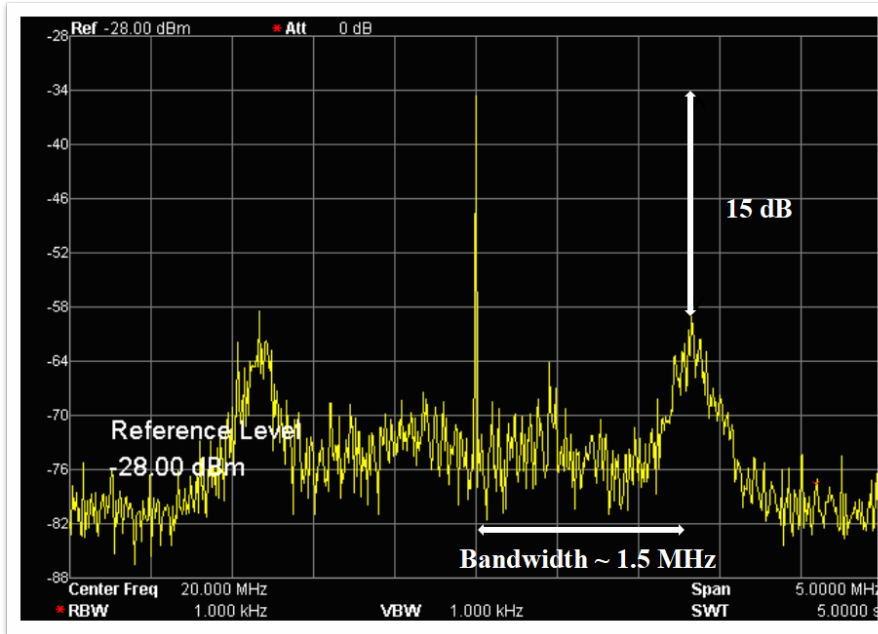


Figure 3.26: Beat-note for the PDH locking setup, use to evaluate the frequency noise of the clock laser after its pre-stabilization on the high-finesse cavity.

to a higher temperature of ~ 450 °C to cause a higher vapor pressure of $\sim 10^{-6}$ mbar. Higher pressure would directly translate into a higher flux of atoms on the two viewports at the two ends of the heat pipe, which will cause their quicker coating. To avoid this negative effect, the inner diameter of the heat pipe is reduced from 18 mm to 8 mm to decrease the solid angle under which the Sr atoms entering the vapor phase can hit the viewports; the heat pipe is filled with $\sim 10^{-3}$ mbar buffering gas, preventing the viewports from coating at the time of minimizing pressure broadening. Finally, the windows at both ends are AR coated for 689 nm radiation.

The spectroscopy setup to frequency stabilize the 689 nm laser on the intercombination transition is shown in Fig. 3.27. The laser beam from the laser diode first passes through the ~ 30 dB isolator then is split into multiple optical paths for different purposes, like being coupled into the fiber switch for monitoring its wavelength, the linewidth narrowing by locking to the high-finesse cavity, sending it into the science chamber to produce the 3D red MOT.

~ 2 mW narrow-linewidth red laser is used for spectroscopy. The frequency tuning (80 MHz) required for the red spectroscopy measurements is obtained by passing the "probe" beam twice through an AOM [195]. The "pump" beam at 689 nm is sent into the heat pipe

without any focusing, thanks to the weak saturation intensity ($\sim 3 \mu\text{W}/\text{cm}^2$) of the $5s^2 \ ^1\text{S}_0 - 5s5p \ ^3\text{P}_1$ transition. With a 1 cm beam waist laser beam, w , interrogating with the hot Sr atoms, the resolution of the spectroscopy is $v_{\text{Sr}}/w \approx 10 \text{ m/s}/0.01 \text{ m} = 1 \text{ kHz}$, where v_{Sr} is the velocity class of the interrogated Sr atoms determined by the frequency tuning. Fig. 3.28 shows the spectral transition lines of the most and second-most abundant Sr isotopes, ^{88}Sr and ^{86}Sr respectively.

We address the transition insensitive at first order to magnetic field, i.e., the $5s^2 \ ^1\text{S}_0(m_F = 0) - 5s5p \ ^3\text{P}_1(m_F = 0)$. We add a vertical magnetic field $B_z = 10 \text{ G}$ using a set of permanent magnets on a parallel-piped to avoid any degeneracy with the other m_F levels (see Fig. 3.29). The fluorescence signal is detected with a photodiode. It shows a narrow sub-Doppler structure on the $5s^2 \ ^1\text{S}_0(m_F = 0) - 5s5p \ ^3\text{P}_1(m_F = 0)$ transition, used to generate the error signal for the absolute frequency definition of the red-cooling laser system.

3.4.3 Optical cavity drift cancellation through red spectroscopy

The linewidth of the red laser stabilized to the high finesse cavity is well below the kHz level (see Sec. 3.4.1), and potentially down to $\sim 10 \text{ Hz}$ as already demonstrated at MENLO with similar parameters; as written already, we will soon characterize the laser features using a frequency comb just installed at LP2N. The high-finesse cavity often exhibits frequency drifts due to mechanical design and the optical resonator's thermal expansion coefficients and needs to be stabilized to more stable references.

Active temperature control wheres stabilize the cavity for its absolute stability; on the one hand, we will exploit [196], i.e., an optical signal at 1542 nm stabilized on an optical clock at SYRTE - Observatoire de Paris and distributed in several French cities via the Renater network when it will be available. On the other hand, the error signal obtained by the red spectroscopy can be used to correct the ultra-stable cavity length by acting on its temperature set point with a very small bandwidth given its high thermal inertia (the temperature setting points updated every 1 s).

At present, we are working on the absolute stabilization of the ultrastable cavity. Once this step is realized, we will use the laser at 689 nm to cool down the atomic ensembles at

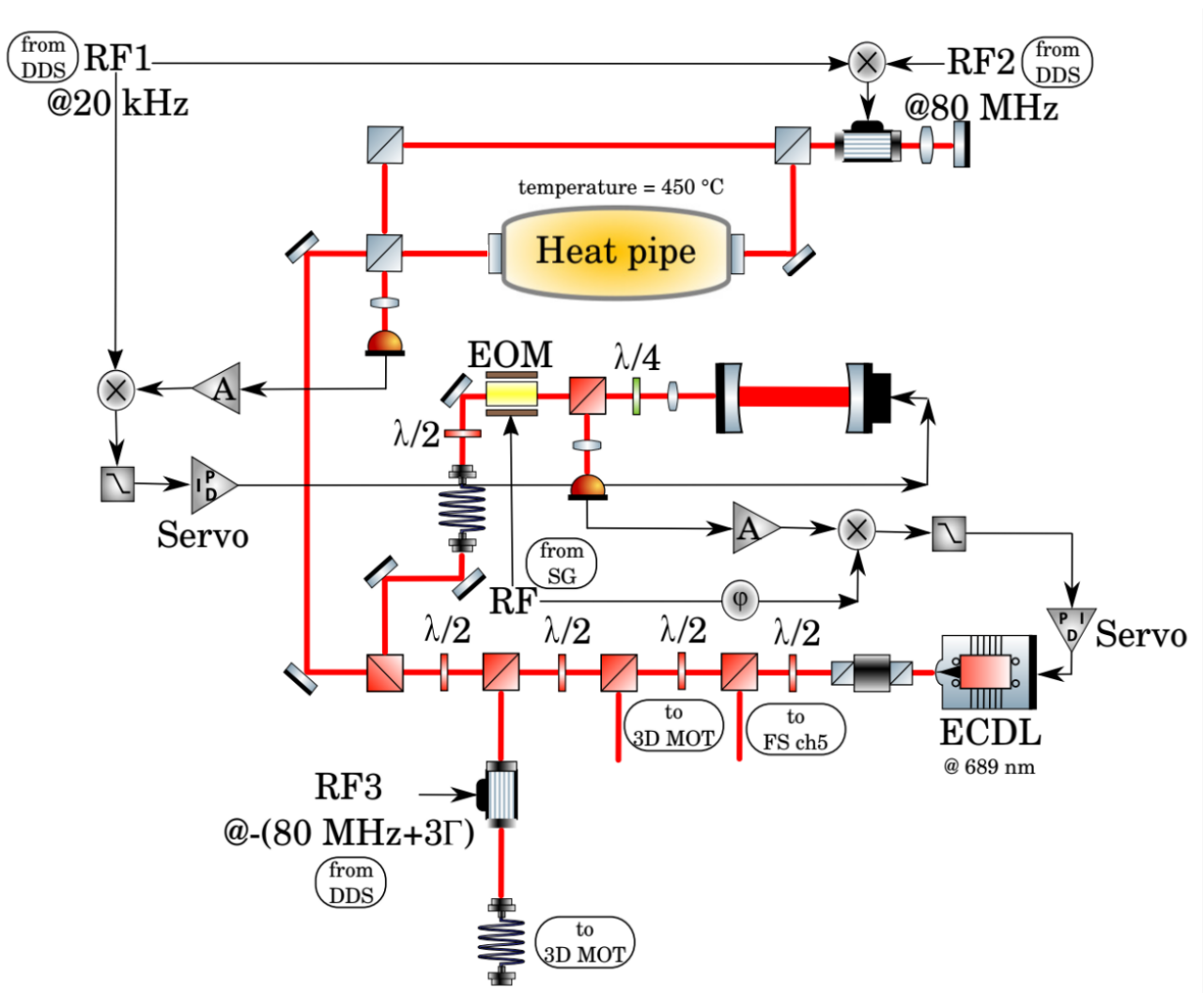


Figure 3.27: Schematic of the red spectroscopy setup. The red solid line represents the optical path, the black solid one the electrical path. EOM: electro-optic modulator; PD: photon detector; LO: local oscillator; LPF: low-pass filter.

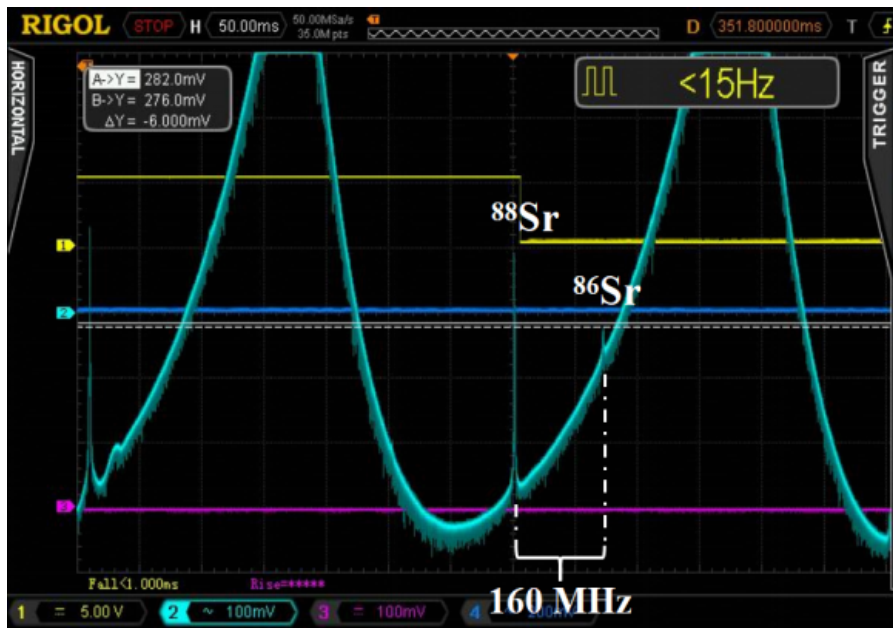


Figure 3.28: Sub-Doppler profile of the $5s^2 \ ^1S_0 \text{ -- } 5s5p \ ^3P_1$ transition.

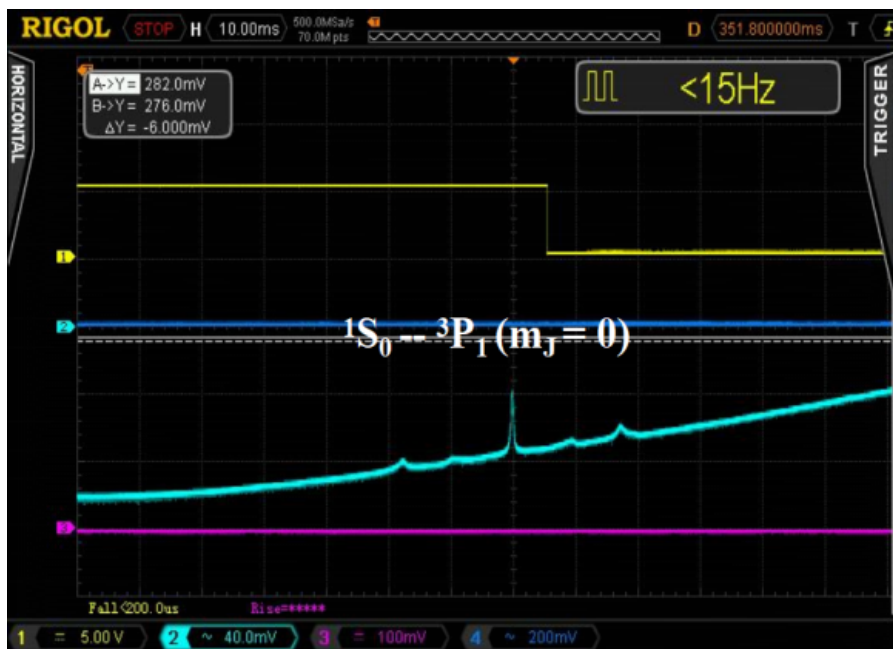


Figure 3.29: Implementing 10 G magnetic field to resolve different m_F states and the crossovers in terms of the $5s5p \ ^3P_1$ transition.

the mK level produced with the blue MOT to achieve a temperature of the order sub-microK.

The frequency shift imposed on the spectroscopy setup (80 MHz) is compensated with a second AOM to obtain the cooling light with a few linewidth red-detuned to the transition $5s^2\ ^1S_0 \rightarrow 5s5p\ ^3P_1$. The same AOM is also adopted to synthetically enlarge the laser spectrum to capture the atomic ensemble produced by the blue MOT at the mK temperature. We apply a frequency chirp in the red-cooling beam to successfully compensate for the Doppler shift of different atomic velocity classes; once the red MOT is distinguished, we progressively reduce the chirping range, which reduces the sample temperature down until the μ K level when the frequency modulation is completely removed.

3.5 Repumpers at 707 nm and 679 nm

Fizeau-based interferometer The Fizeau-based frequency reference is a standard wavelength meter (WS6, HighFinesse GmbH). This wavelength meter can perform wavelength measurements for CW and pulsed lasers in the 330 - 1180 nm range. The optical unit used in our experiment comprises of 8-channel electric-mechanical switch and solid Fizeau interferometer. In the multi-channel fibered switch, each input field is directed to the output sequentially; the output field ($< 100\ \mu$ W) is sent into the interferometer and measured by the CCD. The software records the interference pattern and calculates the wavelength. WS6 wavelength meter has a measurement accuracy of ~ 20 MHz in a broad range, as specified in the wavelength meter product brochure. The absolute accuracy can reach 600 MHz without calibration.

3.5.1 Wavemeter-based multi-frequencies stabilization

The transition at 461 nm used for the blue MOT is not closed, and atoms leak to the $5s5p\ ^3P_{1,2}$ levels via the $5s4d\ ^1D_2$ one. The atoms in the $5s5p\ ^3P_1$ level quickly decay to the fundamental state $5s^2\ ^1S_0$ and are back in the cooling transition, whereas the atoms in the $5s5p\ ^3P_2$ require a repumping stage to do so. This can be accomplished in several ways, as described in [197], using different intermediate levels to pump the atoms. We have chosen the $5s6s\ ^3S_1$ state for

this process and require thus two diode lasers, one at 707 nm and one at 679 nm. The latter laser is necessary to address the atoms falling from the $5s5p\ ^3P_1$ level to the $5s5p\ ^3P_0$ one.

Two repumper lasers (ECDL, Sacher Lasertechnik) at 679 nm and 707 nm have the free-running linewidth with a typical value of 200 kHz. We improve their long-term stability by stabilizing them to the wavelength meter based on solid Fizeau interferometers and digital PID. The locked laser system is successfully used in a ^{88}Sr trapping experiment, which is discussed here both for its hardware configuration and software realization.

To address the Doppler broadened spectrum in the blue MOT, we have chirped the repumpers' frequencies by modulating their current, e.g., 300 mV sinusoidal signal at 6 kHz for 679 nm, and 450 mV sinusoidal signal at 7 kHz for 707 nm.

We develop an optical setup based on a wavelength meter to transfer the absolute frequency stability of one laser (in our case, the blue laser at 461 nm stabilized on the $5s^2\ ^1S_0 - 5s5p\ ^1P_1$ transition) to the two lasers used to repump the Sr atoms. To this aim, the possibility of monitoring several lasers in a rapid sequence via a MEMS-based optical switch (Multichannel Switch, HighFinesse) proves crucial.

3.5.1.1 Hardware

The scheme of the wavemeter locking setup (see Fig. 3.31) is depicted in Fig. 3.30. The output power of each repumper is ~ 25 mW. The main laser beams are combined and sent to the science chamber after passing through an optical telescope to increase the resulting beam waist. A small amount of repumping light from each repumper is instead sent to the wavelength meter via one multi-channel optical switch. A digitized error signal is generated by comparing the real-time wavelength with the setting value and transferred to a low-power single-board BeagleBone Black (BBB, Texas Instruments) for calculating a feedback control signal after PID in the form of temperature. The temperature correction is applied to the corresponding laser via interconnect bus. Both controllers and BBB are mounted into a smart rack, communicating with each other via I²C.

We use the GUI software for WS6 from the Highfinesse company for the readout of the laser wavelengths. To accurately resolve the wavelength value, the input power should be adjusted so that the amplitudes of the displayed interference pattern fit more than 60% of

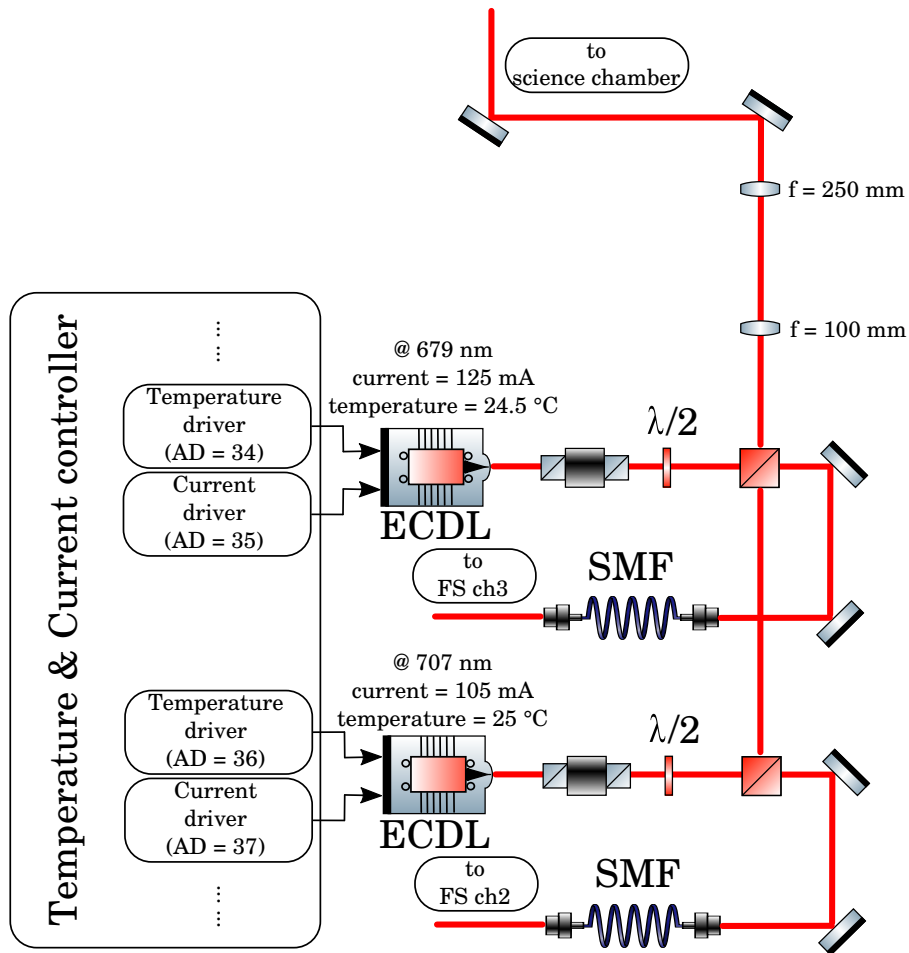
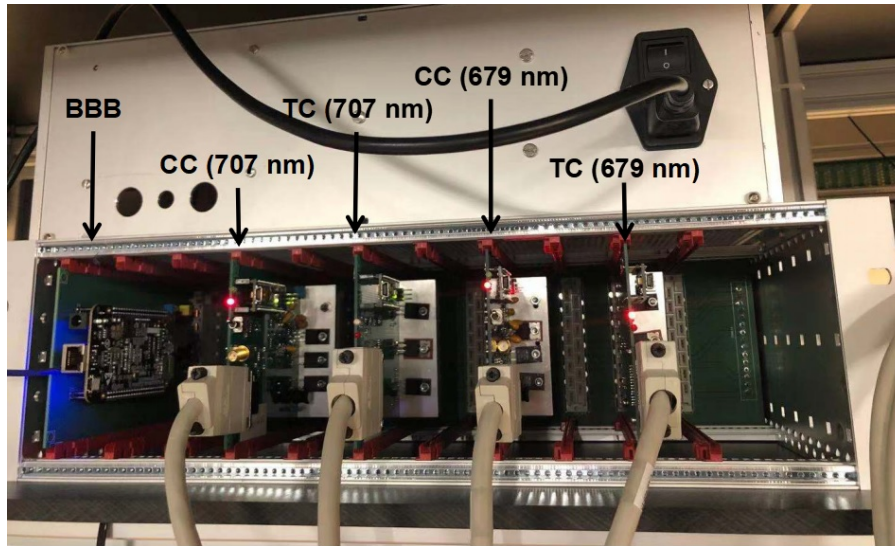
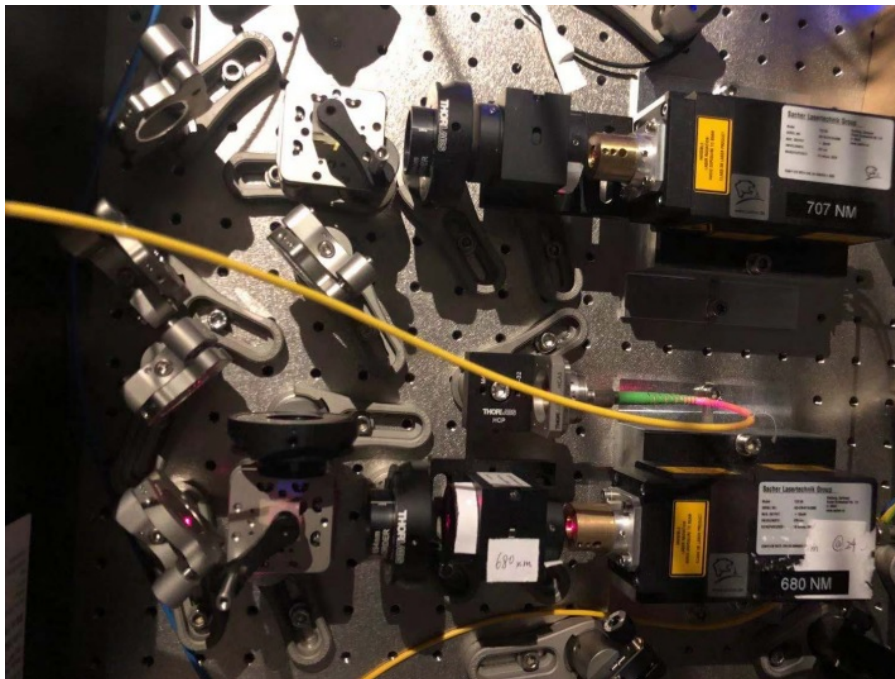


Figure 3.30: Two repumpers are combined and magnified with a 1:3 optical telescope, and the wavelength of each repumper is monitored by the wavelength meter. AD: the address of our I²C bus used to control the current and temperature drivers remotely; FS: fiber switch.



a



b

Figure 3.31: (a) BBB, temperature controllers (TC), and current controllers (CC) for two repumpers. (b) Optical setup.

the chart.

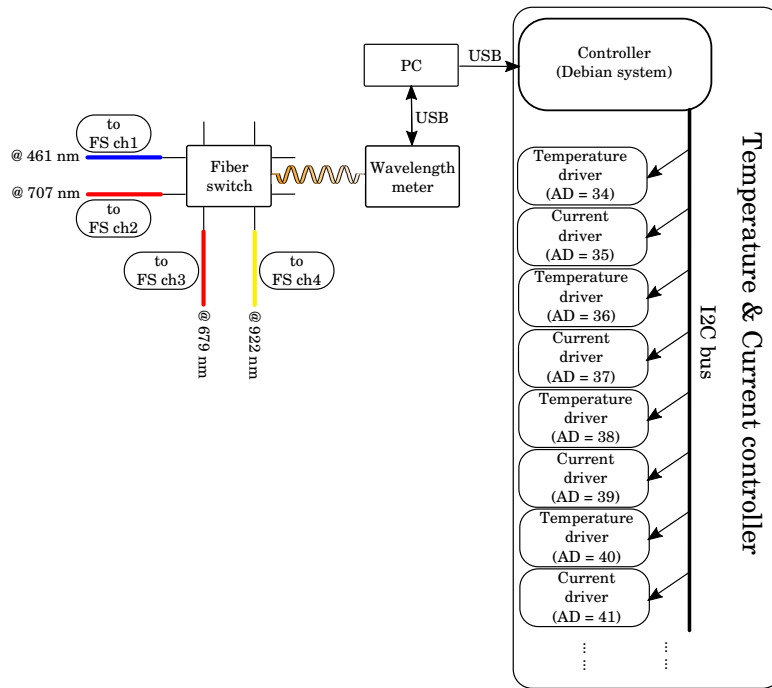
3.5.1.2 Software

The channels of the fiber switch are read sequentially by the wavelength meter, and the acquisition rate for each channel is ~ 10 Hz. Every measurement cycle stores in the Windows PC: the specific channel being read of the optical switch, the laser wavelength, the temperature of the device, and the ambient pressure. We retrieve such information with a Python program that communicates with the operating system's dynamic link library (DLL) and then sends it into the BBB through a universal serial bus (USB) connection. The BBB uses the laser wavelength to produce an error signal for the temperature controller and corrects the laser frequency accordingly by changing the temperature set point via a digital PID. The code is written in C language and can be easily modified to change the PID parameters. Fig. 3.32 presents the locking system as concerning its physical connection and its software implementation.

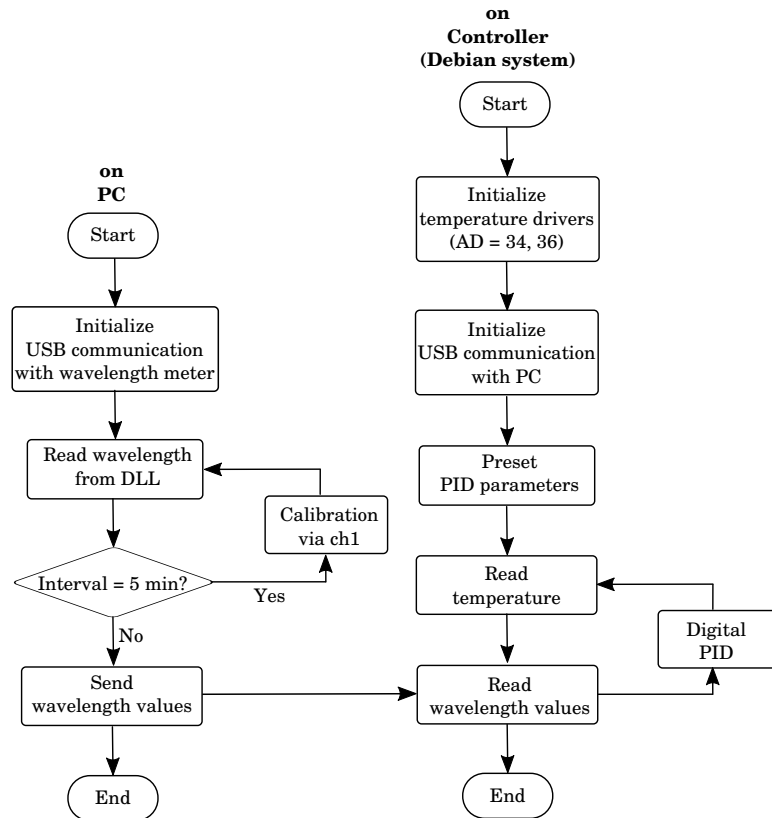
Our wavemeter-locking system bandwidth is determined by the total delay imposed by the feedback system: the wavemeter is one of the major contributors, its exposure time, the switching time in the multi-channel switch, the information processing time in the PC, and the communication time between the PC and the BBB; the other one is about the digital PID bandwidth in the BBB and the temperature response time of the laser diode temperature controller. In our case, >0.1 Hz bandwidth is acceptable, so the parameters mentioned earlier are not crucial. However, they have to be carefully characterized for higher bandwidth locking systems.

The digital PID servo parameters are decided by the temperature transfer function of laser diode. (see Fig. 3.33).

Due to the lack of instruments, e.g., the optical comb, we cannot directly measure the frequency stability of the two frequency-stabilized repumpers. To have a rough idea of the two repumpers frequency stability, we record the frequency values in time from the wavelength meter while free-running and locking lasers to it (see Fig. 3.34), that, over 10-h measurements, at least of 10 times improvement for the peak-to-peak fluctuations is observed.



a



b

Figure 3.32: (a) Schematic of the optical and electronic setup realized to simultaneously lock the two repumper lasers to the wavelength meter through a fiber switch. (b) The flow chart of locking program. The Debian system is embedded into the BBB controller.

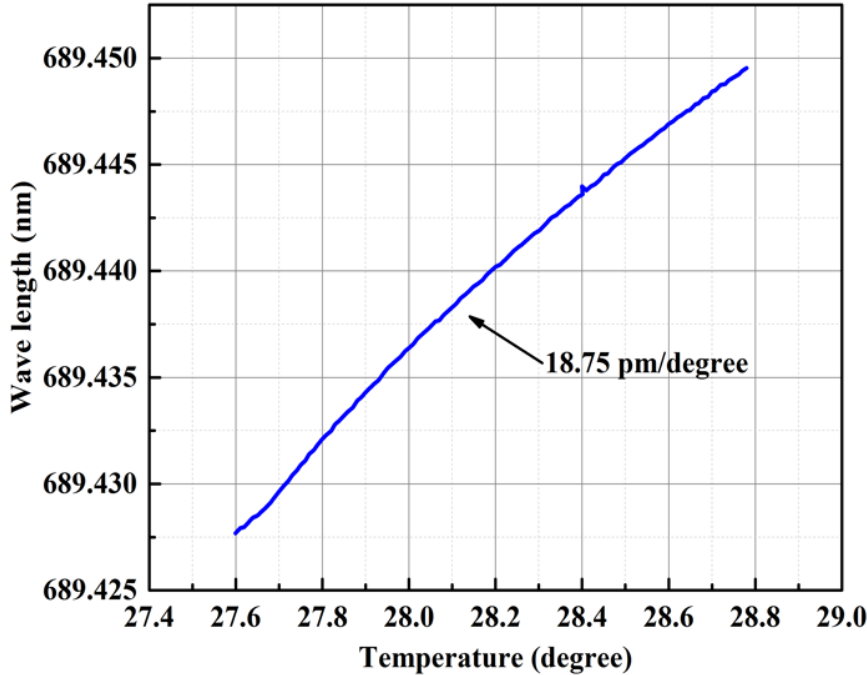


Figure 3.33: Wavelength dependence on the laser temperature, showing a regime with an almost linear regime.

3.6 FPGA-based experimental control system

In AMO experiments, rapid digital and analog signals, taking place with a strict temporal resolution of $10\mu\text{s}$ or even faster, are required to manipulate the magnetic field and produce and probe cold atomic samples. A dedicated control system based on the field-programmable gate arrays (FPGA) is initially developed by Prof. Prevedelli, and the system architecture is depicted in Fig. 1 of the [198] (see Appx. A). The core of the master controller is the board equipped with FPGA clocked with 10 MHz quartz. Both the master board and slave modules (up to 128) are attached parallel to the 24-bit bus (7-bit address bus, 16-bit data address, and 1-bit strobe), and each slave module owns its unique address. The precise timing sequential actions to be performed on the experiment are pre-defined in the PC. The PC software transmits a table of actions to the master board via a USB serial bus. At specific timing decided by the user, the FPGA firmware writes the instructions sequentially on the bus, and a slave board with the correct address updates its state after one 1-bit strobe pulse.

This unified control system applied in the laboratory (see Fig. 3.35) has three types of

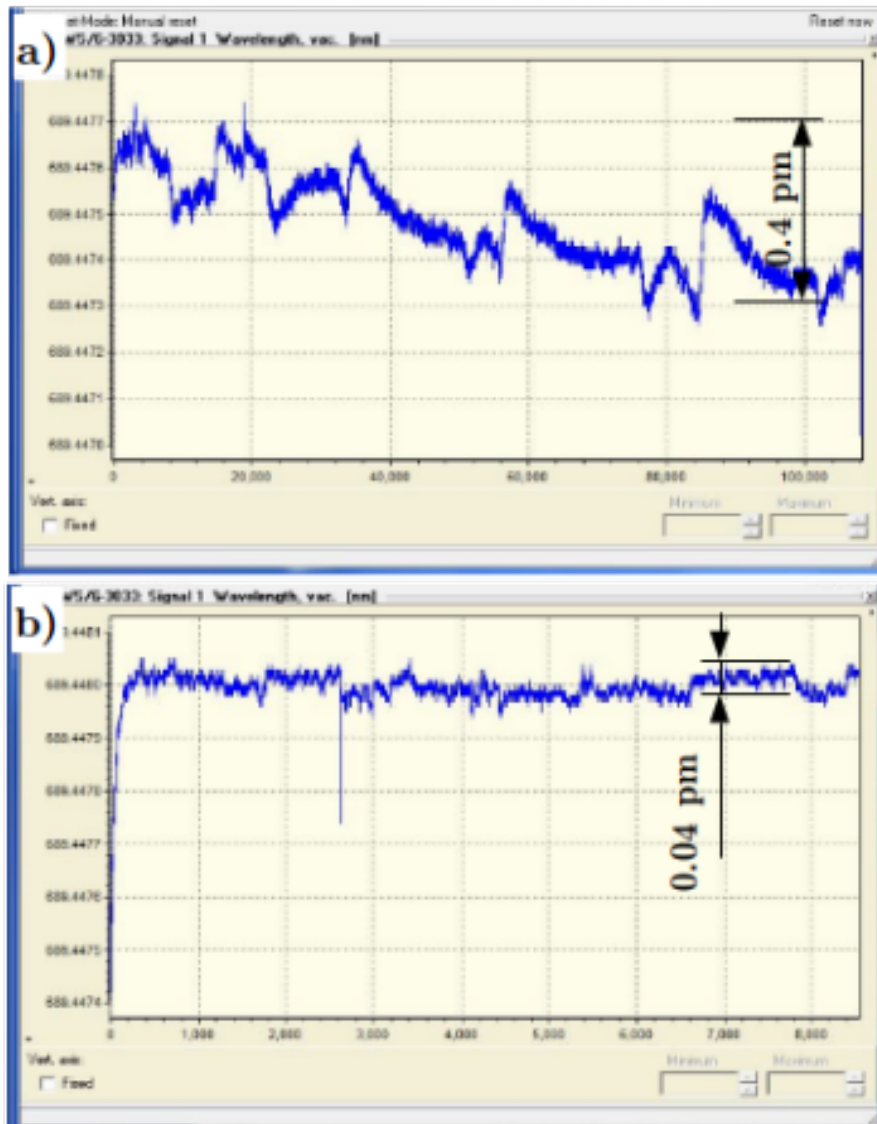


Figure 3.34: Frequency stability of locked repumpers. (a) Free running (b) Locking lasers to the wavemeter.

slave boards: digital output, analog output, and DDS.

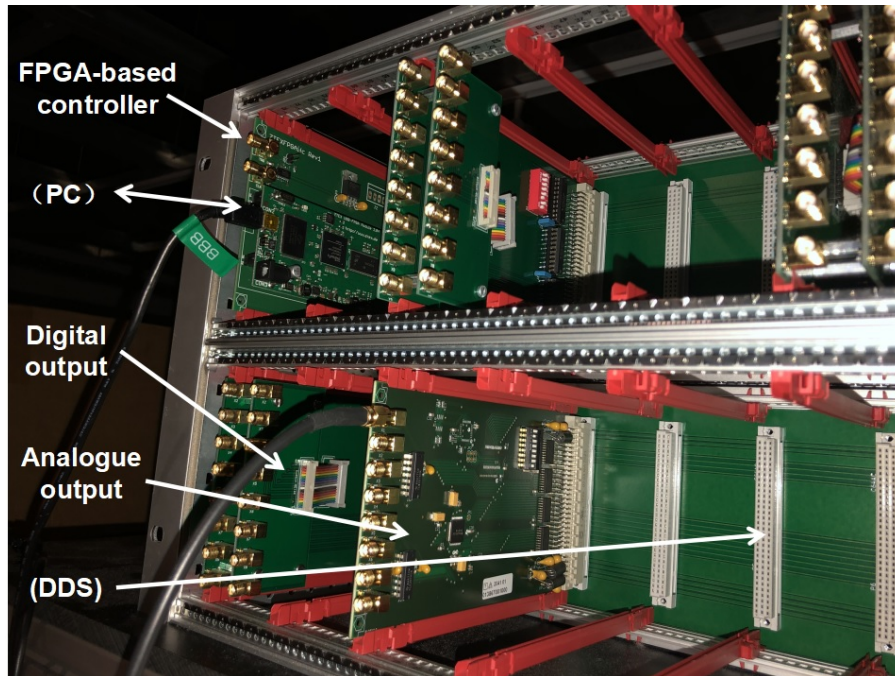


Figure 3.35: FPGA-based controller system realized for the experiment.

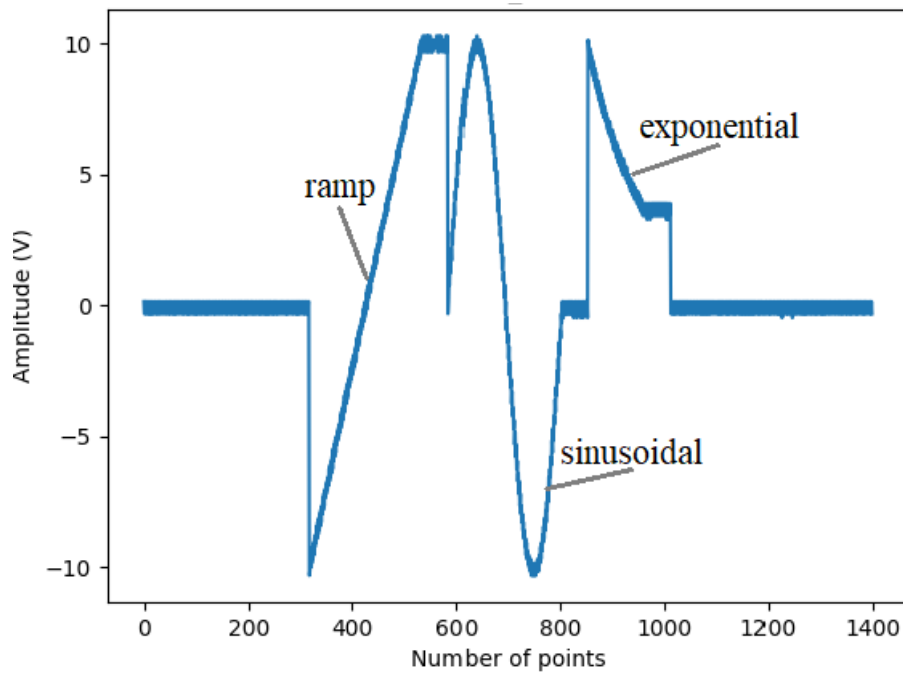


Figure 3.36: Arbitrary waveforms from the analogue output module.

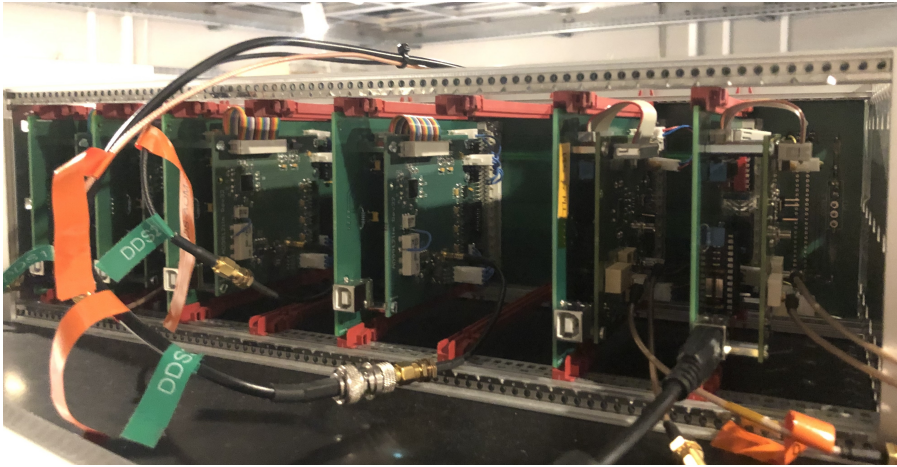


Figure 3.37: DDS rack (for AOMs, EOMs, DPLL).

Digital output The digital output modules are just an address decoder and a 16 bits latch, so when writing to a digital output module, the content of the data bus is stored and transferred to its 16 output lines. All the lines on the same digital output module can be changed simultaneously, while changes on lines on different modules are separated by at least one master clock period.

The TTL states (ON/OFF) from the digital output either control the mechanical shutters to interrupt the laser beams or toggle electronic switches.

Analog output The analog output modules are almost as simple, including a 16 bits DAC per address, generating an analog voltage with customized waveforms, typically in the ± 10 V range (see 3.36), with a sensitivity of 2.5 mV.

DDS The DDS daughterboards are based on AD9854/AD9912/AD9958/AD9959 DDS chip (Analog Devices) with different frequency/amplitude/phase resolutions, output channels, and maximum output frequencies and capability of modulation to satisfy various applications. Motherboards change correspondingly for different daughterboards.

A separated DDS rack (see Fig. 3.37) is designed to drive acousto-and electro-optic modulators.

Chapter 4

Preliminary results with cold atoms

Our atomic source is produced by a 2D-MOT, enhanced with a Zeeman slower. The cooled atoms are transferred to the science chamber via a pushing beam. To estimate the atomic source performance, we have studied the optical and magnetic properties of the 2D-MOT as well as the transfer process regulated by the pushing beam (see Sec. 4.1). After that the atoms are transferred into the science cell, we obtain a continuous 3D-blue-MOT and characterize its properties (see Sec. 4.2). To enhance the flux of the atomic source and, thus, the cold atom numbers in the science cell, we have developed a dual-frequency Zeeman slower (see Sec. 4.3). The maximum fraction of the atomic flux achieves $\sim 50\%$. We quantify the enhancement factor introduced by the double-frequency Zeeman Slower (ZS) while using the loading flux of the 3D-MOT.

Contents

4.1 Atomic source	98
4.1.1 The two-dimensional MOT	98
4.1.2 Single-frequency Zeeman slower	99
4.1.3 The atomic transfer	102
4.2 Cold atoms with the blue MOT	103
4.2.1 The capture velocity	103
4.2.2 Number of atoms and loading rate in the 3D-MOT	103
4.2.3 The repumpers	104
4.3 The analysis of upgraded Zeeman slower	105
4.3.1 The numerical model	106
4.3.2 The single-frequency Zeeman slower	109
4.3.3 The dual-frequency Zeeman slower	112
4.3.4 The enhancement of atomic flux	118

4.1 Atomic source

4.1.1 The two-dimensional MOT

Two-dimensional MOT force The two-dimensional MOT (2D-MOT), two crossing laser beams are retro-reflected, red-detuned, circularly polarized (σ_+ or σ_-) and then combined with the linear magnetic quadruple to slow down the atoms. In the 2D-MOT, the atoms are slowed down with the dissipative force exerted by the light and trapped within the vanishing region of the magnetic field configuration. This trapping occurs due to the position-dependent force introduced by the Zeeman effect. The atoms, considered as two-level sys-

tems, are decelerated only by the MOT force in one dimension. The resulting force is:

$$\begin{aligned} \frac{\vec{F}_{\text{MOT}}}{m} &= \frac{\vec{F}_+(\Delta_+)}{m} + \frac{\vec{F}_-(\Delta_-)}{m} \\ &= \frac{\sqrt{2}\hbar\Gamma}{m} \frac{1}{2} \left(\frac{s\vec{k}}{1+s+4\Delta_+^2/\Gamma^2} + \frac{s\vec{k}}{1+s+4\Delta_-^2/\Gamma^2} \right), \end{aligned} \quad (4.1)$$

where

$$\Delta_+ = (\omega_L - \omega_0) - \frac{1}{\sqrt{2}}\vec{k}\vec{v} + \frac{\mu_B g_J m_J |\vec{B}|}{\hbar}, \quad (m_J = +1), \quad (4.2)$$

and

$$\Delta_- = (\omega_L - \omega_0) - \frac{1}{\sqrt{2}}\vec{k} - \vec{v} + \frac{\mu_B g_J m_J |\vec{B}|}{\hbar}, \quad (m_J = -1), \quad (4.3)$$

with $\mu_B = 1.4$ MHz/G is the Bohr magneton, g_J is the Landé factor, m_J is the projection of the electrical angular momentum along \vec{B} , ω_0 is the transition frequency, ω_L is the laser frequency, and \vec{k} is the wavevector of the laser beam that has an opposite sign than the atomic velocity \vec{v} . The $\sqrt{2}$ factor in the second terms of Eqs. 4.2 and 4.3 arise due to the cooling beams are 45° tilted at the transverse plane, perpendicular to the trajectory of atomic beams. The atoms are only decelerated by absorbing photons from the counter-propagating cooling beam (\vec{k} and \vec{v} have opposite signs). At each position, only one of the forces $\vec{F}_+(\Delta_+)$ and $\vec{F}_-(\Delta_-)$ is dominant (see Fig. 4.1).

Since the size (r_c) of the laser beams is finite, there exists a maximal atom's velocity called capture velocity v_{cap} , over which the MOT cannot trap the atoms. In a MOT, the absorption of a photon by the atom has a preferential direction, whereas the emission is isotropic; hence, the effect on the atom's momentum is only related to the absorption mechanism. A reasonable estimation of v_{cap} is [199],

$$v_{\text{cap}} = \sqrt{ar_c}, \quad (4.4)$$

where r_c is the cooling beam radius, and a is the deceleration, which is $\sim 0.7a_{\text{max}}$. Using the parameters in Tab. 4.1, we estimate that the one-dimensional v_{cap} for the 2D-MOT is 50 m/s.

4.1.2 Single-frequency Zeeman slower

Zeeman slowing force The normal ZS based on a single frequency slowing beam is formed with the tail of the 2D-MOT magnetic field either in the region 1 ($-150 \text{ mm} < \text{position} < -50$

Parameters	Symbol	Unit	2D-MOT
Atomic mass	m	[kg]	1.46×10^{-25}
Wavelength	λ	[nm]	461
Transition linewidth	Γ	[MHz]	30.5
Laser beam $1/e^2$ radius	r_c	[cm]	2
Frequency detuning	Δ	[Γ]	~ -1
Magnetic gradient	∇B	[G/cm]	50
Saturation parameter	s		~ 1

Table 4.1: Parameters applied in the experiment to produce the 2D-MOT and for the numerical estimation of its capture velocity.

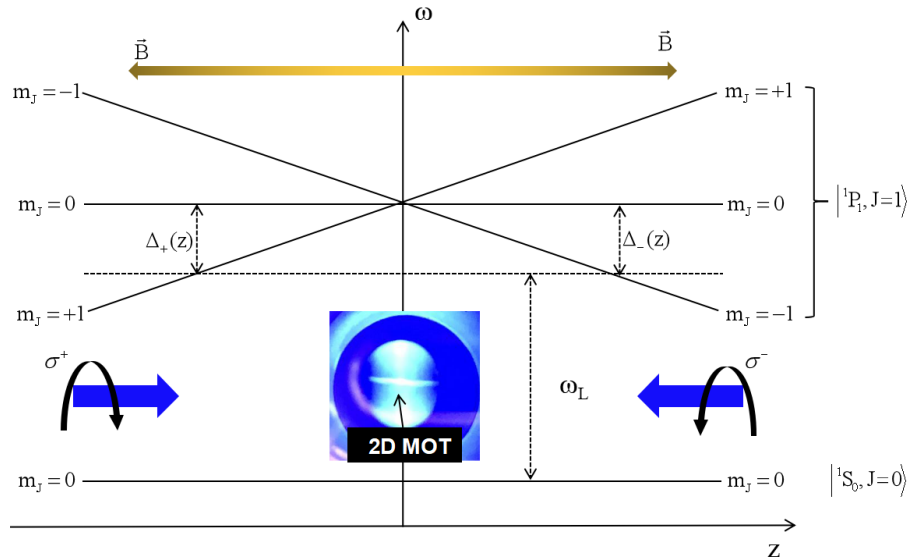


Figure 4.1: The MOT force takes advantage of the Zeeman effect of neutral Sr atoms in the magnetic quadrupole, where the center of the magnetic field coincides with the zero position. The inset shows the fluorescence emitted by the atoms trapped in the 2D-MOT.

mm) or the region 2 ($-50 \text{ mm} < \text{position} < -10 \text{ mm}$) in Fig. 4.2, and a light beam, traveling opposite direction than the atomic beam. Due to the low magnetizability of the stainless steel, we assume that the chamber does not affect the magnetic field distribution. The atoms are decelerated with a 1D-force given by,

$$\frac{\vec{F}}{m} = \frac{\hbar \vec{k} \Gamma}{m} \frac{s}{2(1+s+4\Delta_{\text{eff}}^2/\Gamma^2)}, \quad (4.5)$$

where

$$\Delta_{\text{eff}} = (\omega_L - \omega_0) - \frac{1}{\sqrt{2}} \vec{k} \vec{v} + \frac{\mu_B g_J m_J |\vec{B}|}{\hbar}, \quad (m_J = +1 \text{ or } -1). \quad (4.6)$$

Note that, at most, only half of the power incident into the ZS, based on a similar magnetic configuration as [172], has a well-defined circular polarization [200].

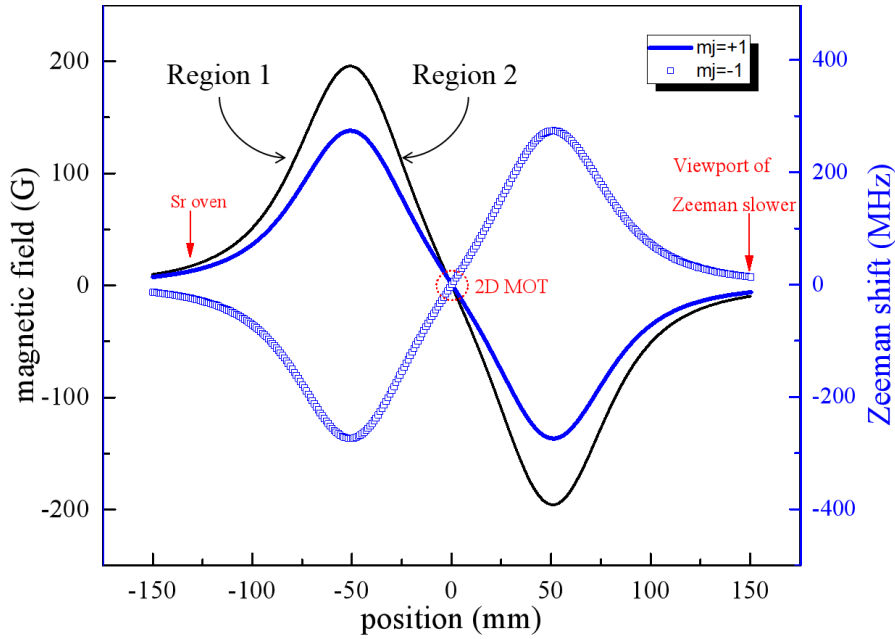


Figure 4.2: The numerically calculated magnetic field, formed by four packs of permanent magnets, splits the 1P_1 ($J = 1$) level due to the Zeeman effect. The B-field in the region 1 can be fitted with the formula $B_1(z) = -1705.19527 - 113.58239z - 2.51382z^2 - 0.02711z^3 - 1.56325 \times 10^{-4}z^4 - 4.64712 \times 10^{-7}z^5 - 5.6087 \times 10^{-10}z^6$ [G], and the region 2 is $B_2(z) = 0.06322 - 5.25421z - 0.00735z^2 - 0.00153z^3 - 3.1921 \times 10^{-5}z^4$ [G]. Here, only the magnetic field sensitive levels ($m_J = +1$, $m_J = -1$) are indicated.

Since the Zeeman slowing beam typically has a red-detuned frequency which is located much further away than the 2D-MOT cooling beams, we assume that the scattering force

from the ZS is independent of the one from the 2D-MOT. The forces from different sources cannot be simultaneously exerted on the atoms. For simplicity, we assume that the atoms in the ZS with final velocities less than the capture velocity of the 2D-MOT are 100% trapped by the 2D-MOT, where the transition effect is not discussed in this proposal dual-frequency ZS.

Parameters	Symbol	Unit	Zeeman slower
Atomic mass	m	[kg]	1.46×10^{-25}
Wavelength	λ	[nm]	461
Transition linewidth	Γ	[MHz]	30.5
Laser beam $1/e^2$ radius	r_c	[cm]	1
Frequency detuning	Δ	[Γ]	-1.5
Saturation parameter	s		0.3

Table 4.2: The parameters for the single-frequency Zeeman slower.

4.1.3 The atomic transfer

In the 2D-MOT, the atoms are cooled and trapped along only with two directions. They remain free along with the third one, which coincides with the line region where the B-field vanishes (see Fig. 4.1). We then add a pushing beam to transfer atoms from the atomic source to the 3D-blue-MOT in the science chamber. The atom transfer efficiency is dependent on the parameters of the pushing beam. We apply a weak ($100 \mu\text{W}$), well-aligned, and near-resonant pushing beam to achieve the transfer of a maximum number of atoms into the 3D-MOT (see Tab. 4.5). There is a lack of photons at lower pushing beam intensity to interrogate all the atoms possessing the right longitudinal velocity in the same atomic source. The increase of pushing beam power enhances the transfer efficiency. The transfer efficiency drops with too high a pushing beam, probably because the atoms are accelerated too much. Their final velocities along the transfer trajectory are higher than the capture velocity of the 3D-MOT. This phenomenon has been studied with a Monte Carlo method [201].

Parameters	Symbol	Unit	Pushing beam
Atomic mass	m	[kg]	1.46×10^{-25}
Wavelength	λ	[nm]	461
Transition linewidth	Γ	[MHz]	30.5
Laser beam $1/e^2$ radius	r_c	[mm]	0.6
Frequency detuning	Δ	[Γ]	0

Table 4.3: The parameters for the pushing beam.

4.2 Cold atoms with the blue MOT

4.2.1 The capture velocity

The atoms transferred to the science chamber are stopped at the center of the magnetic quadruple of the 3D-MOT. Their capture velocity (see Eq. 4.4) can be estimated using the parameters listed in Tab. 4.4.

Parameters	Symbol	Unit	3D blue MOT
Atomic mass	m	[kg]	1.46×10^{-25}
Wavelength	λ	[nm]	461
Transition linewidth	Γ	[MHz]	30.5
Laser beam $1/e^2$ radius	r_c	[cm]	1.35
Saturation parameters	s		0.65
Frequency detuning	Δ	[Γ]	~ -1

Table 4.4: The parameters for trapping atoms inside the science cell.

4.2.2 Number of atoms and loading rate in the 3D-MOT

We characterize the number of atoms trapped in the 3D-blue-MOT by measuring its fluorescence. The atomic fluorescence signal is measured with a Thorlabs Photodiode (PD) (PDF10A2, Thorlabs). To avoid the saturation of the PD, a neutral density filter (NE30A, Thorlabs) is inserted. The total fluorescence power emitted from the 3D-MOT is

$$P_{\text{PD}} = \frac{V_{\text{PD}}}{G_{\text{PD}} R_{\text{PD}} T_{\text{DF}}}, \quad (4.7)$$

where V_{PD} is the measured voltage with a high-impedance configuration, $G_{\text{PD}} = 1 \times 10^{12}$ V/A is the transimpedance gain, $R_{\text{PD}} = 0.25$ A/W is the spectral responsibility (quantum

efficiency) at a wavelength of 461 nm, and $T_{\text{DF}} = 0.1\%$ is the transmission of the density filter.

The scattered power (P_{scat}) of the two-level atoms in the MOT is

$$\begin{aligned} P_{\text{scat}} &= \gamma_{\text{scat}} h\nu \\ &= \frac{\Gamma}{2} \frac{s}{1 + s + 4\Delta^2/\Gamma^2} h \frac{c}{\lambda}. \end{aligned} \quad (4.8)$$

Since the MOT size is much larger than the PD area, a converging lens (LA1805-A-ML, Thorlabs), with a focusing length $f = 30$ mm and a radius $r = 12.7$ mm, is added to focus the fluorescence into the PD. The atom numbers in the 3D MOT [202] is estimated by

$$N = \frac{P_{\text{PD}}}{P_{\text{scat}}} \frac{4\pi f^2}{r^2}. \quad (4.9)$$

The fluorescence curve of the 3D-MOT, with a lifetime of ~ 1 s, is presented in Fig. 4.3 and it indicates that there are $\sim 10^6$ cold atoms, and the loading rate is $\sim 2 \times 10^6$ atoms/s.

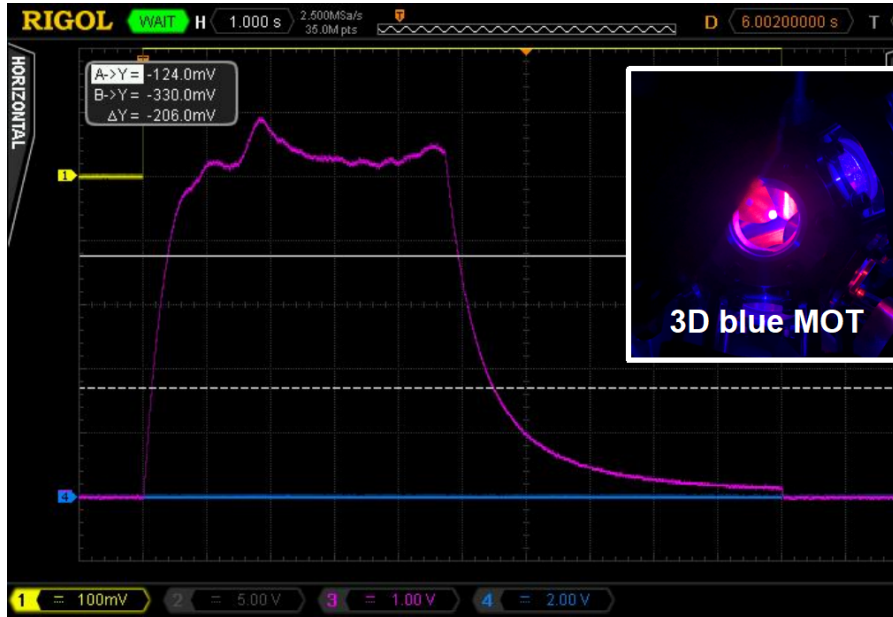


Figure 4.3: Illustration of the fluorescence emitted by the atoms trapped into the 3D-MOT.

4.2.3 The repumpers

The $5s^2 \ ^1S_0 - 5s5p \ ^3P_1$ transition is not fully cycling; hence, there exists a non-negligible leakage channel from the upper channel to the $5s4d \ ^1D_2$ level. One third of the atoms in the $5s4d \ ^1D_2$ level decay into a metastable state $5s5p \ ^3P_2$, representing a big loss channel for the

blue MOT. To bring back the lost atoms into the cooling cycle and increase the number of atoms in the blue MOT and loading rate, we use two diode lasers. These lasers of 707 nm and 679 nm optically pump the atoms accumulated on the metastable state $5s5p\ ^3P_2$ towards the ground state. This way we address both transitions, the $5s5p\ ^3P_2 - 5s6s\ ^3S_1$ and the $5s5p\ ^3P_0 - 5s6s\ ^3S_1$ respectively. These two diode lasers are frequency stabilized using a wavelength meter. Chirping the two repumpers, with a rate of ~ 5 kHz and an amplitude of 300 - 400 mV, to match the atomic velocity spectrum in the blue 3D-MOT can increase the atom numbers by a factor of >5 .

Parameters	Symbol	Unit	$^3P_2 - ^3S_1$	$^3P_0 - ^3S_1$
Wavelength	λ	[nm]	707.20	679.29
Transition linewidth	Γ	[MHz]	$2\pi \times 46$	$2\pi \times 9$
Decay time	τ	ns	3.4	0.7
Saturation intensity	$I_0 = \pi\hbar c/3\lambda^3\tau$	[mW/cm ²]	17	3.7
Laser beam $1/e^2$ radius	r_c	[cm]	1	1
Saturation parameter	s		1.3	2.6

Table 4.5: The parameters for both repumpers.

4.3 The analysis of upgraded Zeeman slower

Cold atomic clouds with a large number N of atoms are often desired in Atomic, Molecular, and Optics physics (AMO) and notably in atom interferometry, where the phase resolution $\Delta\phi$ is typically limited by the quantum projection noise (QPN) [203] and scales as $\Delta\phi \propto 1/\sqrt{N}$.

We are building a sub-microkelvin ^{88}Sr atom interferometer, where we use an atomic source with a compact design, integrating a 2D-MOT and a Zeeman slower [172]. This design reduces systematic errors related to vacuum contamination, thermal-beam collision, and black body radiation. Instead of only using one of the two available magnetic field ramps [172], our system takes advantage of the complete profile of the B-field. It applies a dual-frequency ZS to capture the fast-velocity-class atoms with higher probability densities. Thus, we enhance the atomic source's atomic flux. Sec. 4.3.1 introduces the numerical model we have developed to study the dual-frequency ZS. As a sanity check, we first simulate parameters of interest like the atomic trajectories, the velocity probability density, and the

atomic flux in the common single-frequency ZS (see Sec. 4.3.2). In Sec. 4.3, we analyze the same parameters in the dual-frequency ZS. We demonstrate the enhancement of the new scheme, compared with the single-frequency ZS, with the experimental setup mounted for the ^{88}Sr atom interferometer. So far, we have demonstrated a higher efficiency with the dual-frequency ZS (see Sec. 4.3.4). We are currently working on full scans of the experimental parameters to characterize the protocol entirely.

4.3.1 The numerical model

We consider only the radiation pressure determined by the ZS beam-combined presence and the magnetic field imposed by the 2D-MOT to calculate the atomic dynamics. We ignore other minor contributions as it is the case for both gravity and inter-atomic collisions [204, 205].

The numerical model, inspired by [206], is so far written in Python language thanks to its fully formed built-in and pre-defined library functions. For faster simulation speed, ~ 10 times, we are planning the substitution of the C language. This model is restricted to one-dimensional dynamics, which is good enough for analyzing the velocity evolution of one single atom under a position-dependent scattering force. In the program, a function returns the effective force felt by the atom at each position by specifying the initial atom velocity and the magnetic field along the propagating direction, i.e., the z-direction; the atomic trajectories originate at 15 cm from the 2D-MOT center, i.e., at the oven output; the atom position and velocity along the 1D-trajectory are calculated using a 4th-order Runge-Kutta method [207].

Repeating this calculation for the different atomic velocities generated by the oven, we can calculate how the ZS modify the initial Maxwell-Boltzmann distribution once the atoms reach the 2D-MOT region. Integrating the modified probability density over the velocity range less than the capture velocity of the 2D-MOT, we obtain the fraction of the atomic flux emitted by the oven that the 2D-MOT can capture.

Initial velocity probability density of atoms Hot strontium atoms, considered as an idealized gas, are ejected from the oven with different velocity classes [208]. We assume the

velocities follow the distribution as the function

$$f(v)dv = \left(\frac{m}{2\pi kT}\right)^{3/2} 4\pi v^2 e^{-mv^2/2kT} dv, \quad (4.10)$$

where m is the particle mass and T is the temperature of the oven. Compared with the Maxwell-Boltzmann distribution for particles moving only along one direction, Eq. 4.10 is an integration of probability density over the solid angle. Since the probability to find one particle with any velocity equals to unity, the velocity probability density has a unit of s/m.

Scattering force As highlighted in [172], there are two regions (1 and 2) that can be used for the ZS (see Fig. 4.2). For convenience, we define the ZS1 (ZS2) as the scheme that uses the magnetic field in region 1 (2). The dual-frequency ZS takes advantage of the full B-field profile, both regions, 1 and 2. Therefore, the atoms are decelerated with two forces along with one geometry, given by,

$$\frac{\vec{F}}{m} = \frac{\hbar}{m} \frac{\Gamma}{2} \left(\frac{\vec{k}_1 s_1}{1 + s_1 + 4\Delta_{\text{eff1}}^2/\Gamma^2} + \frac{\vec{k}_2 s_2}{1 + s_2 + 4\Delta_{\text{eff2}}^2/\Gamma^2} \right), \quad (4.11)$$

where

$$\Delta_{\text{eff1}} = (\omega_{L1} - \omega_0) - \vec{k}_1 \vec{v} + \frac{\mu_B g_J m_J |\vec{B}_1|}{\hbar}, \quad (m_J = -1), \quad (4.12)$$

and

$$\Delta_{\text{eff2}} = (\omega_{L2} - \omega_0) - \vec{k}_2 \vec{v} + \frac{\mu_B g_J m_J |\vec{B}_2|}{\hbar}, \quad (m_J = +1). \quad (4.13)$$

The red-detuned light beam in the ZS1 ($\vec{k}_1, s_1, \omega_{L1}$) and ZS2 ($\vec{k}_2, s_2, \omega_{L2}$) exert their action in the region 1 (\vec{B}_1) and 2 (\vec{B}_2) respectively. Two Zeeman slowing beams are shown along the directions where the atoms propagate from the oven toward the 2D-MOT center, and in the counter-propagating direction, therefore the wavevectors \vec{k}_1 and \vec{k}_2 have the same sign.

The Motion of atoms To obtain the infinitesimal variation of the atom velocity at the next position (v_{n+1}) from the current velocity (v_n) and its derivative, we implement the classical 4th-order Runge-Kutta (see Fig. 4.4). The Runge-Kutta method treats every step within successive steps along the trajectory in an identical way. The iterations stop if the atom reaches specific boundary conditions, in our case, the limit of the 2D-MOT capture region, i.e., 5 mm from the vanishing center of the field configuration, and the oven position.

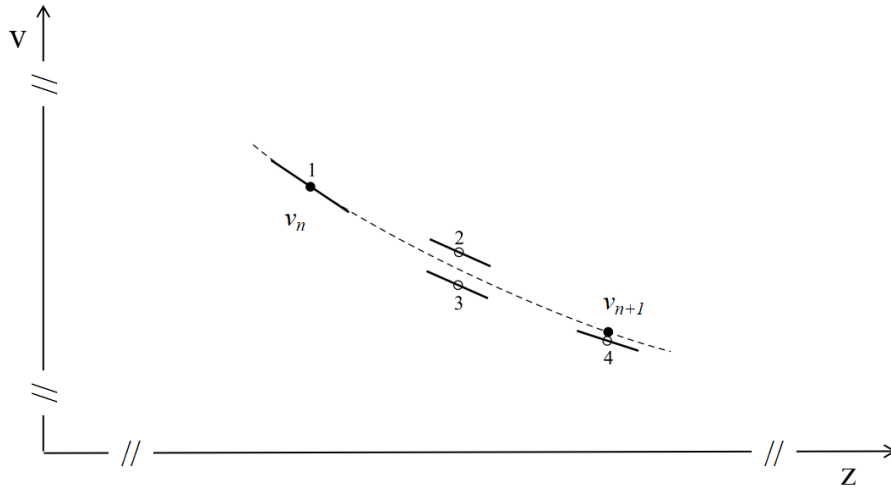


Figure 4.4: One step in 4th-order Runge-Kutta method, modified based on [209]. The solid circles represent the final velocity value, and the open circles represent the temporary ones. The temporary velocity values are discarded once their derivatives are calculated and used. Notably, one open circle is overlapped with the solid one at the initial point.

The modified velocity probability density of atoms The Zeeman slowing beam pushes the high-velocity atoms to lower velocities with the well-chosen frequency detuning and intensity. It results that a fraction of the high-velocity classes are depleted velocities of atoms concentrated at a lower range with a single sharp peak.

The atomic flux The atomic flux generated by the atomic source is estimated by summing over the velocities, with absolute values less than the 2D-MOT capture velocity, following the velocity probability density profile at the input of the 2D-MOT. As we are only interested in enhancing the implementation of the ZS(s), the capture efficiency of the atomic source is characterized by the fraction of atoms trapped into the 2D-MOT.

Discussions In this numerical model, the laser detuning (Δ), saturation parameter (s), magnetic field amplitude (B), atomic mass (m), atomic transition wavenumber (k), and natural linewidth (Γ) can be customized. This flexibility makes the model easy to be extended to other atomic species.

To further increase the flux of the atomic source, one could combine our dual-frequency ZS with the recently demonstrated sideband-enhanced 2D-MOT.

The rest of this chapter focuses on the 1D dynamics of atoms along the propagation trajectory, their modified velocity distributions, and the corresponding generated atom flux from the 2D-MOT in both single-frequency and dual-frequency ZS.

4.3.2 The single-frequency Zeeman slower

4.3.2.1 The atomic trajectories

The Sr-atoms oven is at the spatial coordinates $z = -15$ cm, setting the position of the 2D-MOT center to be at the origin ($z = 0$ cm). The initial velocities of atoms (v_0) are ranged over a large span ($0 \leq v_0 \leq 500$ m/s) with a step of 10 m/s. The applied magnetic field follows the same profile shown in Fig. 4.2, and other inputs parameters are listed in Tab. 4.6.

Parameters	Symbol	Unit	ZS1	ZS2
Atomic mass	m	[kg]	1.46×10^{-25}	
Wavenumber	k	[1/m]	$2\pi/461 \times 10^{-9}$	
Natural Linewidth	Γ	[Hz]	30.5×10^6	
Saturation parameter	s		0.4	
Magnetic field	B	[T]	$ B_1(z) $	$ B_2(z) $
Frequency detuning	Δ	[Γ]	-13	-1.5

Table 4.6: List of the applied parameters in the numerical model for the single-frequency Zeeman slower.

The capture velocity of the 2D-MOT is set as 50 m/s. It represents the target velocity for the atomic flux produced by the ZS. In the ZS1 (see Fig. 4.5), atoms with initial velocities from 40 m/s to 210 m/s can be captured by 2D-MOT. The inset of Fig. 4.7 (a) provides the same information in velocity space. Here, the atomic population has a higher probability at higher velocities. Fig. 4.6 indicates that the atoms in the ZS2 with initial velocities less than 80 m/s do not even reach the 2D-MOT region; the atoms with initial velocities higher than 140 m/s passes through the 2D-MOT region, as their final velocities are higher than the capture velocity of 2D-MOT.

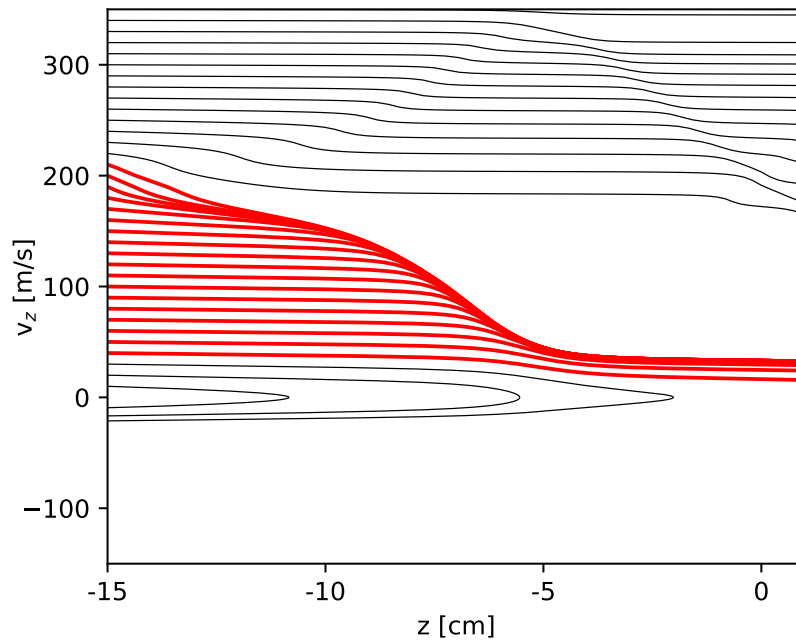


Figure 4.5: The trajectories $v(z)$ of atoms with the ZS1. The red curves represent the trajectories of the atoms ending up to be captured by the 2D-MOT; the grey ones are reflected back in the direction of the oven or that are passing through the 2D-MOT region with too-high velocities to be captured.

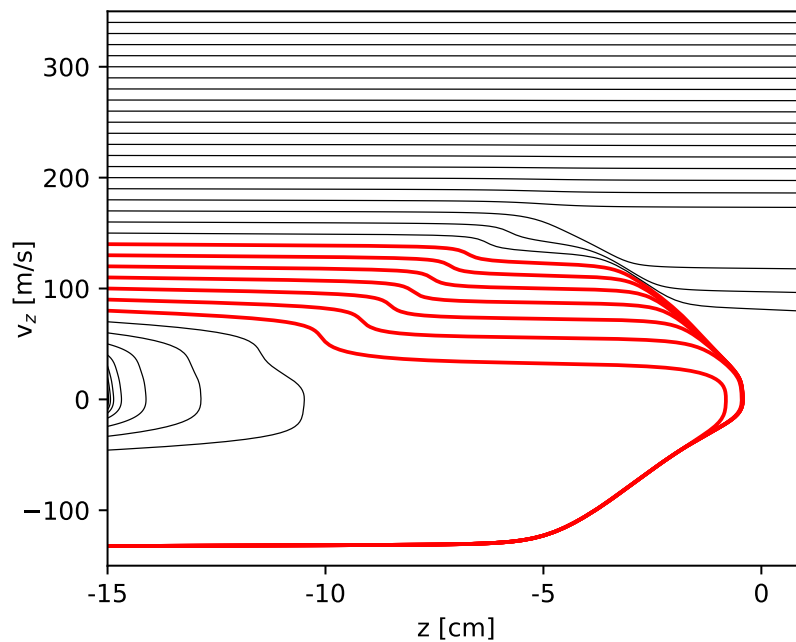


Figure 4.6: The trajectories $v(z)$ of atoms with the ZS2. The red curves represent the trajectories of the atoms ending up to be captured by the 2D-MOT; the grey ones are those that are reflected back into the direction of the oven or that are passing through the 2D-MOT region with too high velocities to be captured.

4.3.2.2 The modified velocity distribution

The Sr-atoms oven is heated up to 585 °C, with a RMS velocity of ~ 500 m/s. The main effect of the Zeeman slowing beam can be seen as a modification of the initial velocity distribution (see Fig. 4.7).

4.3.2.3 The atomic flux

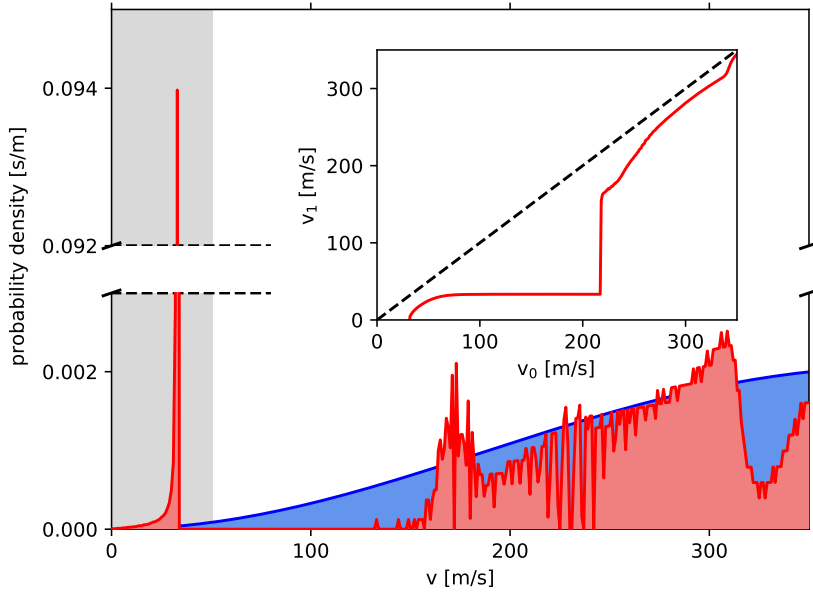
By integrating the atomic probability density over the velocity range below the 2D-MOT capture velocity, we obtain the flux of atoms captured into the 2D-MOT. The integrals calculated for both the single-frequency ZS1 and ZS2 at their optimal working conditions once the laser intensity is fixed to $s = 0.4$, i.e. the value we can now reach in our laboratory. This process results in a captured atomic fraction of 19.8% and 5.4% respectively and is indicated as blue points in Fig. 4.8. For comparison, only 1.4% of the atoms ejected by the oven are captured inside the 2D-MOT alone while no ZS is active.

To obtain the optimal atomic flux, we scan the parameter space (laser intensity and detuning frequency) of the Zeeman slowing beam through a numerical simulation (see Fig. 4.8). The capture efficiency of the atomic source is characterized by the fraction of the atomic flux emitted from the oven at 585 °C. The maximally achievable atomic flux in the ZS1 is $\sim 35\%$ ($9 < s_1 < 60$ and $-18\Gamma < \Delta_1 < -23\Gamma$). It is three times higher than in the ZS2 ($1 < s_2 < 9$ and $-4\Gamma < \Delta_2 < -7.5\Gamma$). We conclude that in the configuration of the single-frequency ZS, with the same beam intensity, the ZS1 is more efficient and captures a higher fraction of the atomic flux than that in the ZS2.

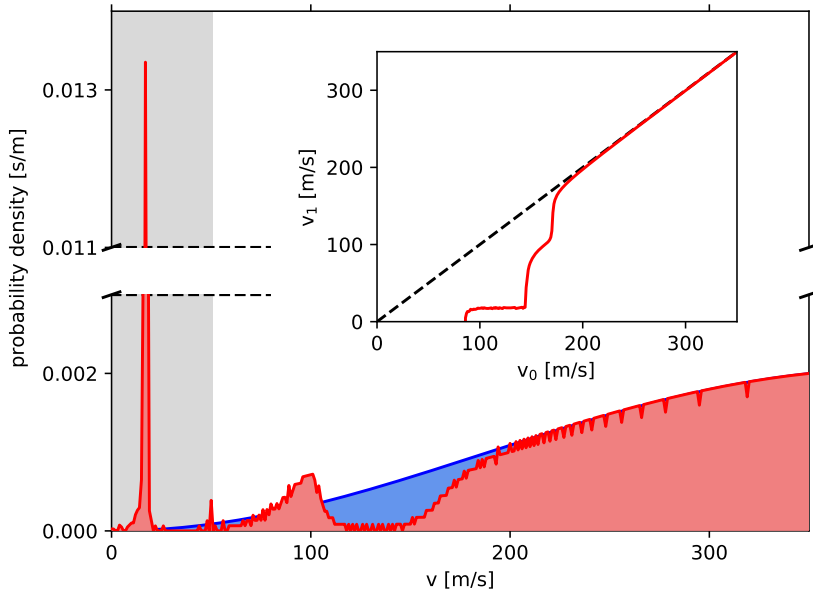
4.3.3 The dual-frequency Zeeman slower

4.3.3.1 The atomic trajectories

Our advanced version of the ZS uses the two available slopes of the B-field (the region in 1 and 2) in a combined fashion to increase the atom flux. In the first region, atoms are only slowed down as much as necessary to be later slowed down further within the capture velocity of the 2D-MOT located into the second region. This configuration requires two



a



b

Figure 4.7: (a) The blue curve represents the Maxwell-Boltzmann distribution for an atomic sample at 585 °C, and the red curve represents the modified velocity distribution due to the action of the ZS1. Inset: the atomic velocity at the 2D-MOT versus the initial velocity at the oven. (b) The blue curve represents the Maxwell-Boltzmann distribution for an atomic sample at 585 °C, and the red curve represents the modified velocity distribution due to the action of the ZS2. Inset: the atomic velocity at the 2D-MOT versus the initial velocity at the oven.

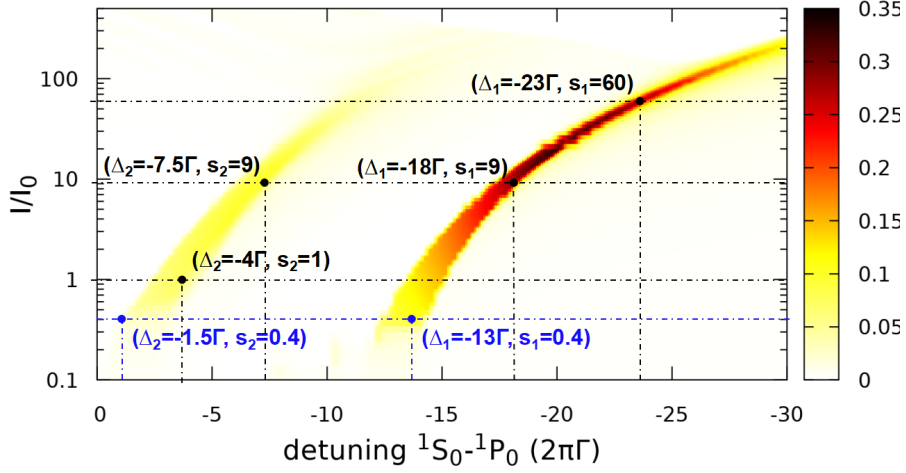


Figure 4.8: Fraction of the atomic flux (in color code) captured inside the 2D-MOT with one single-frequency Zeeman slowing beam.

combined frequencies in the light implementing the Zeeman slower. By applying both, the ZS1 and the ZS2 simultaneously, and relying on the listed parameters reported in Tab. 4.6, a dual-frequency ZS can capture atoms with velocities from 90 to 240 m/s (see Fig. 4.9).

4.3.3.2 The modified velocity distribution

Fig. 4.10 shows how the dual-frequency ZS modify the Maxwell-Boltzmann (MB) velocity distribution.

4.3.3.3 The atomic flux

The main idea of the dual-frequency ZS is to use the ZS2 in the standard way, i.e., to slow down atoms at lower velocities to achieve their capture into the 2D-MOT. In addition, the ZS1 slows down just enough, the higher-velocity classes to have an effective action of the ZS2 on them. With the parameters of the ZS2 fixed to $s_2 = 0.4$ and $\Delta_{ZS2} = -1.5\Gamma_{\text{blue}}$, we optimize the atomic flux that can be captured inside the 2D-MOT by scanning the parameters of ZS2. We obtain the Fig. 4.11(a). The maximum fraction of the atomic flux achieves $\sim 50\%$ ($10 < s_1 < 40$ and $-23\Gamma < \Delta_1 < -25\Gamma$), and the atomic trajectory and velocity distribution are plotted in Fig. 4.12 and 4.13, respectively.

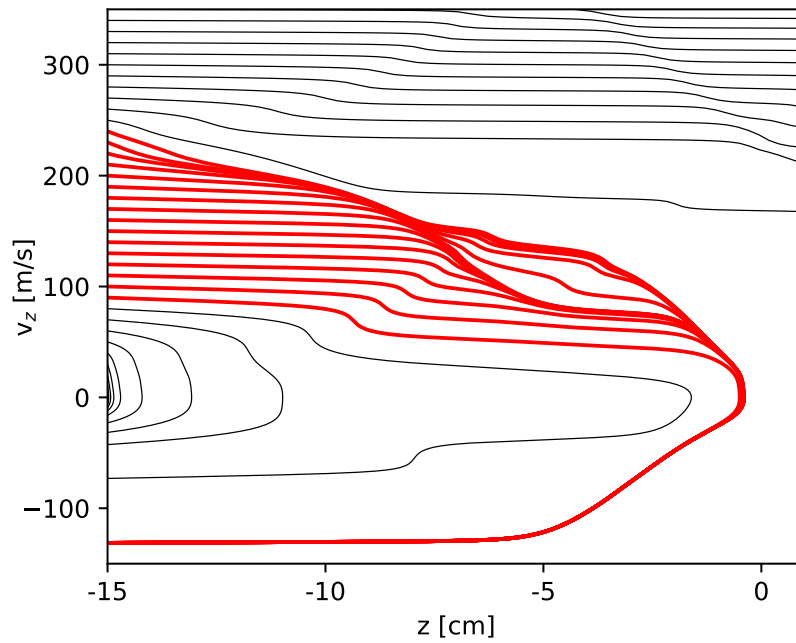


Figure 4.9: The trajectories $v(z)$ of atoms with the dual-frequency Zeeman slower. The red curves represent the trajectories of the atoms ending up to be captured by the 2D-MOT; the grey ones are reflected back into the direction of the oven or that are passing through the 2D-MOT region with too high velocities to be captured.

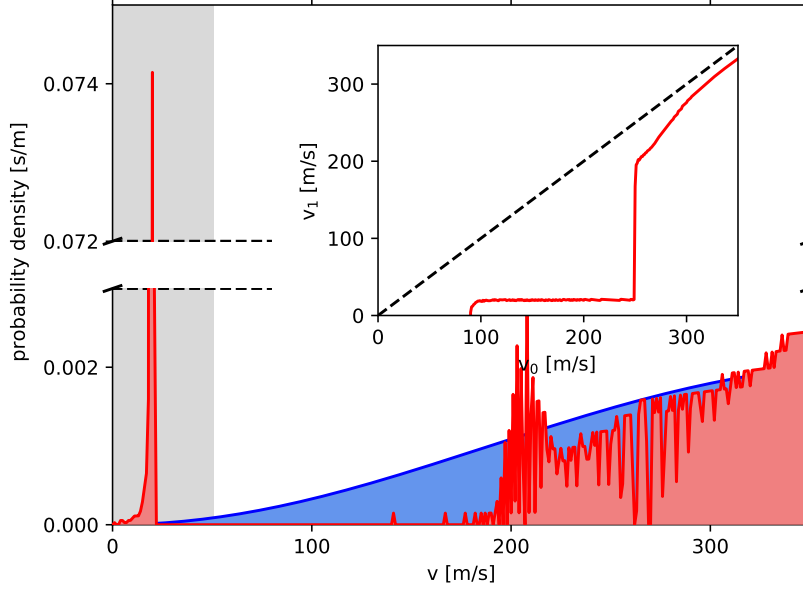


Figure 4.10: The blue curve represents the Maxwell-Boltzmann distribution at 585 °C, and the red curve represents the velocity distribution modified by the action of a dual-frequency Zeeman slowing beam.

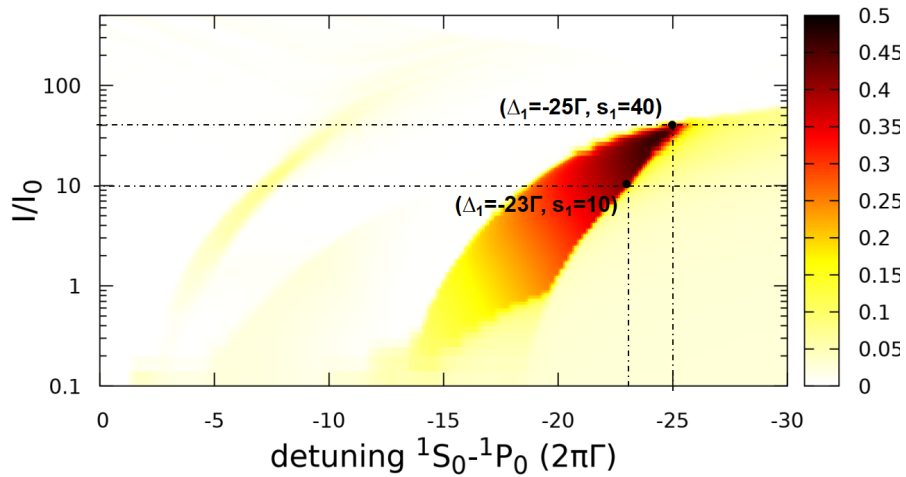


Figure 4.11: Fraction, in color code, of the atoms ejected by the oven captured in the 2D-MOT with dual-frequency Zeeman slowing beams. The ZS2 is operated at $s_2 = 0.4$ and $\Delta_{ZS2} = -1.5\Gamma_{\text{blue}}$. Inset: the atomic velocity at the 2D-MOT versus the initial velocity at the oven; the modification is due to the action of the dual-frequency ZS.

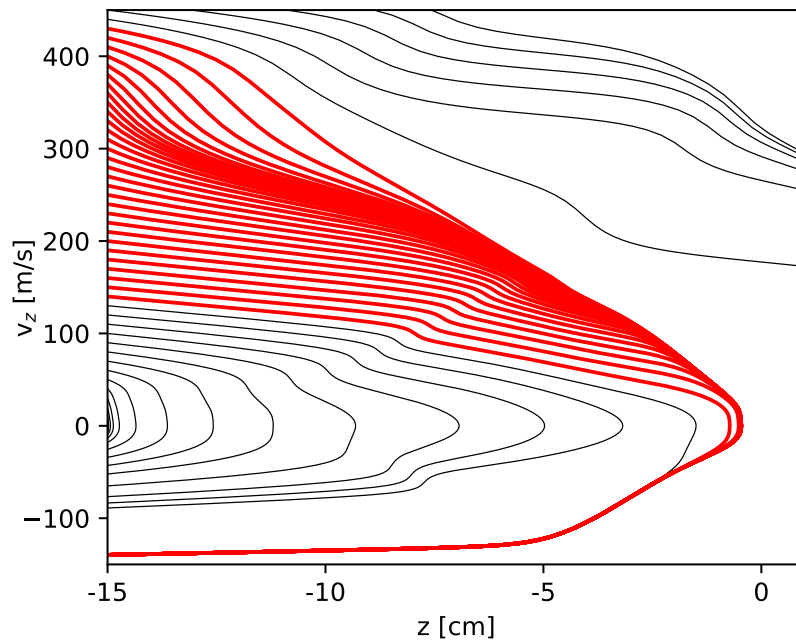


Figure 4.12: The trajectories $v(z)$ of atoms with the optimized dual-frequency Zeeman slower. The red curves represent the trajectories of the atoms ending up to be captured by the 2D-MOT; the grey ones are those that are reflected back into the direction of the oven or that are passing through the 2D-MOT region with too high velocities to be captured.

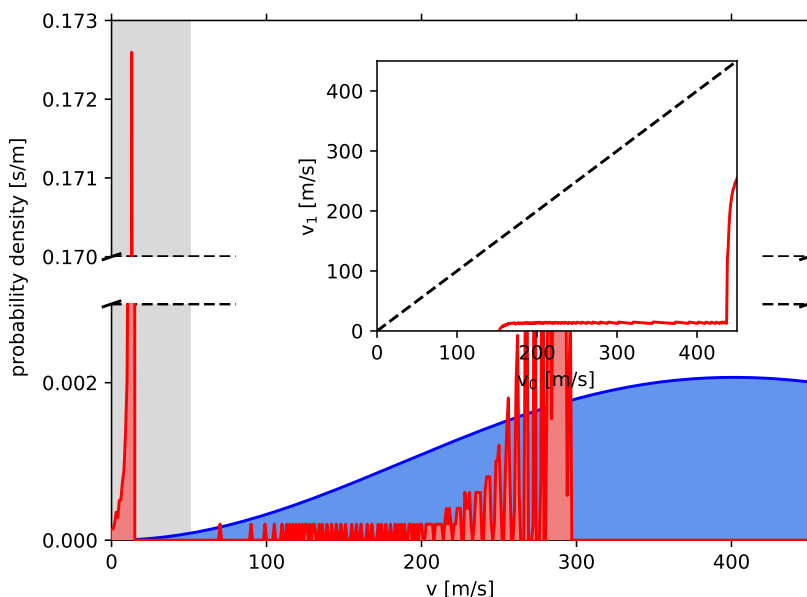


Figure 4.13: The blue curve represents the Maxwell-Boltzmann distribution at 585 °C, and the red curve represents the velocity distribution modified by the action of an optimized dual-frequency Zeeman slowing beam.

4.3.4 The enhancement of atomic flux

To evaluate the enhancement of the atomic flux between the single-frequency and dual-frequency ZS, we fix the intensities of the two beams we used to slow the atoms down to achieve a saturation intensity of 0.4. We scan their detuning for the $^1S_0 - ^1P_1$ transition. All the ZS saturation parameters are set to be 0.4, then scan their red-detuned frequencies. Fig. 4.14 demonstrates that the ZS1 can capture 11.5% of the atoms ejected from the oven, and the ZS2 can only capture 2.5%. The dual-frequency ZS makes the full use of the whole profile of the B-field, and well-tuned frequency shifts of two ZSs realize that the atoms with fast-velocity classes, contributing to higher atomic flux, are firstly slowed down by the ZS1 then further cooled down by the ZS2, thus the capture efficiency increases by 15%.

Limited by the experimental setup, we demonstrate the efficiency of the dual-frequency ZS scheme by measuring a few critical points, and the related results are reported in Tab. 4.7. The single-frequency ZS can enhance the atomic flux by ~ 2.5 ; the dual-frequency ZS can improve the atomic flux by more than six times. The enhancement factor only refers to

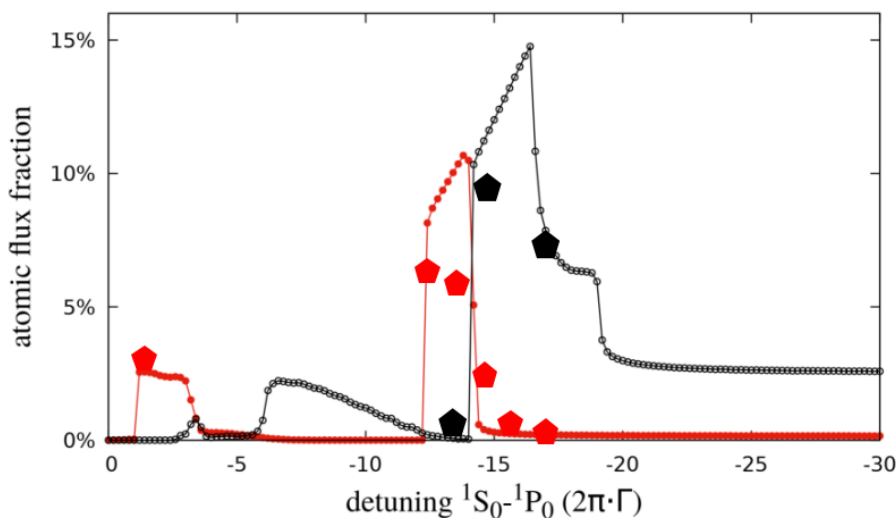


Figure 4.14: This plot reports the atomic flux captured inside the 2D-MOT with a single Zeeman slowing frequency (red curve; the single beam detuning has been changed) and both Zeeman slowing frequencies (black curve; the second beam detuning has been changed, whereas the first remained fixed to a value of -1.5Γ). With the latter, we identify the regions of interest.

the atomic source with a 2D-MOT. Notably, the power for the ZS2 is about 45 mW, and the power for the ZS1 is about 100 mW. After normalization, the experimental data, in diamond symbol, is compared with the simulation result in Fig. 4.14.

$\Delta_{ZS1} \setminus \Delta_{ZS2}$	–	-1.50Γ
–	–	2.67
-12.98Γ	2.50	–
-13.63Γ	2.35	–
-14.61Γ	2.00	6.67
-15.60Γ	1.20	–
-16.25Γ	0.80	3.33

Table 4.7: The atomic flux enhancement with a single-frequency ZS or a double-frequency ZS.

We are now modifying the laser systems to have the possibility to do more delicate scanning of the parameters, including the frequency detuning and/or the intensity of both Zeeman slowing beams.

Chapter 5

Fast control of atom-light interaction via light shift in a narrow-linewidth cavity

Narrow-linewidth cavities are dominant components in fundamental physics [102], metrology [210]. They underpin the ongoing progress about the study of light-matter interaction [211, 212]. For example, the cavity-assisted atom interferometry is increasingly adopted to prepare highly non-classical atomic states [64, 213], implement large momentum separation [61, 214, 63], structure multi-pulse geometries [215], and produce long-hold-time optical lattices [57]. It comes from the high-quality laser beam profile inside the optical cavities. The optical cavity quality factor is proportional to the cavity mode linewidth. However, the measurement possibilities with cavity-assisted atom interferometry can not be expanded by naively narrowing the cavity linewidth by enhancing cavity finesse or/and increasing the cavity length, since narrow-linewidth cavity exploited in cavity-assisted atom interferometry sets fundamental limitation with its finite response time (see Sec. 5.1) [216]. To overcome this issue, we develop a general method which involves an auxiliary control process and applies external fields such as electromagnetic field (see Sec. 5.2) [217]. This field is used to control the atom-light interaction via auxiliary processes. The auxiliary method can apply to many different atomic species, both in trapped and free-fall configurations, controlling the internal and/or external atomic degrees of freedom.

Contents

5.1	Limitation in narrow-linewidth-cavity-assisted atom interferometry	121
5.2	The fast control of the atom-light interaction via a light shift	123
5.2.1	The AC Stark shift	131
5.2.2	The scattering rate	135
5.2.3	Trade-off between energy shift and scattering rate	139
5.2.4	The time interaction between atoms and the light	142
5.2.5	The phase error	144

5.1 Limitation in narrow-linewidth-cavity-assisted atom interferometry

The sensitivity of atom interferometer scales with the phase difference between matter waves traveling along two separate trajectories. Increasing momentum separation between two wavefunctions hence enhances the sensitivity of such devices. For most frequently used two-photon transitions, a large momentum transfer (LMT) interferometer requires the coherent scatter of $2n$ photons from the interferometric laser beam wave number (k), and then the momentum transfer is $2\hbar k$. High laser power is required here to implement LMT [49]. By adopting an optical cavity, the incident laser beam is enhanced by a factor of

$$\left| \frac{E_{circ}}{E_{inc}} \right| = \left| \frac{t_1}{1 - r_1 r_2 e^{2ikL}} \right|, \quad (5.1)$$

where c is the speed of light, L is the cavity length, r relates to coatings of the end mirrors, and t are amplitude reflectivity and transmission, respectively. Optical cavities with high-reflectivity coatings allow very high momentum transfer beamsplitters [218, 219, 220, 221, 222]. Besides, it filters out unwanted spatial cavity mode to a large extent by increasing

effective path length between the end mirrors

$$\mathcal{F} = \frac{\pi}{2 \arcsin\left(\frac{1-r_1r_2}{2\sqrt{r_1r_2}}\right)} \sim \frac{\pi\sqrt{r_1r_2}}{1-r_1r_2}, \quad (5.2)$$

where the finesse \mathcal{F} quantifies the times of a photon bouncing inside the cavity before leaking out or being absorbed; in addition, optical cavities provide self-aligned interferometer geometries by coupling cold atomic cloud into the cavity transverse mode.

In gravitational wave detectors based on atom interferometry, long-baselines L are instead sought to improve the device sensitivity [34],

$$\delta\phi_{tot} \propto hL\omega^2T^2, \quad (5.3)$$

where $\delta\phi_{tot}$ is the total differential phase shift. Accordingly, for the cavity-assisted atom interferometry, long-length cavities are preferred [223]. Furthermore, the proper size of the cavity-enhanced interferometric beam (IB) increases with the cavity length, where a larger beam size accommodates better the size of the atomic cloud as it thermally expands during the whole measurement.

For these reasons, high finesse \mathcal{F} and long-baseline L are desired quantities in the cavity-assisted atom interferometry. Their combination has the effect of reducing the cavity linewidth,

$$\Delta\nu = c/(2nL\mathcal{F}). \quad (5.4)$$

Hence, increasing its response time $\tau_c = 1/\Delta\nu$, where c is the speed of light in vacuum, and n is the index of refraction inside the cavity. However, despite the promise of improved sensor performance, it has been pointed out in [216] that an upper limitation exists for $\Delta\nu$. The coherent manipulation in atom interferometry relies on short (typically tens of μs long) light pulses to split, deflect and recombine the atoms, hence $\Delta\nu$ cannot be much higher than 10 kHz. Otherwise, laser pulses $G(t)$ used to manipulate the atomic wavefunction coherently, undergo severe deformation, which affects the evolution of atomic states by

$$i\frac{dg_n}{dt} = (\omega_r n^2 + \bar{\Omega}G(t))g_n + \frac{1}{2}\Omega(g_{n+2} + g_{n-2}), \quad (5.5)$$

g_n is the amplitude of the state with momentum $n\hbar k$, $\bar{\Omega}$ is the peak amplitude of two-photon Rabi frequency, $G(t)$ is the envelope function of cavity field intensity. Deformed field intensity also worsens the effective optical power enhancement and induces inefficient large-

momentum transfer.

In short, the inherent frequency response of the cavity sets a physical limit to the product $L\mathcal{F}$ and forbids adopting narrow-linewidth resonators for manipulating matter waves. An underground extended baseline atom interferometer to study gravity at a large scale (MIGA project) [8] proposes to exploit a 200-m-long cavity with a finesse of 100, which is beyond the bandwidth limit for both, maximum suppression of HG_{01} and the corresponding beam waist (see Fig. 10 in [216]). To circumvent the limitation imposed by the finite time response, we propose an alternative scheme to manipulate the atomic wavefunction in a narrow-linewidth cavity coherently. Such scheme is based on the atom-light interaction being pulsed not by changing the intensity of the intracavity standing wave, but by modulating the coupling between the intracavity light and the atoms, using an auxiliary process. The light to manipulate the atomic wave function is always injected and locked into the optical resonator; its effective action is controlled through the light shift engineering of the atomic levels and magnetic field-induced transition. These proposals will open new possibilities in cavity-assisted atom interferometry and the preparation of highly non-classical atomic states.

5.2 The fast control of the atom-light interaction via a light shift

We consider as a representative example, the ^{87}Sr atoms in considerable abundance, while they are launched in free-fall, coherently manipulated via hyperfine-induced $E1$ one-photon clock transition, and repeatedly passing through a horizontal cavity (see Fig. 5.1). Our scheme can easily be extended to other configurations relying on cavity-enhanced light-pulses to prepare or to probe the atomic state. The coherent manipulations are performed at each passage of the atoms in the cavity by pulses shorter than the transit interval in the interferometric beam. We consider a 4-pulse-sequence interferometer [224] based on the double-diffraction scheme [225] and with a time separation $T - 2T - T$ ($T = 1/4$ s will be assumed later for numerical evaluations). This geometry relies on a single horizontal IB thanks to a vertical reflection at the middle of the sequence, and other similar configurations could

be considered [226]. At $t = 0$ s the atoms are in A (Fig. 5.1), in state $|2\rangle$ with a velocity $(v_x, v_z) = (0, -gT/2)$, where g is the local acceleration of gravity. Here, they interact with a first splitting pulse. The atomic wavefunction is divided into two components in the state $|1\rangle$ with opposite horizontal velocities $v_x = \pm v_r$, where $v_r = \hbar k/m$ is the recoil velocity. At $t = T/2$, the atoms reach the apogees of their trajectories at the height of $-gT^2/8$ above the IB. At $t = T$, the atoms are again in the IB where a mirror pulse reverses their horizontal velocities without changing their internal states. At $t = 2T$, the two parts of the wavefunction cross in D of Fig. 5.1, with a vertical velocity $v_z = 3gT/2$; they are vertically reflected by optical means [227] and complete the second and symmetric half of the interferometric sequence. Note that the atoms are always in the same internal state during the free evolution, thus canceling many systematic effects. Thus, the resonance condition for the IB is the same for all the pulses.

The narrow linewidth cavity is locked to the linearly polarized IB; the beam intensity is then increased and the spurious spatial mode filtered out. The intracavity enhanced intensity of the interferometric beam is chosen to have a Rabi frequency Ω_R of $2\pi \times 5$ kHz. For a double diffraction, the split and mirror pulses must have a length of $\tau_s = \pi/(\sqrt{2}\Omega_R)$ and $\tau_m = 2\tau_s$ respectively [225] so we obtain $\tau_s \simeq 70\mu\text{s}$ and $\tau_m \simeq 140\mu\text{s}$. The pulses do not couple to spurious momentum states as long as $\tau_m\omega_r \gg 1$ (see Sec. 5.2.4), where ω_r is the recoil frequency, i.e., about 59 kHz for the ^{87}Sr atom.

As aforementioned, we focus on alkali–earth atoms, more specifically ^{87}Sr atoms, where the interferometric beam is tuned on the narrow transition at 698 nm defined by the levels $|1\rangle \equiv ^1\text{S}_0$ and $|2\rangle \equiv ^3\text{P}_0$ [228] (see Fig. 5.2), to implement the coherent manipulation scheme proposed in [229], and recently demonstrated in [230] for ^{88}Sr atoms. An additional Dressing Beam (DB) differentially shifts the levels $|1\rangle$ and $|2\rangle$, breaking the resonance condition for the IB and thus, turning off the coherent action of the interferometric beam when present. Modulating the intensity of the DB will allow switching the resonance with the IB ON and OFF. We can also consider other kinds of atoms and manipulation schemes. For example, in Raman transitions on alkali atoms, we could use a laser on the $D2$ transition like the DB, which creates a light shift with opposite signs on the two-hyperfine levels connected with the Raman transition.

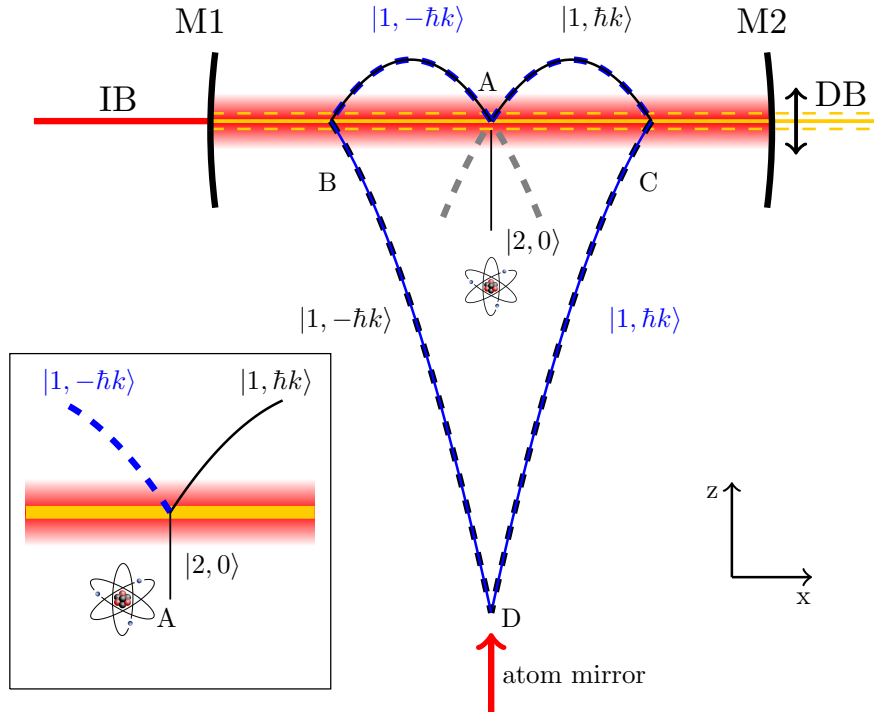


Figure 5.1: Schematic of the proposed experimental setup not to scale: the atomic ensemble, initially in the state $|2\rangle$ and moving in the z -direction. It crosses the cavity-enhanced IB and splits in region A (see inset) into two paths with opposite horizontal velocity $\pm v_r$. The two parts of the wavefunction are horizontally reflected with a mirror pulse in the regions B and C; in D, their vertical velocity is inverted, and after a second mirror pulse, again in C and B, they are recombined in A with the last split pulse. The two trajectories at the output of the interferometer are shown in gray. The horizontal dressing beam (DB) (yellow), not resonant with the cavity, is shone on the atoms and vertically follows their motion to have an optimal overlap. M1, M2: cavity mirrors; v_r , DB, and the atom labeling are defined in the main text.

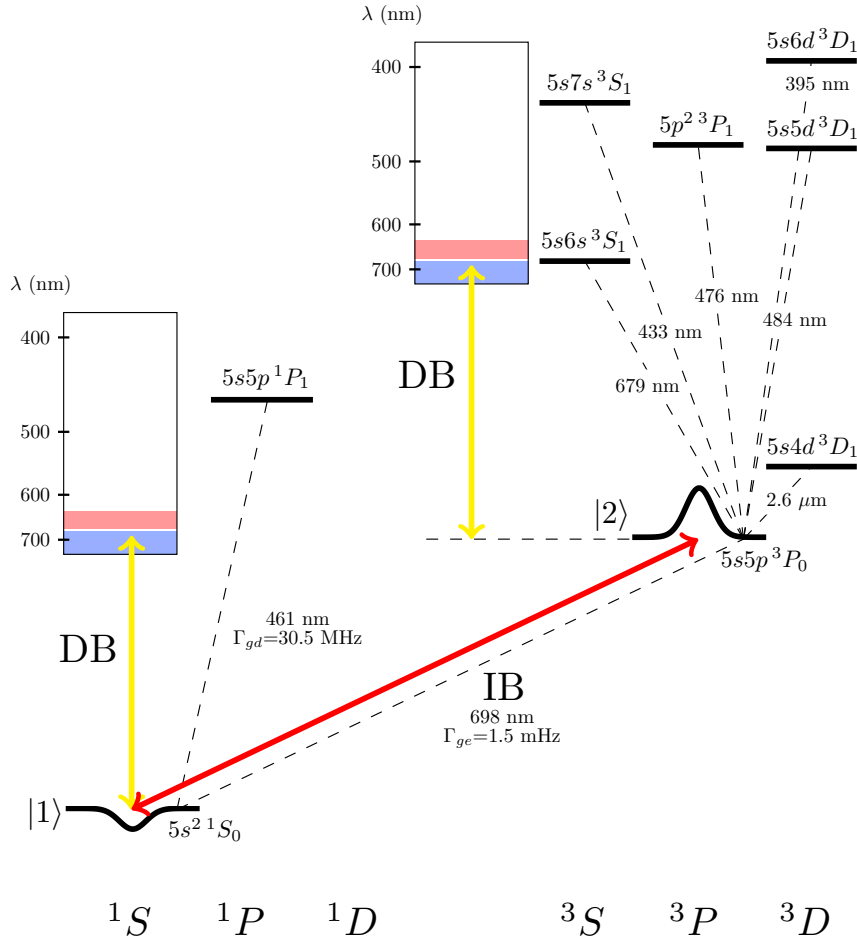


Figure 5.2: Diagram with the relevant levels for ^{87}Sr atoms. The red arrow shows that the IB resonant to the $|1\rangle \rightarrow |2\rangle$ transition at 698 nm adopted for the coherent manipulation of matter waves; the yellow arrows mark the DB used to shift the two levels $|1\rangle$ and $|2\rangle$. The action of the DB is considered when varying its wavelength over the range [380–740] nm, indicated by the vertical bars referenced to the two levels $|1\rangle$ and $|2\rangle$. The narrow red (blue) bands indicate the spectral interval where the DB with parallel (perpendicular) polarization constitutes an effective switch for the coherent action of the IB, by light shifting in a differential fashion, the clock levels $|1\rangle, |2\rangle$. The bands have been obtained as defined in Fig. 5.3. The level structure has been presented in [231, 232].

For numerical applications, we consider a narrow-linewidth cavity that can fit into a conventional laboratory: the cavity parameters are set to be $L = 2$ m and $\mathcal{F} = 10^5$ ($\Delta\nu = 750$ Hz). In this configuration, the fast amplitude modulation of the IB to implement the interferometric pulses would generate strong pulse deformations in the cavity, which is detrimental to the sought of the power enhancement [216].

The ^{87}Sr atoms are considered at very low temperatures, prepared in the $|2\rangle$ state, and launched vertically to reach point A. The spatial extension of the atomic cloud is assumed to be $< 100 \mu\text{m}$ during all the duration of the interferometric sequence. This will require adopting delta-kick collimation techniques [233, 234] to prepare the atomic source. The cavity waist is set to be 1 mm, to obtain a rather homogeneous manipulation of the atomic ensemble on its axis, even when taking into account the vertical displacement of the cloud during the manipulation. To obtain the required Rabi frequency when driving the clock transition ($|1\rangle - |2\rangle$) with linewidth $\Gamma = 1.5$ mHz and wavelength $\lambda = 698$ nm,

$$\Omega_{\text{R}} = \Gamma \sqrt{\frac{I}{2I_{\text{sat}}}}, \quad (5.6)$$

where $I_{\text{sat}} = 0.41$ pW/cm² is saturation intensity for clock transition of ^{87}Sr , the intracavity power of the IB must be $P_0 \simeq 286$ mW [235], which means an input power $P_{\text{in}} \simeq 390 \mu\text{W}$, if two lossless mirrors with equal reflectivity are considered for the cavity.

The atomic interaction with the IB is controlled with the DB (in yellow in Fig. 5.1 and Fig. 5.2), whose role is to induce an additional energy shift $\Delta\omega_{21}$ on the $|1\rangle \rightarrow |2\rangle$ transition, to remove the resonance condition for the cavity enhanced IB. This solution has also the technical advantage of avoiding to have to lock again the laser generating the IB at each pulse to the cavity. To calculate $\Delta\omega_{21}$ when varying the DB wavelength over the range $380 \text{ nm} < \lambda < 740 \text{ nm}$ we considered the relevant levels shown in Fig. 5.2, and the transition parameters reported in [232, 231].

A single DB along the cavity axis (see Fig. 5.1) can dress the atoms along both interferometric trajectories during their passages inside the IB; to maintain a high bandwidth for the variation of the beam intensity and to allow its vertical translation to track the atomic motion the cavity mirrors must be transparent at the DB wavelength, as described below. A DC-applied magnetic field B is added along with the vertical direction to define the quantiza-

tion axis. The DB is linearly polarized, either parallel or perpendicular to the B -field. Details are discussed in the Sec. 5.2.1.

The main unwanted side effect of the DB on the atomic system (see Sec. 5.2.2), is the scattering of photons at a rate Γ_{sc} on the two levels of interest, which represents a decoherence channel reducing the oscillation amplitude of the interferometric fringe with no impact on the interferometric phase. Other effects, like the DB wavefront aberrations, are not considered here; their impact, however, is highly reduced in the differential configuration provided by a gravity-gradiometer. By dividing $\Delta\omega_{21}$ by Γ_{sc} we obtain a normalized light shift $\Xi(\lambda)$ (see Sec. 5.2.3), plotted in Fig. 5.3 for a DB polarized along the magnetic field (continuous curve) and orthogonal to it (dashed curve).

To optimize the DB parameters, we start by arbitrarily fixing the maximum probability to scatter a photon from the DB during the whole interferometric sequence to 3%, which means a subsequent reduction of the interferometer contrast of the same order. At constant DB detuning and power, the contrast reduction is only set by the total amount of time the atoms spend in the DB and not by the number of pulses during the sequence. Suppose the effect is not negligible, for example, in a configuration with the atoms falling in the IB. In that case, one could opt for a scattering-free scheme, for example, by using magnetic field induced spectroscopy to activate the coherent action on bosonic isotopes [236]. Here, considering the atomic vertical speed at each passage in the cavity ($-gT/2 \sim 1.25$ m/s with our choice of T), it means a maximum nominal scattering rate $\Gamma_{\text{sc}} \sim 1$ Hz at the center of the DB. The value is obtained by considering the DB always centered on the atomic cloud during the four crossings of the IB and over the whole vertical spatial interval clipped by the cavity, i.e., about ten times its waist.

The second parameter to set is the minimum differential light shift required to effectively suppress the Rabi oscillation between states $|1\rangle$ and $|2\rangle$. To this aim, the generalized Rabi frequency

$$\tilde{\Omega}_R = (\Omega_R^2 + \Delta\omega_{12}^2)^{1/2}, \quad (5.7)$$

must be $\gg \Omega_R$ when the DB is on, and the RMS uncertainty of the interferometric phase due

to the residual Rabi oscillation is equal to:

$$\delta\phi = \frac{\Omega_R}{\sqrt{2} \Delta\omega_{21}}, \quad (5.8)$$

if $\Delta\omega_{21} \gg \Omega_R$. The phase uncertainty is calculated for a balanced atomic state (see Sec. 5.2.5); a state unbalance $\delta \equiv N_1 - N_2$ determines (i) a reduction factor $\sqrt{1 - \delta^2}$ on the phase uncertainty, and (ii) a systematic phase shift equal to $\sqrt{1 - \delta^2} \cdot \Omega_R / \Delta\omega_{21}$. We set a threshold of 3×10^{-3} - i.e., the quantum projection noise of 10^5 atoms - for the overall phase uncertainty due to the residual Rabi oscillation during the four atomic passages inside the cavity. Any coherent evolution other than between states $|1\rangle$ and $|2\rangle$ (see Fig. 5.2) has been neglected in this calculation. This assumption is valid whenever the DB is far from the specific transition frequencies.

To simultaneously satisfy the scattering rate and residual Rabi oscillation requirements, one must have $|\Xi(\lambda)| > 1.4 \times 10^7$. In the visible, this condition is satisfied for a linearly polarized DB along with (perpendicular to) the DC-applied magnetic field B for $633 \text{ nm} < \lambda < 672 \text{ nm}$ ($\lambda > 679 \text{ nm}$), as shown by the colored bands in Fig. 5.3. At $\lambda = 672 \text{ nm}$, for example, a DB with a waist of $100 \mu\text{m}$ and power $\sim 10 \text{ W}$ determines a residual oscillation amplitude below the threshold mentioned above, for a scattering probability $< 2\%$. To maintain the same intensity and avoid increasing the required power, the last mirror (not shown in Fig. 5.1) directing the beam on the atoms can be mounted on a fast and precise translation stage to track with the DB the atomic cloud motion in the IB: in the interval $[1350 \text{ nm} - 2.5 \mu\text{m}]$ the ratio $|\Xi(\lambda)|$ is compatible with an instrument sensitivity below the quantum projection noise of 10^9 atoms with a 5% contrast reduction, and even better parameters are obtained at CO_2 laser wavelengths. Nevertheless, the required laser power for these wavelengths is in the kiloWatt range.

In the configuration, we studied previously, the interaction between the atoms and the IB is turned off when the DB is ON. A trade-off must be found between having a considerable DB power to effectively switch off the IB and minimizing the residual scattering rate it causes. Another scheme, which is not analyzed in detail in this manuscript, consists in using the DB to turn on the interaction. Photon scattering is strongly reduced because the DB is only ON during the coherent manipulation pulses. As a consequence, the DB can be set closer to a

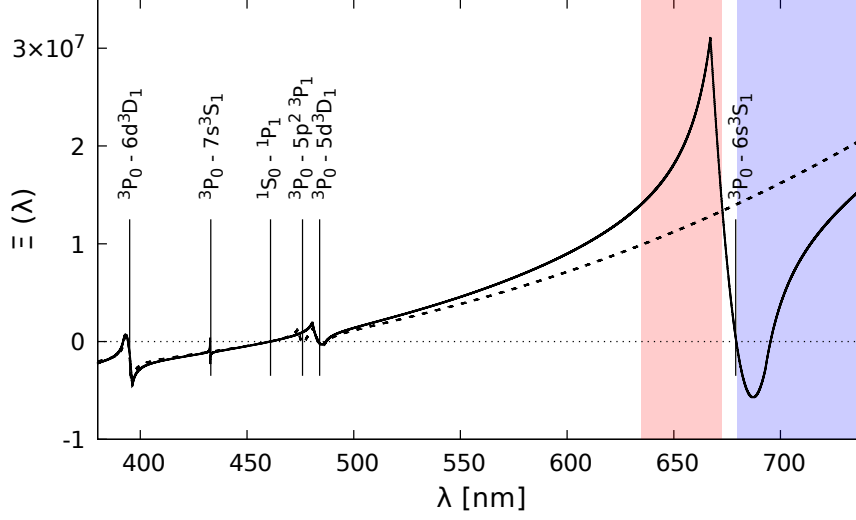


Figure 5.3: Ratio $\Xi(\lambda)$ between the light shift induced on the $|1\rangle - |2\rangle$ transition and the overall scattering rate by a laser at a wavelength λ . The solid (dashed) curve refers to the DB polarization parallel (perpendicular) to the magnetic field. The regions where $\Xi(\lambda) > 1.4 \times 10^7$ are indicated with a red (blue) vertical band for parallel (perpendicular) polarization of the DB. The wavelengths of the relevant transitions contributing to the atomic polarizability in the visible spectrum are indicated with vertical lines and are labelled.

transition between $|2\rangle$ and an excited level. This has two advantages: (i) lowering down the DB power; (ii) adding the IB detuning as a parameter to even further reduce the residual Rabi oscillation. The price to pay is that the control of the coherent manipulation now depends on the stability of the IB and the stability of the DB.

Two other effects of the cavity can affect the coherent manipulation. First, the intracavity IB light intensity can decay during the time the DB is turned off because of the modified effective atomic index of the refraction, which shifts the cavity resonance [237]. The narrow cavity bandwidth prevents the intracavity field from evolving significantly for the duration of the light pulses, which is much shorter than the cavity response time. Secondly, the atomic absorption can spoil the cavity linewidth [238]; again, for the adopted parameters, namely the number of atoms and the threshold set on the allowed scattering rate, the effect has been evaluated to be negligible. Since each photon carries the energy of 2.6×10^{-19} J for the IB at 698 nm, and intracavity field has a power of 0.286 W (J/s), and effective ON-duration is of the order of 100 μ s. They lead to photon numbers of about 1×10^{14} inside the cavity for the

duration of each pulse. As the maximum probability to scatter a photon from the DB during the whole interferometric sequence is set to be 3% for 10^5 atoms, 3,000 photons may scatter. This photon count is much less compared with the total number of photons inside the optical cavity.

Up to here, we have introduced the considered interferometric scheme, where differential light shift induced by the DB is used to pulse off the light-atom interaction between the IB and the cold atomic cloud. However, the DB leads to the problem like scattering. Now, we are detailing the analysis of the crucial parameters and how to trade-off between advantages and drawbacks. In the following, we introduce concepts to make clear the determination of the trade-off: the Sec. 5.2.1 discusses AC stark shift; the Sec. 5.2.2 analyzes scattering rate when the DB is present; the compromise between light shift and scattering rate is made in the Sec. 5.2.3; the Sec. 5.2.4 talks about optimal interaction time between light and atom to avoid being coupled to spurious momentum states, and the Sec. 5.2.5 evaluates the uncertainty caused on the interferometric phase by the residual Rabi oscillation produced by the IB when DB is on.

5.2.1 The AC Stark shift

^{87}Sr atoms are neutral and spherically symmetrical; hence, they do not exhibit any permanent dipole moment. ^{87}Sr atoms are placed in a DB laser field, an induced electric dipole moment (\vec{d}) is created due to a new charge distribution via external field (primarily due to \vec{E}) causing oppositely-oriented forces onto the positive nucleus and the cloud of orbiting negatively-charges, electrons inside each atom,

$$\vec{d} = \alpha \vec{E}, \quad (5.9)$$

where α represents its dipole polarizability. The polarizability characterizes the ability to form instantaneous dipoles and is a property of matter determining the dynamical response of a bound system to external fields. With a far red-detuned laser beam than its clock transition ($\Delta \gg \Omega$), and also far away from all kinds of electrical transitions of bare atoms, the scattering of photons can be controlled to a small enough extent. The main effect of the light field on the atoms is to shift their energy levels. In a homogeneous laser field, atoms feel no

force, given that the conservative force determined by light is equal to

$$\vec{F} = \vec{d} \cdot \vec{\nabla} \vec{E}; \quad (5.10)$$

the only effect is thus a torque rotating the induced electric dipole moment to be aligned with the externally applied electric field. An atom internal structure and energy shift due to its induced electric dipole and external electric field can be deduced from

$$U = \vec{d} \cdot \vec{E}. \quad (5.11)$$

To evaluate the light shifts of clock states of ^{87}Sr atoms, the main issue comes with the calculation or estimation of these states' dipole polarizability. α of a realistic multi-level-structure atomic system placed in a far-detuned laser field is [129]

$$\alpha_a = \frac{2}{\hbar} \sum_k |d_{ak}|^2 \frac{\omega_{ak}}{\omega_{ak}^2 - \omega_L^2}, \quad (5.12)$$

where the subscript a indicates the state $|a\rangle$ being shifted; the subscript k that acts as a summation index indicates any intermediate state $|k\rangle$ dipole coupled to state $|a\rangle$ that contribute to the energy shift of $|a\rangle$; the transition between state $|a\rangle$ and $|k\rangle$ has an angular frequency ω_{ak} and d_{ak} is the dipole matrix element related to the state transition rates, which is required before obtaining the dipole polarizability.

Here, we determine the dipole couplings of specific states with certain L and S quantum numbers (the clock states) under the different orientations of the magnetic field as quantization axis [232]. \vec{B} field shall be perpendicular to the cavity axis, and the IB is linearly polarized since the clock transition ($^1S_0 - ^3P_0$, $J = 0 - J = 0$) requires the absorption of photons with zero angular momenta along the quantization axis. The DB has an orientation concerning the magnetic field that can vary from parallel to perpendicular. This leaves the freedom of the projection of the angular momentum from the photons in the DB along the quantization axis.

To reduce the dipole matrix element from basis of J, L, S to the basis of L, S in the matrix element $|d\rangle$, the Eq. 2.67 from [232] is applied

$$X_{ab} = \frac{|\langle J_a L_a S_a || D^1 || J_b L_b S_b \rangle|^2}{|\langle L_a S_a || D^1 || L_b S_b \rangle|^2} = (2J_a + 1)(2J_b + 1) \left\{ \begin{matrix} L_a & J_a & S_a \\ J_b & L_b & 1 \end{matrix} \right\}^2, \quad (5.13)$$

where the $6 - j$ symbol (terms in curly brackets) is involved. The process to compose three

angular momenta j_1, j_2, j_3 in $6-j$ symbol, J is made in two steps and can be realized in two ways: either summing j_1 and j_2 to obtain j_{12} then adding j_3 to obtain J or summing j_2 and j_3 to obtain j_{23} then adding j_1 in order to resolve the momenta J . Following Landau's book, a $6-j$ symbol with these angular momenta is written as such:

$$\left\{ \begin{array}{ccc} j_1 & j_2 & j_{12} \\ j_3 & J & j_{23} \end{array} \right\} \quad (5.14)$$

In a matrix element $\langle S_a, L_a, J_a, O_a | V | S_b, L_b, J_b, O_b \rangle$, where $S_a = S_b = S$ meaning it is the same spin quantum number in both the initial and final states and V behaves as a vector under rotation, O_a, O_b are the other quantum numbers, i.e., not related to the modulus of the angular momentum (note this, it includes M). Then, we combine $j_1 = S_a, j_2 = L_a$ and $j_3 = 1$ to obtain J_b , where $j_{12} = J_a$ and $j_{23} = L_b$, and to finally evaluate a coefficient in $6-j$ symbol

$$c_{6j} = \left\{ \begin{array}{ccc} S & L_a & J_a \\ 1 & J_b & L_b \end{array} \right\}. \quad (5.15)$$

The reduced matrix element independent from J is represented,

$$\frac{\langle S, L_a, J_a, O_a | V | S, L_b, J_b, O_b \rangle}{\langle S, L_a, O_a || V || S, L_b, O_b \rangle} = (-1)^{j_1+j_2+j_3+J} c_{6j} \sqrt{(2J_a+1)(2L_b+1)}. \quad (5.16)$$

When evaluating the dependence from M of the reduced matrix element, the Wigner-Eckart theorem is used to calculate the Clebsch-Gordan coefficients

$$c_{cg} = \langle l_1, l_2, m_1, m_2 | l_3, m_3 \rangle, \quad (5.17)$$

where $(l_1, m_1), (l_3, m_3)$ refer to the levels interacting with the DB and (l_2, m_2) are the angular momentum quantum numbers of the photons in the DB. The ground state of the interferometric transition has $(l_1, m_1) = (0, 0)$ while the excited state has $(l_3, m_3) = (1, 0)$. If the atoms are prepared in the state $|1\rangle ((l_1, m_1))$, after a translation of value $T_{m_2}^{l_2}$, we obtain a final state of $|3\rangle ((l_3, m_3))$,

$$|\langle n_1, l_1, m_1 | T_{m_2}^{l_2} | n_3, l_3, m_3 \rangle| = \frac{|\langle l_1, l_2, m_1, m_2 | l_3, m_3 \rangle|}{\sqrt{2l_3+1}} |\langle n_1 || T || n_3 \rangle| \quad (5.18)$$

$$= \frac{|c_{cg}|}{\sqrt{2l_3+1}} |\langle n_1 || T || n_3 \rangle|, \quad (5.19)$$

while the magnetic field is perpendicular to the DB. Then, $(l_2, m_2) = (1, 0)$ so the ground

state is coupled to all the 3P_1 states with $M_L = 0$ with

$$|c_{cg}|^2/(2l_3 + 1) = |\langle 0, 1, 0, 0 | 1, 0 \rangle|^2/3 = 1/3. \quad (5.20)$$

The excited state is coupled to the 3S_1 , 3D_1 states, again with $M_L = 0$, with $|c_{cg}|^2/(2l_3 + 1) = 1/3, 2/3$ respectively, but is not coupled to the 3P_1 states. If the DB is instead parallel to the magnetic field and is linearly polarized, $(l_2, m_2) = (1, \pm 1)$. For the ground state, there is again a coupling to the 3P_1 states with $M_L = \pm 1$ so the average coupling is given by

$$|c_{cg}|^2 = \frac{1}{6} |\langle 0, 1, 0, 1 | 1, 1 \rangle|^2 + \frac{1}{6} |\langle 0, 1, 0, -1 | 1, -1 \rangle|^2 = 1/3. \quad (5.21)$$

The excited state is instead coupled to the 3P_1 , 3D_1 states, in both cases, with $c_{cg} = 1/2$ but there is no coupling to the 3S_1 states.

The dipole polarizability is given in various units, depending on the context in which they are determined. The most widely used unit adopted in theoretical atomic physics is atomic units (a.u.), in which e , m_e , $4\pi\epsilon_0$ and the reduced Plank constant \hbar have the numerical value 1. The polarizability in a.u. has the volume dimension, and its numerical values presented here are expressed in units of a_0^3 , where a_0 is the Bohr radius. So the polarizability in a.u. is

$$\alpha_a = \frac{\sum_k \phi_{J_a J_k} \frac{\omega_{cm}^3}{6\pi\epsilon_0 c^3} \Gamma_{L_a L_k} \frac{\omega_{ak}}{\omega_{ak}^2 - \omega_L^2}}{4\pi\epsilon_0 a_0^3}. \quad (5.22)$$

All the required parameters to calculate the dipole polarizability and the energy shift are summarized in Tab. 5.1.

The induced light shift is

$$\Delta\omega_a = \frac{U}{\hbar} = -\frac{1}{4\hbar} \alpha_a E_0^2. \quad (5.23)$$

Since the mean intensity of an electromagnetic wave is proportional to the maximum electric field strength E_0 squared,

$$I_{ave} = \frac{c\epsilon_0 E_0^2}{2}. \quad (5.24)$$

In the case of a Gaussian laser beam, we obtain:

$$I_{ave} = \frac{P}{\pi w^2}, \quad (5.25)$$

where P is the total beam power, and w is the beam waist. Therefore, Eq. 5.23 is rewritten

clock state	intermediate state	ω_{ak} [10^{15} 1/s]	$\Gamma_{L_a L_k}$ [10^6 1/s]	$\Phi_{J_a J_k}$	$c_{ge}(\vec{E}_{IB} \perp \vec{B})$	$c_{ge}(\vec{E}_{IB} \parallel \vec{B})$
$5s^2 \ ^1S_0$	$5s5p \ ^1P_1$	4.087	190.7	1	1	1
	$5s6p \ ^1P_1$	6.423	1.86			
	$5s7p \ ^1P_1$	7.328	4.3			
	$4d5p \ ^1P_1$	7.755	14.5			
	$5s8p \ ^1P_1$	7.755	16.7			
	$5s9p \ ^1P_1$	7.998	11.7			
	$5s10p \ ^1P_1$	8.161	7.6			
	$5s11p \ ^1P_1$	8.276	4.88			
$5s5p \ ^3P_0$	$5s6s \ ^3S_1$	2.773	75.4	1/9	0	1/3
	$5s7s \ ^3S_1$	4.353	17.5			
	$5s8s \ ^3S_1$	4.981	8.22			
	$5s9s \ ^3S_1$	5.299	4.53			
	$5s10s \ ^3S_1$	5.483	2.77			
$5s5p \ ^3P_0$	$5s4d \ ^3D_1$	0.724	0.345	5/9	1/2	2/3
	$5s5d \ ^3D_1$	3.897	60.9			
	$5s6d \ ^3D_1$	4.778	26.7			
	$5s7d \ ^3D_1$	5.190	14.2			
	$5s8d \ ^3D_1$	5.415	8.51			
	$5s9d \ ^3D_1$	5.555	5.51			
$5s5p \ ^3P_0$	$5p^2 \ ^3P_1$	3.961	127	1/3	1/2	0

Table 5.1: Transition parameters are retrieved from [239] for the calculation of the atomic polarizability of the Sr-atom clock states.

as

$$\Delta\omega_a = -\frac{P}{\hbar^2 c \epsilon_0 \pi w^2} \sum_k |d_{ak}|^2 \frac{\omega_{ak}}{\omega_{ak}^2 - \omega_L^2}. \quad (5.26)$$

Assuming the polarization of the linearly polarized DB with the magnetic field \vec{B} form an angle θ , the results of the parallel ($\theta = 0^\circ$) and perpendicular ($\theta = 90^\circ$) cases are studied. Fig. 5.4 and Fig. 5.6 present the energy shifts of the clock states if the DB operates at a large range of wavelengths provided that the DB has a power of 10 W with a waist of 100 μm , where mainly contributing to the transitions, labeled with vertical dashed lines. Fig. 5.5 and Fig. 5.7 are the accordingly differential energy shift of the clock states. Considering the visible spectrum, Fig. 5.8 as their zoomed-in version shows the differential light shift when the DB operates from 350 nm to 750 nm.

5.2.2 The scattering rate

The photon absorption occurs even though the DB laser field is far-detuned than the atomic transition resonance in the regime where the atom-light interaction is dispersive. This resid-

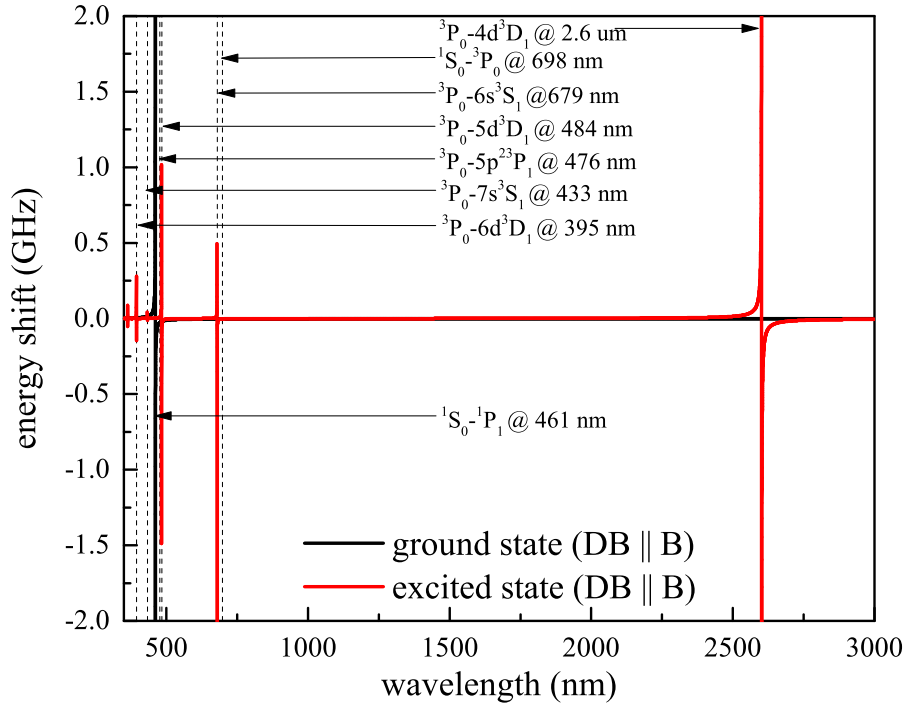


Figure 5.4: The illustration of the energy shift of the ground and excited clock states when the DB is operating at different wavelengths from 350 nm to 3000 nm, and parallel to \vec{B} .

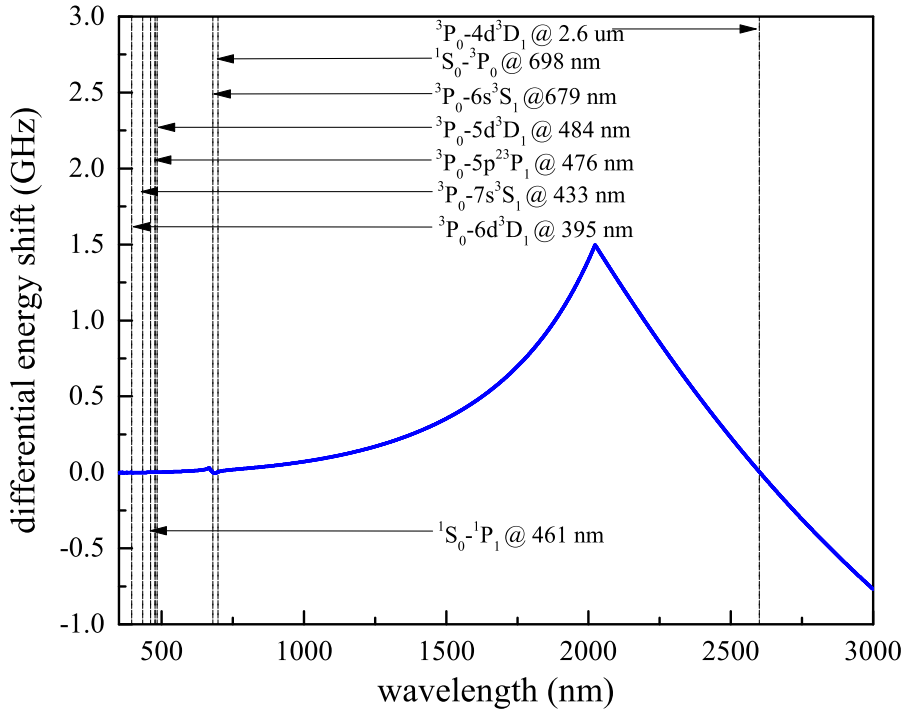


Figure 5.5: Illustration of the differential energy shift of the clock states when the DB is parallel to \vec{B} . Actually, it corresponds to an energy difference between the excited clock states and the ground clock state presented in Fig. 5.4.

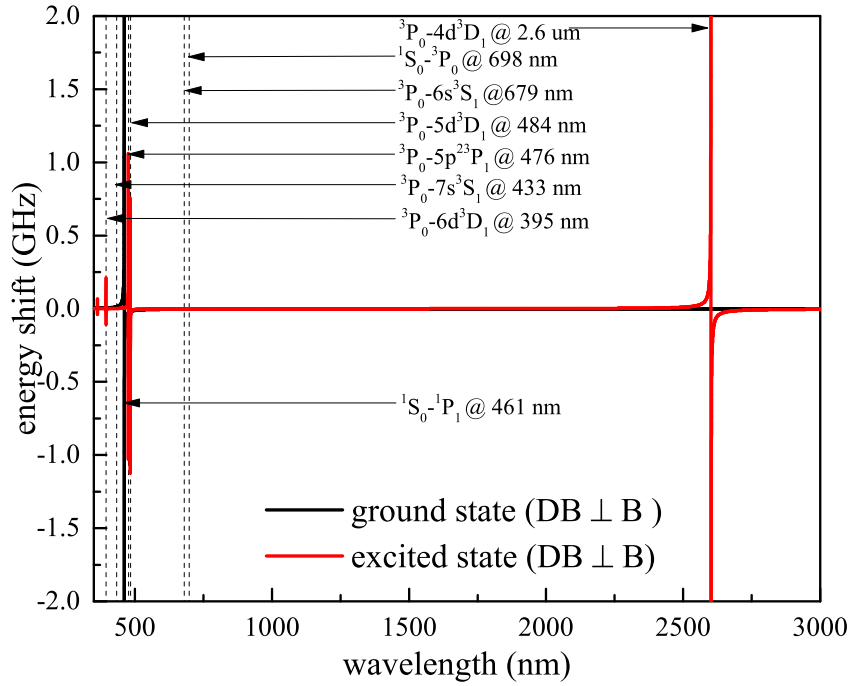


Figure 5.6: Energy shift of ground and excited clock state when DB operating at different wavelengths from 350 nm to 3000 nm is perpendicular to \vec{B} .

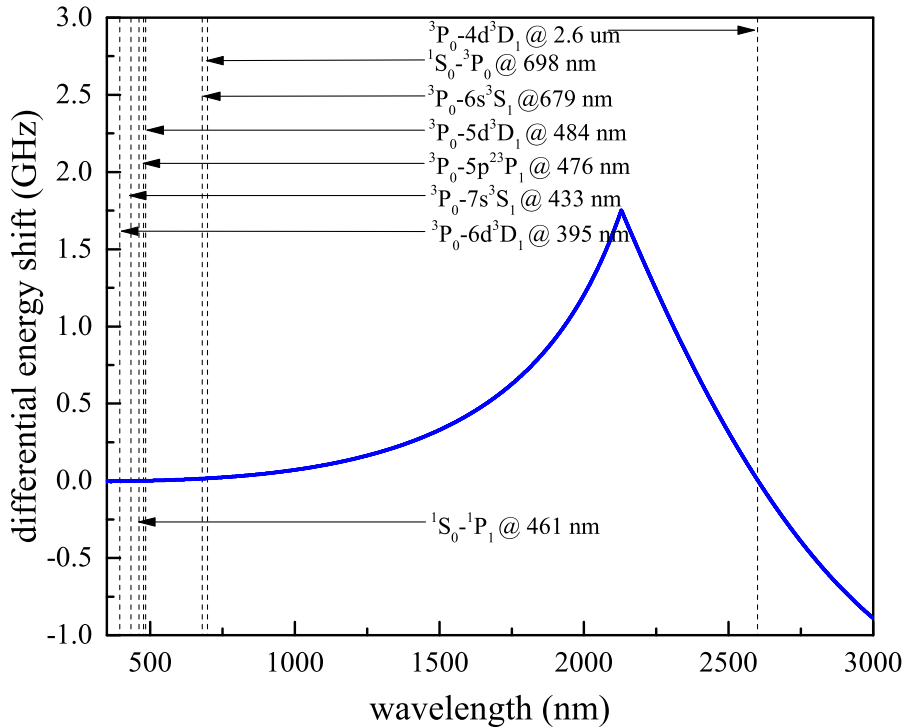


Figure 5.7: Differential energy shift of clock states when the DB is perpendicular to \vec{B} , representing an energy difference between the excited clock state and the ground clock state in Fig. 5.6.

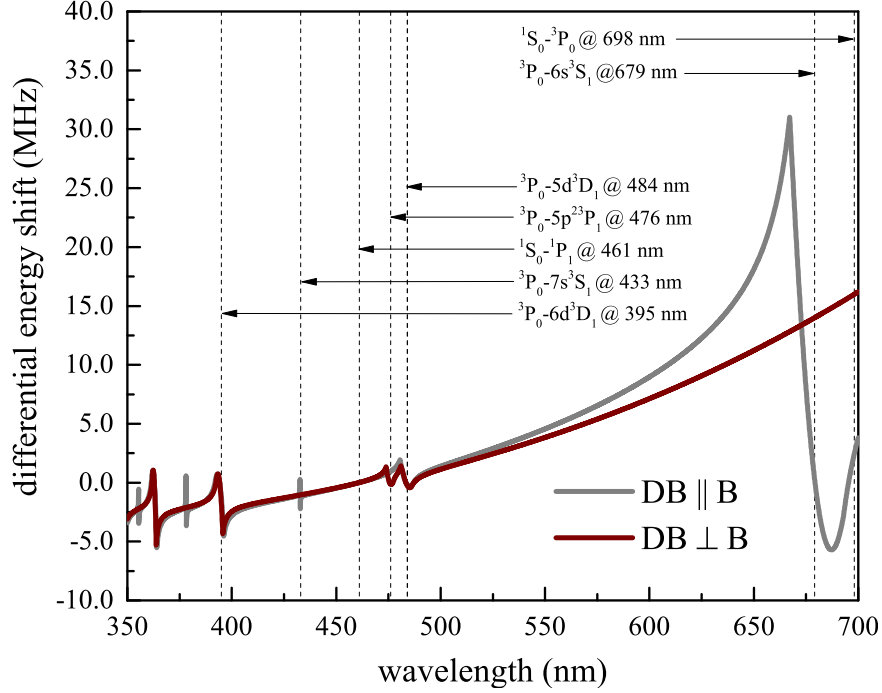


Figure 5.8: Differential energy shift of clock states when the DB operates at different wavelengths from 350 nm to 700 nm either parallel or perpendicular to \vec{B} .

ual atom-photon momentum exchange (via spontaneous decay) heats the atomic sample and, more importantly, decoheres the atomic sample, thus inducing contract loss on the interference signal. The photon scattering rate is written as

$$\Gamma_{scatt} = \sum_k \frac{\Gamma_{LaLk}^2}{\Delta_{ak}} \frac{1}{\hbar} \phi_{J_a J_k} \frac{6\pi\epsilon_0 c^3}{\omega_{cm}^3} \frac{\omega_{ak}}{\omega_{ak}^2 - \omega_L^2} \frac{4P}{\epsilon_0 c \pi \omega_0^2}, \quad (5.27)$$

where Γ corresponds to the spontaneous decay rate of the excited level, ω is the frequency of driving field, and ω_0 is the atomic transition frequency. Moreover,

$$\Gamma = \frac{\omega_0^3}{3\pi\epsilon_0 \hbar c^3} |\langle g | \mu | e \rangle|^2 = \frac{\omega_0^3}{3\pi\epsilon_0 \hbar c^3} |d_{ge}|^2, \quad (5.28)$$

where d_{ge} is the dipole matrix element between the ground ($|g\rangle$) and the excited state ($|e\rangle$). The general formula for the matrix elements is

$$|d_{ge}| = \phi_{J_g J_e} \phi_{m_g m_e} |d_{L_g L_e}|, \quad (5.29)$$

where $d_{L_g L_e}$ is the dipole moment between the $|L_g S_g\rangle$ and $|L_e S_e\rangle$ states, and the magnetic branching term for a lower state with m_g from upper state with m_e is given by

$$\phi_{m_g m_e} = (2J_e + 1) \begin{pmatrix} J_g & 1 & J_e \\ -m_g & p & m_e \end{pmatrix}^2. \quad (5.30)$$

The term in round brackets is the Wigner $3 - j$ symbol and can be expressed by the Clebsch-Gordan coefficients c_{cg} . As well, $\phi_{J_g J_e}$ is the branching ratio for the relative transition line strength (dipole moment squared) between fine multiplets,

$$\phi_{J_g J_e} = (2J_g + 1)(2L_e + 1) \left\{ \begin{matrix} S_g & L_g & J_g \\ 1 & J_e & L_e \end{matrix} \right\}^2, \quad (5.31)$$

where the term in curly brackets is the $6 - j$ symbol and is related to the Racah W coefficient.

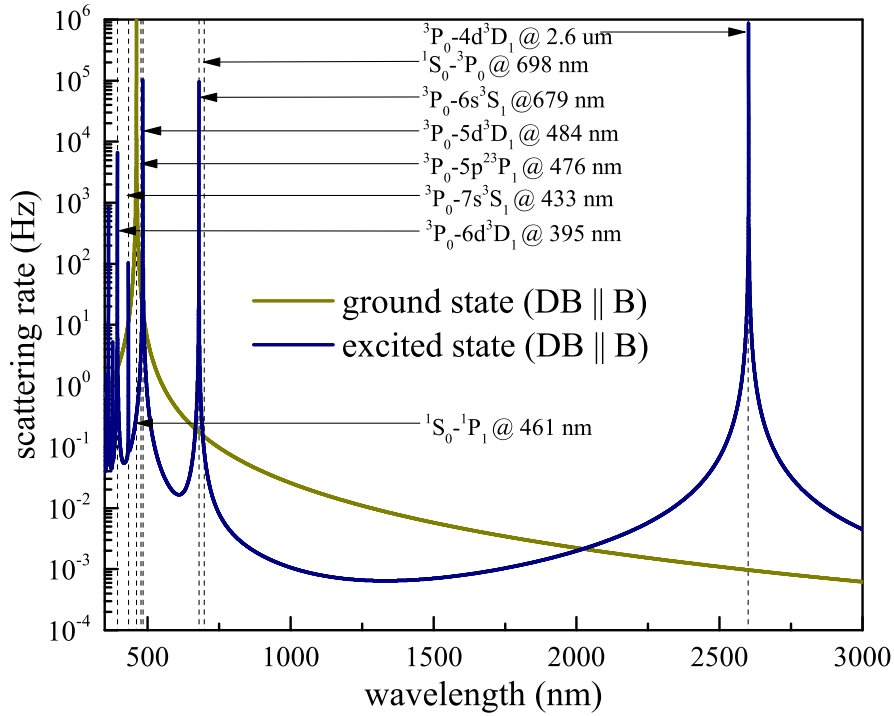


Figure 5.9: It represents the scattering rate of both, the ground and the excited clock states, when the DB is operating at different wavelengths from 350 nm to 3000 nm and parallel to \vec{B} .

5.2.3 Trade-off between energy shift and scattering rate

Since the differential light shift of two dressed atomic levels is

$$\Delta\omega_{21} = (\alpha_2 - \alpha_1) \frac{4P}{\epsilon_0 c \pi \omega_0^2 \hbar}, \quad (5.32)$$

the normalized light shift is

$$\Delta\bar{\omega} = \frac{\Delta\omega_{21}}{\Gamma_{scatt}}. \quad (5.33)$$

The result is plotted in Fig. 5.14.

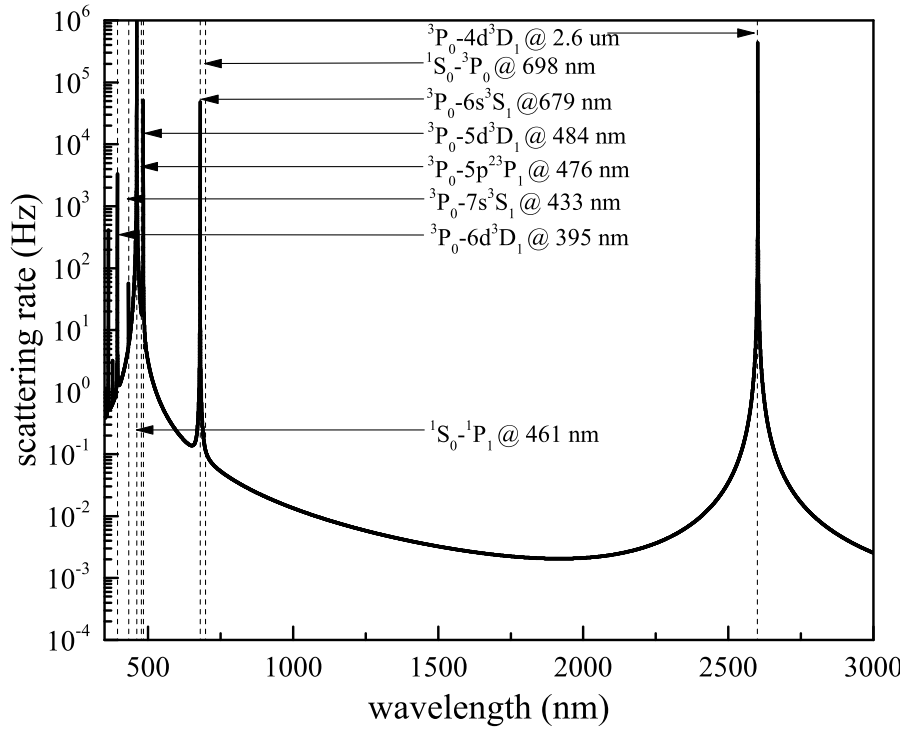


Figure 5.10: Average scattering rate of ground and excited clock states when the DB is operating at different wavelengths from 350 nm to 3000 nm and parallel to \vec{B} .

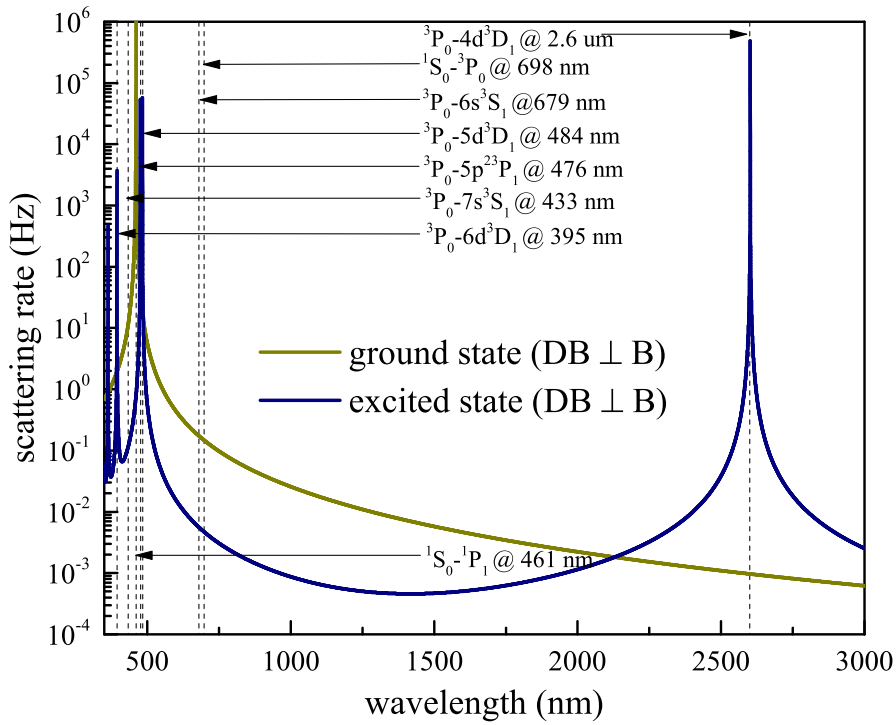


Figure 5.11: Scattering rate of ground and excited clock state when the DB is operating at different wavelengths from 350 nm to 3000 nm and perpendicular to \vec{B} .

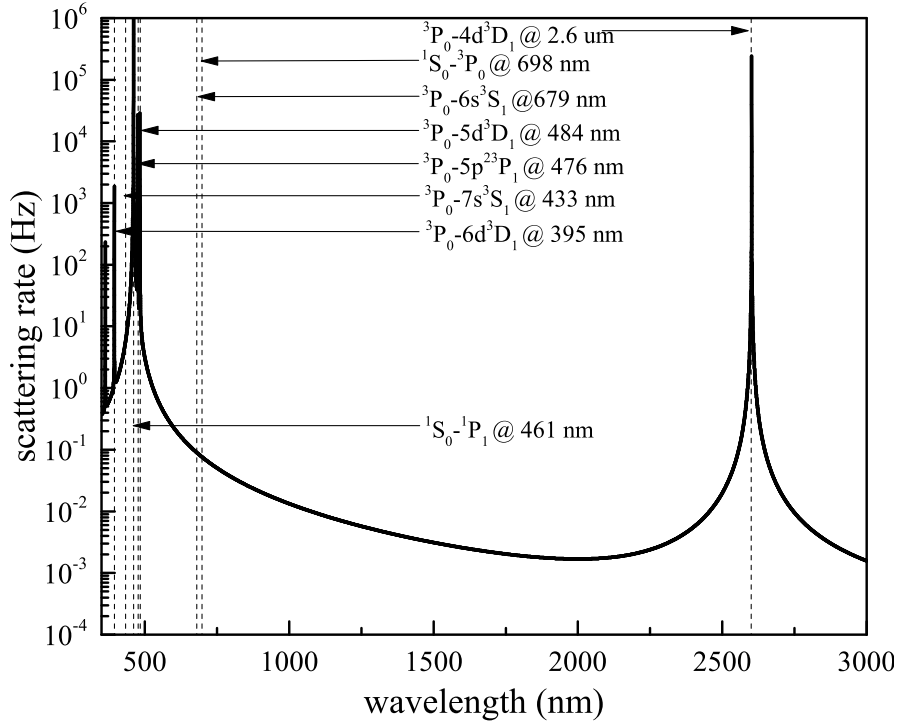


Figure 5.12: Average scattering rate of ground and excited clock states when the DB is operating at different wavelengths from 350 nm to 3000 nm and perpendicular to \vec{B} .

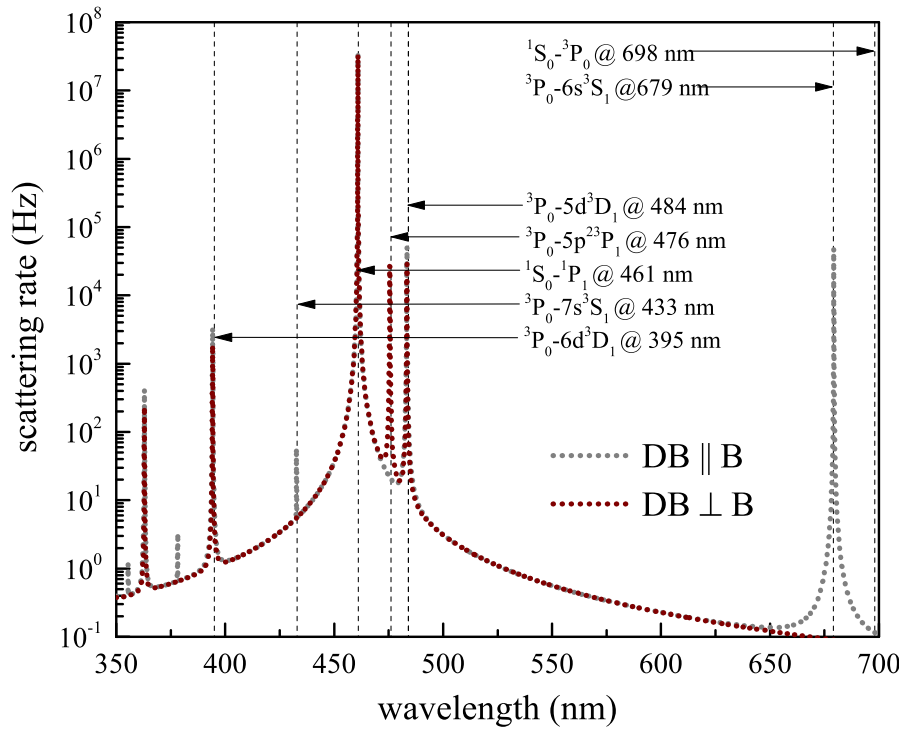


Figure 5.13: Average scattering rate of clock states when the DB operated at different wavelengths from 350 nm to 700 nm, is either parallel or perpendicular to \vec{B} .

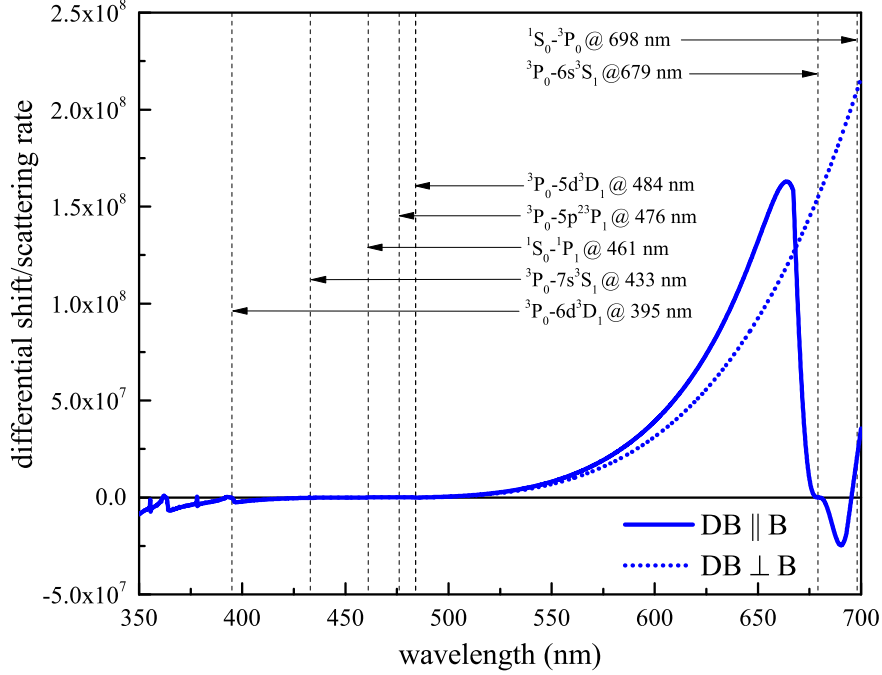


Figure 5.14: Ratio of the differential energy shift and the scattering rate of clock states when the DB operated at different wavelengths from 350 nm to 700 nm, is either parallel or perpendicular to \vec{B} .

5.2.4 The time interaction between atoms and the light

The ^{87}Sr atomic source is prepared at a very low temperature by adopting degenerate Fermion states and/or delta-kick collimation techniques. The cold atomic source is launched almost vertically with a velocity of ~ 1.25 m/s. The vertical displacement of the cloud increases during the manipulation pulses. Therefore, setting the light beam waist to be $100 \mu\text{m}$ ensures a homogeneous manipulation during the light pulses.

To address the atomic ensemble via the clock transition of ^{87}Sr , its saturation intensity is

$$I_{sat} = \frac{2\pi^2 \hbar c \Gamma}{3\lambda^3}, \quad (5.34)$$

where $\Gamma = 2\pi \times 1.5$ mHz, and $\lambda = 698$ nm. Therefore, $I_{sat} = 0.41$ pW/cm². The Rabi frequency is

$$\Omega = \Gamma \sqrt{\frac{I}{2I_{sat}}}. \quad (5.35)$$

If $\Omega = 2\pi \times 5$ kHz, $I = 1$ W.

The analytical method to calculate the pulse duration using a Gaussian beam in the light-

pulses atom interferometer operated at quasi-Bragg regime referring to [240]. For π pulse:

$$\frac{1}{2} \int_{-\infty}^{+\infty} \Omega_{eff}(t') dt' = \frac{\bar{\Omega}^n}{2} \left(\frac{1}{8\omega_r}\right)^{n-1} \frac{\sqrt{2\pi\sigma^2}}{[(n-1)!]^2 \sqrt{n}} = \frac{\pi}{2} \quad (5.36)$$

so we obtain $\sigma = 62.65 \mu\text{s}$. For $\frac{\pi}{2}$ pulse:

$$\frac{1}{2} \int_{-\infty}^{+\infty} \Omega_{eff}(t') dt' = \frac{\bar{\Omega}^n}{2} \left(\frac{1}{8\omega_r}\right)^{n-1} \frac{\sqrt{2\pi\sigma^2}}{[(n-1)!]^2 \sqrt{n}} = \frac{\pi}{4} \quad (5.37)$$

Here, $n = 1$, $\bar{\Omega} = 5 \text{ kHz}$. FWHM for π pulse is $2\sqrt{2ln2}\sigma = 147.53 \mu\text{s}$, and $73.76 \mu\text{s}$ for $\frac{\pi}{2}$ pulse.

To verify this analytical result, we numerically solved the problem using QuTip [241] (see Fig. 5.15). In detail, we limit the number of fence states set as 5, the resonant and the initial states are 1 and -1, respectively.

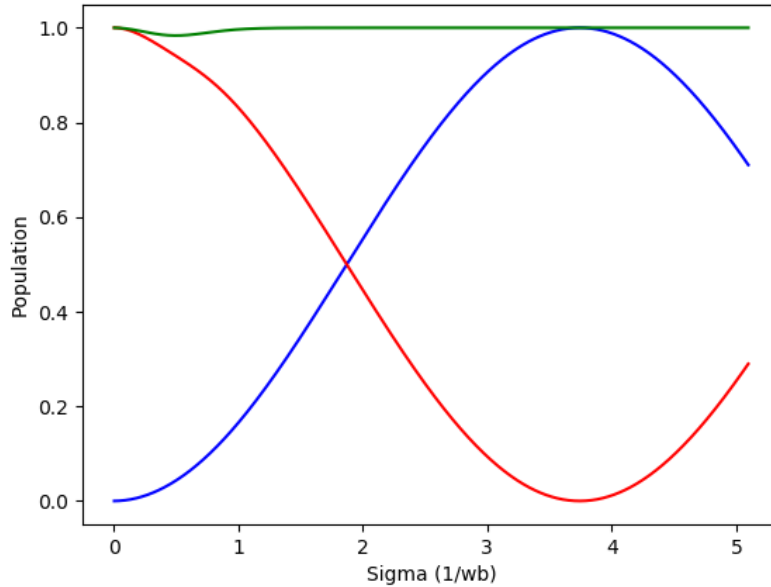


Figure 5.15: The initial (red), final (blue) and total (green) atomic population changes over time with the unit of recoil frequency $\omega_r = 59 \text{ kHz}$ for the ^{87}Sr -atom.

5.2.5 The phase error

The IB produces residual Rabi oscillations when the DB is ON, which causes uncertainty on the interferometric phase. In a two-level system, the pure atomic state is represented as

$$\phi(t) = \alpha(t) |1\rangle + \beta(t) |2\rangle, \quad (5.38)$$

where $\alpha(t = 0)$ and $\beta(t = 0)$ are real, and $\alpha(t)^2 + \beta(t)^2 = 1$. The Bloch vector is written as

$$\vec{\rho} = \begin{pmatrix} u \\ v \\ w \end{pmatrix} = \begin{pmatrix} 2\text{Re}(\alpha\beta^*) \\ 2\text{Im}(\alpha\beta^*) \\ |\beta|^2 - |\alpha|^2 \end{pmatrix} \quad (5.39)$$

subject to a field with Rabi frequency Ω and frequency detuning Δ . The solution for $\rho(t)$ is known as: $\rho(t) = A\rho(0)$ where

$$A = \begin{pmatrix} \frac{\Omega^2 + \Delta^2 \cos\Omega_e t}{\Omega_e^2} & \frac{\Delta \sin\Omega_e t}{\Omega_e} & \frac{\Delta\Omega(\cos\Omega_e t - 1)}{\Omega_e^2} \\ -\frac{\Delta \sin\Omega_e t}{\Omega_e} & \cos\Omega_e t & -\frac{\Omega \sin\Omega_e t}{\Omega_e} \\ \frac{\Delta\Omega(\cos\Omega_e t - 1)}{\Omega_e^2} & \frac{\Omega \sin\Omega_e t}{\Omega_e} & \frac{\Delta^2 + \Omega^2 \cos\Omega_e t}{\Omega_e^2} \end{pmatrix} \quad (5.40)$$

with $\Omega_e = \sqrt{\Delta^2 + \Omega^2}$. In an interferometer, $\cos\phi = w$, where w is the population inversion

$$\begin{aligned} w(t) &= 2\alpha\beta \frac{\Delta\Omega(\cos\Omega_e t - 1)}{\Omega_e^2} + w(0) \frac{\Delta^2 + \Omega^2 \cos\Omega_e t}{\Omega_e^2} \\ &\approx w(0) \left[1 - \frac{\Omega^2}{\Delta^2} (1 - \cos\Delta t) \right] - 2\alpha\beta \frac{\Omega}{\Delta} (1 - \cos\Delta t) \\ &= w(0) \left[1 - \frac{\Omega^2}{\Delta^2} (1 - \cos\Delta t) \right] - \sqrt{1 - w(0)^2} \frac{\Omega}{\Delta} (1 - \cos\Delta t). \end{aligned}$$

Therefore, the standard error propagation can obtain the uncertainty on ϕ due to the out of resonance IB when the DB is ON. But it is obvious that when the output is not a pure state, there is an error term for the amplitude $\Omega/2\Delta$. Note that $w(0)$ has not only a random noise but also, an average bias of value $\Omega\sqrt{1 - w(0)^2}\Delta$.

Chapter 6

On the horizon

Discussions in Ch. 5 on circumventing the finite radiation time in the narrow-linewidth cavity consist of adding one extra laser beam to switch the coupling between cold atoms and the intracavity light field. However, the primary identified limitation of "controlling the atom-light interaction using the light shift" is the phase error introduced by the incoherent scattering rate due to the dressing beam. To overcome such limitations, one can use a different control process to turn the interferometric beam ON and OFF. The external field can be replaced with a magnetic field instead of a laser field. Suppose one considers bosonic isotopes of atoms adopted in optical clocks, as is the case of the even isotopes of Yb and Sr-atoms. In that case, a possible control process is represented by magnetic-field induced spectroscopy, which is widely adopted to allow the optical single-photon excitation on the respective clock transition. This chapter investigates the feasibility of adopting the same technique to modulate the atom-light interaction quickly.

Contents

6.1	Fast control of atom-light interaction via magnetic-field induced transition . . .	146
6.1.1	The magnetic-field-induced transition	146
6.1.2	Fast control of atom-light interaction with magnetic field	147

6.1 Fast control of atom-light interaction via magnetic-field induced transition

6.1.1 The magnetic-field-induced transition

The magnetic-field-induced transition (MIT) spectroscopy has been developed and demonstrated for optical atomic clocks based on neutral atoms confined to an optical lattice, where a weak static magnetic field is applied to enable direct optical excitation of forbidden electric-dipole transitions that are otherwise prohibitively weak [42]. For example, for even isotopes of Sr and Yb-atoms, with zero nuclear spin, there is no hyperfine mixing, and thus the $5s^2 \ ^1S_0 - 5s5p \ ^3P_0$ ($|1\rangle - |2\rangle$) doubly forbidden (spin- and angular momenta) clock transition has an ultra-narrow linewidth (see Fig. 6.1). However, adding a small magnetic field \vec{B} can mix with a controllable fraction of electric-dipole-allowed $5s5p \ ^3P_1$ ($|3\rangle$) state into the $5s5p \ ^3P_0$ ($|2\rangle$) state, separated by a frequency difference of Δ_{32} , and thus, a coupling matrix element is obtained

$$\Omega_B = \langle 2 | \hat{\mu} \cdot \vec{B} | 3 \rangle / \hbar, \quad (6.1)$$

where $\hat{\mu}$ is the magnetic-dipole operator. Now, the single-photon excitation $|1\rangle - |2'\rangle$ is partially allowed due to the mixture of state $|3\rangle$,

$$|2'\rangle = |2\rangle + \frac{\Omega_B}{\Delta_{32}} |3\rangle. \quad (6.2)$$

An optical field \vec{E} interacts with this three-states system mostly via E1-allowed $|1\rangle - |3\rangle$ transition, with a decay rate of γ . Its Rabi frequency is

$$\Omega_L = \langle 3 | \hat{d} \cdot \vec{E} | 1 \rangle / \hbar, \quad (6.3)$$

where \hat{d} is the electric-dipole operator. Therefore, the effective Rabi frequency of the clock transition is

$$\Omega_{12} = \frac{\Omega_L \Omega_B}{\Delta_{32}}. \quad (6.4)$$

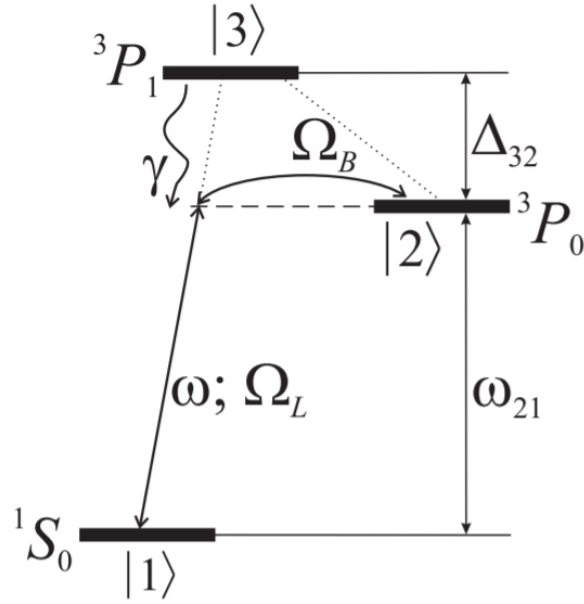


Figure 6.1: MIT transition of a double-forbidden transition in a three-level atomic system (the figure is extracted from [42] under CC-BY 4.0 license), where states are labeled with $^{2S+1}L_J$.

6.1.2 Fast control of atom-light interaction with magnetic field

We propose another practical approach to mitigate the limitation represented by the finite response time in narrow-linewidth cavity-assisted atom interferometry. The atom-laser interaction is enabled/disabled by the fast switching ON/OFF by pulsing a DC-applied external magnetic field instead of the laser field.

6.1.2.1 Choice of atomic species

The basic principle of the "fast control of atom-light interaction via MIT" is to use the external magnetic field to mix the 3P_0 clock state with the state 3P_1 , such that 3P_0 acquires a small E1-transition lifetime. ^{87}Sr and ^{88}Sr are two promising atomic species. On ^{88}Sr , the weak and uniform magnetic field adds one first-order perturbation in its energy,

$$H_B = -\hbar\mu_{BgJ}\vec{J} \cdot \vec{B}, \quad (6.5)$$

where μ_B is the Bohr magneton about $2\pi \times 14$ GHz/T, g_J is the g-factor of total electronic angular momentum,

$$g_J \approx 1 + \frac{J(J+1) - L(L+1) + S(S+1)}{2J(J+1)} = \frac{3}{2} \quad (6.6)$$

for states where $S = 1$, $L = 1$. Also, selecting the z-axis along the B -field, $H_B = -3\hbar\mu_B J_Z B/2$. So the coupling frequency Ω_B in [42] is given by

$$\Omega_B = \frac{3}{2}\mu_B B \langle {}^3P_1 | J_Z | {}^3P_0 \rangle = \frac{\sqrt{3}}{2}\mu_B B \langle {}^3P_1 || \mu || {}^3P_0 \rangle. \quad (6.7)$$

One can use the Wigner-Eckart theorem to remove the dependence on the angular momentum and keep only the reduced magnetic dipole matrix element $\langle {}^3P_1 || \mu_M || {}^3P_0 \rangle$. On the other hand, for the ^{87}Sr -atom, due to the existence of nuclear spin ($\vec{F} = \vec{J} + \vec{I}$), the perturbing term in Eq. 6.5 is modified as

$$H_B = -\hbar\mu_B g_F \vec{F} \cdot \vec{B}. \quad (6.8)$$

We assume that H_B can be treated as a perturbation compared to the hyperfine structure. One obtains

$$g_F \approx \frac{g_J}{2} = \frac{3}{4} \quad (6.9)$$

for the states under consideration. For the specific optical state $|{}^3P_0\rangle = |F = 9/2, F_Z = 0\rangle$, H_B couples it only to $|{}^3P_1\rangle = |F = 11/2, F_Z = 0\rangle$ in the 3P_1 multiplets. The coupling frequency Ω_B is

$$\Omega_B = \frac{3}{4}\mu_B B \langle {}^3P_1 | J_Z | {}^3P_0 \rangle = \frac{\sqrt{33}}{16\sqrt{5}}\mu_B B \langle {}^3P_1 || \mu_M || {}^3P_0 \rangle. \quad (6.10)$$

The ratio $\rho_\Omega = \Omega_B^{87}/\Omega_B^{88}$ for the two isotopes is therefore

$$\rho_\Omega = \sqrt{\frac{11}{320}} \approx 0.185. \quad (6.11)$$

Notably, the electric dipole d_{31} is proportional to $\Omega_B |d_{31}|^2$ whereas the induced Rabi frequency Ω' is proportional to $\Omega_B |d_{31}|$. Here, the states $|1\rangle$, $|2\rangle$ and $|3\rangle$ are 1S_0 , 3P_0 and 3P_0 respectively.

For ^{88}Sr -atoms, $|d_{31}| = |\langle 3 || \mu_E || 1 \rangle|/\sqrt{3}$ while for ^{87}Sr $|d_{31}| = \sqrt{11/240} |\langle 3 || \mu_E || 1 \rangle|$. A ratio ρ_d for the electrical dipole moment matrix elements is given by

$$\rho_d = \sqrt{\frac{11}{80}} \approx 0.371. \quad (6.12)$$

The induced Rabi frequency scaling to the product $\rho_\Omega \rho_d$ has a coefficient for ^{87}Sr -atoms that

is about 14.5 times smaller than that for ^{88}Sr -atoms. Thus, to realize a proof-of-concept experiment, the ^{88}Sr -atom is a better candidate.

6.1.2.2 The scheme

This scheme can be suitably implemented in the cavity-aided atom interferometer where the IB addresses doubly-forbidden clock transitions of ^{88}Sr -atoms, prepared at ground state $|^1S_0\rangle$ with a temperature of $\sim 30\mu\text{K}$. After being launched, the atomic cloud follows the trajectories presented in Fig. 6.2. Since the IB laser is locked to the high finesse cavity via PDH locking, its power is nearly constant with time. The net contribution of AC-stark shift on the phase shift of AI interference is negligible [23]. The largest horizontal separation between two atomic wavefunctions is $|2v_x T| = 1.625\text{ mm}$, and the vertical displacement during a π pulse time is $|v_y \tau_\pi| = 363\ \mu\text{m}$.

6.1.2.3 Some critical parameters to consider

Transition rate The single-photon transition $5s^2\ ^1S_0 - 5s5p\ ^3P_0$ in ^{88}Sr -atom is opened by mixing "perturber" states $5s^2\ ^1S_0 - 5s5p\ ^3P_1$ and $5s^2\ ^1S_0 - ^1P_1$ via a DC-applied magnetic field. The MIT transition rate for $5s5p\ ^3P_0 - 5s^2\ ^1S_0$ is [242]

$$A_{\text{MIT}}(^1S_0, ^3P_0) = \frac{2.02613 \times 10^{18}}{3\lambda^3} \left| \sum_{s=1,3} d_s \langle 5s^2\ ^1S_0 \| P^{(1)} \| 5s5p^s P_1 \rangle \right|^2 \quad (6.13)$$

where λ is the wavelength in meters, d_s is the mixing coefficient, deduced by the first-order perturbation theory

$$d_s = \frac{\langle ^s P_1 \| H_m \| ^3 P_0 \rangle}{E(^3P_0) - E(^sP_1)}, \quad (6.14)$$

where $H_m = (N^{(1)} + \Delta N)|B|$ is the interaction Hamiltonian of an atom in a DC-applied magnetic field $|B|$. The reduced mixing coefficient d_s^R is

$$d_s^R = \frac{\langle ^s P_1 \| N^{(1)} + \Delta N \| ^3 P_0 \rangle}{E(^3P_0) - E(^sP_1)}, \quad (6.15)$$

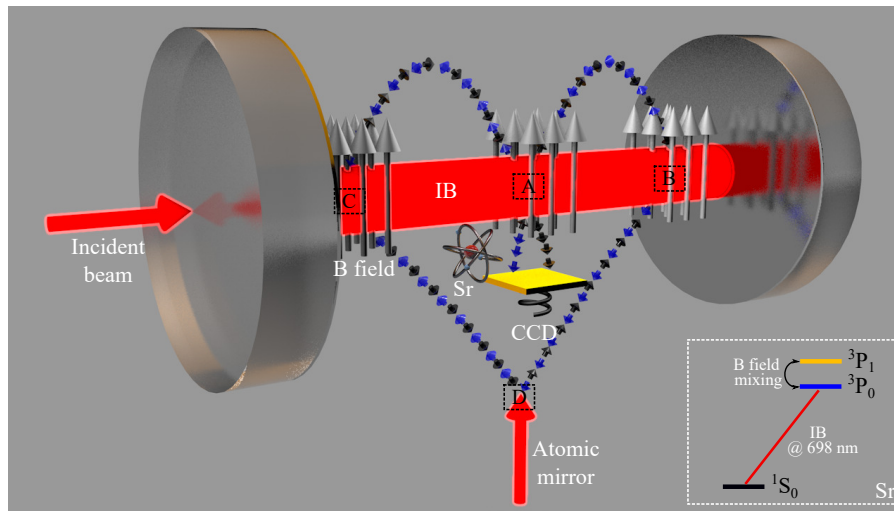


Figure 6.2: The schematic of the atom interferometer operated via magnetic field induced spectroscopy inside an optical resonator (not to scale): the optical resonator is formed with two-end mirrors. The cold atomic source is initially prepared in the ground state $|^1S_0\rangle$. After their vertical launch in free fall, the atomic clouds enter from the bottom the region A. The wavefunction is split into two via double diffraction with a $\pi/2$ pulse. The two parts of the wave function are horizontally reflected with a π pulse in regions B and C. In region D, the vertical velocity of the two trajectories is reflected by optical means. The two trajectories are horizontally reflected and convergent with another π pulse at regions C and B. The two trajectories are recombined in A at the last stage with a last $\pi/2$ pulse. All the pulses are produced with the cavity-enhanced IB. The population of the three output ports is measured using a CCD camera at the detection area. The B -field is applied to control the optical transition rate between $|^1S_0\rangle$ and $|^3P_0\rangle$ states.

computed using the Dirac–Hartree–Fock (DHF) method [243],

$$d_1^R = \frac{\langle {}^1P_1 || N^{(1)} + \Delta N || {}^3P_0 \rangle}{E({}^3P_0) - E({}^1P_1)} = -2.090 \times 10^{-3} \text{ T}^{-1}, \quad (6.16)$$

$$d_3^R = \frac{\langle {}^3P_1 || N^{(1)} + \Delta N || {}^3P_0 \rangle}{E({}^3P_0) - E({}^3P_1)} = 2.507 \times 10^{-7} \text{ T}^{-1}. \quad (6.17)$$

$\langle 5s^2 {}^1S_0 || P^{(1)} || 5s5p^1 P_1 \rangle$ and $\langle 5s^2 {}^1S_0 || P^{(1)} || 5s5p^3 P_1 \rangle$ are the reduced matrix elements for the electric dipole transition; the respective values are 5.28 a.u. and 0.161 a.u. [244]. Eq. 6.13 can thus be rewritten as [243],

$$A_{\text{MIT}}({}^1S_0, {}^3P_0) = 0.198B^2 \quad (6.18)$$

Without the magnetic-field-induced spectroscopy, the lifetime of the upper clock level $5s5p {}^3P_0$ of ${}^{88}\text{Sr}$ -atoms is at the order of thousands of years, with a transition rate of $2\pi \times 5.5 \times 10^{-12} \text{ s}^{-1}$ [124]. To ensure long lifetime at the state $5s5p^3 P_0$, the static magnetic field shall be small around a few 10 Gauss.

The energy shift In the absence of nuclear spin and natural hyperfine interaction, the transition $5s^2 {}^1S_0 - 5s5p {}^3P_0$ of ${}^{88}\text{Sr}$ -atoms is forbidden to all the orders for single-photon excitation. In the presence of magnetic field B , the clock transition is enabled while introducing Zeeman shift at the second-order [43, 42],

$$\begin{aligned} \Delta_B^{(2)} &\approx -\frac{2\alpha^2(g_l - g_s)^2 \mu_0^2}{3(\nu_{3P_1} - \nu_{3P_0})} B^2 \\ &= -23.3B^2 [\text{MHz}/\text{T}^2]. \end{aligned} \quad (6.19)$$

With $B = 18.62 \text{ mT}$, the quadratic Zeeman shift is 4.34 kHz.

The light shift (Δ_L) on the clock transition frequency ω_{21} is [42]

$$\begin{aligned} \Delta_L &= \frac{\Omega_L^2}{4(\nu_{3P_1} - \nu_{3P_0})} \\ &= -18I [\text{mHz}/(\text{mW}/\text{cm}^2)], \end{aligned} \quad (6.20)$$

where I is the intensity of the interferometric laser beam. If we maintain the same intracavity power $P_0 = 289 \text{ mW}$ and the interferometric beam waist at $100 \mu\text{m}$, the light intensity of $I = 3.6 \times 10^6 \text{ mW}/\text{cm}^2$ is obtained, and we obtain an AC Stark shift $\Delta_L = 64 \text{ kHz}$.

The effective Rabi oscillation The effective Rabi frequency for single-excitation of the clock transition, enabled by coupling the $5s5p\ ^3P_0$ and $5s5p\ ^3P_1$ states via the magnetic dipole, is [42]:

$$\begin{aligned}\Omega_R/2\pi &= \frac{1}{\hbar}[d_1^R\langle^1S_0||P^{(1)}||^1P_1\rangle + d_3^R\langle^1S_0||P^{(1)}||^3P_1\rangle](\vec{E} \cdot \vec{B}) \\ &= 0.3\sqrt{\Delta_B\Delta_L}\cos\theta \\ &= 5\text{ [kHz]}\end{aligned}\tag{6.21}$$

The excitation rate For the atomic system we just described, the excitation fraction P is approximated as,

$$P = \frac{\Omega B\tau}{1 + \Omega^2\tau/A_{MIT}}(d_1^R\langle^1S_0||P^{(1)}||^1P_1\rangle + d_3^R\langle^1S_0||P^{(1)}||^3P_1\rangle)\sin(\Omega\pi t).\tag{6.22}$$

A π laser pulse ($t = 1/(2\Omega)$) is used to excite ^{88}Sr atoms from the ground state to the excited state. With a light intensity equal to 3.6 W/cm^2 , the excitation fraction can reach 35%.

This loss of atoms by spontaneous emission causes an increase in the quantum projection noise by a factor of $1/\sqrt{P_r}$, where $\sqrt{P_r}$ is the remaining fraction of atoms in the interferometer ($P_r = \exp[-\frac{4L\cdot N}{c} \cdot \Gamma_0]$), with an excited clock state decay rate Γ_0 , a baseline L , and diffraction order N .

The expansion dynamics At the regime of interest, the thermal bosonic ensemble is non-interacting and collisionless, and its evolution in the phase-space follows Liouville's theorem (phase-space density conservation) [245]. We assume a DKC pulse so short that the spatial distribution is left unchanged while the momentum is changed instantaneously [246]. The size of atomic cloud at $t = t_{\text{DKC}}$ becomes

$$L(t = t_{\text{DKC}}) = L_i/\sqrt{\theta_i}(t_{\text{DKC}}),\tag{6.23}$$

where $L_i = L(t = 0)$ is the initial size of the atomic cloud, θ_i is the scaling factor similar to the spatial scaling parameter and is studied in [247]. After the implementation of the harmonic lensing potential, the atomic cloud experiences a linear expansion during the interferometry sequence ($t_{\text{DKC}} < t < 3T$) like

$$L(t) = 2\sqrt{L^2(t = t_{\text{DKC}}) + t^2 K_B T_a \theta_i(t_{\text{DKC}})/m}.\tag{6.24}$$

The atomic cloud expands after its release from the trapping potential without changing its shape and can then be described by a size $L_i(t)$ evolving with time. i denotes the spatial coordinate x , y , and z .

The required magnetic field In this experimental scheme we propose, the MIT scheme is implemented to control the interaction between cold atom and IB (see Fig. 6.3), instead of conventionally turning OFF the IB. The speed of switching ON/OFF the magnetic field B is critical. The magnetic field is generated by two current-carrying coils (AWG 18) in Helmholtz configuration, creating a homogeneous DC-applied \vec{B} field of ~ 110 Gauss at the center. The self-inductance of the two coils is $2 \times 1.0448 \mu\text{H} = 2.0896 \mu\text{H}$; and the resistance is $2 \times 7.89 \text{ m}\Omega = 15.78 \text{ m}\Omega$. A 20Ω resistor can be added to the current decay path to speed up the energy decay stored in the two coils when the magnetic field is switched off. The time constant is $\tau = L/R = 2.0896/20 \sim 105 \text{ ns}$ [248], which is fast enough to turn ON/OFF the coupling between the light and atom (see Appx. B).

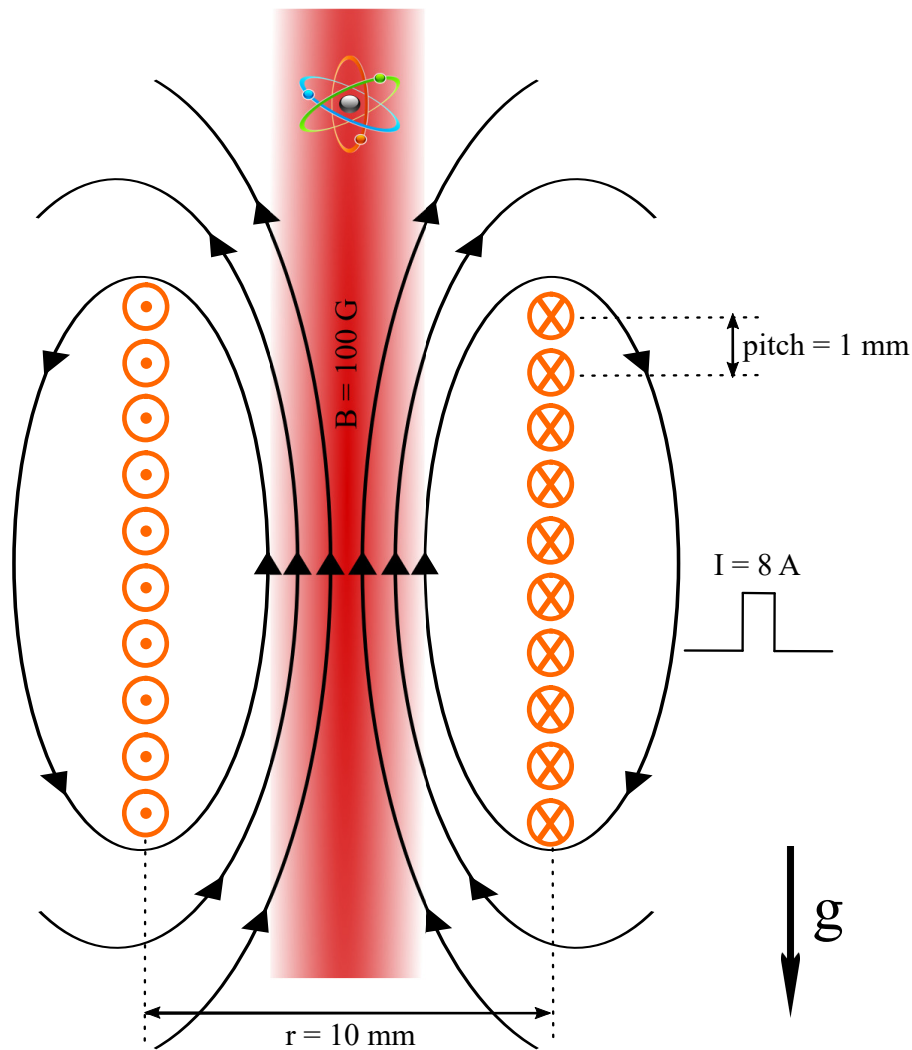


Figure 6.3: In a vertical ^{88}Sr -atom gravimeter, the interaction between cold atom and the IB is enabled/disabled by pulsing ON/OFF a magnetic field \vec{B} generated by a solenoid with a vertical axis. The atoms are falling on the axis of the solenoid, where a light beam resonant with the nominal clock transition is aligned as well.



Appendix

Appendix A

FPGA-based experimental control system

A control hardware based on a field programmable gate array for experiments in atomic physics

Cite as: Rev. Sci. Instrum. 91, 033203 (2020); doi: 10.1063/1.5129595

Submitted: 30 September 2019 • Accepted: 19 February 2020 •

Published Online: 5 March 2020



View Online



Export Citation



CrossMark

A. Bertoldi,¹ C.-H. Feng,¹ H. Eneriz,¹ M. Carey,^{1,2} D. S. Naik,¹ J. Junca,¹ X. Zou,¹ D. O. Sabulsky,¹ B. Canuel,¹ P. Bouyer,¹ and M. Prevedelli^{3,a)}

AFFILIATIONS

¹LP2N, Laboratoire Photonique, Numérique et Nanosciences, Univ. Bordeaux-IOGS-CNRS:UMR 5298, F-33400 Talence, France

²School of Physics and Astronomy, University of Southampton, Highfield, Southampton SO17 1BJ, United Kingdom

³Dipartimento di Fisica e Astronomia, Università di Bologna, Via Bertini-Pichat 6/2, I-40126 Bologna, Italy

^{a)}Author to whom correspondence should be addressed: marco.prevedelli@unibo.it

ABSTRACT

Experiments in Atomic, Molecular, and Optical (AMO) physics require precise and accurate control of digital, analog, and radio frequency (RF) signals. We present control hardware based on a field programmable gate array core that drives various modules via a simple interface bus. The system supports an operating frequency of 10 MHz and a memory depth of 8 M (2^{23}) instructions, both easily scalable. Successive experimental sequences can be stacked with no dead time and synchronized with external events at any instructions. Two or more units can be cascaded and synchronized to a common clock, a feature useful to operate large experimental setups in a modular way.

Published under license by AIP Publishing. <https://doi.org/10.1063/1.5129595>

I. INTRODUCTION

Computer control of experiments is a common task of ever increasing complexity in physics. The implementation of long sequences of events where different instruments must execute commands at a given time is mandatory for all but the simplest experiments.

In the past, the number of computer controlled instruments was relatively small and the type of interfaces was often limited to general-purpose interface bus (GPIB) and RS-232. It is now common to require the control of tens of instruments via the universal serial bus (USB), Ethernet, PXI, VXI, and others, in addition to the legacy interfaces mentioned above. The problem of computer control is aggravated by the need to make frequent changes both to the experimental sequence and the set of instruments; versatility and ease of programming are essential features. Moreover, both software and hardware obsolescence can play a role since the lifetime of an experiment is typically longer than the time scale over which operating systems and computers' architectures evolve. From the software point of view, the problem has been tackled by

developing libraries with a unified syntax for many interfaces¹ and complete frameworks,^{2,3} aimed mostly at large scale experiments in particle physics.

Here, we focus on the specific problem of controlling Atomic, Molecular, and Optical (AMO) experiments where usually outputs are limited to digital and analog signals changing according to a well defined temporal schedule. By "well defined," we mean that most operations must take place with a strict temporal resolution, typically of the order of 10 μ s or better for a cold atom experimental setup. It is generally not possible to fulfill such a constraint with a modern general-purpose multitasking operating system (OS), so dedicated OSs have been developed. Both commercial⁴ and open-source⁵ real-time operating systems (RTOSs) are available. Reasonably complex AMO experiments⁶ have been controlled with the RTOS described in Ref. 5. While the software approach has the advantage of simplicity, versatility and, in the case of open-source solutions, low cost, a hardware one has generally superior performances in terms of temporal resolution. In the latter case, it can actually be implemented in a finite-state machine (FSM) synchronous with a common master clock (MC), where the

digital outputs of the FSM, interpreted as commands by some auxiliary hardware modules, are sent out only at state transitions. The actual execution time of a command clearly depends on the module response time, cable induced delays, etc. Often, however, for a MC in the 1–10 MHz range and typical AMO laboratory size experiments, these effects can be neglected, at least for digital signals, so delay and jitter are both a small fraction of the MC period. A possible implementation of the FSM mentioned above is a digital pattern generator (DPG), i.e., a device that stores in its internal memory a two-column matrix, where the first column represents a time interval expressed in MC cycles, while the second column gives the state that a sufficiently large number of digital outputs should assume at that transition time. Often, as in our case, it is more convenient to store not the absolute time but the interval from the previous transition to increase the maximum time span of a pattern.

Once the matrix is loaded into the DPG memory, execution can be started via a software command or an external hardware trigger. DPGs are commercially available⁷ or have been implemented in software in dedicated microprocessors running a single process, i.e., a delay loop.⁸ The abundance on the market of plug-in modules carrying a field programmable gate array (FPGA), plus a synchronous dynamic random access memory (SDRAM) chip, and some kind of fast interface, usually USB or Ethernet, gives the possibility of implementing high performance DPGs using a low-cost and easily available, credit-card size modules. Note that the most recent, high performance, FPGAs might be available on a module quite before they find their way into full-featured commercial products.

A home-made DPG based on open-source software is more resilient, in our experience, to the main problem plaguing control hardware setups: obsolescence. Closed-source drivers for plug-in PC boards might not be updated for new OS versions after a few years; even the connectors used to fit the boards in the PC may disappear! The shelf life of a FPGA-based module is short, but given its limited cost, it is very convenient to stockpile them while available. When, eventually, the module becomes obsolete, migrating to an updated version requires a relatively minor effort involving redesigning the printed circuit board (PCB) hosting the module and porting mostly open-source software and firmware.

DPGs can be used to drive directly the digital output lines of control hardware, as suggested in Ref. 8, but versatility can be added by connecting a DPG to a primitive digital bus with address and data sections. The DPG acts, then, as a master module and performs timed write operations on auxiliary modules, implementing standard functions such as control of digital and analog outputs (DO and AO, respectively) or radio frequency (RF) outputs (RFO). We define, for brevity, the combination of DPG and auxiliary modules operating synchronously with the MC as “synchronous control hardware” (SCH). A PC, possibly running a RTOS, usually takes care of the rest of the instruments, performing tasks that are not time-critical, using software timers.

This basic architecture has been adopted by many different groups in AMO physics, and multiple designs have been published in the literature ranging from specific applications⁹ to complete general-purpose designs including both software and hardware descriptions.

These solutions allow control of complex AMO experiments developed for diverse research fields ranging from quantum metrology,¹⁰ frequency standards,¹¹ to quantum simulation.¹²

Some recent articles published in this journal are, in chronological order, Refs. 13–19; together with references therein, they give a broad review on the subject. Moreover, various groups report online on their control systems.^{20,21} As we mentioned above, obsolescence is often the main limiting factor for these designs so, usually, any hardware that is maybe ten years old or more is using some outdated or hard to find components. For example, parts of the circuit described in Ref. 13 are implemented with obsolete medium scale integrated circuits, while the control systems described in Refs. 15, 20, and 21 employ PC plug-in and/or PXI cards not in production anymore.

We present here the SCH that we developed for cold atom experiments in atom interferometry²² and cavity QED with Bose-condensed gases,²³ focusing specifically on our latest DPG, capable of storing up to $8\text{ M} = 2^{23}$ instructions (see Ref. 24), controlling up to 128 auxiliary modules and running with a MC of 10 MHz, which could also be used by itself, as a replacement for the design discussed in Ref. 8.

The main difference between our design and most of those recently published is essentially a simpler centralized architecture instead of a distributed one.

As an example, Refs. 17–19 share the same architecture implemented in Ref. 13, where every intelligent module (IM),²⁵ i.e., a module implementing a bidirectional fast communication interface, carrying a FPGA or a central processing unit (CPU), has a comparatively small first-in-first-out (FIFO) instruction buffer but communicates with the PC or other modules to receive data even when executing a sequence of instructions. In this way the maximum sequence length is not limited by the FIFO size.

Moreover, in order to strictly bound the worst case delay for arbitrary large systems, each module usually drives only a rather limited number of outputs, compared to our design. This allows arbitrary expansion of the control hardware without any increase in latency.

By comparison we take advantage of the large amount of SDRAM currently available and its large readout bandwidth to implement a centralized system with just one IM that will be sufficient to drive enough outputs to control most AMO experiments. This reduces the complexity of all the auxiliary modules, since none of them has to be an IM, without a serious loss of performance.

It should be mentioned that an intermediate solution has been also adopted^{14,15} by storing the columns of the DPG matrix in separate devices. A master module stores the first column, i.e., the temporal data, and sends a pseudoclock signal to the auxiliary modules. A pseudoclock has a positive edge transition synchronous to the MC only when any of the auxiliary modules must change its output. Each auxiliary module, in turn, stores its version of the second column of the DPG matrix, i.e., the output data, in an internal FIFO. An excellent discussion of the pros and cons of this approach can be found in Sec. III of Ref. 14.

In the following sections, we describe in detail the architecture of the our SCH (Sec. II) and, specifically the DPG performance and the RFO modules (Sec. III). Finally in Sec. IV we discuss possible improvements.

In order to provide useful material both to those interested in a complete, out-of-the-box, control system and to those that would like to modify our work or to integrate parts of it into other available designs, we provide the complete system documentation²⁶ including hardware design files and full source code for the firmware and the software.

II. SYSTEM ARCHITECTURE

The SCH interfaces with any PC using a USB 2.0 connection and synthesizes digital, analog, and RF signals for the experimental setup, as shown in Fig. 1.

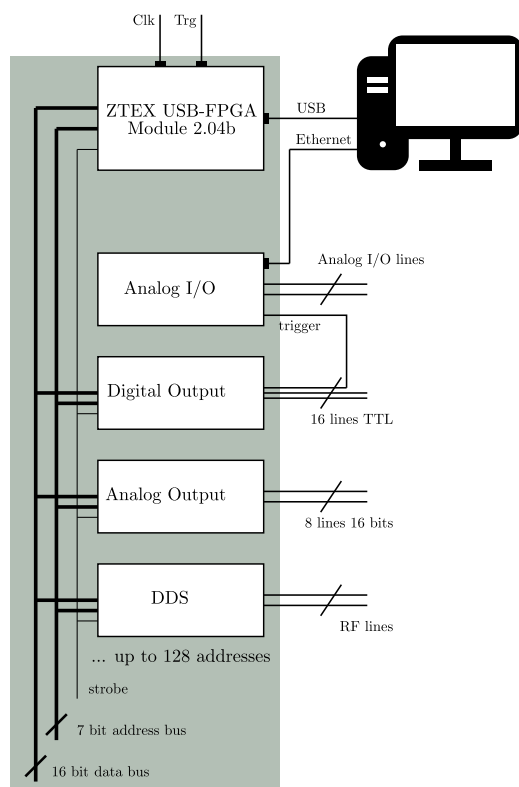


FIG. 1. Typical Architecture of the control hardware. The master controller is a FPGA card, connected to a PC via USB, driving modules via a digital bus. The system can be clocked internally or via an external signal connected on the “Clk” input; the program execution is controlled either via a software trigger from the PC or the “Trg” input. Up to 128 modules providing digital, analog, and RF outputs can be connected on the bus. The system can provide precise trigger signals to other hardware, here represented as a generic analog I/O unit, interfaced to the PC for programming and data acquisition.

The master module stores the instructions received from the PC and, after receiving a software or a hardware trigger signal, executes timed write operations on the bus, thus implementing the synchronous component of the control hardware. The bus has a data width of 16 bits and an address width of 7 bits. The only control signal is a strobe line since a master write is the only allowed bus operation.

To our knowledge this bus was originally developed in Paris about 20 years ago,²⁷ and is still in use at least as reported in Refs. 20 and 21.

Any auxiliary modules latch the content of data bus at the rising edge of the strobe signal when the content of the address bus matches the module’s address.

Due to the primitive nature of the bus, modules cannot return data to the master. Hence, whenever data must be acquired, some specific hardware, e.g., a digital oscilloscope or an analog-to-digital converter (ADC) sampling card, must be programmed by the PC via an external interface before starting the program execution and triggered, when required, by the SCH. Finally, at the end of the experimental sequence, data must be acquired, processed and stored by the PC before starting the next sequence.

A similar approach, based on triggering dedicated external instruments, can also be used for generating complex waveforms when it is impossible or impractical to use a standard AO channel controlled by the SCH. In Fig. 1, a module implementing the last two functions is represented as the generic analog I/O box.

Presently, only one module at a time can be addressed, limiting the possibility of a simultaneous change of the output lines. A detailed discussion on this point together with a possible improvement is deferred to Sec. IV.

A. Master module

The plug-in FPGA module implementing the DPG in the SCH is the USB-FPGA module 2.04b from ZTEX.²⁸ This module includes a Xilinx Spartan 6 FPGA, interfaced to USB 2.0 via a Cypress USB-FX2 microcontroller, and to a 64 Mbytes, double data rate (DDR) SDRAM chip via a 16 bits bus capable of running at 200 MHz. The module hosts a serial EEPROM to store the FPGA firmware.

The FPGA module is used to control the peripheral cards via a parallel and write-only bus. A series of write operations on the bus at specified time intervals can be downloaded in the board memory and later executed sending either a software command or a hardware trigger. We call each timed write operation an *instruction* and a series of instructions a *program*. The maximum size of a program is 8 M instructions, limited by the available SDRAM. For reference, a typical program length in our experiments is of the order of 10^4 instructions.

The module operates with a MC at 10 MHz, provided either from an external source or, for simplicity, synthesized from an onboard 24 MHz quartz of unspecified accuracy. Replacing the quartz with one of known specifications is a simple operation. Internally, the FPGA operates at $f_i = 200$ MHz. If f_c denotes the MC frequency a strobe pulse has a width of $1/2f_c$ and the temporal granularity of the SCH is $1/f_c$, i.e., 100 ns, which is adequate for most AMO experiments. On the other hand, the longest programmable

interval between two instructions is $(2^{36} - 1)/f_c$, corresponding to about 6872 s. Longer intervals can be programmed by inserting “dummy” write operations, i.e., instruction not followed by a strobe pulse. When using the external trigger, the input signal is sampled at f_i to reduce the risk of missing short pulses, but execution will start at the next positive edge of the MC, as expected in a SCH.

Since an instruction is coded by 8 bytes in the module’s SDRAM, the required peak bandwidth between the SDRAM and the FPGA is 76.3 Mbytes/s at $f_c = 10$ MHz. This is more than a factor 10 smaller than the peak bandwidth of 800 Mbytes/s achievable with this module; increasing f_c up to at least 40 MHz should be, therefore, possible.

The program is loaded into the module memory through the USB 2.0 bridge and a parallel interface from the microcontroller and the FPGA, whose bandwidth is limited at a measured average of about 5×10^5 instructions/s by the USB interface.

Break points can be inserted in a program after any instruction, in order to suspend execution with the output lines in a well determined state for debugging purposes or to wait for an external event. Program execution can be resumed with a digital signal or with a software command. This mode of operation can be exploited, for example, to synchronize the experiment with the power line, to reduce noise, and to monitor trap loading and trigger at a specified fluorescence level. A more complex SCH can be implemented by adding a cascade of ancillary master modules waiting for a trigger sent from an upper level in order to implement a tree structure similar to that described in Ref. 18. Clearly, in this case, an external common MC shared by all the modules should be used. This will be discussed in more detail in Sec. IV.

B. Auxiliary modules

Many auxiliary modules have been developed but the most common ones are of three types: DO, AO, and DDS-based RFO. In addition to these modules, a general-purpose analog I/O module for complex operations is often needed. Here we provide a quick overview of our most common modules even if they are not the main focus of this article; the target is to give an overview of all the hardware necessary for assembling a control hardware.

All the modules fit on 100 mm \times 160 mm Eurocard PCBs, to be mounted in 3U, 19” racks, and have their addresses programmed with miniature switches. The master module cannot read from the bus, so the software must have an *a priori* knowledge of auxiliary modules’ addresses and functions. A more advanced, self-configuring design, can be implemented, if desired.

The DO modules are just an address decoder and a 16 bits latch so when writing to a DO module the content of the data bus is stored and transferred to its 16 output lines. All the lines on the same DO module can be changed simultaneously while changes on lines on different modules are separated by at least one MC period.

The AO modules are almost as simple, including a 16 bits DAC per address, generating an analog voltage, typically in the ± 10 V range. Parallel input DAC with the inputs connected to the data bus are particularly convenient and, in order to increase the number of outputs per PCB, we have recently developed an 8 channel, 16 bits DAC with parallel input, based on the Texas

Instruments DAC8728. This AO module responds to 8 addresses, one for each channel. Again writing to different AO channels cannot be simultaneous. The minimum delay of 1 MC period is, however, often negligible when compared with the typical settling time of a DAC chip. As an example the DAC8728 has a settling time to 1 LSB for a full range voltage step of about 15 μ s. We will discuss in Sec. IV possible schemes to overcome this limitation.

The RFO modules are based on DDS chips from Analog Devices. Different chips have been adopted over time, depending on specific applications. Our most commonly used chip has been the AD9958, which has two independent DDSs channels clocked at 400 MHz and can generate RF signals up to 160 MHz with a frequency resolution of about 0.1 Hz. The output includes a +10 bit linear amplitude control. The maximum output power is +10 dBm.

For higher frequency and better resolution we have recently developed a module based on the AD9912 chip, a single channel DDS is capable of a maximum clock frequency of 1 GHz, producing a RF output up to 400 MHz with a resolution in the few μ Hz range. Amplitude control is provided by a programmable logarithmic attenuator with a dynamic range in excess of 30 dB in 0.25 dB steps (Analog Devices HMC759). The module output power is again at least +10 dBm.

We will refer in the following to the single channel and the dual channel modules as RFO1 and RFO2, respectively.

The RFO modules are the most complex modules and pose some challenges for inclusion in the SCH. For a precise arbitrary frequency ramp, some chips, i.e., the AD9954 or the AD9910, include an internal volatile memory where a table of arbitrary frequencies can be stored and later recalled automatically with a programmable delay between consecutive steps. The special case of a linear frequency or amplitude ramp is commonly implemented in hardware in many DDS chips, like the AD9958, so it is often sufficient to program the start and stop values, the step size and the dwell time at each point.

In both cases, however, a rather complex programming sequence is needed. Even a discrete frequency and amplitude step might require sending more than ten bytes to a DDS chip. Most chips have only a serial interface, so some logic is required to convert the 16 bits read from the data bus, decode them, and finally send the proper programming sequence to the DDS. This introduces a delay, between the moment when the command is issued and the one when the RF appears at the output, which can be large when compared with $1/f_c$. Moreover, 16 bits do not contain enough information to fully specify frequency and amplitude even for a single RF channel. There are two possible, simple solutions.

The first consists of assigning a separate address for frequency and amplitude for each RF channel and mapping, linearly, the values on the data bus to the frequency range actually required for a specific application. As an example, consider driving an acousto-optic modulator operating at its central frequency, in this case of $f_0 = 80$ MHz. The -3 dB bandwidth of the modulator is typically limited to $f_0 \pm 30$ MHz so the 2^{16} values on the data bus could specify, a frequency in the interval 50–110 MHz with a frequency resolution of the order of 1 kHz, which is adequate for most applications.

The second possibility is to use the content of the data bus as a pointer to a lookup table (LUT) stored in memory on the RFO module, where the complete state of a DDS driving RF channel is stored. The total number of combinations of frequency and amplitudes typically used in a given experimental sequence is a small fraction of all the possible values given the DDS resolution. This offers versatility at the cost of the increased complexity of generating and sharing the LUT tables between the modules and the PC.

In both cases, the module must include memory and processing capabilities. The two natural choices are a FPGA or a microcontroller. A FPGA will allow driving the DDS serial interface at a speed close to the maximum bandwidth, minimizing the output delay but with greater complexity and cost. A microcontroller, on the other hand, will provide a simple and cheap solution with a larger delay.

Our RFO modules include a microcontroller with USB interface (Microchip PIC 18F2550) and use the LUT model. The LUT is loaded and updated in the microcontroller's flash memory from the PC via USB. Both RFO modules share the same PCB hosting the microcontroller and the bus interface while the DDS and the other RF components are on a separate daughter-board. This modular structure simplifies the upgrades necessary when better DDS chips become available.

The typical delay between a write operation and the RF output change is of the order of a few tens of μs , specifically 30 μs per channel when changing both frequency and amplitude with the RFO2 module and about 25 μs for the same operations for the RFO1 module.

When this sort of delay is not acceptable we can adopt a partial workaround: most DDS chips have double-buffered registers, meaning that the new frequency, amplitude, etc. are preloaded in buffers and transferred to the DDS core only after pulsing a dedicated line. We usually have the microcontroller applying the pulse as soon as the data are sent, but we have the option to delay the pulse with a second write operation on the bus. This means that we can change the RF output synchronously with bus write operations as soon as we allow enough time, as specified above, between two consecutive state changes. Note that for the RFO1 module this method does not apply since the amplitude control is implemented with an external attenuator.

More advanced, albeit more complex, FPGA-based DDS designs have been published in Refs. 16 and 18.

Except for the "Trg" and "Clk" lines (see Fig. 1), this control hardware does not provide integrated input lines, either digital or analog, given the unidirectional nature of the system bus. The possibility to acquire signals is implemented with external hardware synchronized by DO lines: for example, the open-source STEMlab 125-14 module²⁹ can provide 2 inputs sampled at up to 125 MHz, with 50 MHz analog bandwidth and 14 bit amplitude resolution, and auxiliary analog inputs at 250 kHz with 12 bit resolution. The STEMlab board provides analog output lines with comparable bandwidth and resolution, and 16 general-purpose input/output (GPIO) lines. A STEMlab module can be triggered at the desired time by a DO line, while communication with the PC controlling the experiment uses a 1 Gbit/s Ethernet interface, as shown in Fig. 1. Typically this module provides the analog input (AI) function for, i.e., sampling the fluorescence signal of a detection photodiode. The board can process, store and finally notify the PC that the data acquired are available.

For convenience we have prepared a simple PCB hosting the STEMlab board to derive its supply and to be mounted in a 19" rack with the other modules.

C. Software

There are a few different software layers in a control system. In our experience, trying to use open-source or, at least, free software at every layer minimizes obsolescence and portability problems. Hardware and software are as independent as possible in this system, to allow for partial or incremental upgrades.

The firmware required by the auxiliary modules, notably the aforementioned RFO modules, includes the code for the microcontroller written in C and compiled with an open-source compiler for small devices, SDCC³⁰ and some simple Verilog code for a complex programmable logic device (CPLD) that provides the interface to the bus. The LUT size, stored in the microcontroller flash memory, is 16 kbytes, sufficient for storing, for example, 2048 different combinations of amplitude and frequency for the RFO1 module or 1024 combinations of frequency, phase and amplitude for each channel of the RFO2 module.

We have actually developed two different firmware versions for the RFO2 module. The first one, simpler and sufficient for most applications, only sets phase, frequency and amplitude for each channel. The second takes full advantage of the chip's capabilities, allowing linear frequency (amplitude, phase) ramps and frequency-shift (amplitude-shift, phase-shift) keying modulation up to 16 different values.

For the RFO2 module, therefore, specifying values for the LUT is complex enough that we have chosen to implement a description based on the extensible markup language (XML) format, while for the RFO1 a simple text file with frequency-amplitude pairs is used.

The master module requires firmware for the FPGA and for the microcontroller controlling the USB interface.

The master module actually comes with an open-source default firmware for the microcontroller, implementing a high speed bridge from the USB to the FPGA that we found adequate for our purposes. The code can be easily modified and recompiled with SDCC if required.

The firmware for the FPGA is written in Verilog and compiled using the free version of the design software provided by Xilinx.³¹ The code uses, whenever convenient, proprietary black-boxes that are freely available but not open-source. Specifically in this design we take advantage of the SDRAM controller and the FIFO generator. For a migration to full open-source code, we remark that the most complex module is the SDRAM controller and it could be replaced with designs from open-source repositories such as Ref. 32.

The Verilog code includes a main FSM (MFSM) that accepts and executes the commands sent to the FPGA and, finally, replies to the PC when appropriate, a memory interface and the MC-synchronous FSM (SFSM).

The commands follow a simple custom protocol, documented in detail in Ref. 26. Here we provide just a quick overview. Every command is formed by two ASCII characters followed by parameters when required. Commands fall in the following four categories: trigger control, execution control, memory access and status request.

Trigger control commands select between an internal or an external trigger source. Execution control commands arm the trigger in external mode or start/resume execution in internal mode. There are also two stop commands for ending execution after the next instruction or forcing an immediate stop, respectively. This last command is useful since, as mentioned above, the next instruction could be scheduled after more than 6800 s.

Instructions can be loaded one at time in memory in random order. This is less efficient than grouping many consecutive instructions in a single packet but, on the other hand, it allows arbitrary incremental changes on a program already resident in memory, simplifying multiple executions of programs where only some instructions are changed, i.e., for parameter scanning. Due to this choice the command interpreter cannot easily determine if a program is complete so a specific command must be sent after loading the last instruction.

Finally a status request command returns to the PC a packet of data specifying the MFSM status (idle, waiting for trigger, running, stopped at a break point). In the last two cases also the current instruction number is returned.

Presently polling the master module via the status request command is the only way for the PC to determine when a program has terminated due to the USB bus nature (communication can be initiated only by the USB master, i.e., the PC). A possible improvement on this behavior will be discussed in Sec. IV.

As soon as a complete program is loaded, the memory interface starts reading from the SDRAM in bursts of four 16 bits-wide words, so that each burst corresponds to a single instruction, and feeds data to the input of a dual port FIFO 64 bits-wide with a depth of 512 locations inside the FPGA. The FIFO acts as buffer to provide data to the SFSM even when the SDRAM is busy performing refresh cycles. The combination of FIFO depth and average SDRAM bandwidth guarantees, as shown in Sec. III, that the maximum execution rate of an instruction per MC cycle can be sustained indefinitely.

The SFSM fetches the next instruction from the FIFO just one MC cycle before the current instruction is executed and performs a sequence of operations that, as a first step, involve splitting the instruction in its four components:²⁶ the 7 bits address, the 16 bits data, the 36 bits time interval and the 5 control bits. Presently only 3 control bits are used. They are used to mark the last instruction, set a break point and, finally, enable the generation of the strobe pulse. Note that not firing the strobe pulse can be useful both inserting

dummy instructions in order to increase the maximum time interval between instructions and to disable the execution of few selected instructions for testing.

The main control program runs on the PC and it is the last software layer. It is responsible for taking a “user friendly” description of the program, usually a timeline of each output, and translating it into a sequence of instructions for one or more DPGs. The concept of “user friendly” is so highly subjective, that has led to a myriad of different solutions. Here, we mention the most recent ones of which we are aware, namely, Refs. 14, 15, and 18. We point out that while Ref. 15 uses a graphics library that runs only under the Windows OS, Ref. 14 is written in Python and Ref. 18 is written in C++, and both use a graphics library available for the most common OSs.

We are confident that adding support for our SCH to both the programs mentioned above should be relatively simple, however, have ported to our DPG two different programs that were previously developed for different hardware, one written in C and the other in Python, following, respectively, the two approaches described above. The source code for both of them is available.²⁶

A useful feature that we included in both codes is the possibility to write a file with a graphical representation of the program regardless of the way in which it was originally generated, in order to have a quick visual check of the experiment: the IEEE standard 1364-2001³⁴ specifies a format for the output of hardware simulations called value change dump (VCD) for which a full-featured open-source viewer is available.³⁵ A VCD file representing a program is a very helpful tool to check what a program does. Figure 2 shows, as an example, the screenshot of the VCD viewer applied to an experimental sequence involving three signals: the current in two electromagnets and the state of an optical shutter, controlled by a digital output line. The sequence is similar to that reported in Fig. 2 in Ref. 14.

Adopting a control program for an experiment is a choice that ultimately depends on the end-user and will inevitably change over time. We think that a wise choice relies on open-source code that can run on multiple OSs. When designing a master module, the best solution is to use a simple set of commands that can be implemented using as many programming languages as possible, letting the users choose the control program that best suits their needs. As we have seen, our master module communicates through USB packets implementing the commands briefly discussed above, in order to be usable with a broad range of

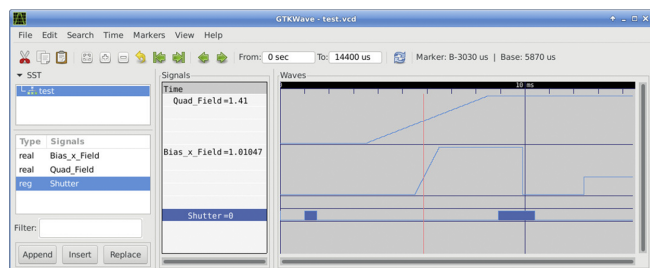


FIG. 2. Screenshot of a VCD file viewer.³³ The traces shown are similar to Fig. 2 from Ref. 14, for comparison, and show the timeline of the current in two electromagnets and the status of a shutter. The viewer offers many possibilities to customize the output format and cursors for measuring times, time differences, and the amplitudes of analog signals.

commercial software programs, such as Labview, or programming languages.

III. CHARACTERIZATION/PERFORMANCES

The modular design of the control hardware allows for easy customization of the configuration to meet the specific requirements of the experiment, in terms of the number and type of output signals. Typical instruments that are controlled directly or through specific drivers by such systems include: optical shutters, acousto- and electro-optic modulators, electromagnets, electronic switches, and CCD cameras. Here we would like to focus mainly on the characteristics of our SCH.

Two features of our master module are noteworthy, namely, its ability to operate at full speed, i.e., to send a command at every MC transition and the possibility to pause and re-trigger using external signals in the same program, at will.

The transmission bandwidth between the SDRAM and the FPGA is sufficient to maintain the peak speed of one instruction per MC cycle, indefinitely at $f_c = 10$ MHz. This is shown in Fig. 3, where a burst of 8 M transitions of a digital output of a DO module, limited only by the SDRAM size, is shown.

Synchronization of the program execution is critical in AMO experiments. The measurement precision can be improved by synchronizing part of the experimental sequence with external signals, as discussed in Sec. II A. Moreover, complex setups composed of independently controlled, spatially separated sub-units require a precise synchronization to achieve optimal performances.

Since break points can be inserted in the program at any instruction and the execution resumed via a software command or hardware trigger using a dedicated “Trg” digital input (see Fig. 1), it is simple to synchronize DPGs and relative modules to a master DPG unit. In Fig. 4, we show an example of break points with hardware retriggering. The toggling of a digital output line (red signal) is suspended three times, and each time execution resumes at the first positive edge of the Trg input (blue line), in this case

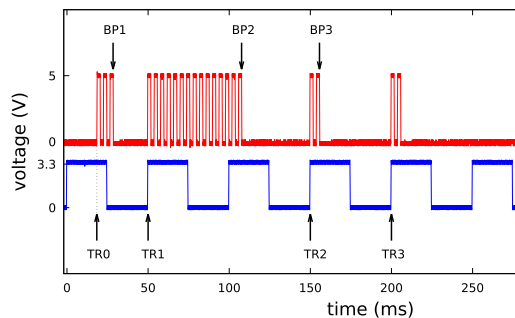


FIG. 4. The sequence in the red trace is triggered via software at a time indicated by TR0 and shows the digital output commutating every 2 ms, hitting 3 break points, after commutating 6, 30, and 4 times, respectively. The three break points are indicated by the labels BP*n*. The sequence resumes on the positive edges of the blue trace, a square wave at 20 Hz, at the times labeled by TR*n*. After TR3, the sequence ends with 4 last commutations of the digital line.

provided by a 20 Hz square wave. Since the output will always be synchronous with the MC and an extra MC cycle is internally used to change state, the worst case latency between the rising edge of Trg and the resuming of execution will be $2/f_c$ or 200 ns in this example. This is, of course, how a SCH is supposed to work and a reduction in latency can only be achieved by increasing f_c .

We have discussed above why, due to the synchronous nature of our hardware, presenting delay and jitter measurements of the DO and AO modules will provide limited information. The delay is dominated by cable length for the DO modules and by DAC settling time for AO modules while jitter is expected to be negligible when compared with $1/f_c$.

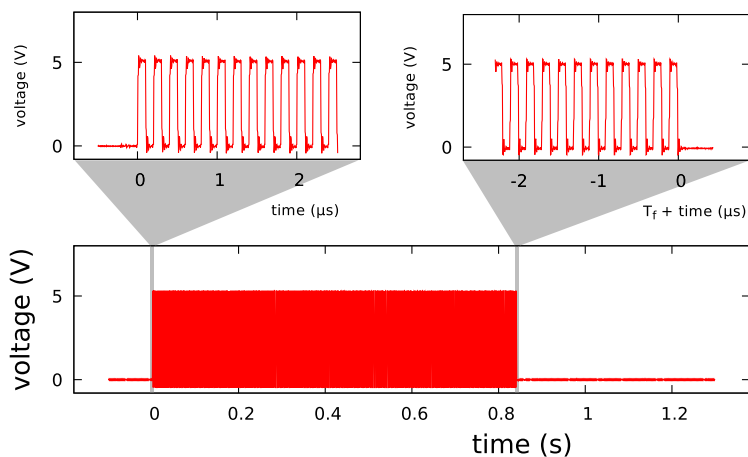


FIG. 3. A digital output line is toggled every 100 ns, i.e., at the full rate given by the 10 MHz signal used to clock the system, for $8\text{ M} = 2^{23}$ times (see Ref. 24). The 5 MHz square wave burst periodicity of the commutating digital output is maintained for the whole sequence, as highlighted by the insets showing the beginning and the end of the program. The time for the final section of the sequence is referred to the falling edge of the last pulse.

It is instead worth showing the use of double-buffered registers in the AD9958 DDS to implement limited strictly synchronous capabilities of the RFO2 module.

Normally a command to the RFO2 module uses the first 10 bits on the data bus to specify an entry in the 1024 elements LUT table. The frequency and amplitude for each channel corresponding to that entry – the phase is not usually changed – are loaded into the the DDS chip by the microcontroller via a serial interface. As mentioned above, this takes about 30 μs per channel. As soon as the DDS registers are loaded, the microcontroller pulses a dedicated line actually forcing the new frequency and amplitude to appear at the RF outputs with a delay of few tens of ns. Both the presence of the update pulse and the action of programming the DDS are independently enabled by separate bits on the data bus. New values can be preloaded in the DDS without forcing an update and, later, an update pulse can be applied, without reprogramming the DDS, to change the output in synchronously to a given MC transition.

This is shown in Fig. 5 where the two channels of a RFO2 module initially at 100 MHz, half power (blue) and 50 MHz, full power (red), exchange frequency and amplitude upon receiving an update command from the master module. The pulse is not shown but, for reference, the black trace shows an output line of a DO module generating a pulse with the rising and falling edges one MC cycle before and after, respectively, the update command.

The RF outputs change amplitude and frequency well within 100 ns, meeting the requirements for synchronous operation. Note that the amplitude changes before the frequency. This is in agreement with the DDS datasheet³⁵ where the minimum latencies for amplitude and frequency are specified as 17 and 29 internal clock cycles. Since the DDS is clocked at 400 MHz, the expected latencies are about 42.5 ns and 72.5 ns, respectively, so amplitudes are expected to change about 30 ns before frequencies. These latencies are limited by the DDS itself, therefore, compare

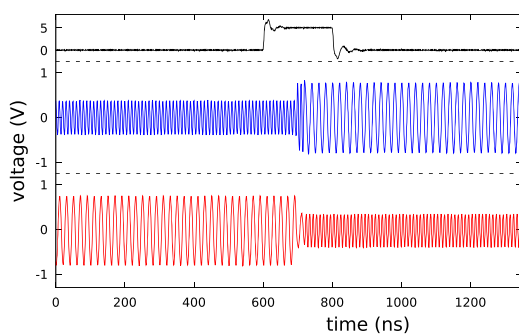


FIG. 5. The RF outputs of a dual channel DDS module initially at 100 MHz, half power (blue trace) and 50 MHz, full power (red trace), exchange frequency and amplitude upon receiving an update command from the master module. For reference a digital line (black trace) generates a 200 ns pulse, centered around the update command. The amplitude change occurring few tens of ns before the phase-continuous frequency change is consistent with the DDS specifications.³⁵

favorably even with those reported using high speed FPGA to DDS interfaces.¹⁶

The update rate is, however, limited to about 16 kHz by the time required to pre-program the DDS registers. Faster rates can be obtained using frequency-shift (amplitude-shift) keying modulation if only one between frequency and amplitude must be changed and no more than 16 different values for a single channel, are required.

The outputs of the RFO2 module share the same clock so keep a definite phase relation when generating the same frequency. The phase offset $\Delta\phi$, however, depends from the previous history of the channels. It is possible to set $\Delta\phi$ to zero by resetting simultaneously the phase accumulators of both channels inside the DDS chip. Later $\Delta\phi$ can be set to any desired value in the $[0, 2\pi]$ interval with a resolution of 14 bits. The option to set $\Delta\phi = 0$ is not implemented in the current firmware version but can be add, if required.

IV. FURTHER DEVELOPMENTS

The DPG performances can be readily improved by adopting a more powerful FPGA module. This also shows how our approach can tackle obsolescence. The ZTEX 2.13a, from the same manufacturer,²⁸ is essentially pin-compatible but uses more recent and powerful components, i.e., a Xilinx Artix-7 FPGA and a 256 MBytes DDR3 SDRAM at 400 MHz, bringing the number of instructions to 64 M and doubling SDRAM peak bandwidth. As a test we have ported, compiled and simulated the Verilog firmware for this module³⁶ but, so far, we have not acquired a physical unit for testing. Note that the ZTEX 2.13a requires a different set of development tools.^{36,37} Using this module pushing f_c to at least 50 MHz should be relatively simple.

Although most experiments will probably need only one DPG module, as we mentioned above, multiple modules can be cascaded and synchronized using break points either for convenience or necessity.

As an example of the first, consider auxiliary modules distributed on 19" racks in different parts of a laboratory. Carrying around long flat cables for distributing the 24 lines of the SCH bus rather than just 2 BNC cables carrying the MC and a DO line from the master DPG rack acting as a trigger would be both unpractical and possibly prone to noise, especially at high f_c .

In the case of the underground, 150 m long atom-laser antenna MIGA (Matter wave-laser based Interferometer Gravitation Antenna),²² a demonstrator we are developing for atom interferometry based gravitational wave detection, multiple DPGs will be instead mandatory. There different atom interferometers, with their electronic subsystems, will be separated by a distance of the order of 100 m so the issue of achieving synchronous operation when the transmission delay is large with respect to the MC period must be addressed.

We have not included in the DPG firmware a syntax for implementing loops which are instead “unrolled” by the PC code before sending a program to the master module. Due to the large amount of memory available and the high communication bandwidth, presently we do not consider this inefficiency as a limiting factor. A more evolved firmware can, nevertheless, be developed.

By using a distribution amplifier and cables with matched lengths, sufficiently coherent copies of the MC can be distributed

among the various subsystem, then the propagation delay between the master DPG and each auxiliary DPG must be determined with an uncertainty better than one MC cycle. Using either BNC cables or optical fibers this corresponds to an uncertainty, in length, that, at $f_c = 10$ MHz, should be small when compared to 20 m. The master DPG then must send a trigger pulse with the correct timing to obtain a distributed SCH.

If simultaneous change of outputs across different DO and AO modules is required, multiple solutions are possible. First, as described above, multiple DPG modules could be used.

As an alternative, with a single DPG, it is possible to reserve a specific address for sending trigger commands. Any DO or AO module decoding both their address and the trigger address could interpret then the content of the data bus as 16 independent trigger lines. This approach requires, however, the design of a new set DO and AO boards where the bus interface is implemented using CPLDs rather than standard TTL chips.

An obvious way to achieve rapid switching of analog outputs is using auxiliary modules containing some 2^n -to-one analog multiplexers, where 2^n analog outputs and n digital outputs are required for a single, fast switching, analog output among 2^n preset values. The cost in term of hardware resources is compensated by a switching time limited not by the DAC but by the multiplexer.

As we mentioned before, a DPG module with only a USB interface has the disadvantage that it cannot initiate communication. Moreover, including an Ethernet interface to our SCH will help integration with other systems. Both issues can be solved by adding a simple auxiliary credit-card size computer with USB and Ethernet interfaces and digital input signals capable of generating interrupts, acting as bridge and, possibly, as protocol translator between the DPG and other hardware. The DPG could use one of the DO lines to fire an interrupt in the auxiliary computer, which will forward a service request to the main PC via Ethernet. An obvious application could be notify program termination instead of relying on polling.

Even without hardware changes there is room for software improvements that, mostly, could improve reliability. A simple example is given by the handling of break points. Presently the software in the PC can easily determine, by polling, how long the DPG has been waiting at a break point. It could be useful to set a sensible timeout policy to resume execution or abort the program and set the experiment in a safe condition.

V. CONCLUSIONS

We have presented a control hardware developed for experiments in AMO physics; it is broadly applicable to experimental science. The system provides up to hundreds of digital, analog, and RF signals controlled with a time resolution of 100 ns, with a wealth of possible configurations. The program execution can be synchronized with external events at multiple times in the same sequence. Several improvements can be easily adopted to the system: the time resolution could be increased by a factor of 5–20 ns by changing the main clock frequency and with simple modifications of the firmware; the maximum number of instructions in a program could be increased by a factor of 4 by adopting a different FPGA board. The modular nature of the system makes it easy to adapt parts of it,

especially the low-cost DPG module, to other applications and make it more resilient against inevitable obsolescence. In general, the system could be engineered to be compatible with portable or space applications, in terms of weight, volume, and power consumption.

ACKNOWLEDGMENTS

This work was partly funded by the “Agence Nationale pour la Recherche” (Grant EOSBECMR No. ANR-18-CE91-0003-01, Grant ALCALINF No. ANR-16-CE30-0002-01, Grant MIGA No. ANR-11-EQPX-0028), Laser and Photonics in Aquitaine (Grant No. ANR-10-IDEX-03-02, project OE-TWR), Horizon 2020 QuanteRA ERA-NET (Grant TAIOL No. ANR-18-QUAN-00L5-02), and the Aquitaine Region (Project IASIG3D Grant No. 2015-1R60307-00005207 and Project USOFF Grant No. 2018-1R50309). M.C. acknowledges support by DSTL-DGA under Contract No. DSTLX-1000097855. M.P. would like to thank M. De Pas, M. Giuntini, and A. Montori for useful discussions and constant support at the electronic workshop of the European Laboratory for Nonlinear Spectroscopy (LENS), Firenze.

REFERENCES

- Virtual Instruments Software Architecture (VISA): www.ivifoundation.org/specifications. Both commercial (www.ni.com/visa) and public domain (github.com/hgrecco/pyvisa, limited to GPIB, USB and RS-232 so far) implementations are available. For the Linux OS an effort to a unified approach to data acquisition is represented by Comedi (comedi.org). We mention commercial products at the sole purpose of identification for helping the reader to reproduce our setup. We do not endorse any specific product. Products with similar or even better performances might be available.
- See www.tango-controls.org for Tango.
- See epics-controls.org for Experimental Physics and Industrial Control System (EPICS).
- See www.ni.com/en-us/shop/select/labview-real-time-module for as an example, National Instruments offers a real-time module for the Labview programming environment.
- Two real-time open source extensions for Linux are RTAI (www.rtai.org) and Xenomai (xenomai.org).
- G. Rosi, F. Sorrentino, L. Cacciapuoti, M. Prevedelli, and G. M. Tino, “Precision measurement of the Newtonian gravitational constant using cold atoms,” *Nature* **510**, 518 (2014).
- See, e.g., the National Instruments series of PCI boards (www.ni.com/en-us/shop/select/digital-waveform-device) or the PulseBlaster series at Spin Core (spincore.com/products/#pulsegeneration).
- R. Hořák and M. Ježek, “Arbitrary digital pulse sequence generator with delay-loop timing,” *Rev. Sci. Instrum.* **89**, 045103 (2018).
- B. S. Malek, Z. Pagel, X. Wu, and H. Müller, “Embedded control system for mobile atom interferometers,” *Rev. Sci. Instrum.* **90**, 073103 (2019).
- L. Pezzè, A. Smerzi, M. K. Oberthaler, R. Schmied, and P. Treutlein, “Quantum metrology with nonclassical states of atomic ensembles,” *Rev. Mod. Phys.* **90**, 035005 (2018).
- A. D. Ludlow, M. M. Boyd, J. Ye, E. Peik, and P. Schmidt, “Optical atomic clocks,” *Rev. Mod. Phys.* **87**, 637–701 (2015).
- I. Georgescu, S. Ashhab, and F. Nori, “Quantum simulation,” *Rev. Mod. Phys.* **86**, 153–185 (2014).
- P. E. Gaskell, J. J. Thorn, S. Alba, and D. A. Steck, “An open-source, extensible system for laboratory timing and control,” *Rev. Sci. Instrum.* **80**, 115103 (2009).
- P. T. Starkey, C. J. Billington, S. P. Johnstone, M. Jasperse, K. Helmerson, L. D. Turner, and R. P. Anderson, “A scripted control system for autonomous hardware-timed experiments,” *Rev. Sci. Instrum.* **84**, 085111 (2013).

- ¹⁵A. Keshet and W. Ketterle, "A distributed, graphical user interface based, computer control system for atomic physics experiments," *Rev. Sci. Instrum.* **84**, 015105 (2013).
- ¹⁶T. Pruttivarasin and H. Katori, "Compact field programmable gate array-based pulse-sequencer and radio-frequency generator for experiments with trapped atoms," *Rev. Sci. Instrum.* **86**, 115106 (2015).
- ¹⁷S. Bourdeauducq *et al.* (2018). "A leading-edge control system for quantum information experiments," Zenodo. <https://doi.org/10.5281/Zenodo.1492176>
- ¹⁸E. Perego, M. Pomponio, A. Detti, L. Duca, C. Sias, and C. E. Calosso, "A scalable hardware and software control apparatus for experiments with hybrid quantum systems," *Rev. Sci. Instrum.* **89**, 113116 (2018).
- ¹⁹S. Donnellan, I. R. Hill, W. Bowden, and R. Hobson, "A scalable arbitrary waveform generator for atomic physics experiments based on field-programmable gate array technology," *Rev. Sci. Instrum.* **90**, 043101 (2019).
- ²⁰See <http://www.strontiumbec.com/Control/Control.html> for Group of F. Schreck (Amsterdam).
- ²¹See <http://ew.lens.unifi.it/> for electronic shop at LENS (Florence).
- ²²B. Canuel, A. Bertoldi, L. Amand, E. P. di Borgo, T. Chantrai, C. Danquigny, M. D. Álvarez, B. Fang, A. Freise, R. Geiger, J. Gillot, S. Henry, J. Hinderer, D. Holleville, J. Junca, G. Lefèvre, M. Merzougui, N. Mielec, T. Monfret, S. Pelisson, M. Prevedelli, S. Reynaud, I. Riou, Y. Rogister, S. Rosat, E. Cormier, A. Landragin, W. Chaibi, S. Gaffet, and P. Bouyer, "Exploring gravity with the MIGA large scale atom interferometer," *Sci. Rep.* **8**, 14064 (2018).
- ²³D. S. Naik, G. Kuyumjian, D. Pandey, P. Bouyer, and A. Bertoldi, "Bose-Einstein condensate array in a malleable optical trap formed in a traveling wave cavity," *Quantum Sci. Technol.* **3**, 045009 (2018).
- ²⁴To avoid confusion, we will always use $M = 2^{20}$ and never $M = 10^6$ when referring to memory size and number of instructions.
- ²⁵We make a distinction between a master module and an intelligent one since in a distributed architecture many auxiliary modules are intelligent.
- ²⁶M. Prevedelli *et al.* (2019), "Yet another control system for AMO physics," Zenodo. <https://doi.org/10.5281/zenodo.3571496>
- ²⁷F. Schreck, "Mixtures of ultracold gases: Fermi sea and Bose-Einstein condensate of Lithium isotopes," Ph.D. thesis, University Pierre et Marie Curie - Paris VI, 2002.
- ²⁸See www.ztex.de for ZTEX FPGA Board with Open Source SDK, Models 2.04b and 2.13a.
- ²⁹See redpitaya.com for STEMLab 125-14, formerly Red Pitaya.
- ³⁰See sdcc.sourceforge.net for downloading the SDCC compiler.
- ³¹See www.xilinx.com/products/design-tools/ise-design-suite/ise-webpack.html for downloading ISE web edition.
- ³²See opencores.org for an open source repository of IP cores.
- ³³See gtkwave.sourceforge.net for downloading the GtkWave viewer.
- ³⁴IEEE Standard Verilog Hardware Description Language, IEEE Std 1364-2001, 1-792, 2001.
- ³⁵See www.analog.com/media/en/technical-documentation/data-sheets/AD9958.pdf for the datasheet of the AD9958 chip.
- ³⁶See www.cypress.com/documentation/software-and-drivers/ez-usb-fx3-software-development-kit for the software development kit for fx3 microcontrollers.
- ³⁷See www.xilinx.com/products/design-tools/vivado/vivado-webpack.html for downloading Vivado web edition.

Appendix B

Fast magnetic-field switch

Analogue switch

A load switch based on MOSFET provides a fast analogue approach to manage power on the load (3D MOT coils), like switching from blue MOT to red MOT. Since the N-channel with majority carriers of electrons has higher mobility than the P-channel with majority carriers of holes, the latter has lower $R_{DS(on)}$ and gate capacitance at the same die area. Blue MOT coils need $I=80$ A current to generate 50 G/cm magnetic field gradient, which belongs to the high current application. The N-channel MOSFET is preferred that less heat is produced ($P = I^2 R_{DS(on)}$). In Fig. B.1, the equivalent circuit of 3D MOT coils is a LR circuit, and the values for the resistance and the inductance of the MOT coils are either estimated or measured. In the case of switching the coil current from ON to OFF, the magnetic field decay time is $\tau = L/R$. The decaying time can be shortened by inserting more resistors in series with coils. The induced voltage (Lenz's law) is dependent on the inductance of the coil loop and current changing rate $\text{emf} = -L \times dI/\tau$. Once EMF is higher than the threshold value of the Zener diode, it is clipped. The Zener diode can also release the energy stored in the coils by $P = E/\tau = 1/2(LI^2)/\tau$, about a few tens kW in a short time duration, which is huge and imposes the caution on the selection of Zener diodes.

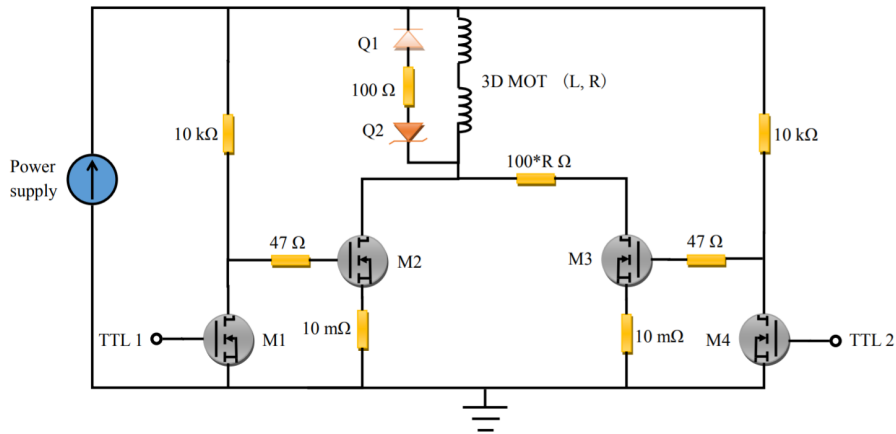


Figure B.1: The sketch of an analogue magnetic field switch of current-carrying coils in high-power applications.

Digital switch

If a digital power supply like Delta electronika (SM7.5-80) is used and the controlling bandwidth less than 1 kHz is required, a simple digital switch can be built by using our developed FPGA-based controller module. The hardware is configured with remote voltage control type (please follow SM800-series_manual).

Appendix C

Atomic source design

Appendix: Atomic source design

NOTES:

1. LEAK CHECK TO 2 X 10⁻¹⁰ SCC/SEC OF He.
2. TOLERANCE FOR ALL FOCAL LENGTHS, TARGET POINTS AND OAL DIMENSIONS ± .030, ANGLES ± 1°.
3. BREAK AND DEBURR ALL NON- SEAL SHARP EDGES .015 MAX.
4. WELD PER ASME SECTION IX. COSMETIC APPEARANCE PER ES0013, CF-3 VALUE.
5. ORIENTATION OF NON-ROTATABLE FLANGE LEAK CHECK GROOVES AS DRAWN.

ZONE REV		DESCRIPTION		DATE	REVISOR	APPROVER
			PRODUCTION RELEASE	09/20/2017	N.MOIRI	J.MOORE

ITEM NO.	PART NO.	DESCRIPTION	QTY.
1	940702	CROSS, 6-WAY W/O FLANGES-1.5"OD TUB	1
2	040217	TUBE, WLD, 304SS, 1.50" OD X .065" W X 9.57" LG	4
3	040217	TUBE, WLD, 304SS, Ø1.5" OD X .065" W X 2.57" LG	1
4	040217	TUBE, WLD, 304SS, Ø1.5" OD X .065" W X 7.295" LG	1
5	110014	FLANGE, DEL SEAL, CF, 2.75" OD, 1.50" TUBE, NON-ROT THRU	4
6	910014	INSERT, DEL SEAL, CF 2-3/4"OD X 1-1/2" TUBE, ROT	4
7	915002	RECEIVER, DEL SEAL, CF 2-3/4"OD, ROT THRU	4
8	040217	TUBE, WLD, 304SS, Ø1.5" OD X .065" W X 5.634" LG	2

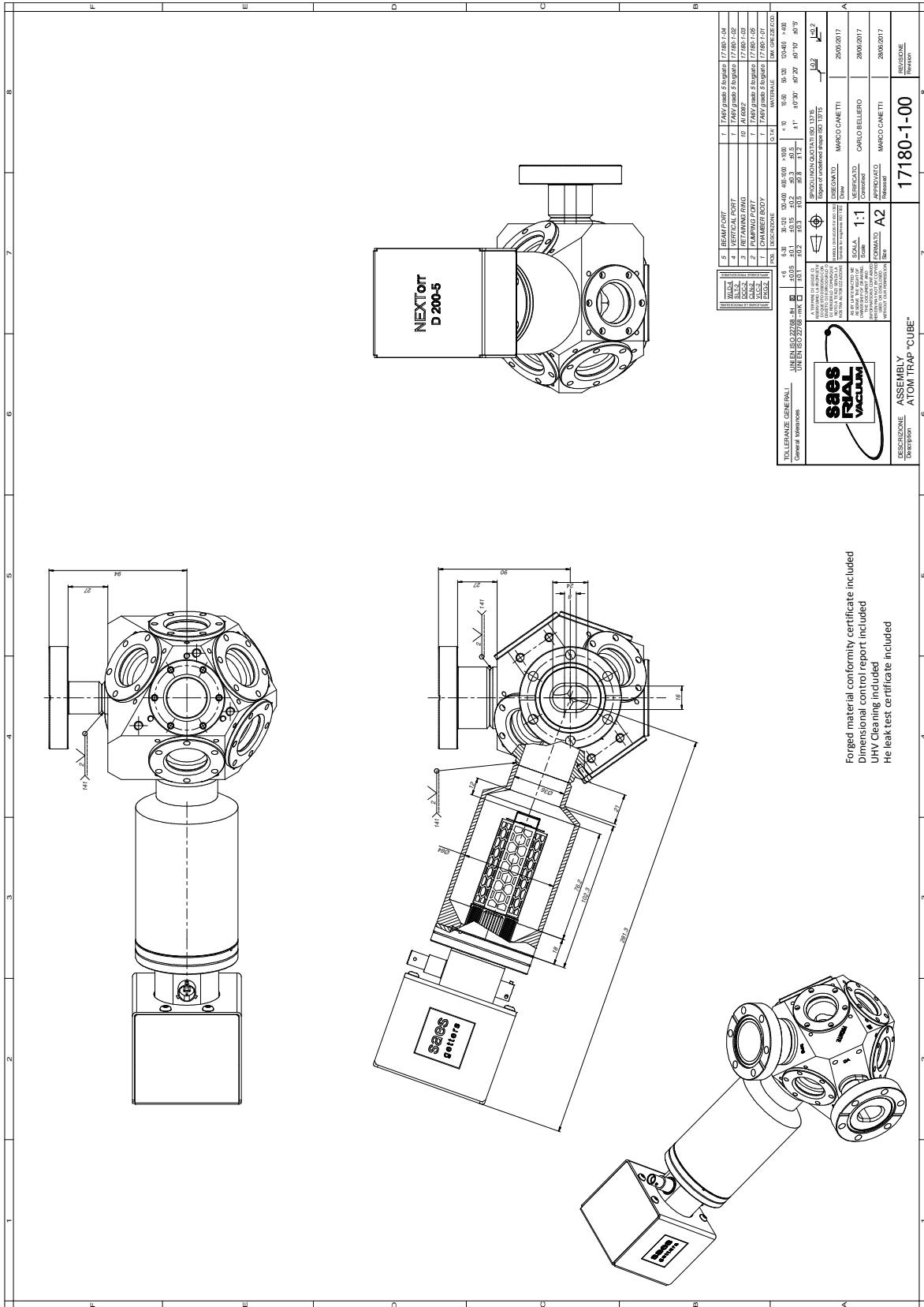
UNION	NANYANG	DRAWING NO.	205350	REV	1
UNION	NANYANG	DATE	09/20/2017	REVISION	
UNION	NANYANG	SCALE	1:1	DESCRIPTION	150-8 - NANYANG ENS-1
BEAD BLAST FINISH BEAD SIZE: 100 MICRONS BEAD TYPE: ALUMINA BEAD SOURCE: 3M					

UNCONTROLLED DRAFT 09/20/2017

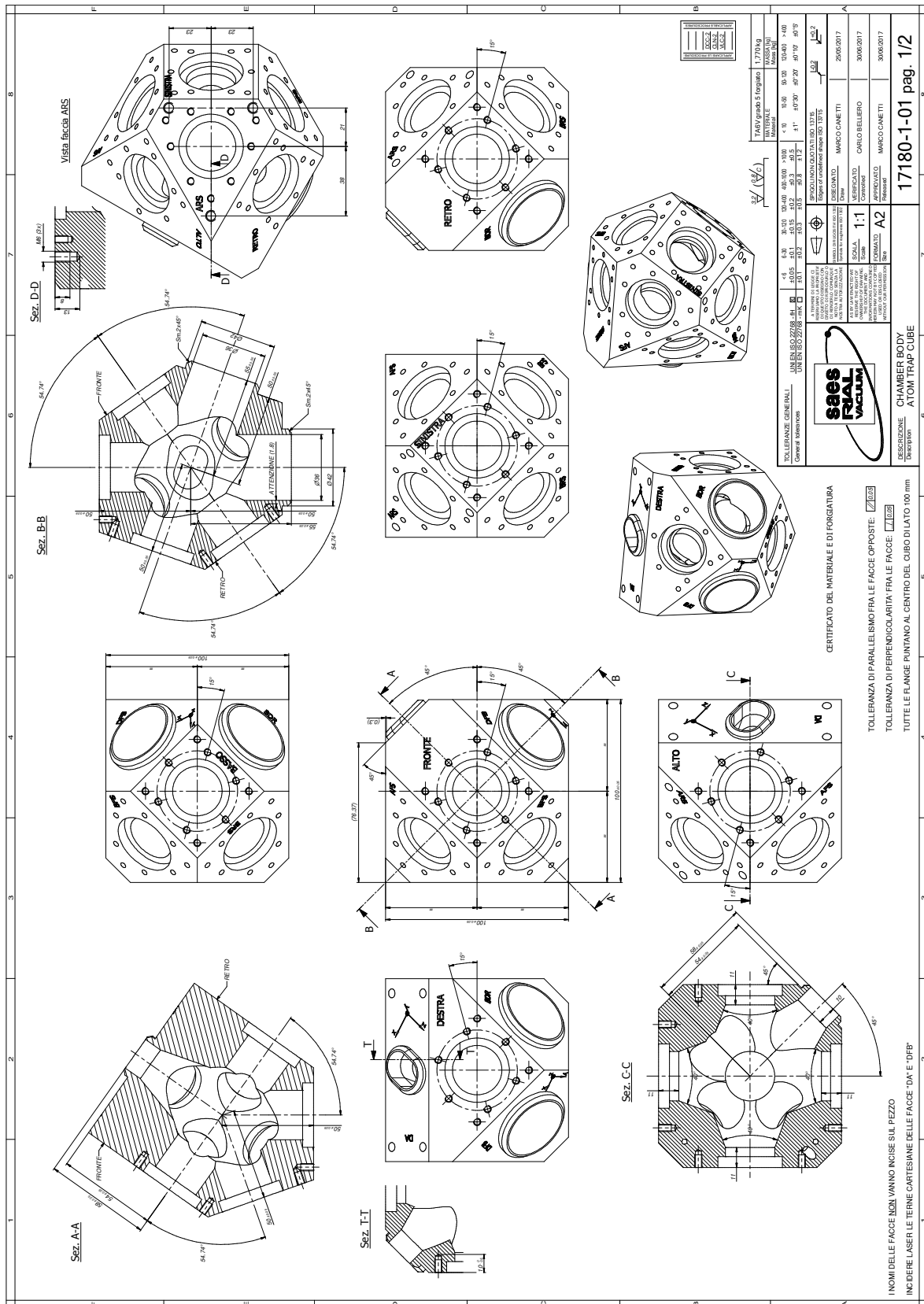
FILE NAME: 205350

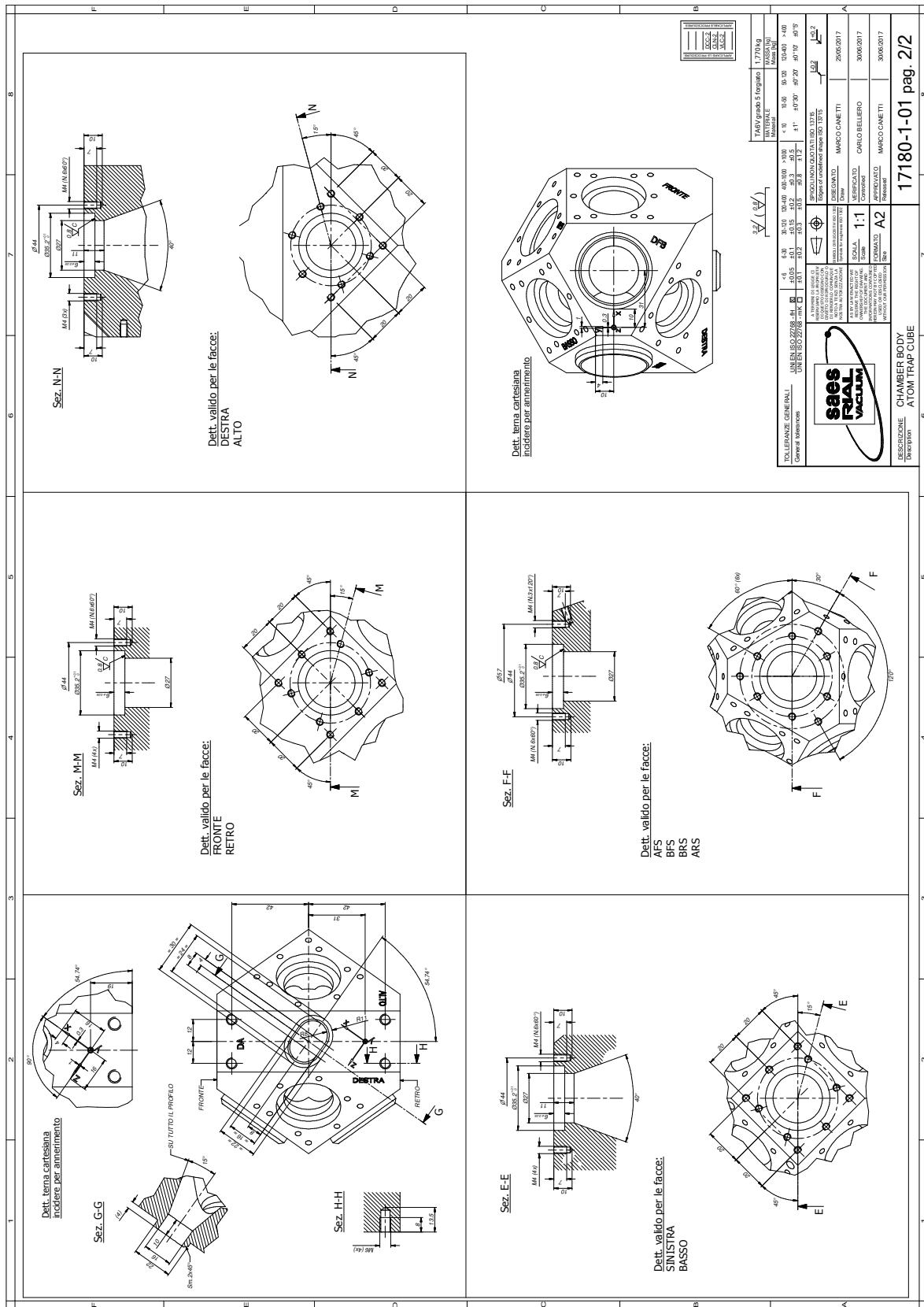
Appendix D

Science cell design



Forged material conformity certificate included
 Dimensional control report included
 UHV Cleaning included
 He leak test certificate included





Appendix E

Scientific production

Peer reviewed articles

1. C.-H. Feng, S. Vidal, P. Robert, P. Bouyer, B. Desruelle, M. Prevedelli, G. Boullet, J. and Santarelli, and A. Bertoldi. High power continuous laser at 461 nm based on a compact and high-efficiency frequency-doubling linear cavity. *Optics Express*, 29(17): 27760–27767, 2021. doi:[10.1364/OE.433179](https://doi.org/10.1364/OE.433179).
2. A. Bertoldi, C.-H. Feng, D. S. Naik, B. Canuel, P. Bouyer, and M. Prevedelli. Fast control of atom-light interaction in a narrow linewidth cavity. *Physical Review Letters*, 127: 013202, June 2021. doi:[10.1103/PhysRevLett.127.013202](https://doi.org/10.1103/PhysRevLett.127.013202).
3. Y. Abou El-Neaj, C. Alpigiani, S. Amairi-Pyka, H. Araújo, A. Balaž, A. Bassi, L. Bathe-Peters, B. Battelier, A. Belić, E. Bentine, et al. AEDGE: Atomic experiment for dark matter and gravity exploration in space. *EPJ Quantum Technology*, 7(1):1–27, 2020. doi:[10.1140/epjqt/s40507-020-0080-0](https://doi.org/10.1140/epjqt/s40507-020-0080-0).
4. A. Bertoldi, C.-H. Feng, H. Eneriz, M. Carey, D.S. Naik, J. Junca, X. Zou, D. O. Sabulsky, B. Canuel, P. Bouyer, et al. A control hardware based on a field programmable gate array for experiments in atomic physics. *Review of Scientific Instruments*, 91(3):033203, 2020. doi:[10.1063/1.5129595](https://doi.org/10.1063/1.5129595).

Peer reviewed conference proceedings

1. S. Vidal, C.-H. Feng, B. Desruelle, G. Santarelli, P. Bouyer, A. Bertoldi, and J. Boullet. High power continuous laser at 461 nm based on a frequency-doubling linear cavity. In *Nonlinear Frequency Generation and Conversion: Materials and Devices XX*, volume 11670, page 116701D. International Society for Optics and Photonics, 2021. doi:[10.1117/12.2580403](https://doi.org/10.1117/12.2580403).

Hardware & software repository

1. M. Prevedelli, A. Bertoldi, C.-H. Feng, H. Eneriz Imaz, M. Carey, D. S. Naik, J. Junca, X. Zou, D. O. Sabulsky, B. Canuel, and P. Bouyer. Yet another control system for AMO physics, December 2019. URL <https://zenodo.org/record/3571496>.

Articles under preparation

1. C.-H. Feng, P. Robert, P. Bouyer, M. Prevedelli, and A. Bertoldi. Double-frequency Zeeman slower for a cold strontium atom source (in preparation).

Bibliography

- [1] F. W. Bessel. On the variations of the proper motions of Procyon and Sirius. *Monthly Notices of the Royal Astronomical Society*, 6:136–141, 1844. URL <http://adsabs.harvard.edu/pdf/1844MNRAS...6R.136B>.
- [2] F. Tisserand. Les travaux de le verrier. In *Annales de l'Observatoire de Paris*, volume 15, pages 23–43, 1880. URL <http://adsabs.harvard.edu/pdf/1880AnPar..15...23T>.
- [3] A. Secchi. L'astronomia in roma nel pontificato DI Pio IX. *Roma*, 1877.
- [4] G. Bertone and D. Hooper. History of dark matter. *Reviews of Modern Physics*, 90(4): 045002, 2018. doi:[10.1103/RevModPhys.90.045002](https://doi.org/10.1103/RevModPhys.90.045002).
- [5] B. P. Abbott, R. Abbott, T. D. Abbott, S. Abraham, F. Acernese, K. Ackley, C. Adams, R. X. Adhikari, V. B. Adya, et al. GWTC-1: A gravitational-wave transient catalog of compact binary mergers observed by LIGO and Virgo during the first and second observing runs. *Physical Review X*, 9:031040, Sep 2019. doi:[10.1103/PhysRevX.9.031040](https://doi.org/10.1103/PhysRevX.9.031040).
- [6] G. Kauffmann and M. Haehnelt. A unified model for the evolution of galaxies and quasars. *Monthly Notices of the Royal Astronomical Society*, 311(3):576–588, 2000. doi:[10.1046/j.1365-8711.2000.03077.x](https://doi.org/10.1046/j.1365-8711.2000.03077.x).
- [7] Y. Abou El-Neaj, C. Alpigiani, S. Amairi-Pyka, H. Araújo, A. Balaž, A. Bassi, L. Bathe-Peters, B. Battelier, A. Belić, E. Bentine, et al. AEDGE: Atomic experiment for dark matter and gravity exploration in space. *EPJ Quantum Technology*, 7(1):1–27, 2020. doi:[10.1140/epjqt/s40507-020-0080-0](https://doi.org/10.1140/epjqt/s40507-020-0080-0).

- [8] B. Canuel, A. Bertoldi, L. Amand, E. P. Di Borgo, T. Chantrait, C. Danquigny, M. D. Álvarez, B. Fang, A. Freise, R. Geiger, et al. Exploring gravity with the miga large scale atom interferometer. *Scientific Reports*, 8(1):1–23, 2018. doi:[10.1038/s41598-018-32165-z](https://doi.org/10.1038/s41598-018-32165-z).
- [9] Ernest Fox Nichols and Gordon Ferrie Hull. A preliminary communication on the pressure of heat and light radiation. *Physical Review (Series I)*, 13(5):307, 1901. doi:[10.1103/PhysRevSeriesI.13.307](https://doi.org/10.1103/PhysRevSeriesI.13.307).
- [10] P. Lebedev. Experimental examination of light pressure. *Nuovo Cimento*, 15(195):195, 1883. URL <http://if.pw.edu.pl/~wierzba/zajecia/ed15/lebedev.pdf>.
- [11] F. Diedrich, J. C. Bergquist, W. M. Itano, and D. J. Wineland. Laser cooling to the zero-point energy of motion. *Physical Review Letters*, 62(4):403, 1989. doi:[10.1103/PhysRevLett.62.403](https://doi.org/10.1103/PhysRevLett.62.403).
- [12] P. D. Lett, R. N. Watts, C. I. Westbrook, W. D. Phillips, P. L. Gould, and H. J. Metcalf. Observation of atoms laser cooled below the Doppler limit. *Physical Review Letters*, 61(2):169, 1988. doi:[10.1103/PhysRevLett.61.169](https://doi.org/10.1103/PhysRevLett.61.169).
- [13] W. D. Phillips and H. Metcalf. Laser deceleration of an atomic beam. *Physical Review Letters*, 48(9):596, 1982. doi:[10.1103/PhysRevLett.48.596](https://doi.org/10.1103/PhysRevLett.48.596).
- [14] S. Chu, L. Hollberg, J. E. Bjorkholm, A. Cable, and A. Ashkin. Three-dimensional viscous confinement and cooling of atoms by resonance radiation pressure. *Physical Review Letters*, 55(1):48, 1985. doi:[10.1103/PhysRevLett.55.48](https://doi.org/10.1103/PhysRevLett.55.48).
- [15] M. H. Anderson, J. R. Ensher, M. R. Matthews, C. E. Wieman, and E. A. Cornell. Observation of Bose-Einstein condensation in a dilute atomic vapor. *Science*, 269(5221):198–201, 1995. doi:[10.1126/science.269.5221.198](https://doi.org/10.1126/science.269.5221.198).
- [16] K. B. Davis, M.-O. Mewes, M. R. Andrews, N. J. van Druten, D. S. Durfee, D. M. Kurn, and W. Ketterle. Bose-Einstein condensation in a gas of sodium atoms. *Physical Review Letters*, 75(22):3969, 1995. doi:[10.1103/PhysRevLett.75.3969](https://doi.org/10.1103/PhysRevLett.75.3969).

- [17] H. Katori. Optical lattice clocks and quantum metrology. *Nature Photonics*, 5(4):203–210, 2011. doi:[10.1038/nphoton.2011.45](https://doi.org/10.1038/nphoton.2011.45).
- [18] I. Dutta, D. Savoie, B. Fang, B. Venon, C. L. G. Alzar, R. Geiger, and A. Landragin. Continuous cold-atom inertial sensor with 1 nrad/sec rotation stability. *Physical Review Letters*, 116(18):183003, 2016. doi:[10.1103/PhysRevLett.116.183003](https://doi.org/10.1103/PhysRevLett.116.183003).
- [19] M. Schioppo, R. C. Brown, W. F. McGrew, N. Hinkley, R. J. Fasano, K. Belloy, T. H. Yoon, G. Milani, D. Nicolodi, J. A. Sherman, et al. Ultrastable optical clock with two cold-atom ensembles. *Nature Photonics*, 11(1):48–52, 2017. doi:[10.1038/nphoton.2016.231](https://doi.org/10.1038/nphoton.2016.231).
- [20] X.-H. Bao, A. Reingruber, P. Dietrich, J. Rui, A. Dück, T. Strassel, L. Li, N.-L. Liu, B. Zhao, and J.-W. Pan. Efficient and long-lived quantum memory with cold atoms inside a ring cavity. *Nature Physics*, 8(7):517–521, 2012. doi:[10.1038/nphys2324](https://doi.org/10.1038/nphys2324).
- [21] T. L. Gustavson, P. Bouyer, and M. A. Kasevich. Precision rotation measurements with an atom interferometer gyroscope. *Physical Review Letters*, 78(11):2046, 1997. doi:[10.1103/PhysRevLett.78.2046](https://doi.org/10.1103/PhysRevLett.78.2046).
- [22] T. L. Gustavson, A. Landragin, and M. A. Kasevich. Rotation sensing with a dual atom-interferometer Sagnac gyroscope. *Classical and Quantum Gravity*, 17(12):2385, 2000. doi:[10.1088/0264-9381/17/12/311](https://doi.org/10.1088/0264-9381/17/12/311).
- [23] M. Kasevich and S. Chu. Measurement of the gravitational acceleration of an atom with a light-pulse atom interferometer. *Applied Physics B*, 54(5):321–332, 1992. doi:[10.1007/BF00325375](https://doi.org/10.1007/BF00325375).
- [24] A. Peters, K. Y. Chung, and S. Chu. Measurement of gravitational acceleration by dropping atoms. *Nature*, 400(6747):849–852, 1999. doi:[10.1038/23655](https://doi.org/10.1038/23655).
- [25] A. Peters, K. Y. Chung, and S. Chu. High-precision gravity measurements using atom interferometry. *Metrologia*, 38(1):25, 2001. doi:[10.1088/0026-1394/38/1/4](https://doi.org/10.1088/0026-1394/38/1/4).

- [26] J. B. Fixler, G. T. Foster, J. M. McGuirk, and M. A. Kasevich. Atom interferometer measurement of the Newtonian constant of gravity. *Science*, 315(5808):74–77, 2007. doi:[Atom interferometer measurement of the Newtonian constant of gravity](#).
- [27] G. Lempore, A. Bertoldi, L. Cacciapuoti, M. Prevedelli, and G. M. Tino. Determination of the Newtonian gravitational constant using atom interferometry. *Physical Review Letters*, 100(5):050801, 2008. doi:[10.1103/PhysRevLett.100.050801](#).
- [28] M. J. Snadden, J. M. McGuirk, P. Bouyer, K. G. Haritos, and M. A. Kasevich. Measurement of the Earth’s gravity gradient with an atom interferometer-based gravity gradiometer. *Physical Review Letters*, 81(5):971, 1998. doi:[10.1103/PhysRevLett.81.971](#).
- [29] G. M. Tino, L. Cacciapuoti, S. Capozziello, G. Lambiase, and F. Sorrentino. Precision gravity tests and the Einstein equivalence principle. *Progress in Particle and Nuclear Physics*, 112:103772, 2020. doi:[10.1016/j.pnpnp.2020.103772](#).
- [30] P. Asenbaum, C. Overstreet, T. Kovachy, D. D. Brown, J. M. Hogan, and M. A. Kasevich. Phase shift in an atom interferometer due to spacetime curvature across its wave function. *Physical Review Letters*, 118(18):183602, 2017. doi:[10.1103/PhysRevLett.118.183602](#).
- [31] D. O. Sabulsky, I. Dutta, E. A. Hinds, B. Elder, C. Burrage, and Edmund J. Copeland. Experiment to detect dark energy forces using atom interferometry. *Physical Review Letters*, 123:061102, Aug 2019. doi:[10.1103/PhysRevLett.123.061102](#).
- [32] A. D. Cronin, J. Schmiedmayer, and D. E. Pritchard. Optics and interferometry with atoms and molecules. *Reviews of Modern Physics*, 81(3):1051, 2009. doi:[10.1103/RevModPhys.81.1051](#).
- [33] L. De Broglie. Waves and quanta. *Nature*, 112(2815):540–540, 1923. doi:[10.1038/112540a0](#).
- [34] S. Dimopoulos, P. W. Graham, J. M. Hogan, M. A. Kasevich, and S. Rajendran. Atomic gravitational wave interferometric sensor. *Physical Review D*, 78(12):122002, 2008. doi:[10.1103/PhysRevD.78.122002](#).

- [35] P. W. Graham, J. M. Hogan, M. A. Kasevich, and S. Rajendran. New method for gravitational wave detection with atomic sensors. *Physical Review Letters*, 110(17):171102, 2013. doi:[10.1103/PhysRevLett.110.171102](https://doi.org/10.1103/PhysRevLett.110.171102).
- [36] J. A. Muniz, D. J. Young, J. R. K. Cline, and J. K. Thompson. Cavity-QED determination of the natural linewidth of the ^{87}Sr millihertz clock transition with 30 μHz resolution. *arXiv preprint*, 2020. URL <https://arxiv.org/abs/2007.07855>.
- [37] S. L. Campbell, R. B. Hutson, G. E. Marti, A. Goban, N. D. Opong, R. L. McNally, L. Sonderhouse, J. M. Robinson, W. Zhang, B. J. Bloom, et al. A Fermi-degenerate three-dimensional optical lattice clock. *Science*, 358(6359):90–94, 2017. doi:[10.1126/science.aam5538](https://doi.org/10.1126/science.aam5538).
- [38] S. Stellmer, M. K. Tey, B. Huang, R. Grimm, and F. Schreck. Bose-Einstein condensation of strontium. *Physical Review Letters*, 103(20):200401, 2009. doi:[10.1103/PhysRevLett.103.200401](https://doi.org/10.1103/PhysRevLett.103.200401).
- [39] S. Stellmer, R. Grimm, and F. Schreck. Production of quantum-degenerate strontium gases. *Physical Review A*, 87(1):013611, 2013. doi:[10.1103/PhysRevA.87.013611](https://doi.org/10.1103/PhysRevA.87.013611).
- [40] I. Pikovski, M. Zych, F. Costa, and Č. Brukner. Universal decoherence due to gravitational time dilation. *Nature Physics*, 11(8):668–672, 2015. doi:[10.1038/nphys3366](https://doi.org/10.1038/nphys3366).
- [41] Alkali-earth matter wave interferometry | ANR: [Project-ANR-16-CE30-0002](https://anr.fr/Projet-ANR-16-CE30-0002).
- [42] A. V. Taichenachev, V. I. Yudin, C. W. Oates, C. W. Hoyt, Z. W. Barber, and L. Hollberg. Magnetic field-induced spectroscopy of forbidden optical transitions with application to lattice-based optical atomic clocks. *Physical Review Letters*, 96(8):083001, 2006. doi:[10.1103/PhysRevLett.96.083001](https://doi.org/10.1103/PhysRevLett.96.083001).
- [43] X. Baillard, M. Fouché, R. Le Targat, P. G. Westergaard, A. Lecallier, Y. Le Coq, G. D. Rovera, S. Bize, and P. Lemonde. Accuracy evaluation of an optical lattice clock with bosonic atoms. *Optics Letters*, 32(13):1812–1814, 2007. doi:[10.1364/OL.32.001812](https://doi.org/10.1364/OL.32.001812).

- [44] T. Hong, C. Cramer, W. Nagourney, and E. N. Fortson. Optical clocks based on ultranarrow three-photon resonances in alkaline earth atoms. *Physical Review Letters*, 94(5):050801, 2005. doi:[10.1103/PhysRevLett.94.050801](https://doi.org/10.1103/PhysRevLett.94.050801).
- [45] M. Takamoto, F.-L. Hong, R. Higashi, and H. Katori. An optical lattice clock. *Nature*, 435(7040):321–324, 2005. doi:[10.1038/nature03541](https://doi.org/10.1038/nature03541).
- [46] J. Rudolph, T. Wilkason, M. Nantel, H. Swan, C. M. Holland, Y. Jiang, B. E. Garber, S. P. Carman, J. M. Hogan, et al. Large momentum transfer clock atom interferometry on the 689 nm intercombination line of strontium. *Physical Review Letters*, 124(8):083604, 2020. doi:[10.1103/PhysRevLett.124.083604](https://doi.org/10.1103/PhysRevLett.124.083604).
- [47] F. Gao, H. Liu, P. Xu, X. Tian, Y. Wang, J. Ren, H. Wu, and H. Chang. Precision measurement of transverse velocity distribution of a strontium atomic beam. *AIP advances*, 4(2):027118, 2014. doi:[10.1063/1.4866983](https://doi.org/10.1063/1.4866983).
- [48] W. H. Bragg and W. L. Bragg. The reflection of X-rays by crystals. *Proceedings of the Royal Society of London. Series A, Containing Papers of a Mathematical and Physical Character*, 88(605):428–438, 1913. doi:[10.1098/rspa.1913.0040](https://doi.org/10.1098/rspa.1913.0040).
- [49] H. Müller, S.-w. Chiow, Q. Long, S. Herrmann, and S. Chu. Atom interferometry with up to 24-photon-momentum-transfer beam splitters. *Physical Review Letters*, 100(18):180405, 2008. doi:[10.1103/PhysRevLett.100.180405](https://doi.org/10.1103/PhysRevLett.100.180405).
- [50] P. J. Martin, B. G. Oldaker, A. H. Miklich, and D. E. Pritchard. Bragg scattering of atoms from a standing light wave. *Physical Review Letters*, 60(6):515, 1988. doi:[10.1103/PhysRevLett.60.515](https://doi.org/10.1103/PhysRevLett.60.515).
- [51] H. Ahlers, H. Müntinga, A. Wenzlawski, M. Krutzik, G. Tackmann, S. Abend, N. Gaaloul, E. Giese, A. Roura, R. Kuhl, C. Lämmerzahl, A. Peters, P. Windpassinger, K. Sengstock, W. P. Schleich, W. Ertmer, and E. M. Rasel. Double Bragg interferometry. *Physical Review Letters*, 116:173601, Apr 2016. doi:[10.1103/PhysRevLett.116.173601](https://doi.org/10.1103/PhysRevLett.116.173601).
- [52] M. Kasevich and S. Chu. Atomic interferometry using stimulated Raman transitions. *Physical Review Letters*, 67(2):181, 1991. doi:[10.1103/PhysRevLett.67.181](https://doi.org/10.1103/PhysRevLett.67.181).

- [53] M. Cadoret, E. de Mirandes, P. Cladé, S. Guellati-Khélifa, C. Schwob, F. Nez, L. Julien, and F. Biraben. Combination of Bloch oscillations with a Ramsey-Bordé interferometer: New determination of the fine structure constant. *Physical Review Letters*, 101:230801, Dec 2008. doi:[10.1103/PhysRevLett.101.230801](https://doi.org/10.1103/PhysRevLett.101.230801).
- [54] Z. Pagel, W. Zhong, R. H. Parker, C. T. Olund, N. Y. Yao, and H. Müller. Symmetric bloch oscillations of matter waves. *Physics Review A*, 102:053312, Nov 2020. doi:[10.1103/PhysRevA.102.053312](https://doi.org/10.1103/PhysRevA.102.053312).
- [55] P. Cladé, S. Guellati-Khélifa, F. Nez, and F. Biraben. Large momentum beam splitter using Bloch oscillations. *Physical Review Letters*, 102(24):240402, 2009. doi:[10.1103/PhysRevLett.102.240402](https://doi.org/10.1103/PhysRevLett.102.240402).
- [56] P. Cladé, S. Guellati-Khélifa, F. Nez, and F. Biraben. Large momentum beam splitter using Bloch oscillations. *Physical Review Letters*, 102:240402, Jun 2009. doi:[10.1103/PhysRevLett.102.240402](https://doi.org/10.1103/PhysRevLett.102.240402).
- [57] S. Kling, T. Salger, C. Grossert, and M. Weitz. Atomic Bloch-Zener oscillations and Stückelberg interferometry in optical lattices. *Physical Review Letters*, 105(21):215301, 2010. doi:[10.1103/PhysRevLett.105.215301](https://doi.org/10.1103/PhysRevLett.105.215301).
- [58] S. B. Cahn, A. Kumarakrishnan, U. Shim, T. Sleator, P. R. Berman, and B. Dubetsky. Time-domain de Broglie wave interferometry. *Physical Review Letters*, 79(5):784, 1997. doi:[10.1103/PhysRevLett.79.784](https://doi.org/10.1103/PhysRevLett.79.784).
- [59] Ch. J. Bordé. Atomic interferometry with internal state labelling. *Physics Letters A*, 140(1-2):10–12, 1989. doi:[10.1016/0375-9601\(89\)90537-9](https://doi.org/10.1016/0375-9601(89)90537-9).
- [60] D. M. Giltner, R. W. McGowan, and S. A. Lee. Atom interferometer based on Bragg scattering from standing light waves. *Physical Review Letters*, 75(14):2638, 1995. doi:[10.1103/PhysRevLett.75.2638](https://doi.org/10.1103/PhysRevLett.75.2638).
- [61] J. M. McGuirk, M. J. Snadden, and M. A. Kasevich. Large area light-pulse atom interferometry. *Physical Review Letters*, 85(21):4498, 2000. doi:[10.1103/PhysRevLett.85.4498](https://doi.org/10.1103/PhysRevLett.85.4498).

- [62] M. Jaffe, V. Xu, P. Haslinger, H. Müller, and P. Hamilton. Efficient adiabatic spin-dependent kicks in an atom interferometer. *Physical Review Letters*, 121(4):040402, 2018. doi:[10.1103/PhysRevLett.121.040402](https://doi.org/10.1103/PhysRevLett.121.040402).
- [63] H. Müller, S.-w. Chiow, Q. Long, S. Herrmann, and S. Chu. Atom interferometry with up to 24-photon-momentum-transfer beam splitters. *Physical Review Letters*, 100:180405, May 2008. doi:[10.1103/PhysRevLett.100.180405](https://doi.org/10.1103/PhysRevLett.100.180405).
- [64] P. Hamilton, M. Jaffe, J. M. Brown, L. Maisenbacher, B. Estey, and H. Müller. Atom interferometry in an optical cavity. *Physical Review Letters*, 114(10):100405, 2015. doi:[10.1103/PhysRevLett.114.100405](https://doi.org/10.1103/PhysRevLett.114.100405).
- [65] H. Müller, S.-w. Chiow, S. Herrmann, and S. Chu. Atom interferometers with scalable enclosed area. *Physical Review Letters*, 102:240403, Jun 2009. doi:[10.1103/PhysRevLett.102.240403](https://doi.org/10.1103/PhysRevLett.102.240403).
- [66] L. Liu, D.-S. Lü, W.-B. Chen, T. Li, Q.-Z. Qu, B. Wang, L. Li, W. Ren, Z.-R. Dong, J.-B. Zhao, et al. In-orbit operation of an atomic clock based on laser-cooled ^{87}Rb atoms. *Nature Communications*, 9(1):1–8, 2018. doi:[10.1038/s41467-018-05219-z](https://doi.org/10.1038/s41467-018-05219-z).
- [67] D. Becker, M. D. Lachmann, S. T. Seidel, H. Ahlers, A. N. Dinkelaker, J. Grosse, O. Hellmig, H. Müntinga, V. Schkolnik, T. Wendrich, et al. Space-borne Bose-Einstein condensation for precision interferometry. *Nature*, 562(7727):391–395, 2018. doi:[10.1038/s41586-018-0605-1](https://doi.org/10.1038/s41586-018-0605-1).
- [68] E. R. Elliott, M. C. Krutzik, J. R. Williams, R. J. Thompson, and D. C. Aveline. NASA’s cold atom lab (CAL): system development and ground test status. *npj Microgravity*, 4(1):1–7, 2018. doi:[10.1038/s41526-018-0049-9](https://doi.org/10.1038/s41526-018-0049-9).
- [69] M. Lezius, T. Wilken, C. Deutsch, M. Giunta, O. Mandel, A. Thaller, V. Schkolnik, M. Schiemangk, A. Dinkelaker, A. Kohfeldt, et al. Space-borne frequency comb metrology. *Optica*, 3(12):1381–1387, 2016. doi:[10.1364/OPTICA.3.001381](https://doi.org/10.1364/OPTICA.3.001381).
- [70] A. N. Dinkelaker, M. Schiemangk, V. Schkolnik, A. Kenyon, K. Lampmann, A. Wenzlawski, P. Windpassinger, O. Hellmig, T. Wendrich, E. M. Rasel, et al. Au-

- tonomous frequency stabilization of two extended-cavity diode lasers at the potassium wavelength on a sounding rocket. *Applied Optics*, 56(5):1388–1396, 2017. doi:[10.1364/AO.56.001388](https://doi.org/10.1364/AO.56.001388).
- [71] K. Döringshoff, F. B. Gutsch, V. Schkolnik, C. Kürbis, M. Oswald, B. Pröbster, E. V. Kovalchuk, A. Bawamia, R. Smol, T. Schuldt, et al. Iodine frequency reference on a sounding rocket. *Physical Review Applied*, 11(5):054068, 2019. doi:[10.1103/PhysRevApplied.11.054068](https://doi.org/10.1103/PhysRevApplied.11.054068).
- [72] J. M. Hogan and M. A. Kasevich. Atom-interferometric gravitational-wave detection using heterodyne laser links. *Physical Review A*, 94(3):033632, 2016.
- [73] P. Collaboration, N. Aghanim, Y. Akrami, M. Ashdown, J. Aumont, C. Baccigalupi, M. Ballardini, A. J. Banday, R. B. Barreiro, N. Bartolo, et al. Planck 2018 results. VI. cosmological parameters. 2020. doi:[10.1051/0004-6361/201833910](https://doi.org/10.1051/0004-6361/201833910).
- [74] W. Hu. Mapping the dark matter through the cosmic microwave background damping tail. *The Astrophysical Journal Letters*, 557(2):L79, 2001. doi:[10.1086/323253](https://doi.org/10.1086/323253).
- [75] G. Bertone, N. Bozorgnia, J. S. Kim, S. Liem, C. McCabe, S. Otten, and R. R. De Austri. Identifying WIMP dark matter from particle and astroparticle data. *Journal of Cosmology and Astroparticle Physics*, 2018(03):026, 2018. doi:[10.1088/1475-7516/2018/03/026](https://doi.org/10.1088/1475-7516/2018/03/026).
- [76] D. Colladay and V. A. Kostelecký. CPT violation and the standard model. *Physical Review D*, 55(11):6760, 1997. doi:[10.1103/PhysRevD.55.6760](https://doi.org/10.1103/PhysRevD.55.6760).
- [77] N. Du, N. Force, R. Khatriwada, E. Lentz, R. Ottens, L. J. Rosenberg, G. Rybka, G. Carosi, N. Woollett, D. Bowering, et al. Search for invisible axion dark matter with the axion dark matter experiment. *Physical Review Letters*, 120(15):151301, 2018. doi:[10.1103/PhysRevLett.120.151301](https://doi.org/10.1103/PhysRevLett.120.151301).
- [78] M. Bauer, M. Neubert, and A. Thamm. Collider probes of axion-like particles. *Journal of High Energy Physics*, 2017(12):1–63, 2017. doi:[10.1007/JHEP12\(2017\)044](https://doi.org/10.1007/JHEP12(2017)044).

- [79] Celine Boehm, Abdelhak Djouadi, and Manuel Drees. Light scalar top quarks and supersymmetric dark matter. *Physical Review D*, 62(3):035012, 2000. doi:[10.1103/PhysRevD.62.035012](https://doi.org/10.1103/PhysRevD.62.035012).
- [80] P. W. Graham, J. M. Hogan, M. A. Kasevich, and S. Rajendran. Resonant mode for gravitational wave detectors based on atom interferometry. *Physical Review D*, 94(10):104022, 2016. doi:[10.1103/PhysRevLett.111.170802](https://doi.org/10.1103/PhysRevLett.111.170802).
- [81] J. Bergé, P. Brax, G. Métris, M. Pernot-Borràs, P. Touboul, and J.-P. Uzan. MICROSCOPE mission: first constraints on the violation of the weak equivalence principle by a light scalar dilaton. *Physical Review Letters*, 120(14):141101, 2018. doi:[10.1103/PhysRevLett.120.141101](https://doi.org/10.1103/PhysRevLett.120.141101).
- [82] K. Freese, J. Frieman, and A. Gould. Signal modulation in cold-dark-matter detection. *Physical Review D*, 37(12):3388, 1988. doi:[10.1103/PhysRevD.37.3388](https://doi.org/10.1103/PhysRevD.37.3388).
- [83] R. M. Wald. *General relativity*. University of Chicago press, 2010.
- [84] J. A. Wheeler. A journey into gravity and spacetime. *Scientific American Library*, 1990.
- [85] T. W. B. Kibble. Topology of cosmic domains and strings. *Journal of Physics A: Mathematical and General*, 9(8):1387, 1976. doi:[10.1088/0305-4470/9/8/029](https://doi.org/10.1088/0305-4470/9/8/029).
- [86] B. P. Abbott, R. Abbott, T. D. Abbott, F. Acernese, K. Ackley, C. Adams, T. Adams, P. Addesso, R. X. Adhikari, V. B. Adya, et al. Constraints on cosmic strings using data from the first Advanced LIGO observing run. *Physical Review D*, 97(10):102002, 2018. doi:[10.1103/PhysRevD.97.102002](https://doi.org/10.1103/PhysRevD.97.102002).
- [87] S. Singh. *The origin of the universe*. Harper Perennial, 2005.
- [88] J. Garcia-Bellido and D. G. Figueroa. Stochastic background of gravitational waves from hybrid preheating. *Physical Review Letters*, 98(6):061302, 2007. doi:[10.1103/PhysRevLett.98.061302](https://doi.org/10.1103/PhysRevLett.98.061302).

- [89] A. Salam. Weak and electromagnetic interactions. In *Selected Papers Of Abdus Salam: (With Commentary)*, pages 244–254. World Scientific, 1994. doi:[10.1142/9789812795915_0034](https://doi.org/10.1142/9789812795915_0034).
- [90] C. Caprini, M. Hindmarsh, S. Huber, T. Konstandin, J. Kozaczuk, G. Nardini, J. M. No, A. Petiteau, P. Schwaller, G. Servant, et al. Science with the space-based interferometer eLISA. II: Gravitational waves from cosmological phase transitions. *Journal of Cosmology and Astroparticle physics*, 2016(04):001, 2016. doi:[10.1088/1475-7516/2016/04/001](https://doi.org/10.1088/1475-7516/2016/04/001).
- [91] I. Mandel, A. Sesana, and A. Vecchio. The astrophysical science case for a decihertz gravitational-wave detector. *Classical and Quantum Gravity*, 35(5):054004, 2018. doi:[10.1088/1361-6382/aaa7e0](https://doi.org/10.1088/1361-6382/aaa7e0).
- [92] C. J. Moore, R. H. Cole, and C. P. L. Berry. Gravitational-wave sensitivity curves. *Classical and Quantum Gravity*, 32(1):015014, 2014. doi:[10.1088/0264-9381/32/1/015014](https://doi.org/10.1088/0264-9381/32/1/015014).
- [93] gwplotter: gwplotter.com/.
- [94] J. Weber. Observation of the thermal fluctuations of a gravitational-wave detector. *Physical Review Letters*, 17(24):1228, 1966. doi:[10.1103/PhysRevLett.17.1228](https://doi.org/10.1103/PhysRevLett.17.1228).
- [95] J. L. Levine. Early gravity-wave detection experiments, 1960-1975. *Physics in Perspective*, 6(1):42–75, 2004. doi:[10.1007/s00016-003-0179-6](https://doi.org/10.1007/s00016-003-0179-6).
- [96] J. H. Taylor, L. A. Fowler, and P. M. McCulloch. Measurements of general relativistic effects in the binary pulsar PSR1913+16. *Nature*, 277(5696):437–440, 1979. doi:[10.1038/277437a0](https://doi.org/10.1038/277437a0).
- [97] J. G. Hartnett and A. N. Luiten. Colloquium: Comparison of astrophysical and terrestrial frequency standards. *Reviews of Modern Physics*, 83(1):1, 2011. doi:[10.1103/RevModPhys.83.1](https://doi.org/10.1103/RevModPhys.83.1).

- [98] M. Kramer and D. J. Champion. The European pulsar timing array and the large European array for pulsars. *Classical and Quantum Gravity*, 30(22):224009, 2013. doi:[10.1088/0264-9381/30/22/224009](https://doi.org/10.1088/0264-9381/30/22/224009).
- [99] R. N. Manchester. The international pulsar timing array. *Classical and Quantum Gravity*, 30(22):224010, 2013. doi:[10.1088/0264-9381/30/22/224010](https://doi.org/10.1088/0264-9381/30/22/224010).
- [100] S. Blasi, V. Brdar, and K. Schmitz. Has NANOGrav found first evidence for cosmic strings? *Physical Review Letters*, 126:041305, Jan 2021. doi:[10.1103/PhysRevLett.126.041305](https://doi.org/10.1103/PhysRevLett.126.041305).
- [101] B. P. Abbott, R. Abbott, R. Adhikari, P. Ajith, B. Allen, G. Allen, R. S. Amin, S. B. Anderson, W. G. Anderson, M. A. Arain, et al. LIGO: the laser interferometer gravitational-wave observatory. *Reports on Progress in Physics*, 72(7):076901, 2009. doi:[10.1088/0034-4885/72/7/076901](https://doi.org/10.1088/0034-4885/72/7/076901).
- [102] B. P. Abbott, R. Abbott, T. D. Abbott, M. R. Abernathy, F. Acernese, K. Ackley, C. Adams, T. Adams, P. Addesso, R. X. Adhikari, et al. Observation of gravitational waves from a binary black hole merger. *Physical Review Letters*, 116(6):061102, 2016. doi:[10.1103/PhysRevLett.116.061102](https://doi.org/10.1103/PhysRevLett.116.061102).
- [103] T. Accadia, F. Acernese, M. Alshourbagy, P. Amico, F. Antonucci, S. Aoudia, N. Arnaud, C. Arnault, K. G. Arun, P. Astone, et al. Virgo: a laser interferometer to detect gravitational waves. *Journal of Instrumentation*, 7(03):P03012, 2012. doi:[10.1088/1748-0221/7/03/P03012](https://doi.org/10.1088/1748-0221/7/03/P03012).
- [104] H. Grote, LIGO Scientific Collaboration, et al. The GEO 600 status. *Classical and Quantum Gravity*, 27(8):084003, 2010. doi:[10.1088/0264-9381/27/8/084003](https://doi.org/10.1088/0264-9381/27/8/084003).
- [105] G. M. Harry, LIGO Scientific Collaboration, et al. Advanced LIGO: the next generation of gravitational wave detectors. *Classical and Quantum Gravity*, 27(8):084006, 2010. doi:[10.1088/0264-9381/27/8/084006](https://doi.org/10.1088/0264-9381/27/8/084006).
- [106] F. Acernese, M. Agathos, K. Agatsuma, D. Aisa, N. Allemandou, A. Allocca, J. Amarni, P. Astone, G. Balestri, G. Ballardin, et al. Advanced Virgo: a second-generation inter-

- ferometric gravitational wave detector. *Classical and Quantum Gravity*, 32(2):024001, 2014. doi:[10.1088/0264-9381/32/2/024001](https://doi.org/10.1088/0264-9381/32/2/024001).
- [107] M. Ando, TAMA collaboration, et al. Current status of TAMA. *Classical and Quantum Gravity*, 19(7):1409, 2002. doi:[10.1088/0264-9381/19/7/324](https://doi.org/10.1088/0264-9381/19/7/324).
- [108] K. Somiya. Detector configuration of KAGRA—the Japanese cryogenic gravitational-wave detector. *Classical and Quantum Gravity*, 29(12):124007, 2012. doi:[10.1088/0264-9381/29/12/124007](https://doi.org/10.1088/0264-9381/29/12/124007).
- [109] F. Badaracco and J. Harms. Optimization of seismometer arrays for the cancellation of Newtonian noise from seismic body waves. *Classical and Quantum Gravity*, 36(14):145006, June 2019. doi:[10.1088/1361-6382/ab28c1](https://doi.org/10.1088/1361-6382/ab28c1).
- [110] W. Chaibi, R. Geiger, B. Canuel, A. Bertoldi, A. Landragin, and P. Bouyer. Low frequency gravitational wave detection with ground-based atom interferometer arrays. *Physical Review D*, 93:021101(R), 2016. doi:[10.1103/PhysRevD.93.021101](https://doi.org/10.1103/PhysRevD.93.021101).
- [111] B. S. Sathyaprakash and B. F. Schutz. Physics, astrophysics and cosmology with gravitational waves. *Living Reviews in Relativity*, 12(1):2, 2009. doi:[10.12942/lrr-2009-2](https://doi.org/10.12942/lrr-2009-2).
- [112] P. Amaro-Seoane, S. Aoudia, S. Babak, P. Binetruy, E. Berti, A. Bohe, C. Caprini, M. Colpi, N. J. Cornish, K. Danzmann, et al. Low-frequency gravitational-wave science with eLISA/NGO. *Classical and Quantum Gravity*, 29(12):124016, 2012. doi:[10.1088/0264-9381/29/12/124016](https://doi.org/10.1088/0264-9381/29/12/124016).
- [113] N. Seto, S. Kawamura, and T. Nakamura. Possibility of direct measurement of the acceleration of the universe using 0.1 Hz band laser interferometer gravitational wave antenna in space. *Physical Review Letters*, 87(22):221103, 2001. doi:[10.1103/PhysRevLett.87.221103](https://doi.org/10.1103/PhysRevLett.87.221103).
- [114] S. Kawamura, T. Nakamura, M. Ando, N. Seto, K. Tsubono, K. Numata, R. Takahashi, S. Nagano, T. Ishikawa, M. Musha, et al. The Japanese space gravitational wave antenna—DECIGO. *Classical and Quantum Gravity*, 23(8):S125, 2006. doi:[10.1088/0264-9381/23/8/S17](https://doi.org/10.1088/0264-9381/23/8/S17).

- [115] K. Yagi and N. Seto. Detector configuration of DECIGO/BBO and identification of cosmological neutron-star binaries. *Physical Review D*, 83(4):044011, 2011. doi:[10.1103/PhysRevD.83.044011](https://doi.org/10.1103/PhysRevD.83.044011).
- [116] J. Luo, L.-S. Chen, H.-Z. Duan, Y.-G. Gong, S. Hu, J. Ji, Q. Liu, J. Mei, V. Milyukov, M. Sazhin, et al. TianQin: a space-borne gravitational wave detector. *Classical and Quantum Gravity*, 33(3):035010, 2016. doi:[10.1088/0264-9381/33/3/035010](https://doi.org/10.1088/0264-9381/33/3/035010).
- [117] M.-S. Zhan, J. Wang, W.-T. Ni, D.-F. Gao, G. Wang, L.-X. He, R.-B. Li, L. Zhou, X. Chen, J.-Q. Zhong, et al. ZAIGA: Zhaoshan long-baseline atom interferometer gravitation antenna. *International Journal of Modern Physics D*, 29(04):1940005, 2020. doi:[10.1142/S0218271819400054](https://doi.org/10.1142/S0218271819400054).
- [118] J. Coleman. MAGIS-100 at Fermilab. *arXiv preprint*, 2018. URL <https://arxiv.org/abs/1812.00482>.
- [119] B. Canuel, S. Abend, P. Amaro-Seoane, F. Badaracco, Q. Beaufiles, A. Bertoldi, K. Bongs, P. Bouyer, C. Braxmaier, W. Chaibi, et al. ELGAR-a European laboratory for gravitation and atom-interferometric research. *Classical and Quantum Gravity*, 2020. doi:[10.1088/1361-6382/aba80e](https://doi.org/10.1088/1361-6382/aba80e).
- [120] L. Badurina, E. Bentine, D. Blas, K. Bongs, D. Bortoletto, T. Bowcock, K. Bridges, W. Bowden, O. Buchmueller, C. Burrage, et al. AION: an atom interferometer observatory and network. *Journal of Cosmology and Astroparticle Physics*, 2020(05):011, 2020. doi:[10.1088/1475-7516/2020/05/011](https://doi.org/10.1088/1475-7516/2020/05/011).
- [121] J. E. Sansonetti and G. Nave. Wavelengths, transition probabilities, and energy levels for the spectrum of neutral strontium (Sr I). *Journal of Physical and Chemical Reference Data*, 39(3):033103, 2010. doi:[10.1063/1.3449176](https://doi.org/10.1063/1.3449176).
- [122] Strontium: [Strontium-distilled-crystals.jpg](#).
- [123] L. R. Hunter, W. A. Walker, and D. S. Weiss. Observation of an atomic stark–electric-quadrupole interference. *Physical Review Letters*, 56:823–826, Feb 1986. doi:[10.1103/PhysRevLett.56.823](https://doi.org/10.1103/PhysRevLett.56.823).

- [124] R. Santra, K. V. Christ, and C. H. Greene. Properties of metastable alkaline-earth-metal atoms calculated using an accurate effective core potential. *Physical Review A*, 69:042510, Apr 2004. doi:[10.1103/PhysRevA.69.042510](https://doi.org/10.1103/PhysRevA.69.042510).
- [125] A. Derevianko. Feasibility of cooling and trapping metastable alkaline-earth atoms. *Physical Review Letters*, 87:023002, Jun 2001. doi:[10.1103/PhysRevLett.87.023002](https://doi.org/10.1103/PhysRevLett.87.023002).
- [126] M. Yasuda and H. Katori. Lifetime measurement of the 3p_2 metastable state of strontium atoms. *Physical Review Letters*, 92:153004, Apr 2004. doi:[10.1103/PhysRevLett.92.153004](https://doi.org/10.1103/PhysRevLett.92.153004).
- [127] I. Courtillot, A. Quessada-Vial, A. Bruschi, D. Kolker, G. D. Rovera, and P. Lemonde. Accurate spectroscopy of Sr atoms. *The European Physical Journal D-Atomic, Molecular, Optical and Plasma Physics*, 33(2):161–171, 2005. doi:[10.1140/epjd/e2005-00058-0](https://doi.org/10.1140/epjd/e2005-00058-0).
- [128] S. Stellmer. *Degenerate quantum gases of strontium*. PhD thesis, University of Innsbruck, 2013.
- [129] R. Grimm, M. Weidemüller, and Y. B. Ovchinnikov. Optical dipole traps for neutral atoms. In *Advances in Atomic, Molecular and Optical Physics*, volume 42, pages 95–170. Elsevier, 2000. doi:[10.1016/s1049-250x\(08\)60186-x](https://doi.org/10.1016/s1049-250x(08)60186-x).
- [130] H. Ammann and N. Christensen. Delta kick cooling: A new method for cooling atoms. *Physical Review Letters*, 78(11):2088, 1997. doi:[10.1103/PhysRevLett.78.2088](https://doi.org/10.1103/PhysRevLett.78.2088).
- [131] S. Stellmer, M. K. Tey, R. Grimm, and F. Schreck. Bose-Einstein condensation of ^{86}Sr . *Physical Review A*, 82(4):041602, 2010. doi:[10.1103/PhysRevA.82.041602](https://doi.org/10.1103/PhysRevA.82.041602).
- [132] M. K. Tey, S. Stellmer, R. Grimm, and F. Schreck. Double-degenerate Bose-Fermi mixture of strontium. *Physical Review A*, 82(1):011608, 2010. doi:[10.1103/PhysRevA.82.011608](https://doi.org/10.1103/PhysRevA.82.011608).
- [133] P. G. Mickelson, Y. N. Martinez De Escobar, M. Yan, B. J. DeSalvo, and T. C. Killian. Bose-Einstein condensation of ^{88}Sr through sympathetic cooling with ^{87}Sr . *Physical Review A*, 81(5):051601, 2010. doi:[10.1103/PhysRevA.81.051601](https://doi.org/10.1103/PhysRevA.81.051601).

- [134] S. Stellmer, B. Pasquiou, R. Grimm, and F. Schreck. Laser cooling to quantum degeneracy. *Physical Review Letters*, 110(26):263003, 2013. doi:[10.1103/PhysRevLett.110.263003](https://doi.org/10.1103/PhysRevLett.110.263003).
- [135] P. Cheinet. *Conception et réalisation d'un gravimètre à atomes froids*. PhD thesis, Université Pierre et Marie Curie-Paris VI, 2006.
- [136] I. Nosske, L. Couturier, F. Hu, C. Tan, C. Qiao, J. Blume, Y. H. Jiang, P. Chen, and M. Weidemüller. Two-dimensional magneto-optical trap as a source for cold strontium atoms. *Physical Review A*, 96(5):053415, 2017. doi:[10.1103/PhysRevA.96.053415](https://doi.org/10.1103/PhysRevA.96.053415).
- [137] G. Lamporesi, S. Donadello, S. Serafini, and G. Ferrari. Compact high-flux source of cold sodium atoms. *Review of Scientific Instruments*, 84(6):063102, June 2013. doi:[10.1063/1.4808375](https://doi.org/10.1063/1.4808375).
- [138] T. P. Meyrath. Electromagnet design basics for cold atom experiments. *University of Texas, Austin*, 2004. URL <https://june.uoregon.edu/experiments/atom-trap/electromagnets.pdf>.
- [139] D. M. Petković and M. D. Radić. Generalization of helmholtz coil problem. *Serbian Journal of Electrical Engineering*, 12(3):375–384, 2015. doi:[10.2298/SJEE1503375P](https://doi.org/10.2298/SJEE1503375P).
- [140] C. J. H. Pagett, P. H. Moriya, R. Teixeira Celistrino, R. F. Shiozaki, M. Hemmerling, and Ph. W. Courteille. Injection locking of a low cost high power laser diode at 461 nm. *Review of Scientific Instruments*, 87(5):053105, May 2016. doi:[10.1063/1.4947462](https://doi.org/10.1063/1.4947462).
- [141] D. Akamatsu, M. Yasuda, T. Kohno, A. Onae, and F.-L. Hong. A compact light source at 461 nm using a periodically poled LiNbO₃ waveguide for strontium magneto-optical trapping. *Optics Express*, 19(3):2046, January 2011. doi:[10.1364/oe.19.002046](https://doi.org/10.1364/oe.19.002046).
- [142] S. Rota-Rodrigo, B. Gouhier, M. Laroche, J. Zhao, B. Canuel, A. Bertoldi, P. Bouyer, N. Traynor, B. Cadier, T. Robin, et al. Watt-level single-frequency tunable neodymium MOPA fiber laser operating at 915–937 nm. *Optics Letters*, 42(21):4557–4560, 2017. doi:[10.1364/OL.42.004557](https://doi.org/10.1364/OL.42.004557).

- [143] R. W. Boyd. *Nonlinear optics*. Academic press, 2020.
- [144] D. Woll, B. Beier, K.-J. Boller, R. Wallenstein, M. Hagberg, and S. O'Brien. 1 W of blue 465-nm radiation generated by frequency doubling of the output of a high-power diode laser in critically phase-matched LiB_3O_5 . *Optics Letters*, 24(10):691, May 1999. doi:[10.1364/ol.24.000691](https://doi.org/10.1364/ol.24.000691).
- [145] B. Leconte, H. Gilles, T. Robin, B. Cadier, and M. Laroche. 75 W blue light generation at 452 nm by internal frequency doubling of a continuous-wave Nd-doped fiber laser. *Optics Express*, 26(8):10000, April 2018. doi:[10.1364/oe.26.010000](https://doi.org/10.1364/oe.26.010000).
- [146] TA-SHG pro from TOPTICA.
- [147] LEO Solutions.
- [148] B. G. Klappauf, Y. Bidel, D. Wilkowski, T. Chaneliere, and R. Kaiser. Detailed study of an efficient blue laser source by second-harmonic generation in a semimonolithic cavity for the cooling of strontium atoms. *Applied optics*, 43(12):2510, April 2004. doi:[10.1364/ao.43.002510](https://doi.org/10.1364/ao.43.002510).
- [149] M. Su, Y. You, Z. Quan, H. Shen, Q. Li, W. Liu, Y. Qi, and J. Zhou. 321 W high-efficiency continuous-wave green laser produced by single-pass frequency doubling of narrow-linewidth fiber laser. *Applied Optics*, 60(13):3836, April 2021. doi:[10.1364/ao.422514](https://doi.org/10.1364/ao.422514).
- [150] H. Mabuchi, E. S. Poizik, and H. J. Kimble. Blue-light-induced infrared absorption in KNbO_3 . *Journal of the Optical Society of America B*, 11(10):2023, October 1994. doi:[10.1364/josab.11.002023](https://doi.org/10.1364/josab.11.002023).
- [151] J. Wei, H. Lu, P. Jin, and K. Peng. Investigation on the thermal characteristic of MgO:PPSLT crystal by transmission spectrum of a swept cavity. *Optics Express*, 25(4):3545, February 2017. doi:[10.1364/oe.25.003545](https://doi.org/10.1364/oe.25.003545).
- [152] B. Beier, D. Woll, M. Scheidt, K.-J. Boller, and R. Wallenstein. Second harmonic generation of the output of an AlGaAs diode oscillator amplifier system in critically phase

- matched LiB_3O_5 and $-\text{BaB}_2\text{O}_4$. *Applied Physics Letters*, 71(3):315–317, July 1997. doi:[10.1063/1.119559](https://doi.org/10.1063/1.119559).
- [153] X. Wen, Y. Han, and J. Wang. Comparison and characterization of efficient frequency doubling at 397.5 nm with PPKTP, LBO and BiBO crystals. *Laser Physics*, 26(4): 045401, February 2016. doi:[10.1088/1054-660x/26/4/045401](https://doi.org/10.1088/1054-660x/26/4/045401).
- [154] M. Bass, E. W. Van Stryland, D. R. Williams, and W. L. Wolfe. *Handbook of optics*, volume 2. McGraw-Hill New York, 1995.
- [155] S. T. Yang, C. C. Pohalski, E. K. Gustafson, R. L. Byer, R. S. Feigelson, R. J. Raymakers, and R. K. Route. 6.5-W, 532-nm radiation by CW resonant external-cavity second-harmonic generation of an 18-W Nd:YAG laser in LiB_3O_5 . *Optics Letters*, 16(19):1493–1495, 1991. doi:[10.1364/OL.16.001493](https://doi.org/10.1364/OL.16.001493).
- [156] S C. Kumar, G. K. Samanta, and M. Ebrahim-Zadeh. High-power, single-frequency, continuous-wave second-harmonic-generation of ytterbium fiber laser in PPKTP and MgO:sPPLT. *Optics Express*, 17(16):13711, July 2009. doi:[10.1364/oe.17.013711](https://doi.org/10.1364/oe.17.013711).
- [157] S. Vidal, C.-H. Feng, B. Desruelle, G. Santarelli, P. Bouyer, A. Bertoldi, and J. Boullet. High power continuous laser at 461 nm based on a frequency-doubling linear cavity. In *Nonlinear Frequency Generation and Conversion: Materials and Devices XX*, volume 11670, page 116701D. International Society for Optics and Photonics, 2021. doi:[10.1117/12.2580403](https://doi.org/10.1117/12.2580403).
- [158] G. D. Boyd and D. A. Kleinman. Parametric interaction of focused Gaussian light beams. *Journal of Applied Physics*, 39(8):3597–3639, 1968. doi:[10.1063/1.1656831](https://doi.org/10.1063/1.1656831).
- [159] W. P. Risk, W. P. Risk, T. R. Gosnell, and A. V. Nurmikko. *Compact blue-green lasers*. Cambridge University Press, 2003.
- [160] E. S. Polzik and H. J. Kimble. Frequency doubling with KNbO_3 in an external cavity. *Optics Letters*, 16(18):1400–1402, 1991. doi:[10.1364/OL.16.001400](https://doi.org/10.1364/OL.16.001400).

- [161] J. T. Lin, J. L. Montgomery, and K. Kato. Temperature-tuned noncritically phase-matched frequency conversion in LiB_3O_5 crystal. *Optics Communications*, 80(2):159–165, December 1990. doi:[10.1016/0030-4018\(90\)90379-8](https://doi.org/10.1016/0030-4018(90)90379-8).
- [162] G. D. Boyd and D. A. Kleinman. Parametric interaction of focused Gaussian light beams. *Journal of Applied Physics*, 39(8):3597–3639, July 1968. doi:[10.1063/1.1656831](https://doi.org/10.1063/1.1656831).
- [163] Amnon Yariv. *Quantum Electronics, 3rd Edition*. Wiley, 1989. ISBN 978-0-471-60997-1.
- [164] T. W. Hansch and B. Couillaud. Laser frequency stabilization by polarization spectroscopy of a reflecting reference cavity. *Optics Communications*, 35(3):441–444, 1980. doi:[10.1016/0030-4018\(80\)90069-3](https://doi.org/10.1016/0030-4018(80)90069-3).
- [165] J. M. Boon-Engering, W. E. Van der Veer, E. A. J. M. Bente, and W. Hogervorst. Stabilization of an optical cavity containing a birefringent element. *Optics Communications*, 140(4-6):285–288, 1997. doi:[10.1016/S0030-4018\(97\)00196-X](https://doi.org/10.1016/S0030-4018(97)00196-X).
- [166] E. S. Polzik and H. J. Kimble. Frequency doubling with KNbO_3 in an external cavity. *Optics Letters*, 16(18):1400–1402, September 1991. doi:[10.1364/ol.16.001400](https://doi.org/10.1364/ol.16.001400).
- [167] S. Rota-Rodrigo, B. Gouhier, M. Laroche, J. Zhao, B. Canuel, A. Bertoldi, P. Bouyer, N. Traynor, B. Cadier, T. Robin, et al. Watt-level single-frequency tunable neodymium MOPA fiber laser operating at 915–937 nm. *Optics Letters*, 42(21):4557–4560, 2017. doi:[10.1364/OL.42.004557](https://doi.org/10.1364/OL.42.004557).
- [168] U. Eismann, M. Enderlein, K. Simeonidis, F. Keller, F. Rohde, D. Opalevs, M. Scholz, W. Kaenders, and J. Stuhler. Active and passive stabilization of a high-power violet frequency-doubled diode laser. In *CLEO: Applications and Technology*. OSA, 2016. doi:[10.1364/cleo_at.2016.jtu5a.65](https://doi.org/10.1364/cleo_at.2016.jtu5a.65).
- [169] M. Kwon, P. Yang, P. Huft, C. Young, M. Ebert, and M. Saffman. Generation of 14.0 W of single frequency light at 770 nm by intracavity frequency doubling. In *CLEO: Applications and Technology*. OSA, 2020. doi:[10.1364/cleo_at.2020.jtu2f.14](https://doi.org/10.1364/cleo_at.2020.jtu2f.14).

- [170] C. Dixneuf, G. Guiraud, H. Ye, Y. Bardin, M. Goepfner, G. Santarelli, and N. Traynor. Robust 17 W single-pass second-harmonic-generation at 532 nm and relative-intensity-noise investigation. *Optics Letters*, 46(2):408–411, January 2021. doi:[10.1364/ol.415532](https://doi.org/10.1364/ol.415532).
- [171] A. Heinz, J. Trautmann, N. Šantić, A. J. Park, and S. Bloch, I. and Blatt. Crossed optical cavities with large mode diameters. *Optics Letters*, 46(2):250–253, January 2021. doi:[10.1364/ol.414076](https://doi.org/10.1364/ol.414076).
- [172] I. Nosske, L. Couturier, F. Hu, C. Tan, C. Qiao, J. Blume, Y. H. Jiang, P. Chen, and M. Weidemüller. Two-dimensional magneto-optical trap as a source for cold strontium atoms. *Physical Review A*, 96(5):053415, 2017. doi:[10.1103/PhysRevA.96.053415](https://doi.org/10.1103/PhysRevA.96.053415).
- [173] J. Appel, A. MacRae, and A. I. Lvovsky. A versatile digital GHz phase lock for external cavity diode lasers. *Measurement Science and Technology*, 20(5):055302, 2009. doi:[10.1088/0957-0233/20/5/055302/meta](https://doi.org/10.1088/0957-0233/20/5/055302/meta).
- [174] L. Winkelmann, O. Puncken, R. Kluzik, C. Veltkamp, P. Kwee, J. Poeld, C. Bogan, B. Willke, M. Frede, J. Neumann, et al. Injection-locked single-frequency laser with an output power of 220 W. *Applied Physics B*, 102(3):529–538, 2011. doi:[10.1007/s00340-011-4411-9](https://doi.org/10.1007/s00340-011-4411-9).
- [175] C. L. Tang and H. Statz. Phase-locking of laser oscillators by injected signal. *Journal of Applied Physics*, 38(1):323–324, 1967. doi:[10.1063/1.1708974](https://doi.org/10.1063/1.1708974).
- [176] A. E. Siegman. Lasers. *Mill Valley, CA*, 37(208):169, 1986.
- [177] C. J. H. Pagett, P. H. Moriya, R. Celistrino Teixeira, R. F. Shiozaki, M. Hemmerling, and Ph. W. Courteille. Injection locking of a low cost high power laser diode at 461 nm. *Review of Scientific Instruments*, 87(5):053105, 2016. doi:[10.1063/1.4947462](https://doi.org/10.1063/1.4947462).
- [178] V. Schkolnik, J. R. Williams, and N. Yu. Generating 500 mW for laser cooling of strontium atoms by injection locking a high power laser diode. *arXiv preprint*, 2020. URL [arXiv:2004.11732](https://arxiv.org/abs/2004.11732).

- [179] C. E. Wieman and L. Hollberg. Using diode lasers for atomic physics. *Review of Scientific Instruments*, 62(1):1–20, 1991. doi:doi.org/10.1063/1.1142305.
- [180] D. L. Troxel, C. J. Erickson, and D. S. Durfee. Note: Updates to an ultra-low noise laser current driver. *Review of Scientific Instruments*, 82(9):096101, 2011. doi:[10.1063/1.3630950](https://doi.org/10.1063/1.3630950).
- [181] K. G. Libbrecht and J. L. Hall. A low-noise high-speed diode laser current controller. *Review of Scientific Instruments*, 64(8):2133–2135, 1993. doi:[10.1063/1.1143949](https://doi.org/10.1063/1.1143949).
- [182] R. D. Niederriter, V. Der Put, I. Marques, and P. Hamilton. Polarization purity for active stabilization of diode laser injection lock. *arXiv preprint*, 2021. URL [arXiv:2106.06871](https://arxiv.org/abs/2106.06871).
- [183] Th. W. Hänsch, I. S. Shahin, and A. L. Schawlow. High-resolution saturation spectroscopy of the sodium d lines with a pulsed tunable dye laser. *Physical Review Letters*, 27(11):707, 1971. doi:[10.1103/PhysRevLett.27.707](https://doi.org/10.1103/PhysRevLett.27.707).
- [184] H. K. Holt. Theory of laser saturation spectroscopy. *Physical Review Letters*, 29(17):1138, 1972. doi:[10.1103/PhysRevLett.29.1138](https://doi.org/10.1103/PhysRevLett.29.1138).
- [185] G. C. Bjorklund. Frequency-modulation spectroscopy: a new method for measuring weak absorptions and dispersions. *Optics Letters*, 5(1):15–17, 1980. doi:[10.1364/OL.5.000015](https://doi.org/10.1364/OL.5.000015).
- [186] W. Demtröder. *Laser spectroscopy: basic concepts and instrumentation*. Springer Science & Business Media, 2013.
- [187] Kurt Richard Vogel. *Laser cooling on a narrow atomic transition and measurement of the two-body cold collision loss rate in a strontium magneto-optical trap*. University of Colorado at Boulder, 1999.
- [188] P. W. Milonni and J. H. Eberly. *Lasers* john wiley and sons. New York, 1988.

- [189] N. V. Vitanov, B. W. Shore, L. Yatsenko, K. Böhmer, T. Halfmann, T. Rickes, and K. Bergmann. Power broadening revisited: theory and experiment. *Optics Communications*, 199(1-4):117–126, 2001. doi:[10.1016/S0030-4018\(01\)01495-X](https://doi.org/10.1016/S0030-4018(01)01495-X).
- [190] JM Farr and WR Hindmarsh. Collision broadening in the strontium resonance line, λ 4607 aa. *Journal of Physics B: Atomic and Molecular Physics*, 4(4):568, 1971. doi:[10.1088/0022-3700/4/4/019](https://doi.org/10.1088/0022-3700/4/4/019).
- [191] R. W. P. Drever, J. L. Hall, F. V. Kowalski, J. Hough, G. M. Ford, A. J. Munley, and H. Ward. Laser phase and frequency stabilization using an optical resonator. *Applied Physics B*, 31(2):97–105, 1983. doi:[10.1007/BF00702605](https://doi.org/10.1007/BF00702605).
- [192] E. D. Black. An introduction to Pound–Drever–Hall laser frequency stabilization. *American journal of physics*, 69(1):79–87, 2001. doi:[10.1119/1.1286663](https://doi.org/10.1119/1.1286663).
- [193] R. W. Fox, C. W. Oates, and L. W. Hollberg. 1. Stabilizing diode lasers to high-finesse cavities. In *Experimental Methods in the Physical Sciences*, volume 40, pages 1–46. Elsevier, 2003. doi:[10.1016/S1079-4042\(03\)80017-6](https://doi.org/10.1016/S1079-4042(03)80017-6).
- [194] See menlosystems.com/products/ultrastable-lasers/orc-cylindric-orc-cubic/.
- [195] E. A. Donley, T. P. Heavner, F. Levi, M. O. Tataw, and S. R. Jefferts. Double-pass acousto-optic modulator system. *Review of scientific instruments*, 76(6):063112, 2005. doi:[10.1063/1.1930095](https://doi.org/10.1063/1.1930095).
- [196] T-REFIMEVE projet: <http://www.refimeve.fr>.
- [197] S. Stellmer, F. Schreck, and T. C. Killian. Degenerate quantum gases of strontium. *Annual Review of Cold Atoms and Molecules*, pages 1–80, 2014. doi:[10.1142/9789814590174_0001](https://doi.org/10.1142/9789814590174_0001).
- [198] A. Bertoldi, C.-H. Feng, H. Eneriz, M. Carey, D.S. Naik, J. Junca, X. Zou, D. O. Sabulsky, B. Canuel, P. Bouyer, et al. A control hardware based on a field programmable gate array for experiments in atomic physics. *Review of Scientific Instruments*, 91(3):033203, 2020. doi:[10.1063/1.5129595](https://doi.org/10.1063/1.5129595).

- [199] K. E. Gibble, S. Kasapi, and S. Chu. Improved magneto-optic trapping in a vapor cell. *Optics Letters*, 17(7):526–528, 1992. doi:[10.1364/OL.17.000526](https://doi.org/10.1364/OL.17.000526).
- [200] G. Lamporesi, S. Donadello, S. Serafini, and G. Ferrari. Compact high-flux source of cold sodium atoms. *Review of Scientific Instruments*, 84(6):063102, 2013. doi:[10.1063/1.4808375](https://doi.org/10.1063/1.4808375).
- [201] M. Barbiero. *Novel techniques for a Strontium Optical Lattice Clock*. PhD thesis, Polytechnic University of Turin, 2019.
- [202] D. Banahene-Sabulsky. *Constraining theories of modified gravity with atom interferometry*. PhD thesis, Imperial College London, 2018.
- [203] G. Santarelli, Ph. Laurent, P. Lemonde, A. Clairon, A. G. Mann, S. Chang, A. N. Luiten, and C. Salomon. Quantum projection noise in an atomic fountain: A high stability cesium frequency standard. *Physical Review Letters*, 82:4619–4622, Jun 1999. doi:[10.1103/PhysRevLett.82.4619](https://doi.org/10.1103/PhysRevLett.82.4619).
- [204] J. M. Kohel, J. Ramirez-Serrano, R. J. Thompson, L. Maleki, J. L. Bliss, and K. G. Libbrecht. Generation of an intense cold-atom beam from a pyramidal magneto-optical trap: experiment and simulation. *Journal of the Optical Society of America B*, 20(6):1161, June 2003. doi:[10.1364/josab.20.001161](https://doi.org/10.1364/josab.20.001161).
- [205] M. Barbiero, M. G. Tarallo, D. Calonico, F. Levi, G. Lamporesi, and G. Ferrari. Sideband-enhanced cold atomic source for optical clocks. *Physical Review Applied*, 13(1), January 2020. doi:[10.1103/physrevapplied.13.014013](https://doi.org/10.1103/physrevapplied.13.014013).
- [206] S. Donadello. A compact high-flux source of cold sodium atoms. Master’s thesis, University of Trento, 2012.
- [207] Runge-Kutta method realized with Python code: www.notebooks/projectile-motion.ipynb.
- [208] H. J. W. Muller-Kirsten. *Basics of statistical physics*. World Scientific Publishing Company, 2013.

- [209] W. H. Press, S. A. Teukolsky, W. T. Vetterling, and B. P. Flannery. Numerical recipes in C, 1988.
- [210] J. M. Robinson, E. Oelker, W. R. Milner, W. Zhang, T. Legero, D. G. Matei, F. Riehle, U. Sterr, and J. Ye. Crystalline optical cavity at 4 k with thermal-noise-limited instability and ultralow drift. *Optica*, 6(2):240, February 2019. doi:[10.1364/optica.6.000240](https://doi.org/10.1364/optica.6.000240).
- [211] H. Ritsch, P. Domokos, F. Brennecke, and T. Esslinger. Cold atoms in cavity-generated dynamical optical potentials. *Reviews of Modern Physics*, 85(2):553–601, April 2013. doi:[10.1103/revmodphys.85.553](https://doi.org/10.1103/revmodphys.85.553).
- [212] P. Haslinger, M. Jaffe, V. Xu, O. Schwartz, M. Sonnleitner, M. Ritsch-Marte, H. Ritsch, and H. Müller. Attractive force on atoms due to blackbody radiation. *Nature physics*, 14(3):257–260, December 2017. doi:[10.1038/s41567-017-0004-9](https://doi.org/10.1038/s41567-017-0004-9).
- [213] Z. Pagel, W. Zhong, R. H. Parker, C. T. Olund, N. Y. Yao, and H. Müller. Symmetric bloch oscillations of matter waves. *Physical Review A*, 102(5):053312, 2020. doi:[10.1103/PhysRevA.102.053312](https://doi.org/10.1103/PhysRevA.102.053312).
- [214] S.-w. Chiow, T. Kovachy, H.-C. Chien, and M. A. Kasevich. $102 \hbar k$ large area atom interferometers. *Physical Review Letters*, 107(13):130403, 2011. doi:[10.1103/PhysRevLett.107.130403](https://doi.org/10.1103/PhysRevLett.107.130403).
- [215] P. Berg, S. Abend, G. Tackmann, C. Schubert, E. Giese, W. P. Schleich, F. A. Narducci, W. Ertmer, and E. M. Rasel. Composite-light-pulse technique for high-precision atom interferometry. *Physical Review Letters*, 114(6):063002, 2015. doi:[10.1103/PhysRevLett.114.063002](https://doi.org/10.1103/PhysRevLett.114.063002).
- [216] M. Dovale-Álvarez, D. D. Brown, A. W. Jones, C. M. Mow-Lowry, H. Miao, and A. Freise. Fundamental limitations of cavity-assisted atom interferometry. *Physical Review A*, 96(5):053820, nov 2017. doi:[10.1103/physreva.96.053820](https://doi.org/10.1103/physreva.96.053820).
- [217] A. Bertoldi, C.-H. Feng, D. S. Naik, B. Canuel, P. Bouyer, and M. Prevedelli. Fast control of atom-light interaction in a narrow linewidth cavity. *Physical Review Letters*, 127:013202, June 2021. doi:[10.1103/PhysRevLett.127.013202](https://doi.org/10.1103/PhysRevLett.127.013202).

- [218] P. Hamilton, M. Jaffe, J. M. Brown, L. Maisenbacher, B. Estey, and H. Müller. Atom interferometry in an optical cavity. *Physical Review Letters*, 114(10):100405, mar 2015. doi:[10.1103/physrevlett.114.100405](https://doi.org/10.1103/physrevlett.114.100405).
- [219] Matt Jaffe, V. Xu, P. Haslinger, H. Müller, and P. Hamilton. Efficient adiabatic spin-dependent kicks in an atom interferometer. *Physical Review Letters*, 121(4):040402, jul 2018. doi:[10.1103/physrevlett.121.040402](https://doi.org/10.1103/physrevlett.121.040402).
- [220] S. L. Kristensen, M. Jaffe, V. Xu, C. D. Panda, and H. Müller. Raman transitions driven by phase-modulated light in a cavity atom interferometer. *Physical Review A*, 103:023715, Feb 2021. doi:[10.1103/PhysRevA.103.023715](https://doi.org/10.1103/PhysRevA.103.023715).
- [221] R. Nourshargh, S. Lellouch, S. Hedges, M. Langlois, K. Bongs, and M. Holynski. Circulating pulse cavity enhancement as a method for extreme momentum transfer atom interferometry. 2020. URL <https://arxiv.org/abs/2012.06426>.
- [222] I. Riou, N. Mielec, G. Lefèvre, M. Prevedelli, A. Landragin, P. Bouyer, A. Bertoldi, R. Geiger, and B. Canuel. A marginally stable optical resonator for enhanced atom interferometry. *Journal of Physics B*, 50(15):155002, jul 2017. doi:[10.1088/1361-6455/aa7592](https://doi.org/10.1088/1361-6455/aa7592).
- [223] B. Canuel et al. Exploring gravity with the MIGA large scale atom interferometer. *Scientific Reports*, 8(1):14064, sep 2018. doi:[10.1038/s41598-018-32165-z](https://doi.org/10.1038/s41598-018-32165-z).
- [224] K.-P. Marzlin and J. Audretsch. State independence in atom interferometry and insensitivity to acceleration and rotation. *Physical Review A*, 53(1):312–318, January 1996. doi:[10.1103/physreva.53.312](https://doi.org/10.1103/physreva.53.312).
- [225] T. Lévèque, A. Gauguet, F. Michaud, F. Pereira Dos Santos, and A. Landragin. Enhancing the area of a Raman atom interferometer using a versatile double-diffraction technique. *Physical Review Letters*, 103(8):080405, August 2009. doi:[10.1103/physrevlett.103.080405](https://doi.org/10.1103/physrevlett.103.080405).
- [226] C. Schubert, D. Schlippert, S. Abend, E. Giese, A. Roura, W. P. Schleich, W. Ertmer,

- and E. M. Rasel. Scalable, symmetric atom interferometer for infrasound gravitational wave detection. *arXiv preprint*, 2019. URL <https://arxiv.org/abs/1909.01951>.
- [227] S. M. Dickerson, J. M. Hogan, A. Sugarbaker, D. M. S. Johnson, and M. A. Kasevich. Multiaxis inertial sensing with long-time point source atom interferometry. *Physical Review Letters*, 111(8):083001, aug 2013. doi:[10.1103/physrevlett.111.083001](https://doi.org/10.1103/physrevlett.111.083001).
- [228] S. L. Campbell, R. B. Hutson, G. E. Marti, A. Goban, N. Darkwah Oppong, R. L. McNally, L. Sonderhouse, J. M. Robinson, W. Zhang, B. J. Bloom, and J. Ye. A Fermi-degenerate three-dimensional optical lattice clock. *Science*, 358(6359):90–94, oct 2017. doi:[10.1126/science.aam5538](https://doi.org/10.1126/science.aam5538).
- [229] P. W. Graham, J. M. Hogan, M. A. Kasevich, and S. Rajendran. New method for gravitational wave detection with atomic sensors. *Physical Review Letters*, 110(17):171102, apr 2013. doi:[10.1103/physrevlett.110.171102](https://doi.org/10.1103/physrevlett.110.171102).
- [230] L. Hu, N. Poli, L. Salvi, and G. M. Tino. Atom interferometry with the Sr optical clock transition. *Physical Review Letters*, 119(26):263601, dec 2017. doi:[10.1103/physrevlett.119.263601](https://doi.org/10.1103/physrevlett.119.263601).
- [231] The National Institute of Standards and Technology (NIST) database. available at <http://www.nist.gov/pml/data>.
- [232] A. D. Ludlow. *The Strontium Optical Lattice Clock: Optical Spectroscopy with Sub-Hertz Accuracy*. PhD thesis, University of Colorado, 2008.
- [233] H. Müntinga, H. Ahlers, M. Krutzik, A. Wenzlawski, S. Arnold, D. Becker, K. Bongs, H. Dittus, H. Duncker, N. Gaaloul, C. Gherasim, E. Giese, C. Grzeschik, T. W. Hänsch, O. Hellmig, W. Herr, S. Herrmann, E. Kajari, S. Kleinert, C. Lämmerzahl, W. Lewoczko-Adamczyk, J. Malcolm, N. Meyer, R. Nolte, A. Peters, M. Popp, J. Reichel, A. Roura, J. Rudolph, M. Schiemangk, M. Schneider, S. T. Seidel, K. Sengstock, V. Tamma, T. Valenzuela, A. Vogel, R. Walser, T. Wendrich, P. Windpassinger, W. Zeller, T. van Zoest, W. Ertmer, W. P. Schleich, and E. M. Rasel. Interferometry with Bose-Einstein

- condensates in microgravity. *Physical Review Letters*, 110(9):093602, February 2013. doi:[10.1103/physrevlett.110.093602](https://doi.org/10.1103/physrevlett.110.093602).
- [234] T. Kovachy, J. M. Hogan, A. Sugarbaker, S. M. Dickerson, C. A. Donnelly, C. Overstreet, and M. A. Kasevich. Matter wave lensing to picokelvin temperatures. *Physical Review Letters*, 114(14):143004, apr 2015. doi:[10.1103/physrevlett.114.143004](https://doi.org/10.1103/physrevlett.114.143004).
- [235] S. Loriani, D. Schlippert, C. Schubert, S. Abend, H. Ahlers, W. Ertmer, J. Rudolph, J. M. Hogan, M. A. Kasevich, E. M. Rasel, and N. Gaaloul. Atomic source selection in space-borne gravitational wave detection. *New Journal of Physics*, 21(6):063030, June 2019. doi:[10.1088/1367-2630/ab22d0](https://doi.org/10.1088/1367-2630/ab22d0).
- [236] A. V. Taichenachev, V. I. Yudin, C. W. Oates, C. W. Hoyt, Z. W. Barber, and L. Hollberg. Magnetic field-induced spectroscopy of forbidden optical transitions with application to lattice-based optical atomic clocks. *Physical Review Letters*, 96(8):083001, mar 2006. doi:[10.1103/physrevlett.96.083001](https://doi.org/10.1103/physrevlett.96.083001).
- [237] R. Long, A. K. Tuchman, and M. A. Kasevich. Multiple frequency modulation for low-light atom measurements in an optical cavity. *Optics Letters*, 32(17):2502, aug 2007. doi:[10.1364/ol.32.002502](https://doi.org/10.1364/ol.32.002502).
- [238] L. Salvi, N. Poli, V. Vuletić, and G. M. Tino. Squeezing on momentum states for atom interferometry. *Physical Review Letters*, 120(3):033601, jan 2018. doi:[10.1103/physrevlett.120.033601](https://doi.org/10.1103/physrevlett.120.033601).
- [239] A. D Ludlow. The strontium optical lattice clock: optical spectroscopy with sub-Hertz accuracy, 2008.
- [240] H. Müller, S. W. Chiow, and S. Chu. Atom-wave diffraction between the Raman-Nath and the Bragg regime: Effective Rabi frequency, losses, and phase shifts. *Physical Review A*, 77(2):023609, February 2008. doi:[10.1103/physreva.77.023609](https://doi.org/10.1103/physreva.77.023609).
- [241] J. R. Johansson, P. D. Nation, and F. Nori. Qutip: An open-source python framework for the dynamics of open quantum systems. *Computer Physics Communications*, 183(8):1760–1772, 2012. doi:[10.1016/j.cpc.2012.02.021](https://doi.org/10.1016/j.cpc.2012.02.021).

- [242] J. Li, J. Grumer, W. Li, M. Andersson, T. Brage, R. Hutton, P. Jönsson, Y. Yang, and Y. Zou. Theoretical investigation of magnetic-field-induced $2p^5 3s \ ^3P_{0,2} - 2p^6 \ ^1S_0$ transitions in Ne-like ions without nuclear spin. *Physical Review A*, 88(1):013416, 2013. doi:[10.1103/PhysRevA.88.013416](https://doi.org/10.1103/PhysRevA.88.013416).
- [243] B. Lu, Y. Wang, J. Han, S. Zhang, J. Li, and H. Chang. Exploration of the magnetic-field-induced $^3P_0 - 5s^2 \ ^1S_0$ forbidden transition in bosonic Sr atom. *Journal of Physics Communications*, 1(5):055017, 2017. doi:[10.1088/2399-6528/aa9da5](https://doi.org/10.1088/2399-6528/aa9da5).
- [244] S. G. Porsev, M. G. Kozlov, and Y. G. Rakhlina. High-precision calculations of the $^3,1P_0^1 \rightarrow ^1S_0$ E1 amplitudes for magnesium, calcium, and strontium. *Journal of Experimental and Theoretical Physics Letters*, 72(12):595–598, 2000. doi:[10.1134/1.1351197](https://doi.org/10.1134/1.1351197).
- [245] S. Loriani, D. Schlippert, C. Schubert, S. Abend, H. Ahlers, W. Ertmer, J. Rudolph, J. M. Hogan, M. A. Kasevich, E. M. Rasel, et al. Atomic source selection in spaceborne gravitational wave detection. *New Journal of Physics*, 21(6):063030, 2019. doi:[10.1088/1367-2630/ab22d0/meta](https://doi.org/10.1088/1367-2630/ab22d0/meta).
- [246] G. Condon, A. Fortun, J. Billy, and D. Guéry-Odelin. Phase-space manipulations of many-body wave functions. *Physical Review A*, 90:063616, Dec 2014. doi:[10.1103/PhysRevA.90.063616](https://doi.org/10.1103/PhysRevA.90.063616).
- [247] P. Pedri, D. Guéry-Odelin, and S. Stringari. Dynamics of a classical gas including dissipative and mean-field effects. *Physical Review A*, 68:043608, Oct 2003. doi:[10.1103/PhysRevA.68.043608](https://doi.org/10.1103/PhysRevA.68.043608).
- [248] V. I. Borovkov and I. V. Yeletsikh. A generator for the fast switching-off of the magnetic field in experimental observations of the spin state dynamics of radical ion pairs in low magnetic fields. *Instruments and Experimental Techniques*, 48(1):75–77, 2005. doi:[10.1007/s10786-005-0013-2](https://doi.org/10.1007/s10786-005-0013-2).
- [249] C.-H. Feng, S. Vidal, P. Robert, P. Bouyer, B. Desruelle, M. Prevedelli, G. Boullet, J. and Santarelli, and A. Bertoldi. High power continuous laser at 461 nm based on a

- compact and high-efficiency frequency-doubling linear cavity. *Optics Express*, 29(17): 27760–27767, 2021. doi:[10.1364/OE.433179](https://doi.org/10.1364/OE.433179).
- [250] M. Prevedelli, A. Bertoldi, C.-H. Feng, H. Eneriz Imaz, M. Carey, D. S. Naik, J. Junca, X. Zou, D. O. Sabulsky, B. Canuel, and P. Bouyer. Yet another control system for AMO physics, December 2019. URL <https://zenodo.org/record/3571496>.
- [251] C.-H. Feng, P. Robert, P. Bouyer, M. Prevedelli, and A. Bertoldi. Double-frequency Zeeman slower for a cold strontium atom source (in preparation).